

Prepared for Normandeau Associates, Inc., Bedford, NH
as Appendix 3 to their report: *316(a) Demonstration in Support of a
Request for Increased Discharge Temperature Limits at Vermont Yankee
Nuclear Power Station During May Through October*

Hydrothermal Modeling of the Cooling Water Discharge from the Vermont Yankee Power Plant to the Connecticut River

ASA Report 02-088

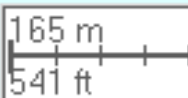
Final Report

April 2004 (Revision)

Craig Swanson
Hyun-Sook Kim
Sankar Subbayya
Paul Hall
Jiganesh Patel



*Applied Science Associates, Inc.
70 Dean Knauss Drive
Narragansett, RI 02882*



Executive Summary

The Vermont Yankee Nuclear Power Station (Vermont Yankee), an electric-generating station, is located on the Connecticut River in Vermont above the Vernon Dam. Vermont Yankee uses a sophisticated cooling system that varies from an open cycle, once-through cooling water configuration to a closed cycle, cooling tower configuration that recirculates the cooling water. In support of a request to increase discharge temperature limits during the summer period pursuant to a 316(a) of the Clean Water Act, Applied Science Associates, Inc. (ASA) was contracted to assess the thermal discharge from the plant and its effects on the River using a state-of-the-art, boundary fitted computer simulation model accepted by the United States Environmental Protection Agency and numerous state regulators.

The model was calibrated and confirmed to data collected from a set of continuous monitoring thermistors as part of a field program from May through October 2002. The data also included river flows and water temperatures obtained from permanently deployed instruments used in Vermont Yankee's operations. The model calibration and confirmation exercises used data sets acquired in August and June – July 2002, respectively. The August calibration period was chosen to be representative of warm river temperatures and low river flows. The June – July confirmation period was chosen to include warm river temperatures occurring during fishway operations.

Results of the calibration and confirmation indicated that the model predicted both flows and temperatures well. The flow predictions for the calibration and confirmation periods were very successful, exhibiting RME and ECV values less than 3% and 4%, respectively, which were smaller (better) than U. S. EPA guidance levels (30% and 10%, respectively). Correlations between the prediction and observations were excellent, with r^2 values of 0.92 and 0.98 for the calibration and confirmation periods, respectively, which were larger (better) than the guidance level of 0.88.

The calibration results indicated that temperature predictions were also good. Best results were obtained at the upper layer, but they became somewhat reduced with depth. Squared correlation coefficients at the surface were usually larger (better) than the U. S. EPA guidance level of 0.71, and the correlations became smaller with depth. However, RME and ECV for all three layers ranged between 0 and 5.6%, showing that they were smaller (better) than the EPA guidance levels (25% and 45%, respectively) and suggesting that the predictions throughout the water column were acceptable.

The confirmation results indicated that the model performed excellently in simulating the thermal conditions of June – July 2002. The surface temperature predictions showed RME values ranging between 0.6% to 3.0% compared to the guidance level of 25%, ECV values between 2.6% and 8.1% compared to the guidance level of 45%, and r^2 greater than 0.66 compared to the guidance level of 0.71. Similar variations in model error statistics were found at the middle and bottom layers. Based on the successful calibration and confirmation, the model could then be used for predictions under selected plant and river conditions.

Two sets of scenario simulations were performed for the August and June – July periods separately, to investigate the effect of proposed new temperature limits within the portion of the lower Vernon Pool affected by the Vermont Yankee discharge during the summer permit compliance period and during the period of fishway operation, respectively. For the August period, a 1°F (0.6°C) increase from 2°F (1.1°C) to 3°F (1.7°C) resulted in a marginal increase in the temperature of the water column or on the bottom. For worst conditions occurring only 1% of the time, 30% of the bottom area increased by at least 0.3°C (0.5°F) and 20% increased by a maximum of 0.4°C (0.7°F). For typical conditions occurring 50% of the time, 30% of the bottom area increased by at least 0.1°C (0.2°F), 20% increased by at least 0.2°C (0.4°F) and 10% increased by a maximum of 0.6°C (1.1°F). Similar results were obtained for changes in water column volume.

Temperature predictions during June and July when the fishway was operating with warmest river temperatures indicated that a 1°F increase in temperature rise generally resulted in similar increases (0.4°C) [0.7°F] in water temperature regardless of whether conditions were worst (1% of the time), infrequent (10% of the time) or typical (50% of the time). There was a slight increase in effects under typical conditions of higher river flow and therefore higher plant flow. Results also indicated that the ambient water temperature primarily influenced the temperature in the fishway rather than Vermont Yankee's rejected heat.

Based on the hydrothermal modeling results, a 1°F (0.6°C) increase in the permit limit from 2°F (1.1°C) to 3°F (1.7°C) resulted in *de minimus* changes in the thermal structure of the Vernon Pool.

Table of Contents

1. Introduction.....	1
2. Description of Study Area	2
3. Thermal Plume Mapping	4
3.1 Historical Studies.....	4
3.2 2002 Field Data	4
3.2.1 Data Descriptions.....	4
3.2.1.1 Vernon Pool Temperature.....	4
3.2.1.2 River Flow and Temperature	7
3.2.1.3 Plant Operations.....	8
3.2.1.4 Meteorological Conditions	8
3.2.2 August 2002	10
3.2.2.1 Lower Vernon Pool Temperatures.....	10
3.2.2.2 River Flow and Temperature	18
3.2.2.3 Vermont Yankee Station Operations	19
3.2.2.4 Meteorological Conditions	19
3.2.3 June - July 2002	20
3.2.3.1 Vernon Pool Temperatures	20
3.2.3.2 Plant Operations.....	24
3.2.3.3 Meteorological Conditions	24
4. Hydrothermal Model.....	25
4.1 Model Description - WQMAP	25
4.2 WQMAP System.....	27
4.3 Application to the Vernon Pool.....	28
4.3.1 Grid Generation.....	28
4.3.2 Bathymetry	31
4.3.3 Boundary Conditions	31
4.3.3.1 Model Calibration and Confirmation.....	32
4.3.3.2 Scenario Simulations	36
4.4 Model Calibration and Confirmation	40
4.4.1 Calibration to August 2002 Period.....	43
4.4.2 Confirmation to June – July 2002 Period.....	53
4.4.3 Discussion	62
5. Thermal Plume Simulations.....	65
6. Conclusions.....	73
7. References.....	75

Appendices

Appendix A August 2002 Data
Appendix B June - July 2002 Data
Appendix C Hydrodynamic Model Description (Muin and Spaulding, 1997)
Appendix D Development of an Estuarine Thermal Environmental Model in a Boundary-Fitted, Curvilinear Coordinate System (Mendelsohn, 1998).
Appendix E WQMAP Description

List of Figures

Figure 3-1. Location of thermistor stations for long-term thermistor deployment. The lower image is a detailed view of lower Vernon Pool immediately upstream of Vernon Dam. .	6
Figure 3-2. Location of Orange Municipal Airport met station relative to Vermont Yankee.	9
Figure 3-3. A comparison of air temperature and atmospheric pressure at Orange, MA and Vermont Yankee for the August survey period. Pressure records have been corrected for the difference in elevation between the two locations.....	10
Figure 3-4. Temperature profiles for the C stations on 8/05/02 17:00.	12
Figure 3-5. Temperature profiles for the D stations on 8/05/02 17:00.	12
Figure 3-6. Temperature profiles for the E stations on 8/05/02 17:00.....	13
Figure 3-7. Temperature profiles for the C stations on 8/06/02 17:00.	13
Figure 3-8. Temperature profiles for the D stations on 8/06/02 17:00.	14
Figure 3-9. Temperature profiles for the E stations on 8/06/02 17:00.....	14
Figure 3-10. Temperature profiles for the C stations on 8/10/02 17:00.	15
Figure 3-11. Temperature profiles for the D stations on 8/10/02 17:00.	15
Figure 3-12. Temperature profiles for the E stations on 8/10/02 17:00.....	16
Figure 3-13. Temperatures recorded by surface thermistors of C (top), D (middle) and E (bottom) stations during the August survey period. Each of the above plots therefore represents the time evolution of an across-channel transect at the surface of Vernon Pool at the given location.....	17
Figure 3-14. Temperatures recorded by surface thermistors of ‘1/2’ (top), ‘3/4’ (middle) and ‘5/6’ (bottom) stations during the August survey period. Each of the above plots therefore represents the time evolution of an along-channel transect at the surface of Vernon Pool at the given location.	18
Figure 3-15. Temperatures recorded by surface thermistors of C (top), D (middle) and E (bottom) stations during the June-July survey period. Each of the above plots therefore represents the time evolution of an across-channel transect at the surface of Vernon Pool at the given location.....	22
Figure 3-16. Temperatures recorded by surface thermistors of ‘1/2’ (top), ‘3/4’ (middle) and ‘5/6’ (bottom) stations during the August survey period. Each of the above plots therefore represents the time evolution of an along-channel transect at the surface of Vernon Pool at the given location.	23
Figure 4-1. Model grid for the Vernon Pool study area: Blue shaded cells represent downstream boundary and green shaded cells represent intake, discharge and upstream river boundary.....	30
Figure 4-2. Model bathymetry of the lower area of the study domain.	32
Figure 4-3. Vermont Yankee Station operations with computed rejected heat for the calibration period from 1 to 24 August 2002.	34
Figure 4-4. Vermont Yankee Station operations with computed rejected heat for the confirmation period from 25 June to 9 July.	35
Figure 4-5. Typical daily variations of air temperature and solar radiation for the August and June-July periods.	37
Figure 4-6. Downstream flow comparison between the prediction and observations.....	44
Figure 4-7. Comparison of observed (thick) and simulated temperatures (thin) at the surface, middle and bottom layers for string C3.	46

Figure 4-8. Comparison of observed (thick) and simulated temperatures (thin) at the surface, middle and bottom layers for string D3.....	47
Figure 4-9. Comparison of observed (thick) and simulated temperatures (thin) at the surface, middle and bottom layers for string E3.	48
Figure 4-10. Comparison of observed (thick) and simulated temperatures (thin) for monitoring stations 7 (top) and 3 (bottom).....	49
Figure 4-11. Comparison of the observed (thick) and predicted flows (thin-dashed) across the Vernon Dam.	54
Figure 4.12 Comparison of the observed (thick line) and predicted (thin-dashed) temperatures at the surface, mid and bottom layers at station C3.....	56
Figure 4.13 Comparison of the observed (thick line) and predicted (thin-dashed) temperatures at the surface, mid and bottom layers at station D5.....	57
Figure 4.14 Comparison of the observed (thick line) and predicted (thin-dashed) temperatures at the surface, mid and bottom layers at station E1.....	58
Figure 4-15. Comparison of predicted and observed temperatures at the fishway during the confirmation period.	62
Figure 5-1. Predicted surface temperature distribution for August scenario 50%-3°F.	65
Figure 5-2. Predicted middle-layer temperature distribution for August scenario 50%-3°F..	66
Figure 5-3. Predicted bottom-layer temperature distribution for August scenario 50%-3°F. 66	
Figure 5-4. Model grid area (shaded in purple) used for the computation of the thermally effected area.....	68
Figure 5-5. Mean percent bottom area coverages versus temperature for the four August scenarios.	69
Figure 5-6. Mean percent water column volume coverages versus temperature for the four August scenarios.....	69
Figure 5-7 Maximum percent bottom area coverages versus temperature for the four August scenarios.	70
Figure 5.8 Maximum percent volume coverages versus temperature for the four August scenarios.	71
Figure 5-9. Percent time coverages of mean surface-layer temperature at the fishway.	72

List of Tables

Table 3-1. Location and total water depth for field study thermistor stations.	7
Table 3-2. Thermistor depths by station.	7
Table 3-3. Statistical analysis of meteorological data for the summer survey period.	20
Table 3-4. Statistical analysis of meteorological data for the summer survey period.	24
Table 4-1. Summary of parameters for August scenarios. Vermont Yankee Temp denotes the plant discharge temperature.	38
Table 4-2. Summary of parameters for the June –July scenarios. Vermont Yankee Temp denotes the plant discharge temperature.	39
Table 4-3. Summary of model parameters used in the calibration and testing.	40
Table 4-4. Model calibration and confirmation guidance (McCutcheon et al., 1990).	43
Table 4-5. Quantitative comparisons of predicted and observed surface temperatures for the calibration period from 1 to 24 August 2002.	51
Table 4-6. Quantitative comparisons of predicted and observed temperatures at the middle layer for the calibration period from 1 to 24 August 2002.	52
Table 4-7. Quantitative comparisons of the predicted and observed bottom temperatures for the calibration period from 1 to 24 August 2002.	53
Table 4-8. Quantitative comparisons of the predicted and observed temperatures at the surface layer for the confirmation period from 25 June to 9 July 2002.	59
Table 4-9. Quantitative comparisons of the predicted and observed temperatures at the middle depth for the confirmation period from 25 June to 9 July 2002. N/A stands for no data available.	60
Table 4-10 Quantitative comparisons of the predicted and observed temperatures at the bottom layer for the confirmation period from 25 June to 9 July 2002.	61
Table 4-11. Vernon Pool hydrothermal model calibration and confirmation evaluation in comparison with EPA guidance (McCutcheon et al., 1990)	63

1. Introduction

Entergy Nuclear Vermont Yankee, LLC (Entergy VY) owns the Vermont Yankee Nuclear Power Station (Vermont Yankee), an electric-generating station located in Vermont, on the Connecticut River (River) above the Vernon Dam, a hydroelectric facility owned by PG&E National Energy Group. Vermont Yankee uses a sophisticated cooling system that varies from an open cycle, once-through cooling water configuration to a closed cycle, cooling tower configuration that recirculates the cooling water. In support of a request to increase discharge temperature limits during the summer period pursuant to a 316(a) of the Clean Water Act, Applied Science Associates, Inc. (ASA) was contracted through Normandeau Associates, Inc. to assess the thermal discharge from the plant and its effects on the River using a state-of-the-art, boundary fitted computer simulation model accepted by the United States Environmental Protection Agency and numerous state regulators.

The purpose of this study was to determine what effects, if any, the increased Vermont Yankee thermal discharge would have on the thermal structure of the River, particularly during the late summer period of low River flow and warm River temperatures. The study included a field program (i.e., collection) component to characterize the physical thermal regime in the Vernon Pool. A hydrothermal modeling study designed to characterize the circulation and temperature distribution in the River followed. The modeling study was designed to evaluate the potential effects of Vermont Yankee's proposed increase on the temperature distribution in the River under expected and worst-case conditions.

This report documents the hydrothermal model application, calibration and confirmation, which then provided predictions of the thermal regime in the Vernon Pool under relevant scenarios. Section 1 provides an introduction to the study, including background and purpose, and structure of the report. Section 2 describes the study area, the Vernon Pool, on the Connecticut River above the Vernon Dam and the relevant information about dam and plant operations and layout. Section 3 describes the thermal plume mapping and other field studies and data used in the modeling study. Section 4 describes the hydrothermal model (BFHYDRO) and the Water Quality Mapping and Analysis Package (WQMAP) system, of which the model is a part. This section also describes the application of the model to the Vernon Pool and the results of the calibration and confirmation procedures. Section 5 presents the thermal plume simulations for a series of selected environmental and plant operating conditions. Section 6 presents a summary and conclusions. Section 7 lists references. Presentations of the environmental, dam and plant data during selected periods are included as appendices as are descriptions of the BFHYDRO model and the WQMAP system.

2. Description of Study Area

Vernon Pool is located on the Connecticut River and situated on the border of Vermont and New Hampshire. The entire pool is 41.8 km (26 mi) long and 770 m (0.48 mi) in maximum width, with a total volume of $49.3 \times 10^6 \text{ m}^3$ ($1.7 \times 10^9 \text{ ft}^3$). The area of interest for this study is the lower portion of the pool including the area from the Vernon Dam at the southern extent to 7.2 km (4.5 mi) north.

Vermont Yankee is located about 840 m (0.5 mile) north of the Vernon Dam on the west shore (Vermont). The plant discharges heated water with a maximum heat rejection of 1,100 megawatts (MW) thermal (in June 2002, for example), by taking relatively cool river water from an intake structure 570 m (1,870 ft) north of the discharge.

The Connecticut River flows, and therefore the flows through the Vernon Pool past Vermont Yankee, are highly regulated by hydroelectric generation activities both upstream and downstream from Vermont Yankee. Five hydroelectric dams and three storage dams exist on the main-stem Connecticut River upstream from Vernon Dam, and there are three hydroelectric dams and one pumped-storage facility downstream. The U. S. Geological Survey (USGS) operated a Connecticut River gauging station located just below Vernon Dam from 1936 until 1973. Operation of the Northfield Mountain Pumped Storage generating facility (downstream from Vernon Dam) and modification of the next downstream dam at Turner's Falls reduced the efficacy of the stage height-discharge rating and USGS ceased use of the gauging station in 1973.

Vernon Station, a 26 MW hydroelectric generating facility located on the west (VT) side of the 366 m (1,200-ft) long Vernon Dam, passes about $283 \text{ m}^3/\text{s}$ ($10,000 \text{ ft}^3/\text{s}$) of generation flow. When river discharge exceeds this capacity, the station generates continuously and the surplus flow is spilled from crest gates or deep gates. When River discharge is less than Vernon Station's capacity, all of the river discharge past Vernon Dam is controlled by the facility. The stipulated minimum flow at Vernon Station is $35 \text{ m}^3/\text{s}$ ($1,250 \text{ ft}^3/\text{s}$) or inflow if it is less than $35 \text{ m}^3/\text{s}$ ($1,250 \text{ ft}^3/\text{s}$). This situation leads to two characteristic patterns of regulated discharge: one of high and gradually varying flow, and one of daily cycling between minimum and capacity flows characterized by rapid transitions.

Vernon Station owns and operates for certain periods during each year a fish ladder and a downstream fish passage conduit to facilitate both the upstream and downstream passage of anadromous fishes, including Atlantic salmon and American shad. The fishway was installed and became operational in 1981, and the downstream fish conduit (pipe) was first operated in 1991. The fishway, located near the western bank of the Connecticut River, is typically run between mid-May and early July of each year. The fishway is a concrete structure consisting of a vertical slot ladder from the tailrace leading up to a fish trap and viewing gallery, and an ice harbor style ladder that provides passage from the trap up to Vernon Pool. The fish ladder is supplied with a continuous flow of $1.8 \text{ m}^3/\text{s}$ ($65 \text{ ft}^3/\text{s}$) during the period of operation, and an attraction flow of $1.1 \text{ m}^3/\text{s}$ ($40 \text{ ft}^3/\text{s}$) is also discharged near the foot of the ladder. The "pipe" supplying the additional attraction flow was converted in 1994 into a "fish pipe" and

is presently used as an alternate downstream fish passage device. The primary downstream fish passage conduit (fish tube) is located in the center of the powerhouse, and 9.9 m³/s (350 ft³/s) of bypass flow is supplied through a 2.7 m (9-ft) by 1.8-m (6-ft) gate and tube that constricts to a 1.2-m (4-ft) by 1.5-m (5-ft) opening at the discharge end. The downstream fish passage conduit and the fish pipe are operated continuously from April through July and from September through October of each year.

3. Thermal Plume Mapping

3.1 Historical Studies

Prior to the present survey, a joint hydrological-biological study of Vernon Pool was conducted between 1974 and 1977 (Binkerd et al., 1978). The hydrological study featured a thermal survey of Vernon Pool using both a long-term deployment of *in situ* temperature probes and a series of short-term surveys using a towed temperature probe. The towed device was used to determine temperatures at a given depth along a series of across-channel transects. In addition, the towed probe was used to obtain profiles of temperature with depth at fixed locations around the pond.

This study concluded that discharge of cooling water from Vermont Yankee results in two distinct flow patterns within Vernon Pond. During periods of relatively high river flow the strong river currents shear the plume as it emerges from the Vermont Yankee discharge and is deflected to flow along the Vermont shore. In contrast, during periods of low river flow the plume extends far into the river channel before being swept downstream. In both of these flow regimes, warm plumes were found to sink if the ambient water temperature in the river was less than 4 °C (39.2 °F), the temperature at which water attains its maximum density.

3.2 2002 Field Data

Data considered here derive from a field survey conducted by Normandeau from May through December of 2002. The data presented here come from two periods during this survey: 1-23 August and 25 June – 9 July. The August period was determined by a joint Normandeau-ASA review to be representative of low flow, high temperature summer conditions in the river. The June – July period was chosen by Normandeau as period during which both the fishway was in active operation and the river temperatures were warm. Data available for review included temperature data from a long-term thermistor network deployed in the study area by Normandeau, meteorological data, and information on river flow and the flow of cooling water through Vermont Yankee.

3.2.1 Data Descriptions

3.2.1.1 Vernon Pool Temperature

Spatial and temporal variations in the thermal structure of the study area were monitored using the state-of-the-art temperature acquisition system deployed during 2002 to obtain thermal data for calibration of the hydrothermal model. Onset StowAway® TidbiT® 32K, temperature data loggers were deployed to measure the thermal regime of lower Vernon Pool of the Connecticut River during June through November 2002. These temperature loggers have a manufacturer's reported measurement range of -4°C to +37°C, and a reported accuracy of $\pm 0.4^\circ\text{C}$. All of the temperature loggers were set to record data at simultaneous five-minute intervals. Two strings of temperature data loggers were deployed in close proximity to each other at each of 11 stations in Lower Vernon Pool for redundancy.

Stations, shown in Figure 3.1, are referred to by transect (F was the most upstream; C, D, E were the most downstream, respectively) and by station number (1-6). Station numbers were also assigned systematically, with stations 1 and 2 being the pairs of temperature loggers located proximate to the Vermont shore, stations 3 and 4 were in the center of the channel, and stations 5 and 6 were proximate to the New Hampshire shore. Upstream control stations (F1/F2 and F3/F4) were located upstream from the influence of the discharge, while the remaining transects were at or downstream of the Vermont Yankee discharge. For example, Station E5/E6 included the pair of temperature strings located on transect E proximate to the New Hampshire shore on the most downstream transect below the discharge. All station locations were marked with GPS latitude and longitude coordinates (Table 3-1).

Nine of the 11 stations were established along three bank-to-bank transects in the Lower Vernon Pool at locations representing the expected exposure to the thermal gradient from the Vermont Yankee discharge. One transect (C) was perpendicular to the river flow, located immediately downstream of the discharge weir, and had samplers deployed at quarter points along this transect (25%, 50% and 75% of the distance from the Vermont shore). A second transect (D) was also perpendicular to the river flow, located downstream from the discharge weir one-third of the distance towards Vernon Dam, and had samplers deployed at quarter points along the transect (25%, 50% and 75% of the distance from the Vermont shore). A third transect (E) was also perpendicular to the river flow, located downstream from the discharge weir two-thirds of the distance towards Vernon Dam, and had samplers deployed at quarter points along the transect (25%, 50% and 75% of the distance from the Vermont shore).

The remaining two of the 11 stations were established as an upstream control station transect (F). These stations were located within the Vernon Pool upstream from the influence of the thermal gradient along a transect perpendicular to the river flow, with samplers deployed at 25% and 50% of the distance from the Vermont shore.

Three temperature data loggers were attached to each string and arrayed from surface to bottom (Table 3-2). One temperature data logger was deployed at the surface depth (1 foot below the surface, referred to as surface or “S” when used as a suffix to Station number), a second logger was deployed at mid-depth (half way between the surface and bottom = “M”), and a third logger was deployed at one foot above the river bottom (bottom or “B”) at each station. Therefore, a total of 66 temperature data loggers were deployed for this study (2 pairs per station x 11 stations x 3 depths). All depth measurements were relative to the total water column depth observed at a station at the time of deployment (Table 3-1).

Data from the thermistor arrays were downloaded on a weekly basis. These raw data were then filtered with a 3-hour low-pass filter and subsampled at hourly intervals. The 3-hour low-pass filter is a centered 3-hour moving average. This is an appropriate data conditioning step because the model input data is on a one-hour timestep and the model therefore cannot simulate processes that occur at frequencies less than one hour. The model-data comparison is thus more accurate. Resulting time series are shown in Appendix A, Figures A1-A33; (August 2002) and Appendix B, Figures B1-B22, (June – July 2002).

Data from the thermistor arrays, which were set to record temperatures at 5-minute intervals, were downloaded on a weekly basis. These raw data were then filtered with a 3-hour low-pass filter and subsampled at hourly intervals. The 3-hour low-pass filter was a centered 3-hour moving average. This is an appropriate data-conditioning step because the model input data is on a one-hour timestep and the model therefore cannot simulate processes that occur at frequencies less than one hour. The subsequent model-data comparison is thus more accurate. The resulting time series are shown in Appendix A, Figures A1-A33, and Appendix B, Figures B1-B22.



Figure 3-1. Location of thermistor stations for long-term thermistor deployment. The lower image is a detailed view of lower Vernon Pool immediately upstream of Vernon Dam.

Table 3-1. Location and total water depth for field study thermistor stations.

Station	Latitude (N)	Longitude (W)	Depth (m (ft))
C1/C2	42° 46.636'	72° 30.598'	5.2 (17)
C3/C4	42° 46.628'	72° 30.499'	5.2 (17)
C5/C6	42° 46.623'	72° 30.395'	4.3 (14)
D1/D2	42° 46.527'	72° 30.620'	6.1 (20)
D3/D4	42° 46.493'	72° 30.499'	4.3 (14.1)
D5/D6	42° 46.475'	72° 30.427'	7.0 (23)
E1/E2	42° 46.411'	72° 30.680'	11.9 (39)
E3/E4	42° 46.369'	72° 30.598'	4.0 (13)
E5/E6	42° 46.336'	72° 30.510'	1.5 (5)
F1/F2	42° 47.399'	72° 31.316'	4.0(13)
F3/F4	42° 47.437'	72° 31.258'	6.4 (21)

Table 3-2. Thermistor depths by station.

Station	Surface (S) Thermistor Depth (m (ft))	Middle (M) Thermistor Depth (m (ft))	Bottom (B) Thermistor Depth (m (ft))
C1/C2	0.3 (1)	2.6 (8.5)	4.9 (16)
C3/C4	0.3 (1)	2.6 (8.5)	4.9 (16)
C5/C6	0.3 (1)	2.1 (7)	4.0 (13)
D1/D2	0.3 (1)	3.1 (10)	5.8 (19)
D3/D4	0.3 (1)	2.1 (7)	4.0 (13)
D5/D6	0.3 (1)	3.5 (11.5)	6.7 (22)
E1/E2	0.3 (1)	5.9 (19.5)	11.6 (38)
E3/E4	0.3 (1)	2.0 (6.5)	3.7 (12)
E5/E6	0.3 (1)	0.8 (2.5)	1.2 (4)
F1/F2	0.3 (1)	2.0 (6.5)	3.7 (12)
F3/F4	0.3 (1)	3.2 (10.5)	6.1 (20)

3.2.1.2 River Flow and Temperature

Measurements of river flow at the Vernon Dam were provided by Vermont Yankee, based upon information obtained from the dam owner. River flow was reported at hourly intervals throughout the deployment period. This raw hourly data was processed with a 3-hour low-pass filter (Appendix A, Figures A34-A36; Appendix B, Figures B23-B24).

Water temperatures both upstream and downstream of the study area are also monitored and were reported by Vermont Yankee. Temperature upstream of the study area was measured at Monitoring Station 7 (42° 49.364' N, 72° 32.745' W) and downstream temperature was measured at Monitoring Station 3 (42° 45.921' N, 72° 30.400' W), shown in Figure 3.1. Temperatures were recorded at hourly intervals at both locations and are presented here without any additional processing (Appendix A, Figures A34-A36; Appendix B, Figures B23-B24).

During the period from May to July each year, water temperatures were monitored during fishway operations at the Vernon Dam. Measurements were taken at hourly intervals. Figure B27 and B28 show a portion of the observations for 25 June to 9 July 2002.

3.2.1.3 Plant Operations

Cooling water flow and temperature data for Vermont Yankee were calculated based on the actual station operating conditions, upstream river water temperature at Station 7, and total river discharge at Vernon Dam using the thermal compliance equation. The temperature and volume flux of water discharged from the station into the river were reported at hourly intervals for the duration of the study period. These data are reported here without any additional processing (Appendix A, Figures A37-A39; Appendix B, Figures B25-B26).

3.2.1.4 Meteorological Conditions

Atmospheric forcing can affect the hydrothermal model via two distinct mechanisms: mechanical and thermal. First, wind induces a shear stress on the surface of the water, which can cause the water, particularly near the surface, to move in the general direction of the wind. Wind energy can also cause mixing in the upper layers of the water column that tends to homogenize the distribution of water properties with depth. The magnitude of these effects is a function of both the speed and direction of the wind. Second, transfer of heat between the water and the atmosphere can modify the thermal structure of the water body. This process is driven by solar radiation, which is a measure of the thermal energy reaching the surface of the water, with ancillary factors such as air and dew point temperatures also of importance.

Meteorological data for this study derive from two separate sources. Wind speed and direction were measured at a meteorological tower located at Vermont Yankee. Measurements were taken at 15-minute intervals at a height of approximately 11 m (36.1 ft) above the ground. Since the meteorological data was not reported exactly on the hour, a cubic spline curve fit was applied to the observations (passing exactly through the surrounding four data points) to generate one-hour estimates. These data were then filtered with a centered 3-hour moving average. The resulting time series are shown in Appendix A, Figures A40-A42, and Appendix B, Figures B29-B30.

Observations of air temperature, dew point temperature, relative humidity and atmospheric pressure, some of which (i.e., dew point temperature, relative humidity) were not available at Vermont Yankee, were obtained from the National Climate Data Center for the weather station at the Orange Municipal Airport in Orange, MA, the nearest such site to Vermont Yankee. The station is located approximately 30 km (18.6 mi) SE of Vermont Yankee at 42° 34' N, 72° 17' W (Figure 3-2). The station sits at an elevation of 169.2 m (555.1 ft) above sea level. For comparison, the normal average elevation of the surface of Vernon Pond is approximately 66.7 m (218.8 ft). The validity of approximating meteorological conditions at Vermont Yankee with those at Orange, MA is born out by a comparison of air temperature and atmospheric pressure records from the two locations (Figure 3-3). Data from the Orange, MA station was reported at hourly intervals. Cubic splines were used to synchronize this data to the wind data from Vermont Yankee. The splined data were then filtered with a 3-hour low-pass filter (Appendix A, Figures A43-A45; Appendix B, Figures B31-B34).

In addition, calculated values of solar radiation at Orange, MA were obtained from the Northeast Regional Climate Center. Solar radiation is reported hourly and the data are presented here with no additional processing (Appendix A, Figures A46-A48; Appendix B, Figures B31-B32).

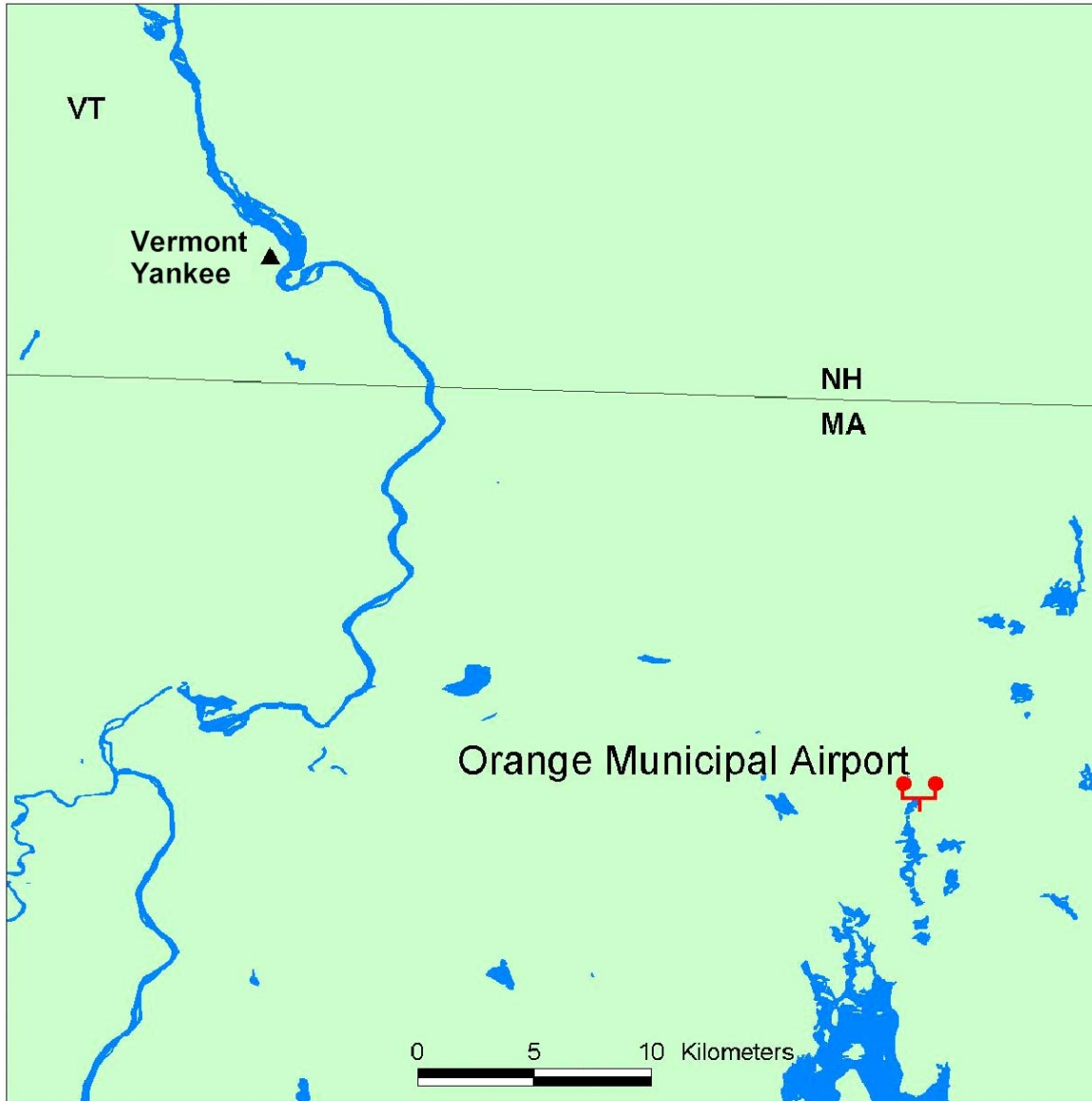


Figure 3-2. Location of Orange Municipal Airport met station relative to Vermont Yankee.

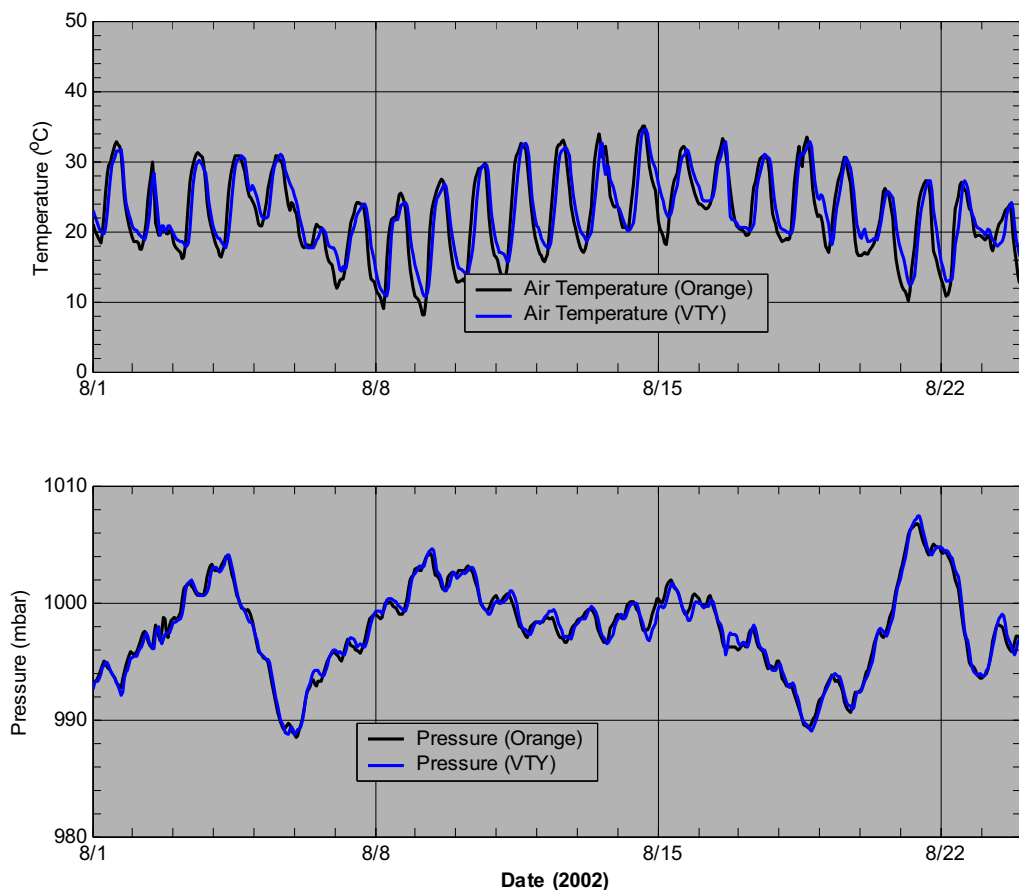


Figure 3-3. A comparison of air temperature and atmospheric pressure at Orange, MA and Vermont Yankee for the August survey period. Pressure records have been corrected for the difference in elevation between the two locations.

3.2.2 August 2002

The August survey period covers the period from 1 to 24 August 2002 and is representative of low flow, high temperature conditions. Survey data for this period are presented in Appendix A.

3.2.2.1 Lower Vernon Pool Temperatures

Temperatures at the C stations (Figures A1-A9), arrayed across the Vernon Pool at the outfall location (Figure 3-1), ranged from a low of just under 24 °C (75.2 °F) (C6 bottom, 1 August) to approximately 29.5 °C (85.1 °F) (C4 surface, 18 August). Note that shortly after noon on 15 August the surface thermistor at C4 comes online. This is related to the weekly downloading of data from the thermistor strings. Surface thermistors at the C stations exhibit a diurnal variation in temperature of 1-2 °C, while thermistors at mid-depth show a variation of at most 1 °C. Deep thermistors show no diurnal variation. This diurnal variation may be due to variations in the temperature and volume flux of water discharged from the station as well as solar heating.

Missing data between 1-15 August 2002 for the thermistor located at the surface at Station C4 in lower Vernon Pool is seen in Figures A4-A5. Data loggers were downloaded on 14 and 15 August 2002, during which three files were irretrievable. The loggers were sent to Onset where data sets from two of the loggers were retrieved by the instrument manufacturer. The data from the station C4S logger could not be retrieved due to instrument failure, resulting in a loss of data for that point from 31 July to 15 August 2002. Station C3S, the duplicate of C4S, was downloaded without data loss during that period. Because all thermistor loggers were deployed in redundant pairs, there was no effective loss of relevant data. Even though the C4S temperature data logger failed out of the 66 deployed, the success rate of 65/66 or 98.5% is, in the experience of the consultant team (ASA and Normandeau), exceptionally good. Losses of data are fairly routine when loggers are deployed *in situ*, and, because of redundant deployment design, this loss did not affect the usefulness of the data for the study.

Thermistors at the D stations (Figures A10-A18), arrayed across the river several hundred meters downstream of the outfall (Figure 3-1), recorded temperatures ranging from a low of just under 24 °C (75.2 °F) (D6 bottom, 12 August) to approximately 29.3 °C (D5 surface, 17 August). Overall, temperatures at these stations resemble those of the C stations. Diurnal temperature variations at the D stations are on the order of 1-1.5 °C for the surface thermistors and 1 °C for the middle thermistors. No diurnal variation is evident in the deep thermistors.

Thermistors at the E stations (Figures A19-A27), arrayed across the river just upstream of the dam (Figure 3-1), recorded temperatures ranging from a low of just under 24.4 °C (75.9 °F) (E2 bottom, 1 August) to approximately 29.8 °C (85.6 °F) (E5 surface, 17 August). The individual E stations exhibit a wide range of behavior, reflecting the differences in the depth of the water column (and the thermistors) at each location. Diurnal variations at these stations fall in the range of 1.5 – 2 °C for the surface thermistors.

Temperatures recorded at the C, D and E stations indicate that water column stratification is similar at each of these locations. For example, temperatures show considerable stratification at all stations from 1-5 August, with the deep thermistors recording significantly lower temperatures than the surface and middle thermistors (Figures 3-xx-3-xx). However, on 6 August this temperature difference decreases at almost all stations and the water column becomes well mixed for a period of several days (Figures 3-xx-3-xx). Stratification is then re-established around 10 August at all stations (Figures 3-xx-3-xx). This stratification lasts until 21 August, when it begins to break down again. Some small deviations from the larger trend are apparent at some of the E stations. For example, Station E1/E2 shows the same pattern of stratification breaking down and re-establishing as do the C and D stations. However, while the station is very deep, the total temperature difference between the top and bottom thermistors is only approximately 2 °C (3.6 °F), substantially less than the difference seen at stations upstream, particularly given that the water column is much deeper here. Station E3/E4 behaves similarly to station E1/E2, except that stratification is somewhat weaker. This reflects the fact that the deep and middle thermistors are deployed at much shallower depths than at Station E1/E2 (Table 3-2). Station E5/E6, located in extremely

shallow water, exhibits almost no stratification at all, with no more than approximately 1.5 °C difference between the surface and deep thermistors.

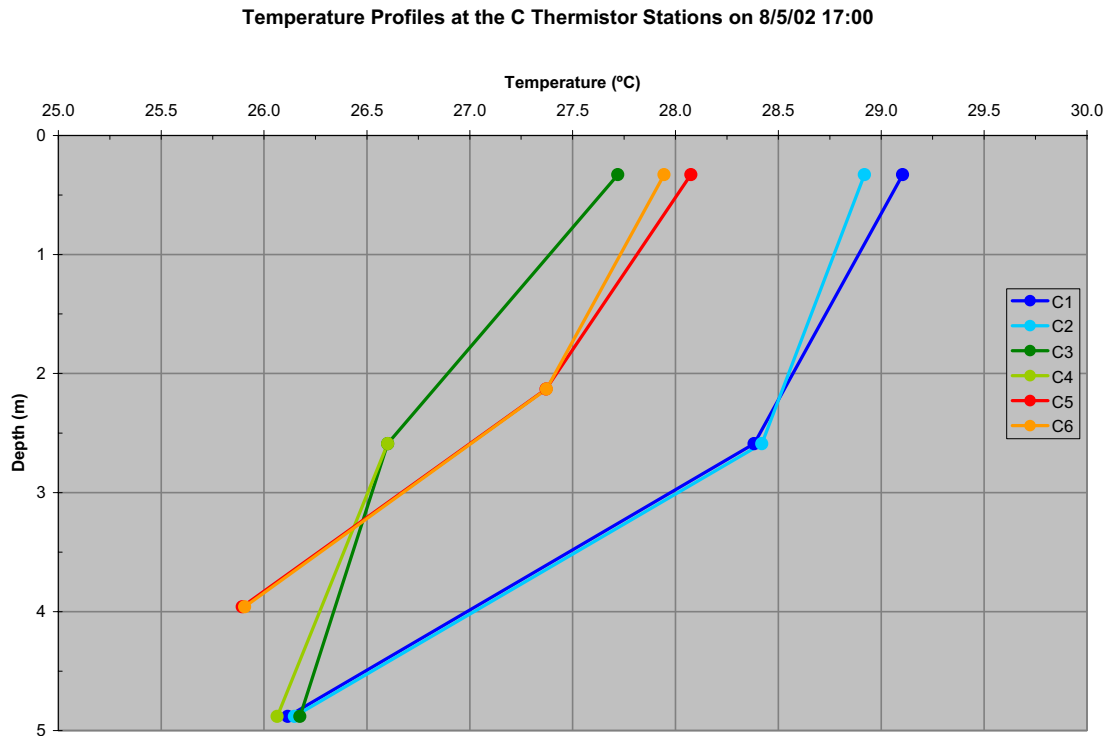


Figure 3-4. Temperature profiles for the C stations on 8/05/02 17:00.

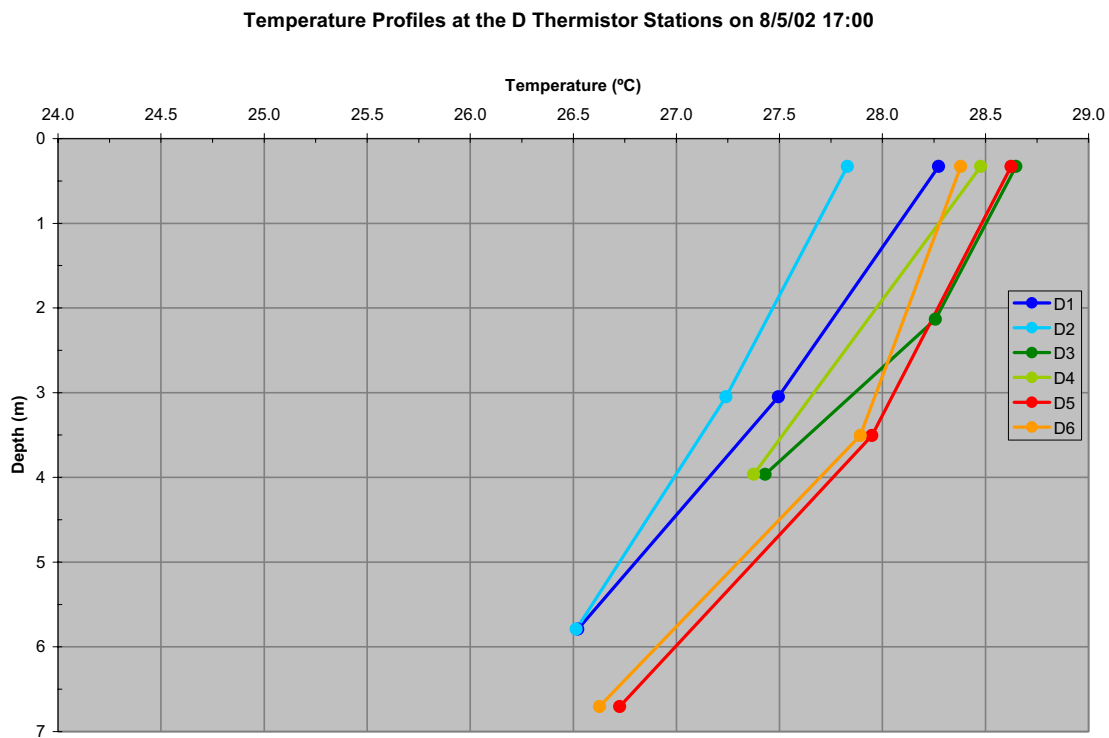


Figure 3-5. Temperature profiles for the D stations on 8/05/02 17:00.

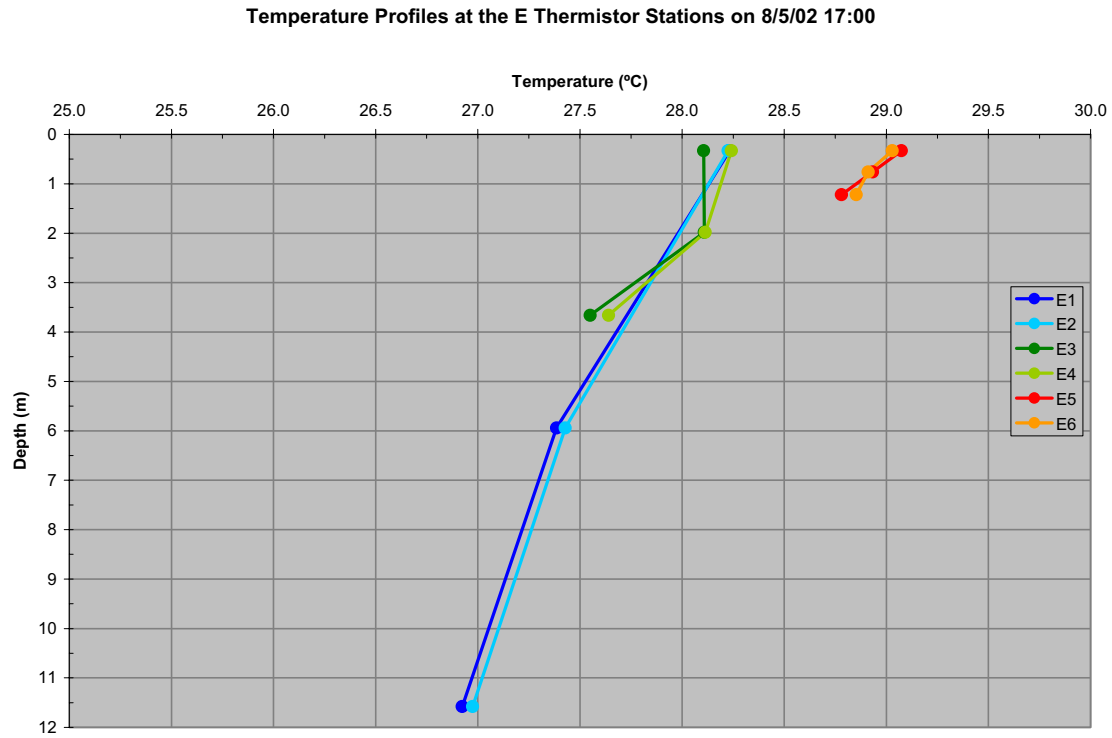


Figure 3-6. Temperature profiles for the E stations on 8/05/02 17:00.

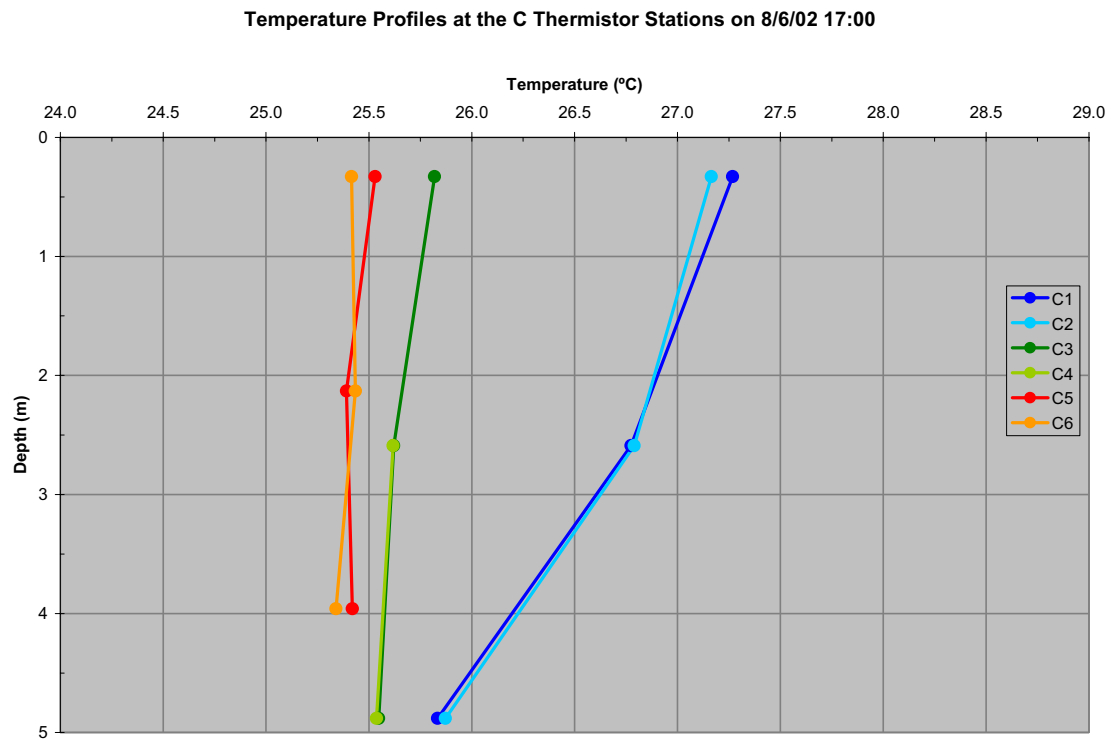


Figure 3-7. Temperature profiles for the C stations on 8/06/02 17:00.

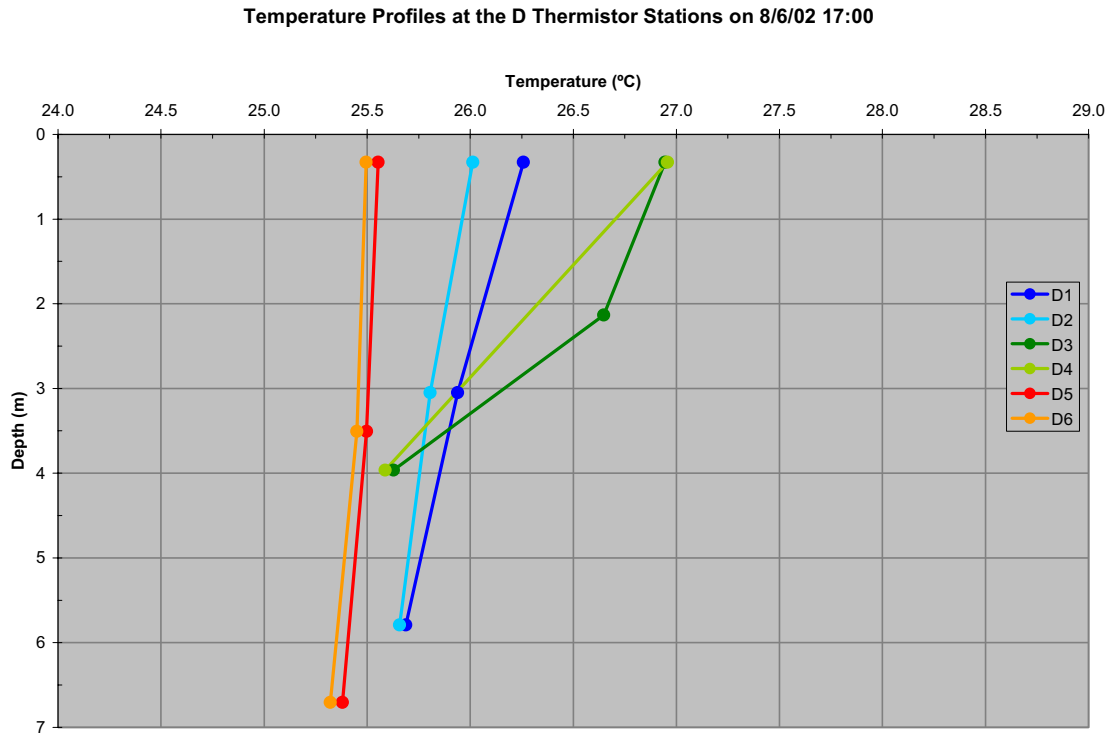


Figure 3-8. Temperature profiles for the D stations on 8/06/02 17:00.

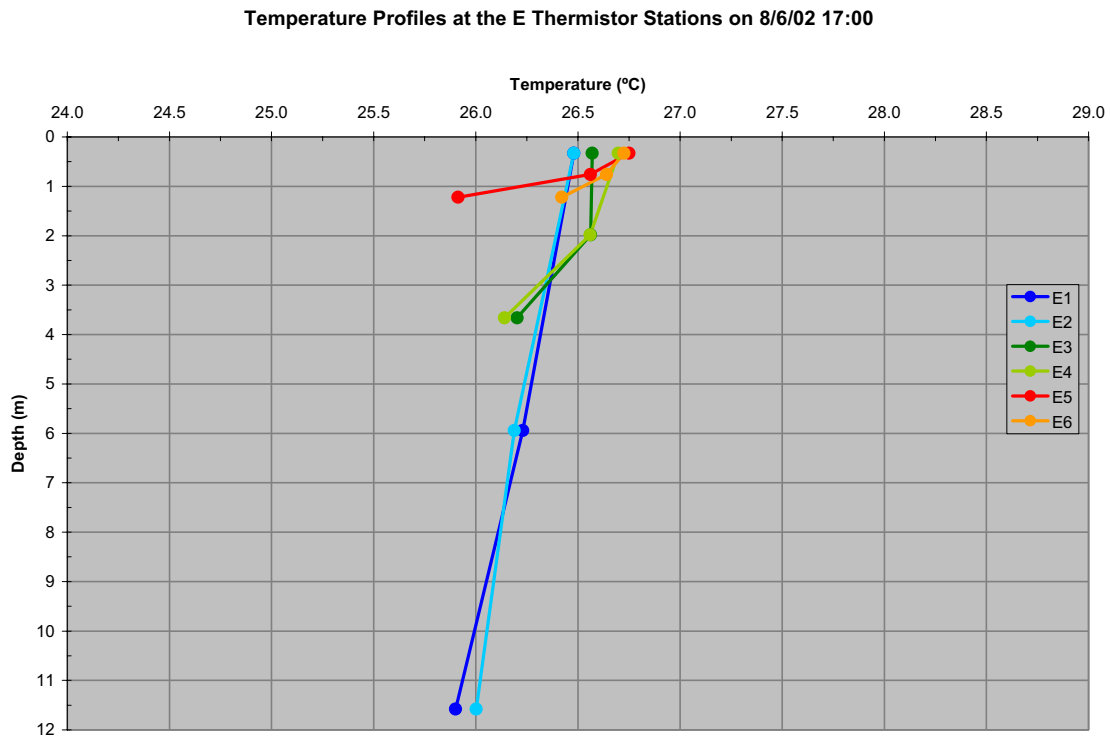


Figure 3-9. Temperature profiles for the E stations on 8/06/02 17:00.

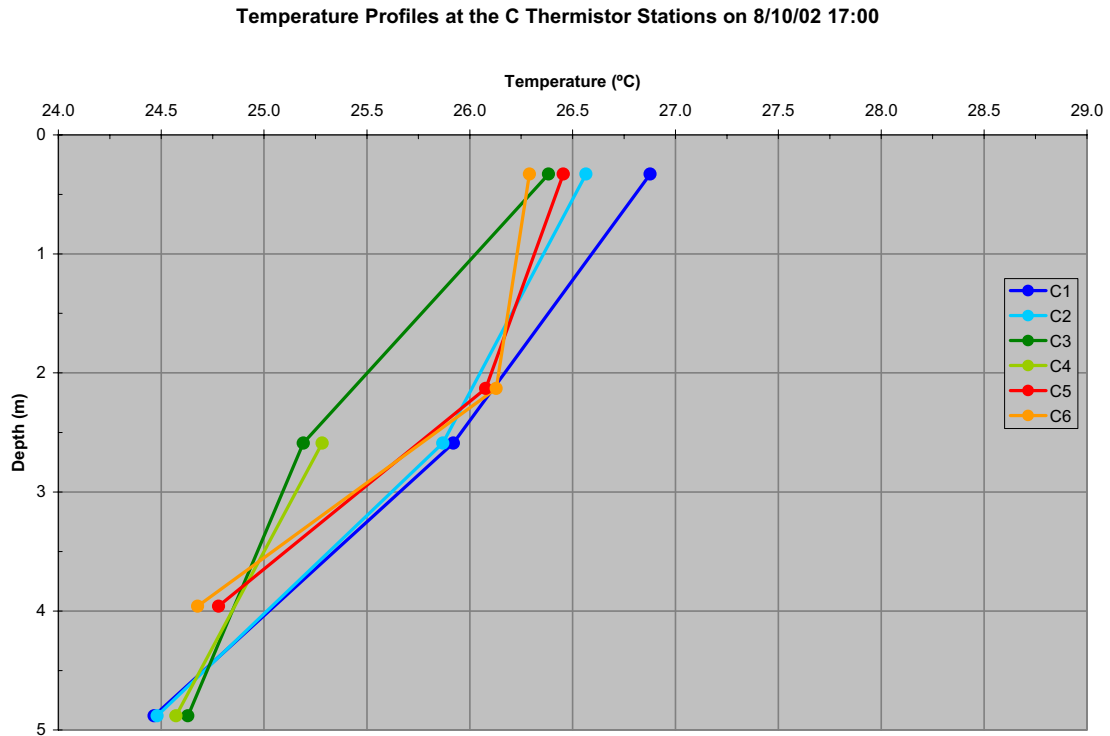


Figure 3-10. Temperature profiles for the C stations on 8/10/02 17:00.

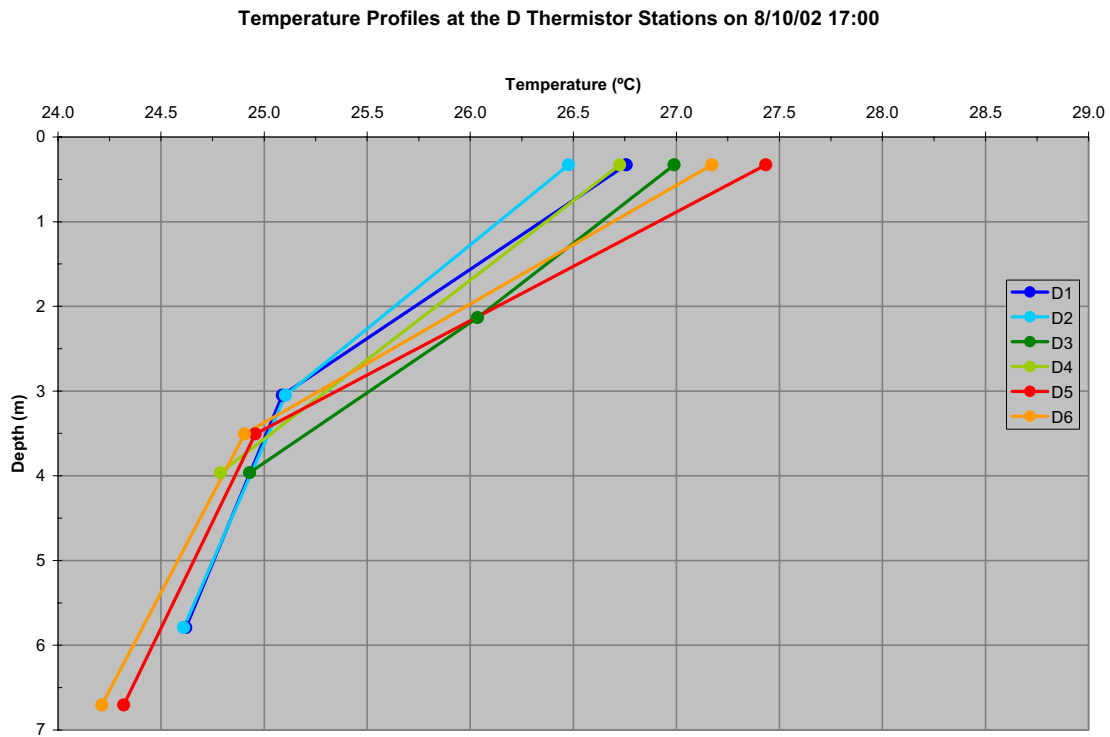


Figure 3-11. Temperature profiles for the D stations on 8/10/02 17:00.

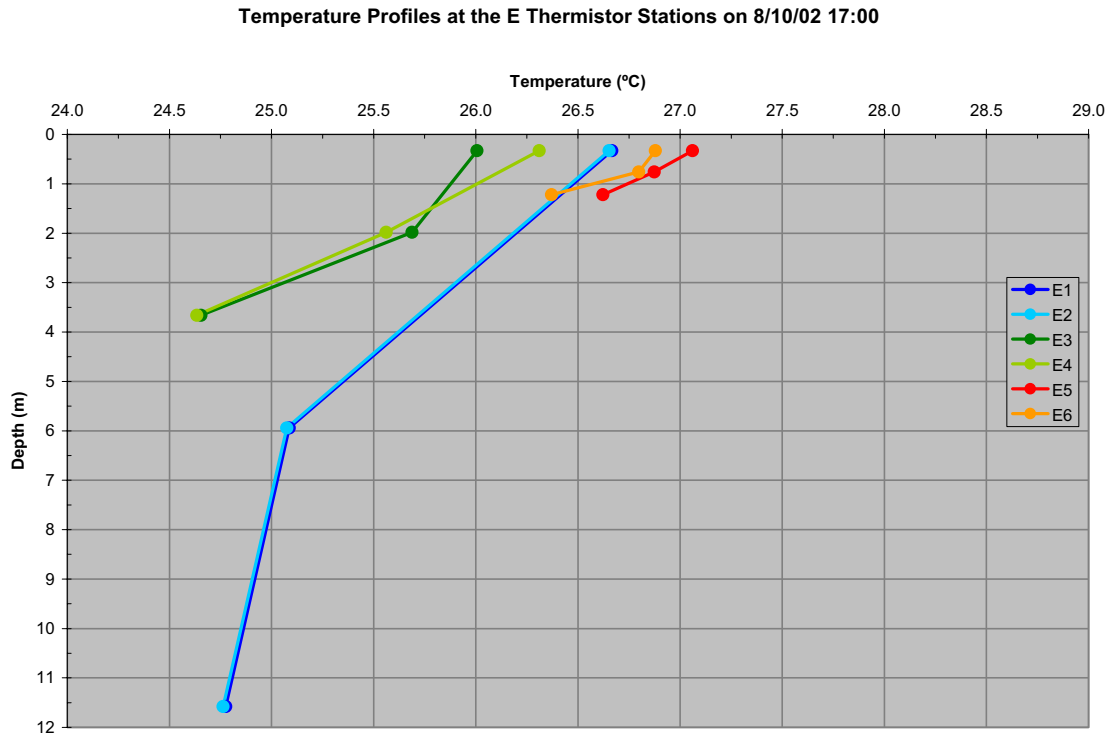


Figure 3-12. Temperature profiles for the E stations on 8/10/02 17:00.

Thermistors at the F stations (Figures A28-A33), located upstream of the station intake (Figure 3-1), measure temperatures during this time ranging from a low of 23.8 °C (74.8 °F) (F4 bottom, 1 August) to a high of 28.8 °C (83.8 °F) (F3 surface, 19 August). Both the F1/F2 and the F3/F4 stations exhibit trends similar to those seen at the C and D stations downstream. However, the stratification at the F stations is generally weaker than at the other stations. Temperature differences between surface and deep thermistors at the F stations can be as much as approximately 3 °C, but appears to be more typically on the order of 1.5 °C. Note that the surface and mid-depth thermistors at Station F4 go offline shortly before noon on 14 August and remain inactive for the remainder of the period. Diurnal temperature variations at the F stations are as much as 1 °C at the surface, less than 0.5 °C at mid-depth and essentially non-existent in the deep water.

Spatial variations in the temperature of the surface water in Vernon Pool can be investigated by considering across-channel and along-channel transects of temperature with time. During the August survey period, temperatures along the across-channel transects defined by the C, D and E thermistor stations (Figure 3-13) show little spatial variation. In general, temperatures for a given transect are within approximately 1 °C (1.8 °F) of each other at any given time, and the temperature record is dominated by a diurnal signal associated with a combination of solar heating and plant operations. The C1/C2 station has slightly higher temperatures than the C3/C4 or C5/C6 stations throughout most of the survey period, while the D5/D6 and E5/E6 stations consistently report the highest temperatures along their respective transects. A consideration of along-axis transects (Figure 3-14) reveals similar

trends. Temperatures stay within approximately 1 °C (1.8 °F) of each other at any time along a given transect.

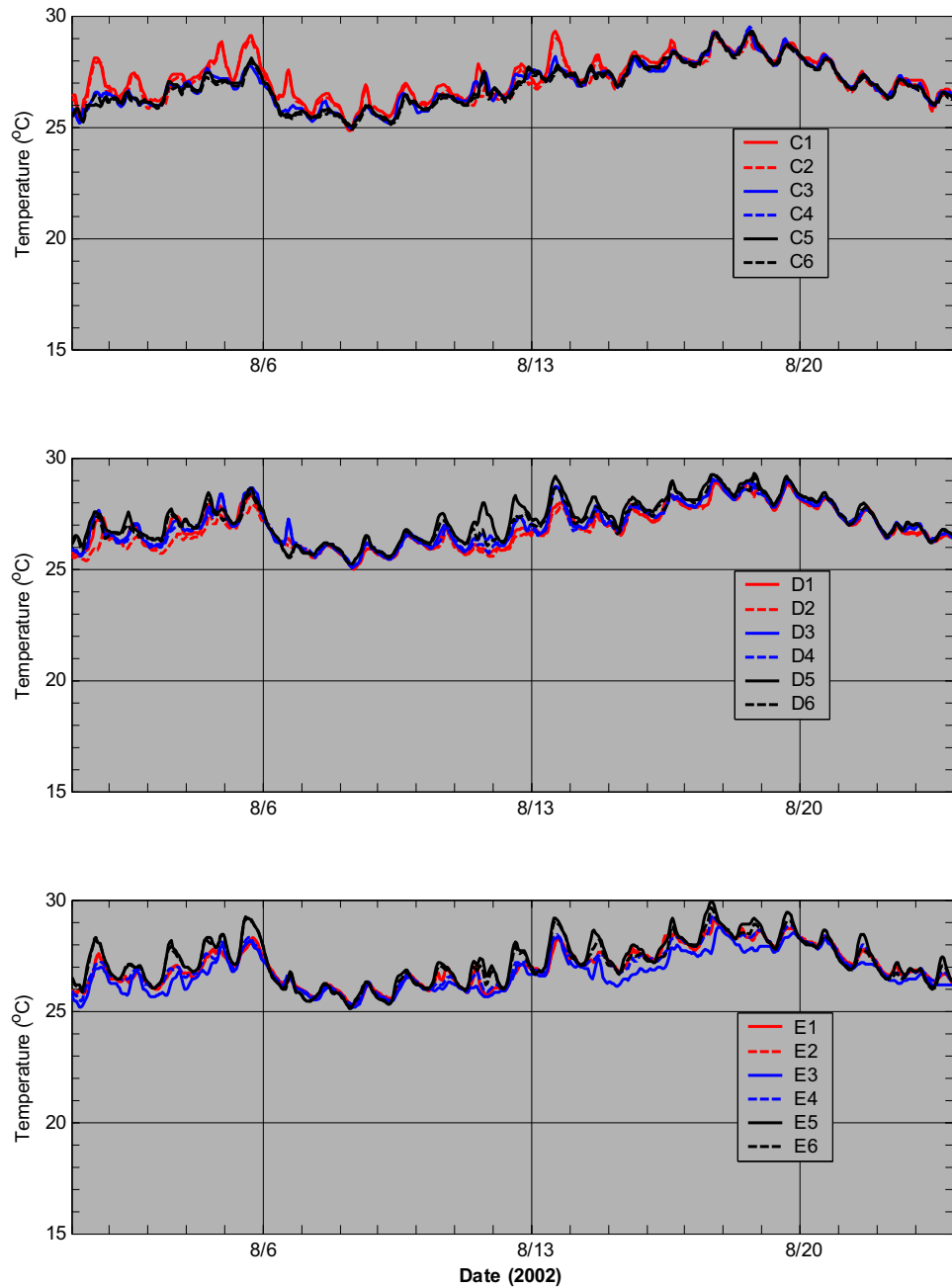


Figure 3-13. Temperatures recorded by surface thermistors of C (top), D (middle) and E (bottom) stations during the August survey period. Each of the above plots therefore represents the time evolution of an across-channel transect at the surface of Vernon Pool at the given location.

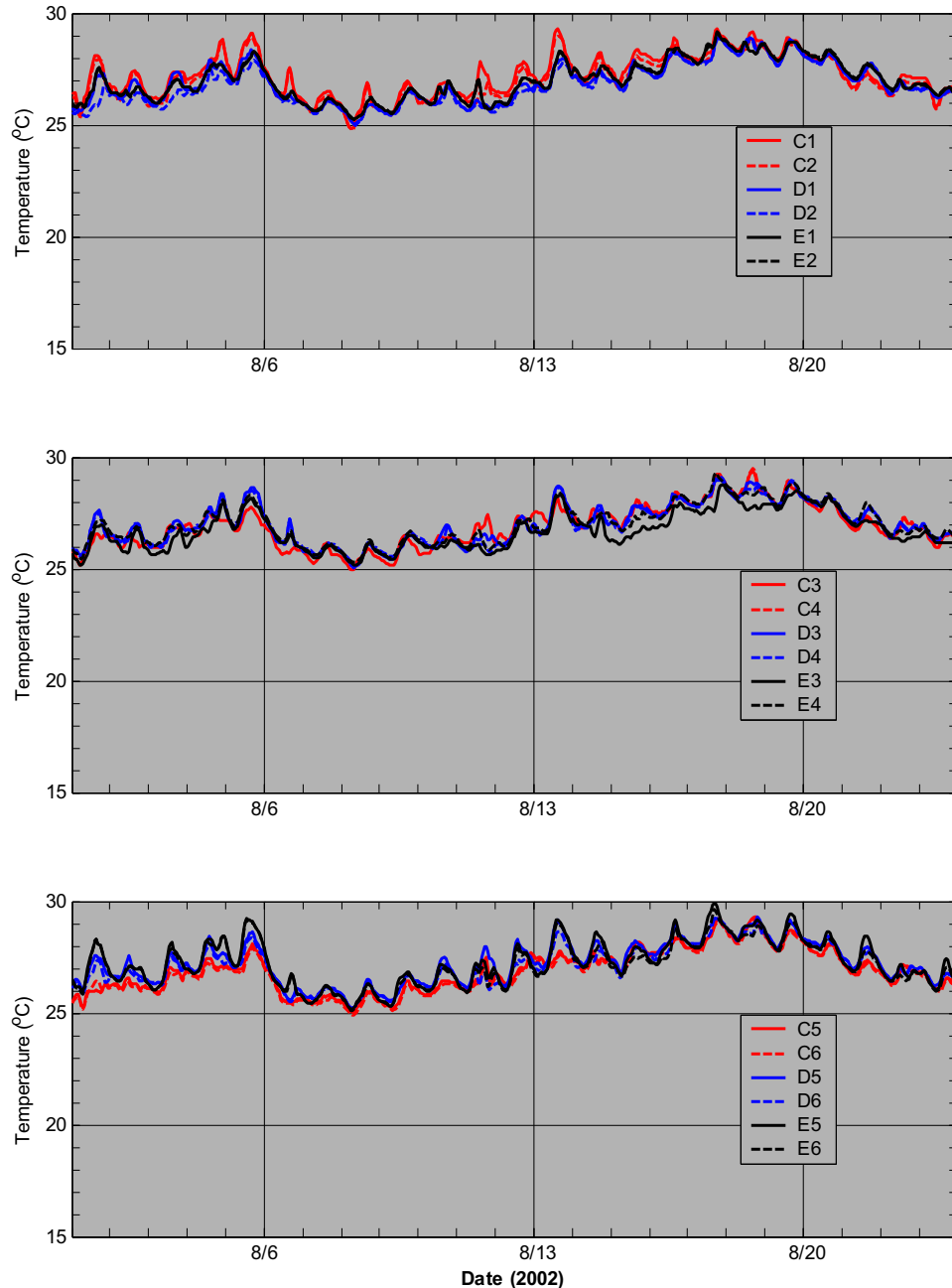


Figure 3-14. Temperatures recorded by surface thermistors of ‘1/2’ (top), ‘3/4’ (middle) and ‘5/6’ (bottom) stations during the August survey period. Each of the above plots therefore represents the time evolution of an along-channel transect at the surface of Vernon Pool at the given location.

3.2.2.2 River Flow and Temperature

River flow, as measured at the Vernon Dam, fluctuated considerably between 1 and 17 August and then remained relatively constant from 17 to 24 August (Figures A34-A36). Flow during the earlier period exhibited a diurnal variation, with flow generally reaching a maximum in the late afternoon/early evening and a minimum in the early morning. The

period of 17-24 August stands in marked contrast to this, with a mean flow of 42 m³/s (1,483 ft³/s) that remained nearly constant throughout the entire week (Figure A36). Overall, flow during the August period ranged from 36 to 194 m³/s (1,271 to 6,851 ft³/s), with an average value of 66 m³/s (2,331 ft³/s).

Section 3.1.2 of the Demonstration details the nature of flow regulation at Vernon Dam. As discussed therein, Connecticut River flow is highly regulated by numerous upstream storage and hydroelectric stations. Although storage in the Vernon headpond provides some flexibility of flow release from Vernon Dam independent of inflow, the upriver hydro stations and Vernon Station are generally operated more or less in unison to maximize power output during times of peak power demand. The hourly flow record for Vernon Dam provides (Figures A34-A36) direct evidence of the highly regulated nature of the whole River.

Measured Upstream Station 7 Temperatures are slightly cooler (approximately 1.6 °C (2.9 °F) on average) than Measured Downstream Station 3 Temperatures (Figures A34-A36). The Measured Upstream Station 7 Temperature shows no evidence of a diurnal temperature variation, and in general correlates well with the deepest thermistor readings from Stations F1-F4 for this period. For the August period, Measured Upstream Station 7 Temperatures ranged between 23.8 and 25.7 °C (74.8 and 78.3 °F), averaging 24.8 °C (76.6 °F).

The Measured Downstream Station 3 Temperature shows a marked diurnal variation of approximately 1 °C (1.8 °F) during the period from 1-15 August and a somewhat less prominent diurnal variation thereafter. During the August survey, Measured Downstream Station 3 Temperatures ranged between 24.9 and 28.0 °C (76.8 and 82.4 °F) with an average temperature of 26.4 °C (79.5 °F).

3.2.2.3 Vermont Yankee Station Operations

The flow of cooling water discharged from the station varied considerably and sharply between 1 and 17 August, while flow varied less dramatically between 17 and 24 August (Figures A37-A39). Overall, flow varied between 0.2 and 19.9 m³/s (7.1 and 702.8 ft³/s) for the period, with an average flow rate of 8.8 m³/s (310.8 ft³/s).

The temperature of the discharged cooling water averaged 31.6 °C (88.9 °F) for the August survey period. The maximum discharge temperature during this period was 36.1 °C (97.0 °F) while the minimum discharge temperature was 25.7 °C (78.3 °F).

3.2.2.4 Meteorological Conditions

Winds were generally light during this period (Figures A40-A42), with a maximum speed of 6.7 m/s (15.0 mph). The average wind speed for the period was 1.9 m/s (4.3 mph). Winds were predominantly from the west for the period, with an average wind direction of 209°.

The air temperature record at this time is dominated by a diurnal signal with amplitude typically in excess of 10 °C (18 °F) (Figures A43-A45). Dew point temperature, in contrast, shows very little diurnal variation during this period, and little variation at all between 1 and 5 August. Relative humidity, which is a function of both air and dew point temperatures,

consequently displays a strong diurnal variation. In general, relative humidity achieves a minimum value at midday, when air temperatures are at their highest, and a maximum value around midnight, when air temperatures reach their lowest values. Atmospheric pressure during the study period changed smoothly over periods of days and remained bounded within a relatively narrow range of approximately 20 mbar. A summary statistical analysis of the data records for this time frame is presented in Table 3-3.

Solar radiation during this period exhibits a regular diurnal variation with a maximum peak magnitude of approximately 941.8 W/m² (1 August), a minimum peak magnitude of 621.1 W/m² (23 August), and a mean peak magnitude of 839.7 W/m² (Figures A46-A48). Irregularities in the peaks are due to local variations in atmospheric conditions (e.g., cloud cover).

Table 3-3. Statistical analysis of meteorological data for the summer survey period.

	Air Temperature °C (°F)	Dew Point °C (°F)	Relative Humidity	Pressure mbar
Mean	22.3 (72.1)	15.9 (60.6)	0.71	997.8
Minimum	8.0 (46.4)	6.6 (43.9)	0.29	988.5
Maximum	35.0 (95.0)	23.3 (73.9)	1.00	1006.8

3.2.3 June - July 2002

The June - July survey period spans from 25 June to 9 July 2002. Survey data for this period are presented in Appendix B.

3.2.3.1 Vernon Pool Temperatures

Temperatures at the C stations (Figures B1-B6), arrayed across the river at the outfall location (Figure 3-1), ranged from a low of just under 19.5 °C (67.1 °F) (C1 bottom, 1 July) to approximately 27.5 °C (81.5 °F) (C1 surface, 4 July) during this period. All C stations display episodes of stratification during the period, during which deep thermistors register temperatures as much as 3.5 °C (6.3 °F) lower than those recorded at the surface. The C1/C2 station appears most inclined towards stratification, remaining stratified almost without interruption for the period of 1-9 July. Surface thermistors at the C stations exhibit diurnal variations in temperature on the order of 0.5 °C (0.9 °F) during periods with little water column stratification. This signal appears to propagate throughout the entire depth of the water at these locations.

Thermistors at the D stations (Figures B7-B12), arrayed across the river several hundred meters downstream of the outfall (Figure 3-1), recorded temperatures ranging from a low of 19.6 °C (67.3 °F) (D1 bottom, 25 June) to approximately 28.3 °C (82.9 °F) (D5 surface, 3 July). Overall, the water column at the D stations appears to be more regularly stratified than at the C stations. The D1/D2 station, in particular, shows regular stratification throughout the June-July period, with temperature differences across the water column of approximately 2.5 °C (4.5 °F). The D3/D4 and D5/D6 stations exhibit more intermittent stratification during

this period. Diurnal temperature variations at these stations are on the order of 0.5 °C (0.9 °F) at the surface for periods with no stratification (e.g., D3/D4, 28 June – 1 July).

Thermistors at the E stations (Figures B13-B18), arrayed across the river just upstream of the dam (Figure 3-1), recorded temperatures ranging from a low of 19.3 °C (66.7 °F) (E2 bottom, 25 June) to approximately 27.7 °C (81.9 °F) (E5 surface, 5 July). The individual E stations exhibit a wide range of behavior, reflecting the differences in the depth of the water column (and the thermistors) at each location. Station E1/E2 shows substantial stratification throughout the June-July period. However, while the station is very deep, the total temperature difference between the top and bottom thermistors is only approximately 2 °C, substantially less than the difference seen at stations upstream, particularly given that the water column is much deeper here. Station E3/E4 exhibits weak stratification between 25 June and 1 July, but is relatively well mixed after that. The mid-depth thermistors were not operational at this station during this period. Station E5/E6, located in extremely shallow water, exhibits almost no stratification at all. Diurnal variations at these stations fall in the range of 1 °C (1.8 °F) for the surface thermistors at these stations.

Thermistors at the F stations (Figures B19-B22), located upstream of the station intake (Figure 3-1), measure temperatures during this time ranging from a low of 19.5 °C (67.1 °F) (F1 bottom, 25 June) to a high of 25.0 °C (77.0 °F) (F1 surface, 5 July). Both the F1/F2 and the F3/F4 stations show little stratification during the study period. Diurnal temperature variations at the F stations are as much as 1 °C (1.8 °F) at the surface. This signal attenuates with depth.

Spatial variations in the temperature of the surface water in Vernon Pond can be investigated by considering across-channel and along-channel transects of temperature with time. During the June-July survey period, temperatures along the across-channel transects defined by the C, D and E thermistor stations (Figure 3-15) show significant spatial gradients in temperature for much of the survey period. Temperatures across channel can vary by as much as 3 to 4 °C (5.4 to 7.2 °F) at a given instant in time. The C1/C2 station reports higher temperatures than the C3/C4 or C5/C6 stations throughout most of the survey period. The exception to this is the period between 28 June and 1 July, during which all C stations report nearly identical temperatures. This period corresponds to a period of particularly strong river flow ($> 300 \text{ m}^3/\text{s}$ ($10,594 \text{ ft}^3/\text{s}$)) (Figure B23). Temperatures along the D and E transects show substantial gradients between 25 June and 4 July, but are homogenous after 4 July. A consideration of along-axis transects (Figure 3-16) reveals a similar degree of structure. While there are periods of homogeneity, in general gradients of 2 to 3 °C (3.6 to 5.4 °F) exist along a given transect.

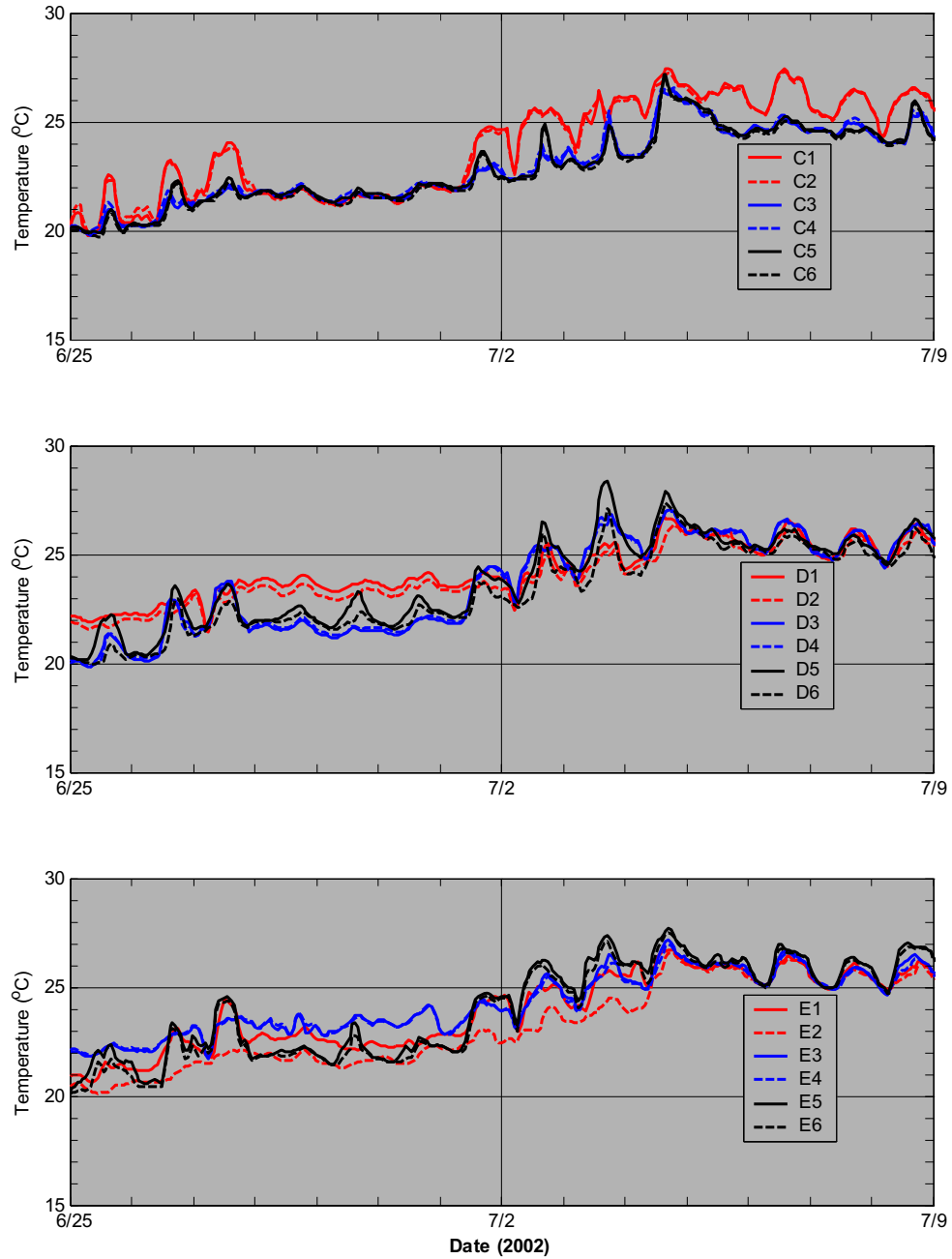


Figure 3-15. Temperatures recorded by surface thermistors of C (top), D (middle) and E (bottom) stations during the June-July survey period. Each of the above plots therefore represents the time evolution of an across-channel transect at the surface of Vernon Pool at the given location.

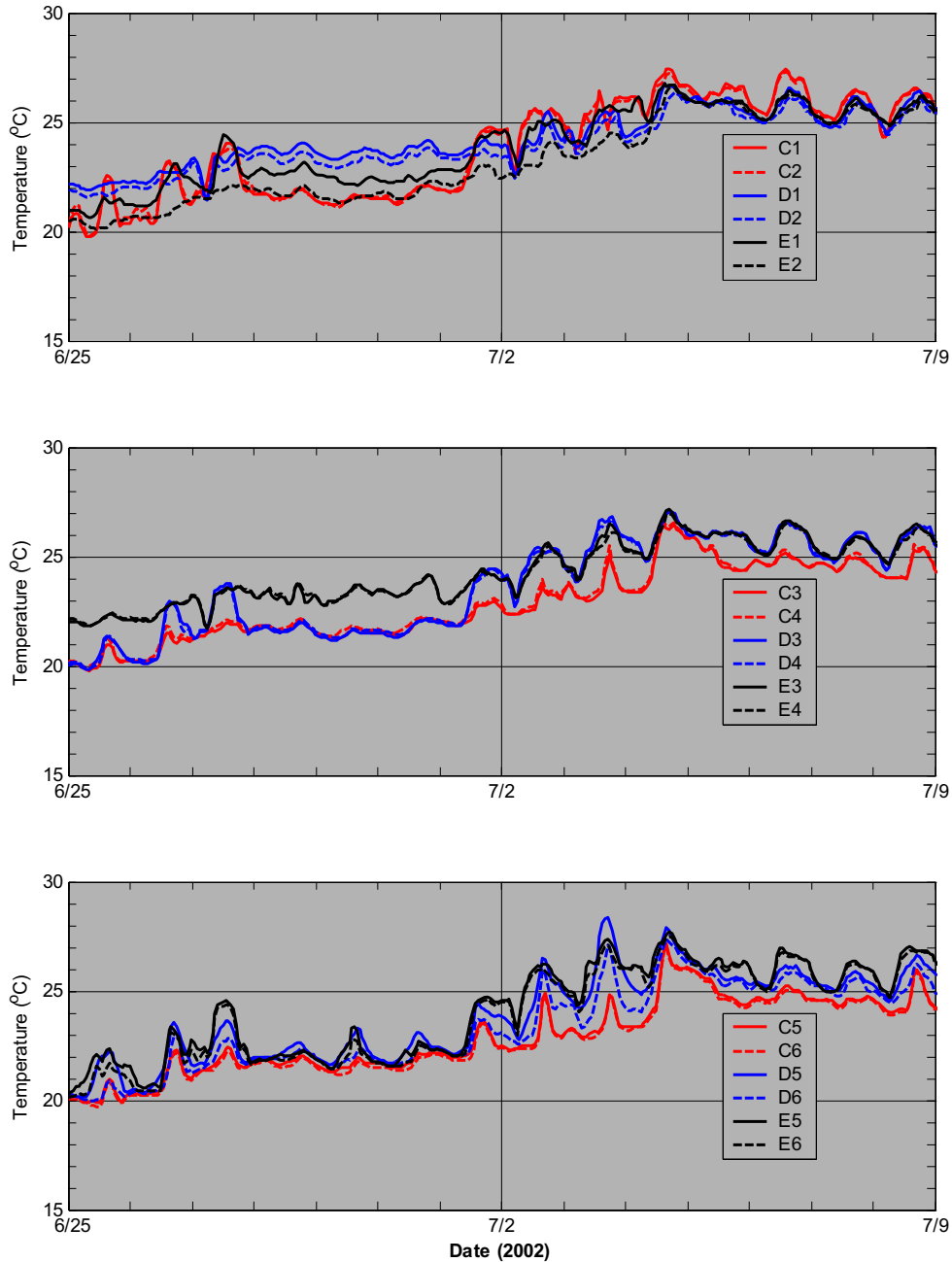


Figure 3-16. Temperatures recorded by surface thermistors of ‘1/2’ (top), ‘3/4’ (middle) and ‘5/6’ (bottom) stations during the August survey period. Each of the above plots therefore represents the time evolution of an along-channel transect at the surface of Vernon Pool at the given location.

Measured Upstream Station 7 Temperatures are cooler than Measured Downstream Station 3 Temperatures by an average of 2.4 °C (4.3 °F) for the period (Figures B23-B24). The Measured Upstream Station 7 Temperature shows little evidence of a diurnal temperature variation during this period, and in general correlates well with the deepest thermistor readings from Stations F1-F4. Overall, Measured Upstream Station 7 Temperatures ranged between 18.7 and 23.8 °C (65.7 and 74.8 °F), averaging 21.5 °C (70.7 °F).

The Measured Downstream Station 3 Temperature shows a diurnal variation of approximately 1 °C (1.8 °F) during the period from 2-9 July. Measured Downstream Station 3 Temperatures for the period ranged between 20.7 and 26.2 °C (69.3 and 79.2 °F) with an average temperature of 23.5 °C (74.3 °F).

During the June-July survey period a thermistor was deployed to record water temperatures at the Fishway at hourly intervals (Figures B27-B28). Fishway temperatures during the study period ranged from a minimum of 20.8 °C (69.5 °F) to a maximum of 27.1 °C (80.8 °F), averaging 23.8 °C (74.8 °F).

3.2.3.2 Plant Operations

The flow of cooling water discharged from Vermont Yankee averaged 18.0 m³/s (635.7 ft³/s) for the June-July study period (Figures B25-B26). The maximum flow rate achieved during the period was 30.8 m³/s (1087.7 ft³/s).

The temperature of the discharged cooling water averaged 32.7 °C (90.9 °F) for the June-July survey period. The maximum discharge temperature during this period was 35.7 °C (96.3 °F) while the minimum discharge temperature was 28.2 °C (82.8 °F).

3.2.3.3 Meteorological Conditions

The maximum wind speed during the June-July study period was 5.4 m/s (12.1 mph) (Figures B29-B30). The average wind speed for the period was 1.7 m/s (3.8 mph). Winds were predominantly from the west for the period, with an average wind direction of 222°.

The air temperature record at this time is dominated by a diurnal signal with amplitude typically in excess of 10 °C (18 °F) (Figures B31-B32). Dew point temperature shows very little diurnal variation during this period. Relative humidity, which is a function of both air and dew point temperatures, consequently displays a strong diurnal variation. In general, relative humidity achieves a minimum value around midday, when air temperatures are at their highest, and a maximum value around midnight, when air temperatures reach their lowest values. Atmospheric pressure during the study period changed smoothly over periods of days. A summary statistical analysis of the data records for this time frame is presented in Table 3-4.

Solar radiation during this period exhibits a regular diurnal variation with a maximum peak magnitude of approximately 988.9 W/m² (30 June), a minimum peak magnitude of 759.2 W/m² (5 July), and a mean peak magnitude of 882.2 W/m² (Figures B31-B32). Irregularities in the peaks are due to local variations in atmospheric conditions (e.g., cloud cover).

Table 3-4. Statistical analysis of meteorological data for the summer survey period.

	Air Temperature °C (°F)	Dew Point °C (°F)	Relative Humidity	Pressure mbar
Mean	23.0 (73.4)	16.5 (61.7)	0.71	995.1
Minimum	10.7 (51.3)	6.6 (43.9)	0.28	985.3
Maximum	34.4 (93.9)	23.9 (75.0)	1.00	1004.1

4. Hydrothermal Model

The hydrothermal model used to predict the velocity and temperature structure of the lower Vernon Pool is part of a modeling system known as WQMAP. The model calculates the circulation and thermal characteristics in the area known as the far field where the initial plume momentum has dissipated and the plume is affected only by the ambient currents. If needed, a near field model can optionally be used to predict plume dilution in the vicinity of the discharge in the relatively small area where the discharge plume is primarily influenced by its own momentum. Since the focus of the study was on the lower Vernon Pool and not the immediate area around the discharge, the use of such a near field model was not considered necessary. In any event, the geometry of the Vermont Yankee discharge did not lend itself to the use of such a model (i.e. CORMIX3). The CORMIX3 model could not directly simulate the plant discharge geometry since there is a built-in model limitation that the discharge depth to width ratio be at least 0.05. The Vermont Yankee discharge geometry has a depth to width ratio of 0.005 (depth of 0.54 ft, width of 100 ft), 10 times less than the minimum, making CORMIX3 an inappropriate model.

4.1 Model Description - WQMAP

A state-of-the-art, boundary-fitted computer model (Swanson et al, 1989; Muin and Spaulding, 1997; Huang and Spaulding, 1995b) was used to predict pool elevations, flow, velocities and temperature distributions in the Vernon Pool. The boundary-fitted model matches the model coordinates with the shoreline boundaries of the water body, accurately representing the study area. This system also allows the user to adjust the model grid resolution as desired. This approach is consistent with the variable geometry of shoreline features of the Connecticut River. Development of the boundary fitted model approach has proceeded over the last decade (Spaulding, 1984; Swanson et al., 1989; Muin, 1993; and Huang and Spaulding, 1995a). The model may be applied in either two or three dimensions depending on the nature of the problem and the complexity of the study.

The boundary fitted method uses a set of coupled quasi-linear elliptic transformation equations to map an arbitrary horizontal multi-connected region from physical space to a rectangular mesh structure in the transformed horizontal plane (Spaulding, 1984). The three dimensional conservation of mass and momentum equations, with approximations suitable for lakes, rivers, and estuaries (Swanson, 1986; Muin, 1993) that form the basis of the model, are then solved in this transformed space. In addition a sigma stretching system is used in the vertical to map the free surface and bottom onto coordinate surfaces. The resulting equations are solved using an efficient semi-implicit finite difference algorithm for the exterior mode (two dimensional vertically averaged) and by an explicit finite difference leveled algorithm for the vertical structure of the interior mode (three dimensional) (Swanson, 1986). The velocities are represented in their contra-variant form. A sigma stretching system is used to map the free surface and bottom to resolve bathymetric variations.

A detailed description of the basic model being used for the Vernon Pool study with associated test cases is included as Appendix C (Muin and Spaulding, 1997). The publication was originally part of a Ph.D. dissertation (Muin, 1993), which extended the boundary fitted model capabilities, applying a contra-variant velocity formulation to the transformed momentum equations. A brief description of the model follows.

The basic equations are written in spherical coordinates to allow for accurate representation of large model areas. The conservation equations for water mass, momentum (in three dimensions) and constituent mass (temperature [heat] and salinity) form the basis of the model. It is assumed that the flow is incompressible, that the fluid is in hydrostatic balance, the horizontal friction is not significant and the Boussinesq approximation applies.

The boundary conditions are as follows:

- At land the normal component of velocity is zero.
- At open boundaries the free surface elevation must be specified and temperature and salinity specified on inflow.
- On outflow temperature (heat) and salinity is advected out of the model domain.
- A bottom stress or a no slip condition is applied at the bottom. No temperature (heat) is assumed to transfer to or from the bottom.
- A wind stress and appropriate heat transfer terms are applied at the surface.
- The surface heat balance includes all of the primary heat transfer mechanisms for environmental interaction. These include evaporative and sensible heat exchange with the air just above the water surface, and long wave radiation exchange between the water surface and the sky, and net short wave solar radiation between the loss due to reflection and the gain due to absorption at the water surface.

There are a number of options for specification of vertical eddy viscosity, A_v , (for momentum) and vertical eddy diffusivity, D_v , (for constituent mass [temperature and salinity]). The simplest formulation is that both are constant, A_{v0} and D_{v0} , throughout the water column. They can also be functions of the local Richardson number, which, in turn, is a function of the vertical density gradient and vertical gradient of horizontal velocity. A more complex formulation adds the dependence on mixing length and turbulent energy. Details can be found in Appendix C.

The set of governing equations with dependent and independent variables transformed from spherical to curvilinear coordinates, in concert with the boundary conditions, is solved by a semi-implicit, split mode finite difference procedure (Swanson, 1986). The equations of motion are vertically integrated and, through simple algebraic manipulation, are recast in terms of a single Helmholtz equation in surface elevation. This equation is solved using a sparse matrix solution technique to predict the spatial distribution of surface elevation for each grid.

The vertically averaged velocity is then determined explicitly using the momentum equation. This step constitutes the external or vertically averaged mode. Deviations of the velocity field from this vertically averaged value are then calculated, using a tridiagonal matrix technique. The deviations are added to the vertically averaged values to obtain the vertical

profile of velocity at each grid cell thereby generating the complete current patterns. This constitutes the internal mode. The methodology allows time steps based on the advective, rather than the gravity, wave speed as in conventional explicit finite difference methods, and therefore results in a computationally efficient solution procedure (Swanson, 1986; Swanson et al., 1989; Muin, 1993).

The environmental heat transfer model at the water surface contains a balance of the important terms governing the flow of heat including:

- short wave solar radiation
- long wave atmospheric radiation
- long wave radiation emitted from the water surface
- convection (sensible) heat transfer between water and air
- evaporation (latent) heat transfer between water and air

A detailed description of the equations used for the environmental heat transfer model is given in Appendix D.

4.2 WQMAP System

ASA personnel have developed and applied many computer modeling tools. In conducting aquatic environmental analyses we have developed a PC-based system, which integrates geographic information (land use, watersheds, etc.), environmental data (water quality parameters, surface elevations and velocities, stream flows, bathymetry, etc.) and models (analytical and numerical, hydrodynamic, pollutant transport, etc.). The power of such a system, called WQMAP (Water Quality Mapping and Analysis Program) (Mendelsohn, et al., 1995), is that it allows the user to model conditions and analyze alternatives to determine the optimal solution to a particular problem. A graphical user interface simplifies user inputs and allows a graphical display of model output. In addition, one of the modeling components within ASA's WQMAP has been specifically developed for application to the study of thermal effluents in coastal waters. More details on WQMAP can be found in Appendix E.

The geographic information component of WQMAP holds user-specified layers of data appropriate for the task. For instance, in this project such layers might include shorelines, intake locations, thermal diffusers or canals, monitoring data locations, etc. Each data layer can be easily input, either directly into WQMAP with a mouse and screen forms or through import from existing geographic information systems such as ARC/INFO, MAPINFO or AUTOCAD. Data can be exported as well. Each layer can be displayed separately or in any combination. Graphics can be generated and sent directly to a printer (color or black and white) or stored for later use in a computer driven slide show.

The environmental data component of WQMAP stores and displays actual environmental data, which are needed for analysis or used in model input or calibration. This component links to standard PC software such as databases, spreadsheets, and data contouring packages. Importing to and exporting from other systems is also possible.

A suite of tools in WQMAP can be used to import, export and manipulate environmental data. Time series of data at single or multiple stations can be imported, processed and

displayed. Other measuring systems (e.g., moored current meters, sea surface radars, acoustic Doppler current profilers) can also be accessed and provided into the model.

Another feature of WQMAP is its display capabilities. Color or black and white hard copies of any geographic, environmental, or model data screen display can be made. In addition, WQMAP is a powerful tool to inform audiences, both lay and technical, about project goals, methodology, and results. WQMAP is typically installed on Pentium class PCs and can be used to drive large screen monitors (for small audiences) or projector displays (for larger audiences).

4.3 Application to the Vernon Pool

4.3.1 Grid Generation

The first step in generating a grid is to define the study area of interest, e.g., the Vernon Pool in the Connecticut River above the Vernon Dam. Experience with previous model applications suggests that open boundaries should ideally be located away from the specific area of interest at natural constrictions, since there will be no significant lateral variability. This principle suggests that the model boundaries be located at the Vernon Dam and Bellows Falls (Figure 4-1).

The WQGRID component of WQMAP consists of a set of tools to generate a boundary fitted grid. The grid is specified by locating grid points along shorelines and bathymetric features. Each point has assigned grid counters to keep track of how each grid point relates to its neighbors. The grid spacing in the domain is roughly determined by grid spacing at land boundaries. Finer grid resolution is specified for increased flow resolution of the thermal discharge from Vermont Yankee. Once the boundary grid points along the shoreline have been specified, and any interior bathymetric feature grid points located, the gridding model generates all the remaining interior points. These points are constrained to obey a Poisson equation and their locations are solved iteratively by a Poisson solver. Technical details can be found in the WQMAP User's Manual (ASA, 1996).

Figure 4-1 shows the model grid. Here the full grid covers a 42 km (26 mile) extent of the Connecticut River known as the Vernon Pool, with a total of 3131 water grid cells in each of 11 layers. The grid is finer (20 m \times 20 m [65 ft \times 65 ft]) in the area near the Vermont Yankee discharge to better resolve the circulation and thermal plume. The grid upstream from the lower Vernon Pool is purposely coarse to minimize the model computations required yet still provide accurate downstream predictions.

In general the grid aspect ratio reflects *a priori* estimates of expected flows. This means that the longer grid dimension, if any, is oriented along the major axis of the flow. This approach is necessary because the hydrodynamic model has inherent time step restrictions based on the ratio of grid size to flow speed. Faster model runs are possible when the grid is optimized in this manner.

The 11-layer grid covers the entire modeled area, regardless of the pool depth. In shallow areas, the local cell thicknesses are smaller (thinner), while in deeper areas the local cell

thicknesses are larger (thicker). The local cell thickness is always 1/11 of the local water depth. The advantage of this type of approach is that, regardless of the water depth, the model effectively resolves the vertical structure finely with 11 layers given the relatively shallow depth of the River in Vernon Pool. This can be contrasted with models that are limited to constant local cell thicknesses (i.e., 1 m [3 ft] everywhere) resulting in lower resolution in shallow areas.

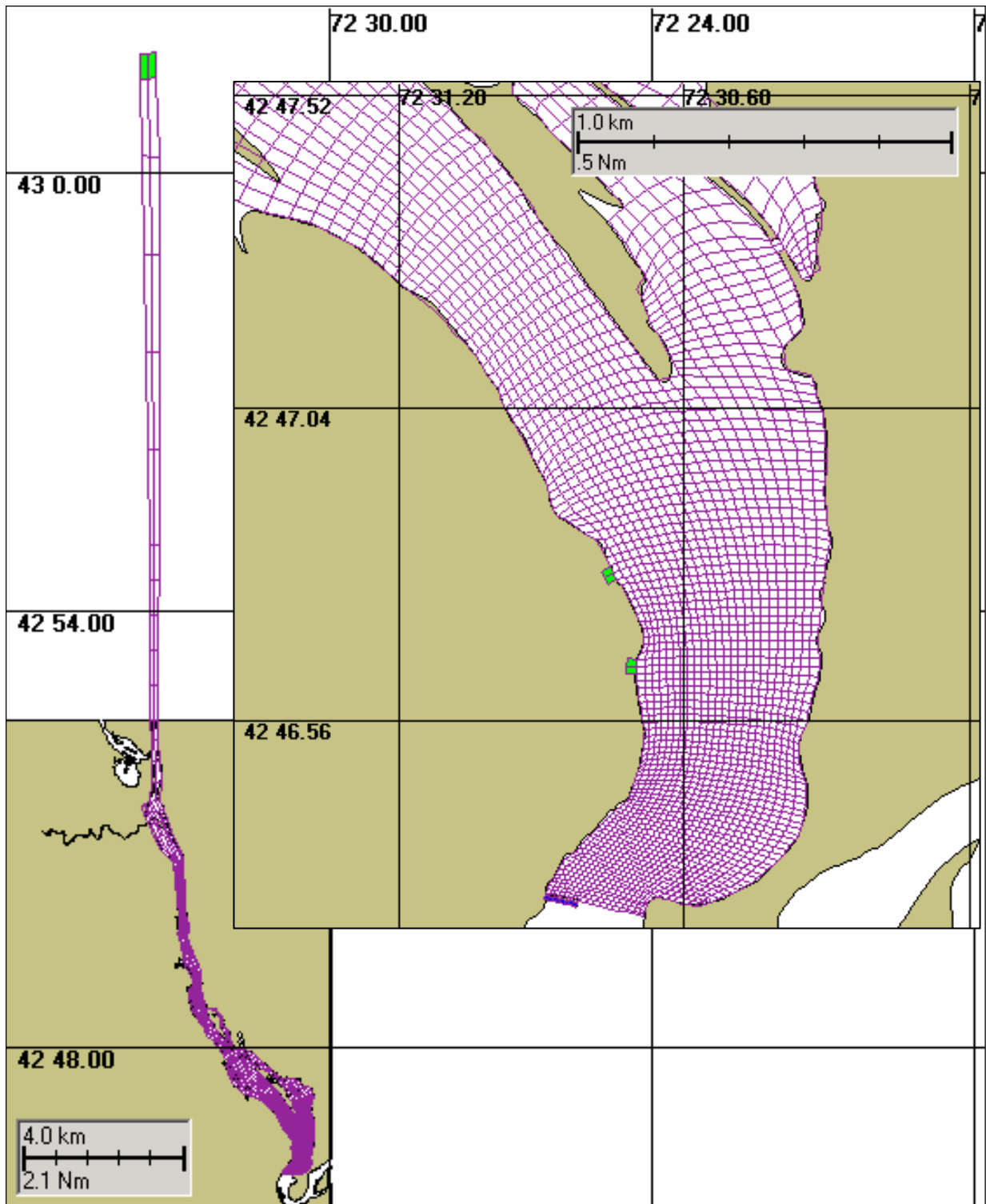


Figure 4-1. Model grid for the Vernon Pool study area: Blue shaded cells represent downstream boundary and green shaded cells represent intake, discharge and upstream river boundary.

4.3.2 Bathymetry

A depth value must be assigned to each cell in the model grid. Two methods were combined to create the array of grid depths. First, the bathymetric soundings from a field study conducted by Normandeau in June 2002 with associated latitude and longitude for the area were combined into a digital data set. Each grid cell was automatically assigned a depth value by interpolation from the data based on a distance-weighting algorithm for soundings close to the grid location. Once the bathymetric measurements were applied, the WQGRID result was generated.

The second method to assign depths is based on the experience of the modeler to more accurately specify depths. Tools from WQGRID were used to select individual cells or groups of cells and specify depth values. This procedure is necessary to accurately represent bathymetry in an area where the automatic interpolation may not capture the actual depth or no data is available, for example just upstream of the Vernon Dam.

Figure 4-2 shows a plan view of the resulting model bathymetry in the lower Vernon Pool. Most immediately noticed is the deep water-depth along the river axis (~ 5 m [16 ft]), becoming deeper approaching the Vernon Dam (~12 m [40 ft]). Also seen is a somewhat deeper area near the intake. These are important features controlling the flow in the area. Another notable feature is the shallow, relatively flat area in the eastern portion of the Pool.

4.3.3 Boundary Conditions

There are three steps involved in any thermal dispersion modeling study: calibration, confirmation and simulations. The 11-layer, 3-dimensional boundary fitted hydrodynamic model (BFHYDRO) employed to determine the circulation and thermal distribution requires a set of boundary forcing conditions for each step. River flow, surface elevation and winds are major forcing functions important in driving the circulation, and solar radiation and auxiliary parameters such as air and dew temperature, relative humidity and pressure play an important role in determining the thermal field.

The model calibration was conducted for August 2002, while the confirmation was performed for late June and July 2002. For the modeling, flow observed at Vernon Dam and temperature at upstream station 7 was specified at the upstream river boundary. All the data were collected at hourly intervals (as described in Section 3). This section documents boundary forcings including river flow and temperature, environmental conditions and plant operations, required for model simulations each period.

It was assumed that the discharge from the Bellows Falls Dam, upstream of the Vernon Pool, is well-mixed, an appropriate assumption given that water passing through hydroelectric facilities is well mixed as is confirmed by the Vernon Dam tailrace temperature data. Thus the upstream boundary condition should have no significant vertical structure, except that atmospheric heat transfer can and does cause periodic stratification of the water column as the water moves downstream through the Vernon Pool. The Station 7 temperature is indicative of the well-mixed water column Bellows Fall Dam discharge, since it is less affected by diel atmospheric effects due to its depth. These assumptions were corroborated during the model calibration process.

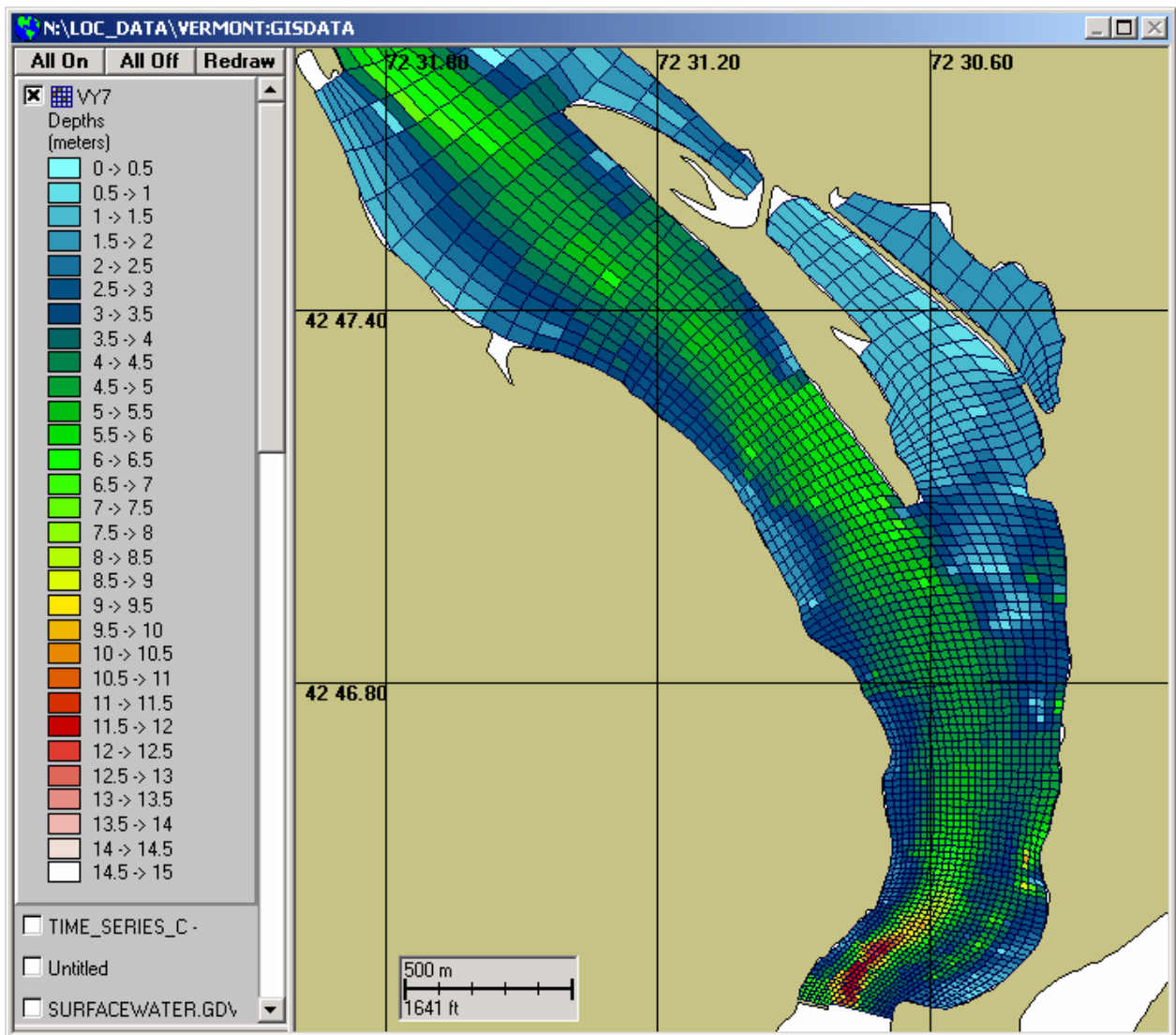


Figure 4-2. Model bathymetry of the lower area of the study domain.

4.3.3.1 Model Calibration and Confirmation

Two periods were chosen for the model calibration and confirmation, based on warm environmental conditions with low river flow (calibration) and fishway operation (confirmation). The calibration period extended from 1 through 24 August when air temperature was in general warmer than any other month and river temperatures were warmest. The confirmation period extended from 25 June to 9 July, which was the latter portion of the fishway operation period (mid May through early July) to capture the time of warmest river temperatures.

Figures A40 through A48 show environmental conditions for the August period, including two major heat-flux parameters (air temperature and solar radiation). Mean air temperature for the August period was 0.8°C (1.4°F) warmer than the second warmest month (July), and ranged from 8 (46°F) to 35°C (95°F) (Figures A43 – A45). Diurnal variations were apparent

during the period, showing a maximum range of 19.4°C (35°F) on 9 August. Temperature at night occasionally dropped to 10°C (50°F). Solar radiation was almost constant during the period, except when more cloud coverage occurred on 20 and 24 August, with maximum radiation lower by about 240 W/ m² than the peak radiation.

Figures B29 through B34 shows atmospheric forcing parameters for the June-July period. Air temperature varied between 9°C (48°F) and 34°C (93°F) showing a mean temperature of 23°C (73°F). Diurnal variation of the temperature was similar as that in the August period. Solar radiation was also the same magnitude as the August period.

River environmental conditions were quite different for these two periods, however. Figures A35-A36 and Figures B23-B24 present river flow and upstream and downstream water temperatures. The flow for the August period was relatively low at 50 m³/s (1,766 ft³/s) with occasional high flows as large as 200 m³/s (7,063 ft³/s), whereas the flow for the June-July period was greater than 200 m³/s (7,063 ft³/s) for most of the period. Mean flows were 66 m³/s (2,317 ft³/s) and 266 m³/s (9,394 ft³/s) for the August and June-July periods, respectively.

Based on information presented in the Demonstration (Table 3-1, page 7), August median flow at North Walpole is about 106 m³/s (3,735 ft³/s) while the 95th percentile flow (August flow that exceeds this flow 95% of the time) is 51 m³/s (1,797 ft³/s). Flows during the August modeling period were therefore substantially below “normal”, but well within the historic range. The average flow during the August modeling period has an exceedance value of about 85% and that the lowest flow (50 m³/s) would be expected to be exceeded more than 95% of the time. Similarly, based on Table 3-1, the median flow during the June/July modeling was about 167 m³/s (5,900 ft³/s). The 95th percentile flow is expected to be about 79 m³/s (2,800 ft³/s) during the same period. This means that average flow during the modeling period was considerably higher than historic median flow (~25% exceedance value), but still well within historic ranges. The minimum flow during this period was very low, exceeded nearly 95% of the time. Thus, flows that occurred during the time periods used for model calibration and verification were often well below historic median flows, but all were well within recorded ranges.

While the measured upstream temperature was almost constant at 25°C (77°F) for the August period, the temperature for the June-July period gradually increased from 19°C (66°F) to 24°C (75°F) and finally leveled off from 6 through 9 July.

The power plant operations were also different for the periods. Figures 4-3 and 4-4 show the variation of plant discharge flow, ΔT and rejected heat for the August and June-July periods, respectively. In August, rejected heat was at 200 MW for the most of period, except times when the discharge flow was high with relatively high ΔT . The maximum flow and ΔT were 20 m³/s (706 ft³/s) and 11°C (20°F), respectively. For the June-July period, the plant discharge flow was constant at 20 m³/s (706 ft³/s) from 25 June to 2 July, and showed large daily variations. A similar response was seen for ΔT and rejected heat. ΔT and heat for the first six days were at 13°C (23°F) and 1,100 MW, respectively. For the rest of the period, ΔT

varied between 5°C (9°F) and 13°C (23°F), and reject heat changed between 200 MW and 1,100 MW.

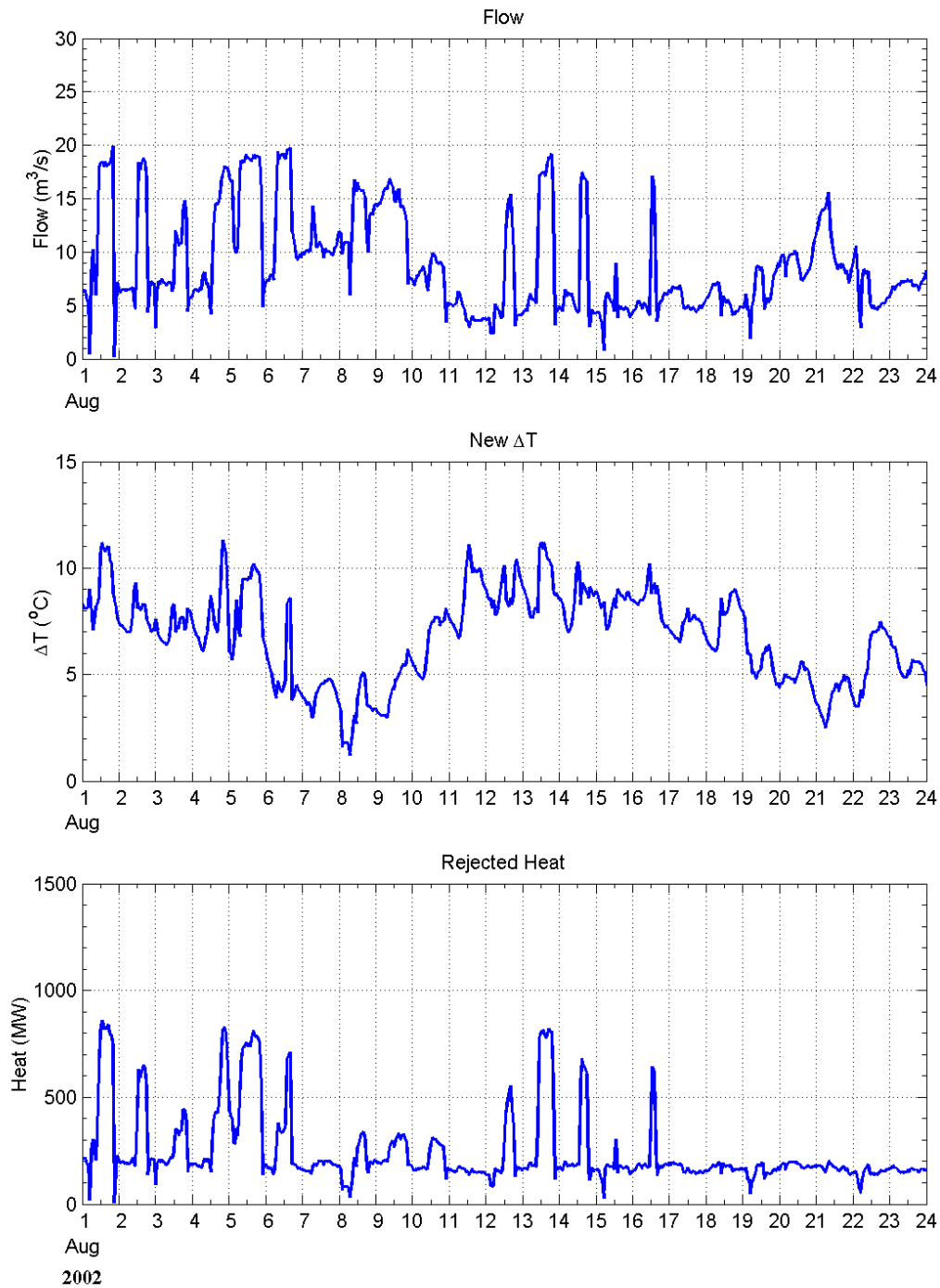


Figure 4-3. Vermont Yankee Station operations with computed rejected heat for the calibration period from 1 to 24 August 2002.

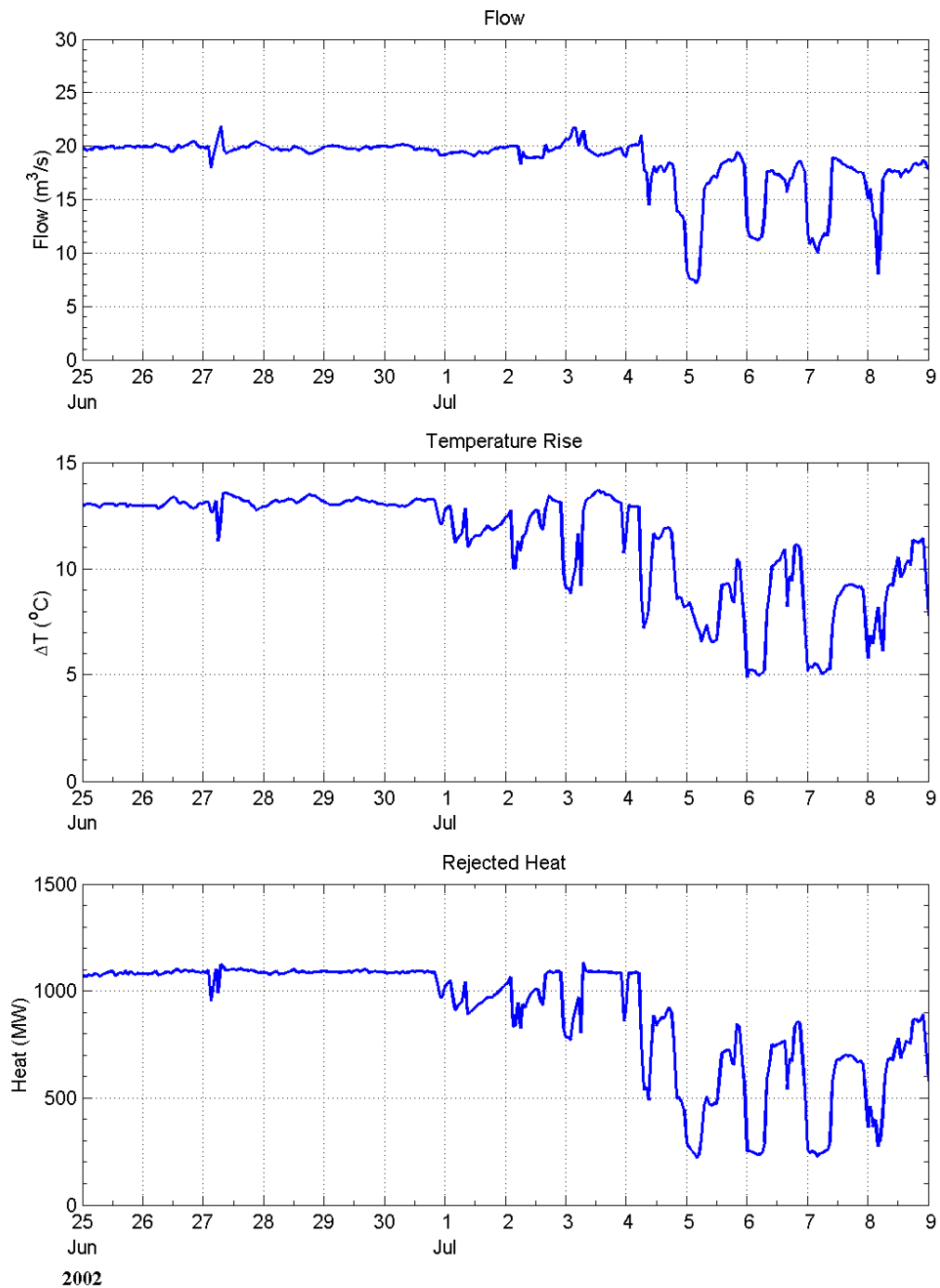


Figure 4-4. Vermont Yankee Station operations with computed rejected heat for the confirmation period from 25 June to 9 July.

4.3.3.2 Scenario Simulations

A total of ten scenarios were developed by Normandeau with combinations of various hypothetical Vermont Yankee Station operations and river conditions. Four scenarios were chosen for the August period, and six scenarios were selected for the June-July period. Tables 4-1 and 4-2 summarize the scenarios. The scenarios for the August period included both a worst case (low river flow and high river temperature conditions occurring less than 1% of the time) and an average case (river flow and temperature conditions occurring 50% of the time). Both the existing permit ΔT of 2°F and the proposed new permit ΔT of 3°F were evaluated for each case (Table 4-1). The scenarios for the June-July period included both the worst and average cases plus a case where low flow and high temperature conditions occurred less than 10% of the time. Again both the existing permit ΔT of 2°F and the proposed new permit ΔT of 3°F were evaluated for each case (Table 4-2). The period of record from which 1% and 50% occurrences of low flow and high temperature were derived for both the July-August and mid-May-mid-July periods of evaluation was the most recent five year period, 1998 – 2002.

Atmospheric forcing for the scenario simulations used monthly mean values for all parameters except air temperature and solar radiation. Because the heat exchange varied dramatically over a 24-hr period due to variations in air temperature and solar radiation, typical daily profiles were determined for these parameters. Figure 4-5 shows the daily variations of air temperature and solar radiation for the August and June-July periods obtained by taking an average for each hour in the day for 30 days between 1 to 30 August, and between 15 June to 15 July, respectively. The mean air temperature for August varied between 15°C (59°F) and 27°C (81°F), and the radiation peaked at 765 W/m². Mean values used for dew temperature, pressure and relative humidity were 14.9°C (58.8°F), 999 mbar and 73%, respectively. For the June-July period, air temperature and solar radiation were 0.7°C (1.3°F) lower and 31 W/m² higher than those in August, respectively. All monthly mean values of the atmospheric forcing functions, as well as the mean daily variations in air temperature and solar radiation used for the modeling scenarios were based on actual data from the 1-30 August and 15 June – 15 July periods of 2002, consistent with the calibration and confirmation periods.

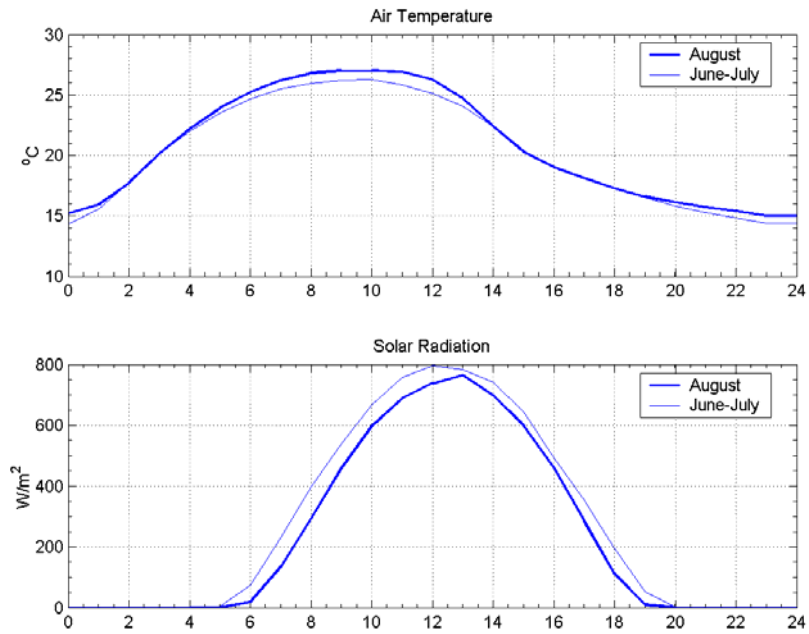


Figure 4-5. Typical daily variations of air temperature and solar radiation for the August and June-July periods.

Table 4-1. Summary of parameters for August scenarios. Vermont Yankee Temp denotes the plant discharge temperature.

Scenario	River Flow	Vermont Yankee Flow	Intake Temp	Vermont Yankee Temp	Vermont Yankee ΔT	Heat	Description
	m ³ /s (ft ³ /s)	m ³ /s (ft ³ /s)	°C (°F)	°C (°F)	°C (°F)	MW	
1%-2°F rise	36.1 (1,275)	3.4 (121)	26.1 (79)	37.8 (100)	11.7 (21)	168	1% occurrence of low flow and high temperature conditions with existing permit ΔT of 2°F
1%-3°F rise	36.1 (1,275)	5.2 (182)	26.1 (79)	37.8 (100)	11.7 (21)	253	1% occurrence of low flow and high temperature conditions with proposed new permit ΔT of 3°F
50%-2°F rise	96.8 (3,420)	7.3 (258)	23.1 (73.5)	37.8 (100)	14.7 (26.5)	449	50% occurrence of low flow and high temperature condition with existing permit ΔT of 2°F
50%-3°F rise	96.8 (3,420)	11.0 (387)	23.1 (73.5)	37.8 (100)	14.7 (26.5)	673	50% occurrence of low flow and high temperature condition with proposed new permit ΔT of 3°F

**Table 4-2. Summary of parameters for the June –July scenarios. Vermont Yankee
Temp denotes the plant discharge temperature.**

Scenario	River Flow	Vermont Yankee Flow	Intake Temp	Vermont Yankee Temp	Vermont Yankee ΔT	Heat	Description
	m ³ /s (ft ³ /s)	m ³ /s (ft ³ /s)	°C (°F)	°C (°F)	°C (°F)	MW	
1%-2°F rise	45.2 (1,660)	3.6 (128)	23.9 (75.1)	37.8 (100)	13.8 (24.9)	208	1% occurrence of low flow and high temperature conditions with existing permit ΔT of 2°F
1%-3°F rise	45.2 (1,660)	5.4 (192)	23.9 (75.1)	37.8 (100)	13.8 (24.9)	323	1% occurrence of low flow and high temperature conditions with proposed new permit ΔT of 3°F
10%-2°F rise	47.6 (1,685)	3.4 (120)	22.6 (72.6)	37.8 (100)	15.2 (27.4)	217	10% occurrence of low flow and high temperature conditions with existing permit ΔT of 2°F
10%-3°F rise	47.6 (1,685)	5.2 (184)	22.6 (72.6)	37.8 (100)	15.2 (27.4)	329	10% occurrence of low flow and high temperature conditions with proposed new permit ΔT of 3°F
50%-2°F rise	156.8 (5,558)	9.2 (325)	18.8 (65.0)	37.8 (100)	18.9 (34.1)	726	50% occurrence of low flow and high temperature conditions with existing permit ΔT of 2°F
50%-3°F rise	156.8 (5,558)	13.8 (488)	18.8 (65.0)	37.8 (100)	18.9 (34.1)	1,090	50% occurrence of low flow and high temperature conditions with proposed new permit ΔT of 3°F

4.4 Model Calibration and Confirmation

The calibration or confirmation of numerical models is a complex process. Much literature has been published over the past few decades describing various approaches (McCutcheon et al., 1990; Hess and Bosley, 1992; Lynch and Davies, 1995). In general the calibration process is an organized procedure to select model coefficients to best match observations.

The calibration should be based on two principles (McCutcheon et al., 1990):

- the simplest model formulation should be used to solve the problem at hand, and
- the model coefficients and parameters should be uniform in space and time unless there is strong evidence in the experimental data that they should change.

The calibration procedure (McCutcheon et al., 1990) can be summarized as follows for the Vermont Yankee hydrothermal application:

- reproduce velocities and flows at selected locations by adjusting bottom friction, eddy viscosity coefficients and open/river boundary specifications.
- reproduce temperature distributions by adjusting eddy diffusivities, flux rates to the atmosphere and the plant heat loading rates.

For the calibration application a matrix of computer runs were executed to determine the sensitivity of the model to variations in model parameters and find the set that gave the best model results in comparison with observations. The resulting hydrodynamic model parameters ultimately chosen included a quadratic bottom friction coefficient of 0.005 and a vertical eddy viscosity of 0.005 m²/s (0.016 ft²/s). The horizontal and vertical eddy diffusivities for temperature were 1 m²/s (3.28 ft²/s) and 0.7×10⁻⁴ m²/s (0.2×10⁻⁴ ft²/s), respectively. These are summarized in Table 4-3 indicating the range of values tested as well as a comparison to literature value ranges. The calibration process tested values over a range from at least one half to at least twice the ultimate value used. This extensive testing provided confidence that the calibration process used the optimum set of parameters

Table 4-3. Summary of model parameters used in the calibration and testing.

Parameter	Units	Value Used	Range of Values Tested	Literature Values
Quadratic bottom friction coefficient	n/a	0.005	0.0025-0.03	0.0002-0.016* in Ambrose et al. (1988)
Vertical eddy viscosity	m ² /s	0.005	0.001-0.01	0.0-0.2 in Cole and Wells (undated)
Horizontal eddy diffusivity	m ² /s	1.0	0.5-2.0	0.0001 - 100 in Bowie et al. (1985)
Vertical eddy diffusivity	m ² /s	7*10 ⁻⁵	5*10 ⁻⁵ – 10 ⁻²	2*10 ⁻⁶ - 10 ⁻⁴ in Bowie et al., 1985

* Based on a range of Manning coefficients given as 0.01 to 0.08.

The upstream river boundary forcings used actual flow and temperature. The downstream open boundary forcing used zero relative elevation. The net surface heat fluxes were computed using observed solar radiation and other environmental parameters (air

temperature, dew temperature, winds and relative humidity). During the confirmation period, the computed net heat flux varied between -94 W/ m^2 for a cloudy day and 88 W/ m^2 for a sunny day.

These hydrodynamic and temperature parameters were selected to minimize the difference between model predictions and observations, using the qualitative and quantitative evaluation metrics described below.

The sensitivity study showed that the currents and flows were generally insensitive to bottom friction. Progressively increasing the horizontal and vertical diffusivities systematically reduced the horizontal and vertical gradients of temperature, with lower values resulting in stronger gradients and stratification. Decreasing the heat transfer coefficient increased heating in the shallow water areas, and 98% of the coefficient suggested in Thomann and Mueller (1987) was chosen for simulation.

Qualitative Comparisons

The comparison of model results and observations depends on data dimensionality. For example, a time series of data collected at a particular site can be plotted together with model output to provide a visual comparison. This comparison can provide information on the suitability of the model to simulate the range of variability evident in the observations. Each process that affects the observations has a characteristic frequency or set of frequencies. The data can be filtered to remove low, mid or high frequencies, as an aid in understanding the important physical processes and their time scales. No model can simulate the entire range of frequencies since neither the forcing functions (e.g. winds) are known with sufficient precision nor is the model grid fine enough to resolve the small scales. It is often necessary to filter the observations (i.e., remove the high frequencies) when comparing to model results. Care must be taken to avoid removing any important frequencies, however.

The most direct way to provide a qualitative comparison is to plot the model predictions and the observed data for each variable over the time of the simulation. This can be done with time series plots of the variables of interest or contour plots when looking at spatially varying patterns.

Quantitative Comparisons

Quantitative comparisons are statistical measures that can be applied to the model predictions and field data sets that provide a numerical assessment of the comparison. These statistical measures can be grouped into two major components: those measures that describe an individual set of data (e.g., a time series of one variable) and those that relate the degree of difference (error) between two data sets (e.g. time series of model predictions and field observations). Individual statistical measures include the mean, standard deviation, percentiles, minimum, and maximum. The independent variable can be time, depth or distance in these data. The quantitative comparisons between data sets include relative error, root mean square error, linear regression, comparison of means and correlation coefficient. McCutcheon et al (1990) describes these quantitative comparisons in detail and provide guidance on acceptable values. Each statistical measure is briefly discussed below.

Relative Mean Error (RME)

The relative error measures the difference between calculated and observed mean values and can be defined in a variety of ways. The *relative mean error* is the relative difference of the means

$$rme = \frac{|\bar{x} - \bar{c}|}{\bar{x}}$$

where \bar{x} is the mean of the observation values and \bar{c} is the mean of the model-predicted or calculated values. Evaluation of this statistic over space and time can be made to provide a cumulative frequency of error (median error, percentile exceedances). The relative error is expressed as a percentage. This statistic can be unreliable for small values of the mean and does not provide information on the variability in the data but is a useful indicator for general model performance.

Error Coefficient of Variation (ECV)

The error coefficient of variation is the ratio of the root mean square error to the mean. It is defined as:

$$ecv = \frac{1}{\bar{x}} \sqrt{\frac{\sum (x_i - c_i)^2}{N}}$$

and expressed as a percentage.

Square of Correlation Coefficient (r^2)

The correlation coefficient (r) relates to the linear interdependence of the predictions to observations. It is defined as the ratio of the covariance and the standard deviations of predicted and observed values.

The squared correlation coefficient is the square of r , and lies between -1 and 1. A value of zero indicates no correlation between two observations and predictions, 1 represents perfect positive correlation and -1 implies perfect negative correlation.

The U. S. EPA has published guidance on the acceptable statistical measure values for model calibration/confirmation (McCutcheon et al., 1990). Table 4-4 shows a summary of the guidance for different measures and properties. The statistical measures have been defined above and the properties include flow and temperature. There is a unique value presented for each property. McCutcheon, et al. (1990) state that these guidance values are representative of a mean level of calibration/confirmation among multiple comparisons and are not to be considered an upper limit (RME, ECV) or lower limit (r^2) for individual comparisons.

Table 4-4. Model calibration and confirmation guidance (McCutcheon et al., 1990).

Error Measure	Property	Value
Relative Mean Error, RME	Flow	30%
	Temperature	25%
Error Coefficient of Variation, ECV	Flow	10%
	Temperature	45%
Squared Correlation Coefficient, r^2	Flow	0.88
	Temperature	0.71

4.4.1 Calibration to August 2002 Period

The primary focus of the calibration process is to adjust appropriate model parameters to optimize the comparison to a data set of observations. The parameters, as discussed in the previous sections, include bottom friction, horizontal and vertical dispersion, and atmospheric exchange rates. A period from 1 through 24 August was chosen for calibration because the river was in a low flow, high temperature regime.

The observed data used for the model calibration are hourly flow measurements at Vernon Dam and temperature data from the thermistor string array. Each thermistor station had three thermistors at different depths, 0.3 m (1 ft) below the surface, mid-depth and 0.3 m (1 ft) off the bottom. Results of the comparison with the model predictions are presented below.

Flow Comparisons

Figure 4-6 shows predicted flow at Vernon Dam (dash – dot), together with the observed flow (solid). The predicted flow is highly correlated with the observations, showing a squared correlation coefficient of 0.96. Mean values for the predictions and observations are $67 \text{ m}^3/\text{s}$ ($2,366 \text{ ft}^3/\text{s}$) and $66 \text{ m}^3/\text{s}$ ($2,331 \text{ ft}^3/\text{s}$), respectively. The RME is 3%, the ECV is 0% and r^2 is 0.92. The model calibration results show that the model predictions of flow agree well with observations, exhibiting statistical measures with values well within U.S. EPA guidance levels of 30% for RME, 10% for ECV and 0.88 for r^2 .

Between predictions and observations, however, there is a time lag of 1.5 hrs, which is due to the travel time of a parcel of water between the upstream and downstream boundaries. There also exists an oscillation at a period of about 5 hours, especially seen after a large change in flow amplitude. . The overshoots and artificial oscillations in the modeled flow predictions are typical for an under-damped system responding to step inputs. The step inputs are due to the regulated flow in the River attributable to the hydroelectric project operations, as discussed above and in Section 3.1.2 of the Demonstration. The large, almost instantaneous change in flow, often by a factor of four from $50 \text{ m}^3/\text{s}$ to $200 \text{ m}^3/\text{s}$ ($1760 \text{ to } 7060 \text{ ft}^3/\text{s}$), is sufficient to generate an overshoot response followed by a damped oscillation. The period of oscillation is approximately 5 hrs, which corresponds to the natural frequency of the Vernon Pool. Conservation of water mass is preserved during these transient events. These small variations have no appreciable effects on temperature predictions.

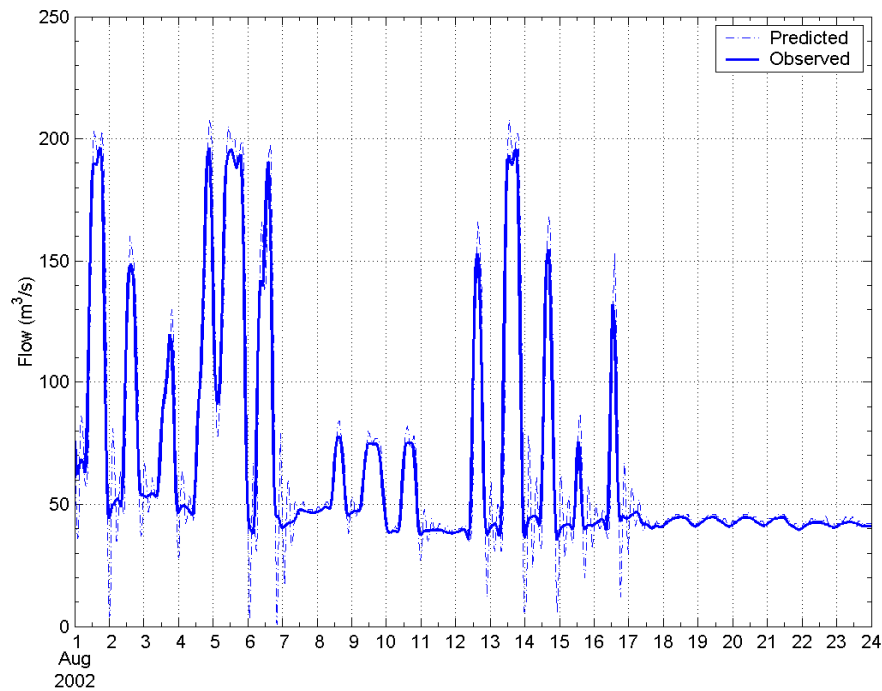


Figure 4-6. Downstream flow comparison between the prediction and observations.

Temperature Comparisons

Temperature comparisons between the predictions and observations are shown as time series for each of the three thermistor depths on a string. Figures 4-7 to 4-9 show the surface, middle and bottom layer temperatures for representative strings (C3, D3 and E3) located in the center of the pool from discharge to the dam. Quantitative comparisons (statistical measures) are presented for all the thermistors in Tables 4-5 through 4-7. The locations of the thermistor strings are shown in Figure 3-1. String C3 is located 278 m (910 ft) east of Vermont Yankee, and Strings D3 and E3 are located 384 m (1,258 ft) and 517 m (1,695 ft) southeast of the station, respectively.

The model predictions and observations for the surface layer at String C3 compare well for the entire simulation period (Figure 4-7), exhibiting RME of 1%, ECV of 1.9% and r^2 of 0.82 (Table 4-5). The maximum difference for the layer is 0.6°C (1.1°F) occurring on 11 August, but the mean difference is only 0.3°C (0.5°F). The mid-depth temperatures agree well with the observations (0.9% RME, 2.5% ECV and 0.7 r^2) except 1 – 5 August and 11 – 15 August when the observed bottom temperatures are higher than the mid-depth temperature. The bottom comparison diverges somewhat more than that for the mid-depth.

The observed temperatures at String D3 exhibit a large diurnal variation at both the surface and middle layers, but less at the bottom layer (Figure 4-8). The predictions at the surface agree well with the observations, with r^2 of 0.82, RME of 1.1% and ECV of 2.0% (Table 4-5). However, the model slightly under predicts the mid-depth temperature for most of the period, except 14 – 16 August, showing a 0.3°C (0.5°F) difference in temperature. The model error

statistics for this layer are 1.3% for RME, 2.2% for ECV and 0.74 for r^2 (Table 4-6). The bottom comparison is good except under predictions of peaks.

Figure 4-9 shows the temperature comparisons at String E3. The surface observations exhibit relatively large temperature peaks on 1 – 2, 4 -5 and 13 August, which are probably due to the heated flow from Vermont Yankee. The model predicts the peaks well but sometimes under predicts (8 – 9 August) or over predicts (14 – 16 August). The statistics for the layer show low RME, ECV and r^2 (0.1%, 2.7% and 0.57, respectively). The predictions for the mid-depth agree well with the observations, especially predicting the long-term variation. However, the model under predicts the temperature peaks both at mid depth and bottom. The r^2 value decreases with depth. The RME values decrease from 0.8% for the middle layer to 0.5% for the bottom layer, whereas the ECV values increase from 2.6% for the mid-depth to 2.9% for the bottom.

The temperature comparisons show that the model sometimes predicts a larger amplitude of the diurnal temperature variation at the surface. This may be due to the fact that the source of air temperature data was the weather station at the Orange Municipal Airport in Orange, MA, which is 35 km (22 mi) southeast of Vermont Yankee. Although some meteorological parameters were available at Vermont Yankee, the surface heat transfer submodel of the hydrothermal model required additional meteorological parameters not measured at Vermont Yankee, so the data from Orange were used. Some differences exist in parameters from the two stations. For instance, the daily air temperature variation at Orange has an amplitude of 1 to 3°C (1.8 to 5.4°F) larger than at Vermont Yankee. From previous model applications, the surface water temperature variation is typically one-half of the air temperature variation, which would result in a amplitude 0.5 to 1.5°C (0.9 to 2.7°F) larger than the observations. Thus the model calibration would have been even better using the local Vermont Yankee temperatures. In any event, the model was shown to be well calibrated, indicating the Orange data was suitable for use.

Figure 4-10 shows predicted temperatures at upstream and downstream stations 7 and 3, superimposed on the measurements. Stations 7 and 3 are located 6.4 km (4 mile) north and 1.8 km (1.1 mile) south of Vermont Yankee, respectively. Since station 7 is located far north of the plant, there should be no impact by the rejected heat from the plant. The measurements at stations 7 and 3 are used as an indicator of background water temperature and the effects of plant operation, respectively.

The predicted temperatures at station 7 agree well with the observations. The maximum difference found between the two data sets is only 0.7°C (1.3°F) occurring on 6 August (model underprediction). Temperature comparisons at station 3 also show good agreement with a maximum difference in temperature of 1°C (1.8°F). This occurs on 15 August during a 6-day over prediction period (14 – 19 August). Since such an over prediction for the period is also observed at the same layers for other stations, it may be related to an under prediction of vertical stratification but is not significant.

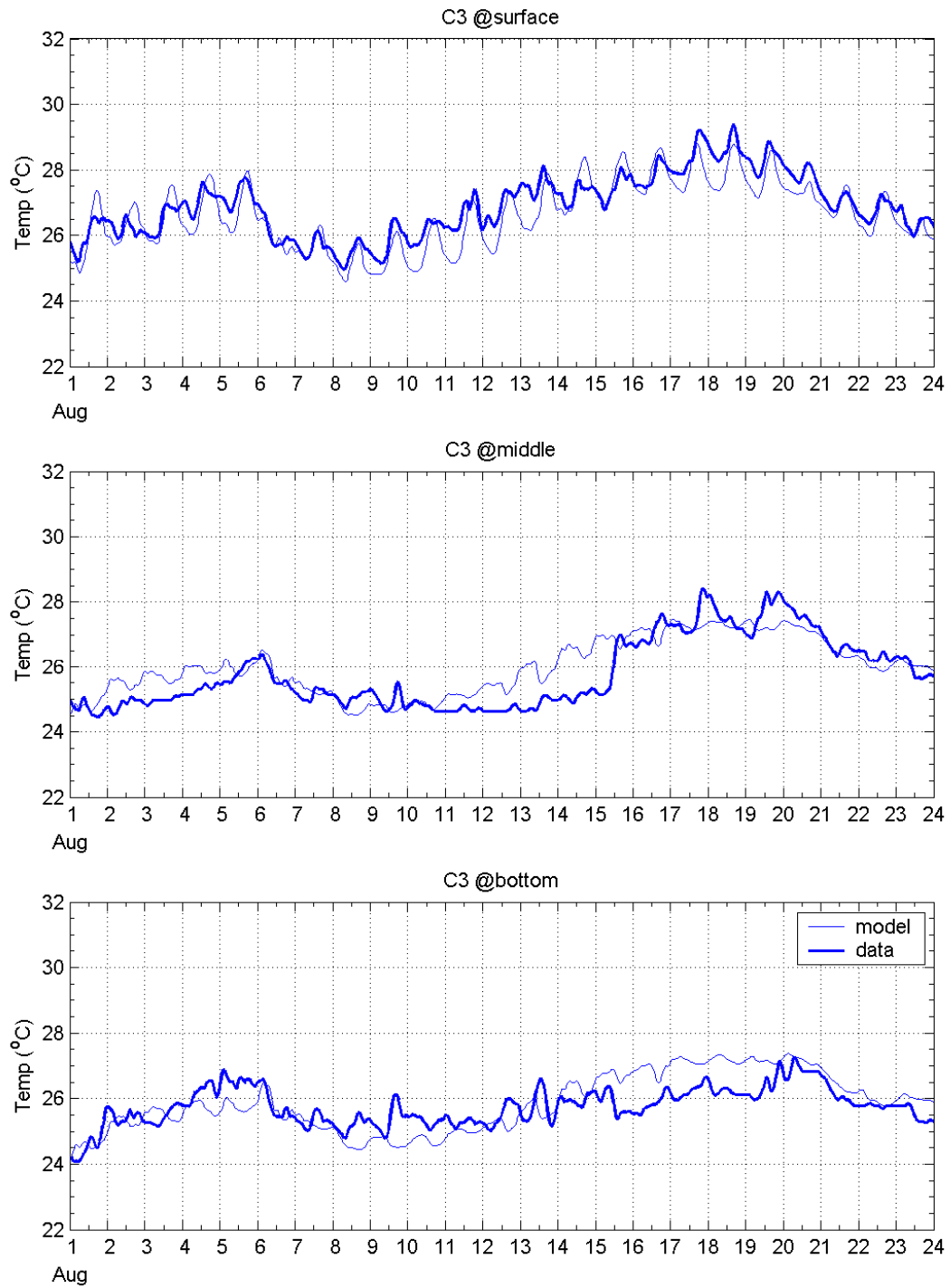


Figure 4-7. Comparison of observed (thick) and simulated temperatures (thin) at the surface, middle and bottom layers for string C3.

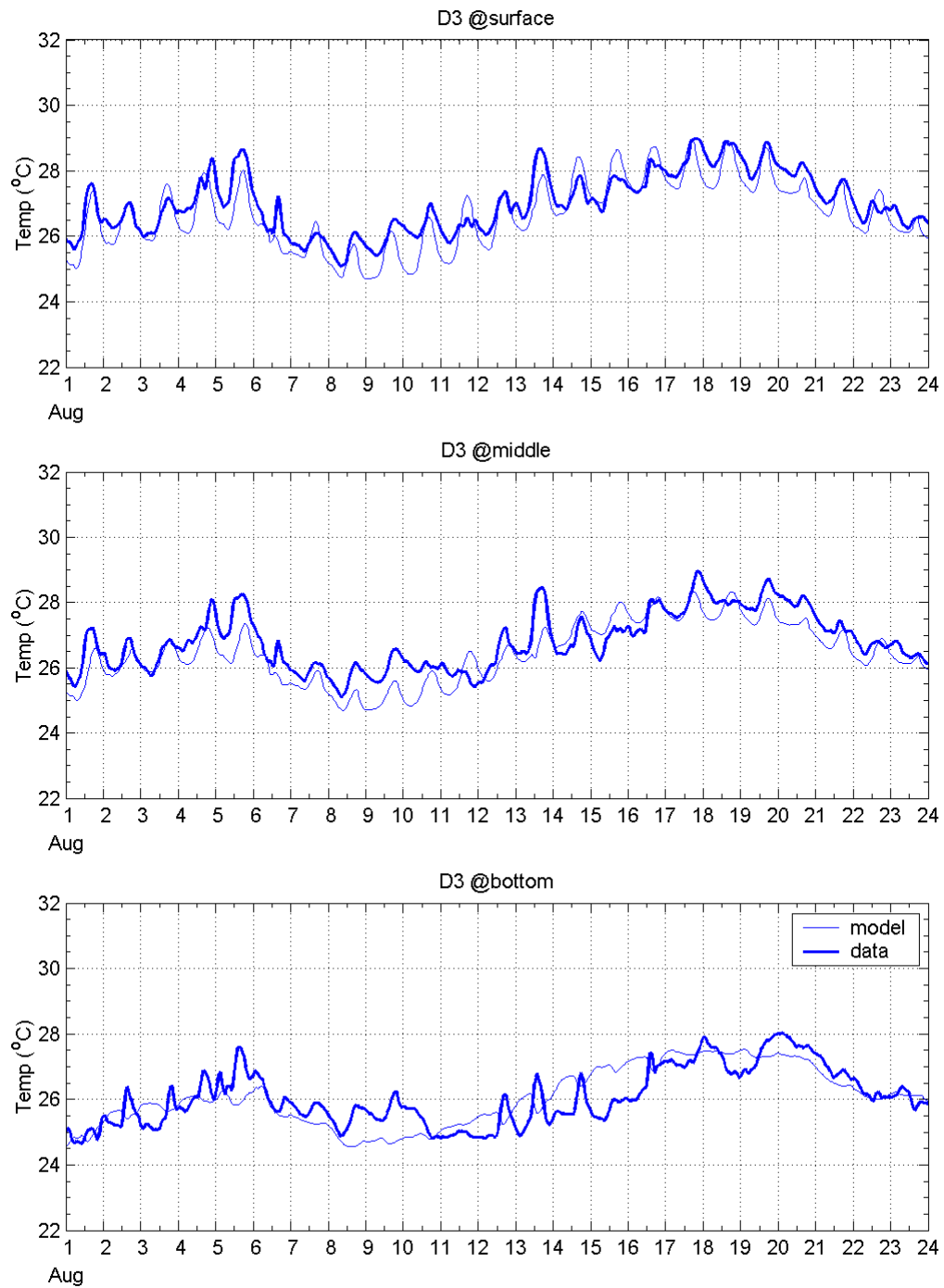


Figure 4-8. Comparison of observed (thick) and simulated temperatures (thin) at the surface, middle and bottom layers for string D3.

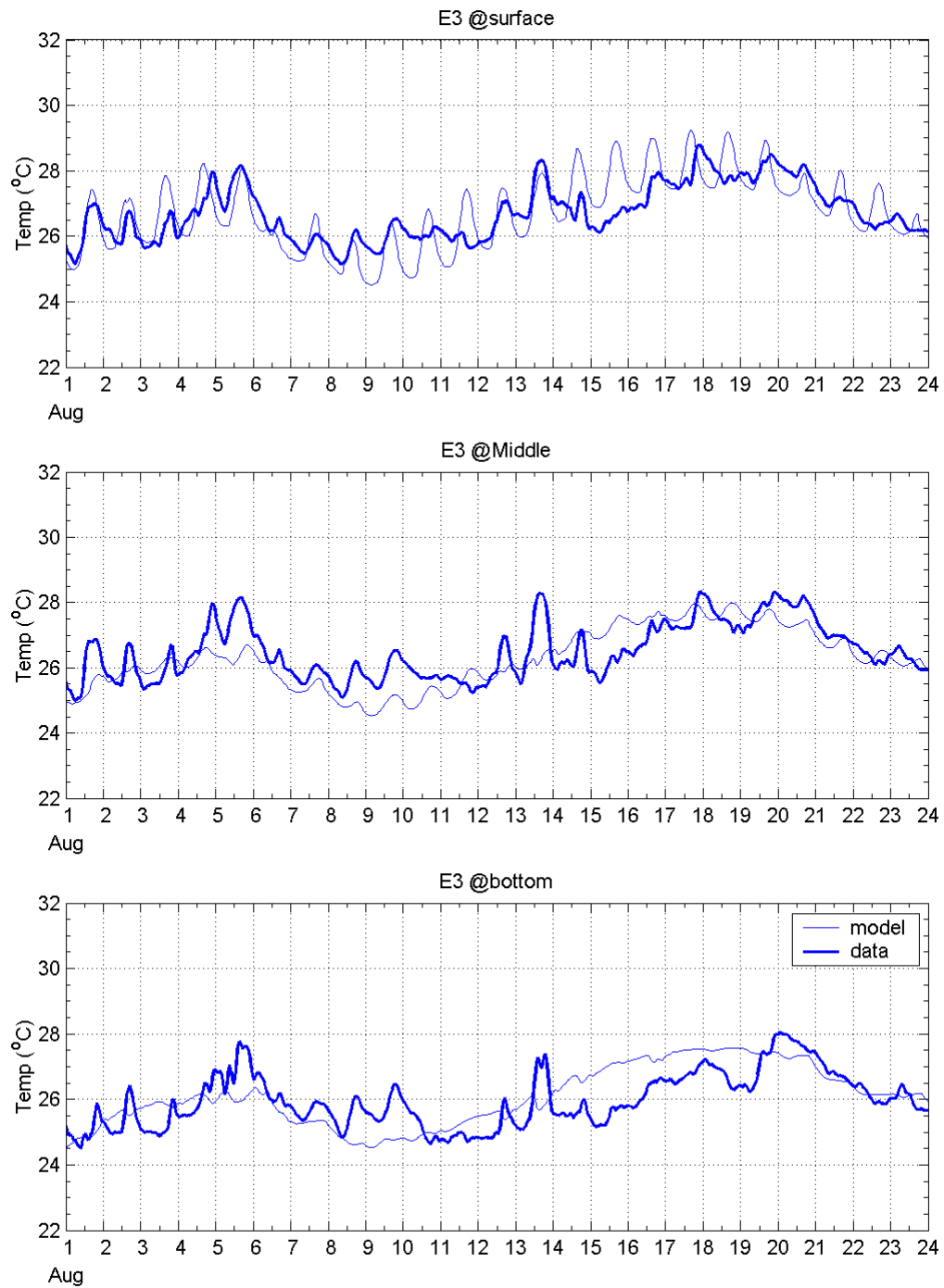


Figure 4-9. Comparison of observed (thick) and simulated temperatures (thin) at the surface, middle and bottom layers for string E3.

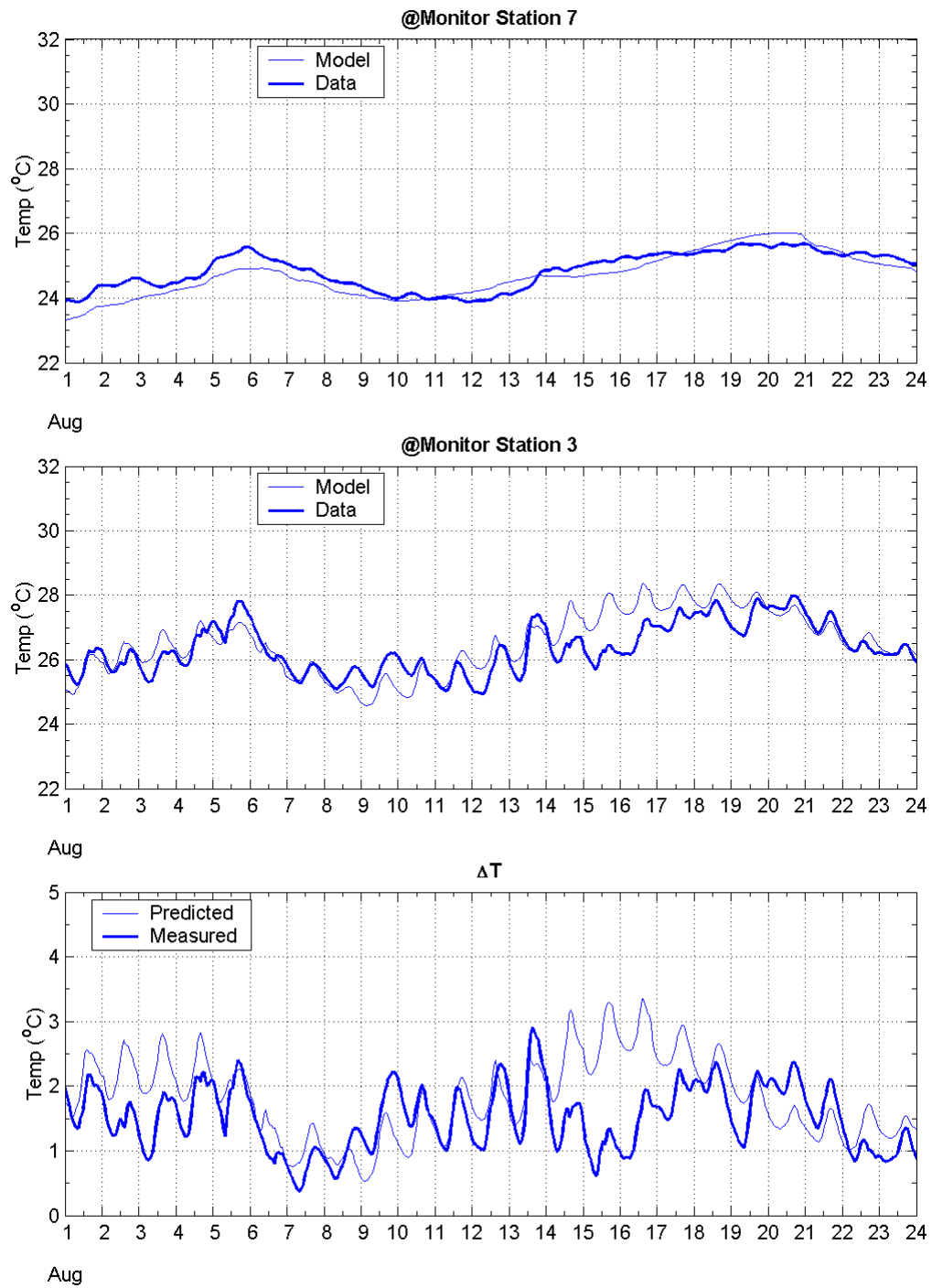


Figure 4-10. Comparison of observed (thick) and simulated temperatures (thin) for monitoring stations 7 (top) and 3 (bottom).

The river ΔT can be defined as the temperature at downstream station 3 minus the temperature at upstream station 7. The predicted river ΔT for this period ranges between 0.5°C (0.9°F) and 3.4°C (6.1°F), whereas the measured ΔT varies from 0.4°C (0.7°F) to 2.9°C (5.2°F). Mean values for river ΔT are 1.8°C (3.2°F) and 1.5°C (2.7°F) for model and data, respectively, exhibiting only a 0.3°C (0.5°F) over prediction compared to the measurements. This is mostly due to the difference existing during the over prediction period (14 – 19 August).

Quantitative comparisons for all the thermistors are summarized in Tables 4-5 to 4-7. Parameters presented in the tables are model and data statistical measures: mean, relative mean error (RME), error coefficient of variance (ECV), and squared correlation coefficient, r^2 . Also presented in each table is U. S. EPA guidance levels for each statistical measure.

Tables 4-5 through 4-7 present statistics for surface-, middle- and bottom-layer temperature predictions at all 22 thermistor strings, respectively. Squared correlation coefficients for the surface temperature prediction vary from 0.46 (String F4) to 0.86 (String C2) with an average for all surface thermistors of 0.74, slightly higher than the U. S. EPA guidance level of 0.71. RME for the surface temperature predictions ranges between 0% (String C1) and 3.5% (String C4) with an average of 1.1%, and ECV varies from 1.1% (String C4) to 2.9% (String D5) with an average of 2.2%. Compared to the U. S. EPA guidance levels of 25% (RME) and 45% (ECV), the RME and ECV values are much smaller, implying that the model predicts the surface temperature well. Tables 4-6 through 4-7 show similar results except that the r^2 values become smaller with depth. However, excellent comparisons in terms of RME and ECV are found for these layers. Average values of RME and ECV for the middle layer are 1.5% and 2.5%, respectively, and the values for the bottom layers are 1.9% and 3.3%. The calibration for temperatures hence is acceptable, according to the guidance levels.

Table 4-5. Quantitative comparisons of predicted and observed surface temperatures for the calibration period from 1 to 24 August 2002.

Thermistor	Model – Mean (°C)	Data - Mean (°C)	RME (%)	ECV (%)	r ²
C1	27.2	27.2	0.0	1.5	0.84
C2	27.8	27.5	1.0	1.6	0.85
C3	26.6	26.9	1.0	1.9	0.82
C4	26.6	27.6	3.5	1.1	0.86
C5	26.5	26.9	1.7	2.6	0.76
C6	26.5	26.8	1.4	2.4	0.77
D1	27.1	26.9	0.7	1.8	0.80
D2	27.0	27.0	0.1	1.6	0.79
D3	26.7	27.0	1.1	2.0	0.82
D4	26.5	27.0	2.0	2.5	0.80
D5	26.6	27.3	2.4	2.9	0.81
D6	26.6	27.1	1.9	2.6	0.78
E1	27.0	27.0	0.1	1.9	0.77
E2	27.0	27.0	0.1	1.9	0.77
E3	26.7	26.7	0.1	2.7	0.57
E4	26.7	27.0	1.0	2.4	0.72
E5	26.7	27.3	2.1	2.8	0.80
E6	26.7	27.2	1.7	2.8	0.74
F1	26.1	26.3	0.8	2.6	0.61
F2	26.1	26.3	0.8	2.6	0.61
F3	26.1	26.3	0.7	2.7	0.58
F4	26.1	25.9	0.6	2.3	0.46
Average			1.1	2.2	0.74
Guidance			25	45	0.71

Table 4-6. Quantitative comparisons of predicted and observed temperatures at the middle layer for the calibration period from 1 to 24 August 2002.

Thermist or	Model – Mean (°C)	Data - Mean (°C)	RME (%)	ECV (%)	r ²
C1	27.0	26.6	1.4	2.9	0.57
C2	27.6	27.1	2.0	2.7	0.72
C3	26.0	25.8	0.9	2.5	0.70
C4	26.0	26.2	0.6	1.8	0.76
C5	26.2	26.6	1.3	2.2	0.77
C6	26.2	26.6	1.6	2.4	0.77
D1	26.8	26.1	2.9	4.2	0.33
D2	26.8	27.5	2.5	1.0	0.59
D3	26.5	26.8	1.3	2.2	0.74
D4	26.3	27.5	4.3	1.2	0.69
D5	26.0	26.2	0.6	2.9	0.47
D6	26.0	26.2	0.4	2.9	0.47
E1	26.5	26.1	1.5	3.2	0.43
E2	26.5	26.1	1.5	3.2	0.43
E3	26.3	26.5	0.8	2.6	0.52
E4	26.3	26.4	0.6	2.6	0.52
E5	26.7	27.1	1.6	2.6	0.76
E6	26.7	27.1	1.4	2.7	0.72
F1	25.6	26.1	2.0	2.6	0.73
F2	25.6	26.0	1.7	2.4	0.73
F3	25.4	25.5	0.4	1.8	0.67
F4	25.4	25.1	1.2	1.5	0.27
Average			1.5	2.5	0.61
Guidance			25	45	0.71

Table 4-7. Quantitative comparisons of the predicted and observed bottom temperatures for the calibration period from 1 to 24 August 2002.

Thermistor	Model – Mean (°C)	Data - Mean (°C)	RME (%)	ECV (%)	r ²
C1	26.5	25.3	4.8	5.6	0.36
C2	27.2	25.8	5.6	6.0	0.42
C3	25.9	25.8	0.4	2.5	0.49
C4	26.6	26.0	2.4	2.9	0.66
C5	25.7	25.5	0.6	2.3	0.60
C6	25.7	25.5	0.9	2.4	0.59
D1	26.6	25.5	4.4	5.3	0.39
D2	26.6	25.5	4.5	5.4	0.39
D3	26.1	26.1	0.0	2.4	0.55
D4	26.9	26.8	0.5	2.0	0.40
D5	25.9	25.4	1.9	4.0	0.26
D6	25.9	25.3	2.2	4.0	0.34
E1	26.4	25.7	2.5	3.7	0.45
E2	26.4	25.7	2.5	3.8	0.44
E3	26.1	26.0	0.5	2.9	0.41
E4	26.1	25.9	0.6	2.9	0.41
E5	26.1	26.8	2.8	3.7	0.63
E6	26.1	26.8	2.7	3.6	0.68
F1	25.3	25.5	1.1	1.9	0.73
F2	25.3	25.5	1.0	1.9	0.72
F3	25.2	25.1	0.5	1.8	0.62
F4	24.7	24.6	0.3	1.9	0.23
Average			1.9	3.3	0.49
Guidance			25	45	0.71

4.4.2 Confirmation to June – July 2002 Period

The primary focus of the confirmation process is to compare the model predictions with observations for a different period, keeping the model coefficients the same as that arrived at during the calibration process. The model predicted flows across the Vernon Dam and the predicted temperatures at all stations were compared with the observed data. Quantitative evaluation of the model predictions with the observations are given in terms of the RME, ECV and r², as was done for the calibration period results.

Flow Comparisons

The model-predicted flows through the Vernon Dam compare well with the observations as shown in Figure 4-11. The correlation for the flows is high (r² of 0.99). The mean value of observations and predictions are 266 m³/s (9,394 ft³/s) and 273 m³/s (9,641 ft³/s), respectively. The RME and ECV are 2.5% and 3.6%, respectively, lower than U. S. EPA guidance levels of 30% and 10%. The r² is 0.98, above the U.S. EPA guidance level of 0.88, implying that the prediction is successful.

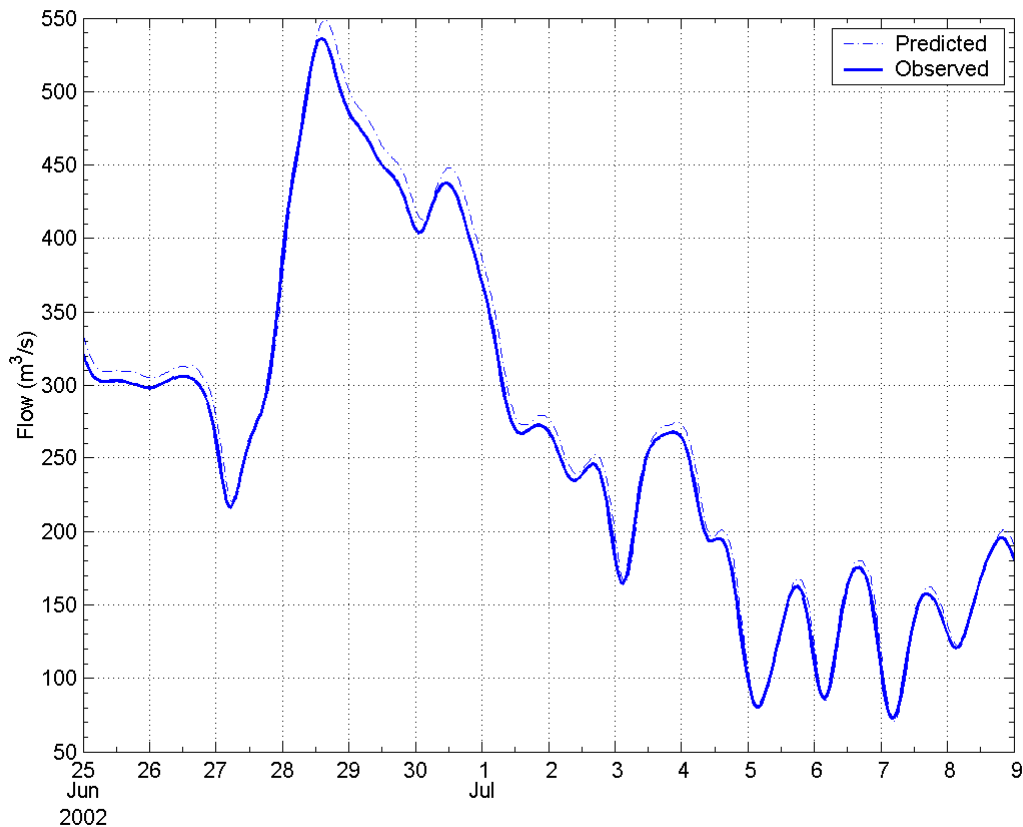


Figure 4-11. Comparison of the observed (thick) and predicted flows (thin-dashed) across the Vernon Dam.

Temperature Comparisons

Figure 4-12 through 4-14 shows comparisons of temperature predictions and observation at Strings C3, D5 and E1 respectively. The observed temperatures at String C3 show little variations with depth, except on 4 June when the surface temperature appears high. The model predicts the temperatures well for all three layers, exhibiting high correlation coefficients (r^2) of 0.80, 0.94 and 0.95 for the surface, middle and bottom layers, respectively (see Tables 4-8, 4-9 and 4-10). RME and ECV values for the surface comparison are 2.2% and 4.1%, respectively. The values are somewhat lower for the two deep layers (see Tables 4-9 and 4-10). At String D5 located 298 m (979 ft) southwest of String C3, observed surface temperature exhibits a strong diurnal variation, which does not exist at String C3. The model predicts the variation and also the long-term trend well. As the diurnal variation diminishes in the observations, the model still predicts the variation persistently, but the predicted amplitude is smaller with depth. Squared correlation coefficients, r^2 , are 0.89 for the surface layer (Table 4-8), 0.87 for the middle layer (Table 4-9) and 0.89 for the bottom layer (Table 4-10). RME and ECV values are smaller with depth, 1.4% and 3.2% for the surface layer, respectively. Good comparisons are found for all three layers at String E1, showing r^2 values of 0.89, 0.92 and 0.91 for the surface, middle and bottom layers, respectively.

The statistical evaluations of the model predictions are summarized in Tables 4-8 through 4-10. For the surface temperature, RME values for all strings are less than 4.5% (String E2), with an average of 1.89%. Range for the ECV values is between 2.6% (String D1) and 8.1% (String F1), showing an average of 4.2%. Both the RME and ECV are much lower than U. S. EPA guidance levels of 25% and 45%, respectively. The lowest r^2 of 0.66 is found to occur at String F1 and for all other stations r^2 is higher than U. S. EPA guidance level of 0.71. The model predictions show excellent comparison with observations. Tables 4-9 and 4-10 show the statistical evaluation of the model temperature predictions at mid-depth and bottom, respectively. The model predicted temperatures show excellent comparisons, with the r^2 exceeding 0.71 at all stations, except at String F1. Average RME values for the two layers are 1.6% and 2.7%, respectively, lower than 25% U. S. EPA guidance level. The ECV comparison shows a similar result with the RME. The average r^2 values were 0.87 and 0.91 for the lower layers, better (larger) than the guidance level of 0.71. Therefore, the model temperature predictions are acceptable, based on the statistical measures.

Figure 4-15 shows a comparison of the model predictions for the fishway temperature with the observations. The model predicts temperatures well for the first three days and for the second half of the simulation period (1 – 9 July), exhibiting an r^2 of 0.86, comparing well to the U. S. EPA guidance of 0.71. The model, however, under predicts temperatures by 1.5°C (3.2°F) on average for the period between 28 and 30 June, when the river flooded (see Figure B-23). Mean predicted temperature is 0.1°C (0.2°F) larger than the observed mean (23.8°C [74.8°F]). RME and ECV values between model predictions and observations are only 0.67% and 3.15%. These are smaller than the 25% and 45% U. S. EPA guidance levels, respectively, suggesting that the predictions are very good.

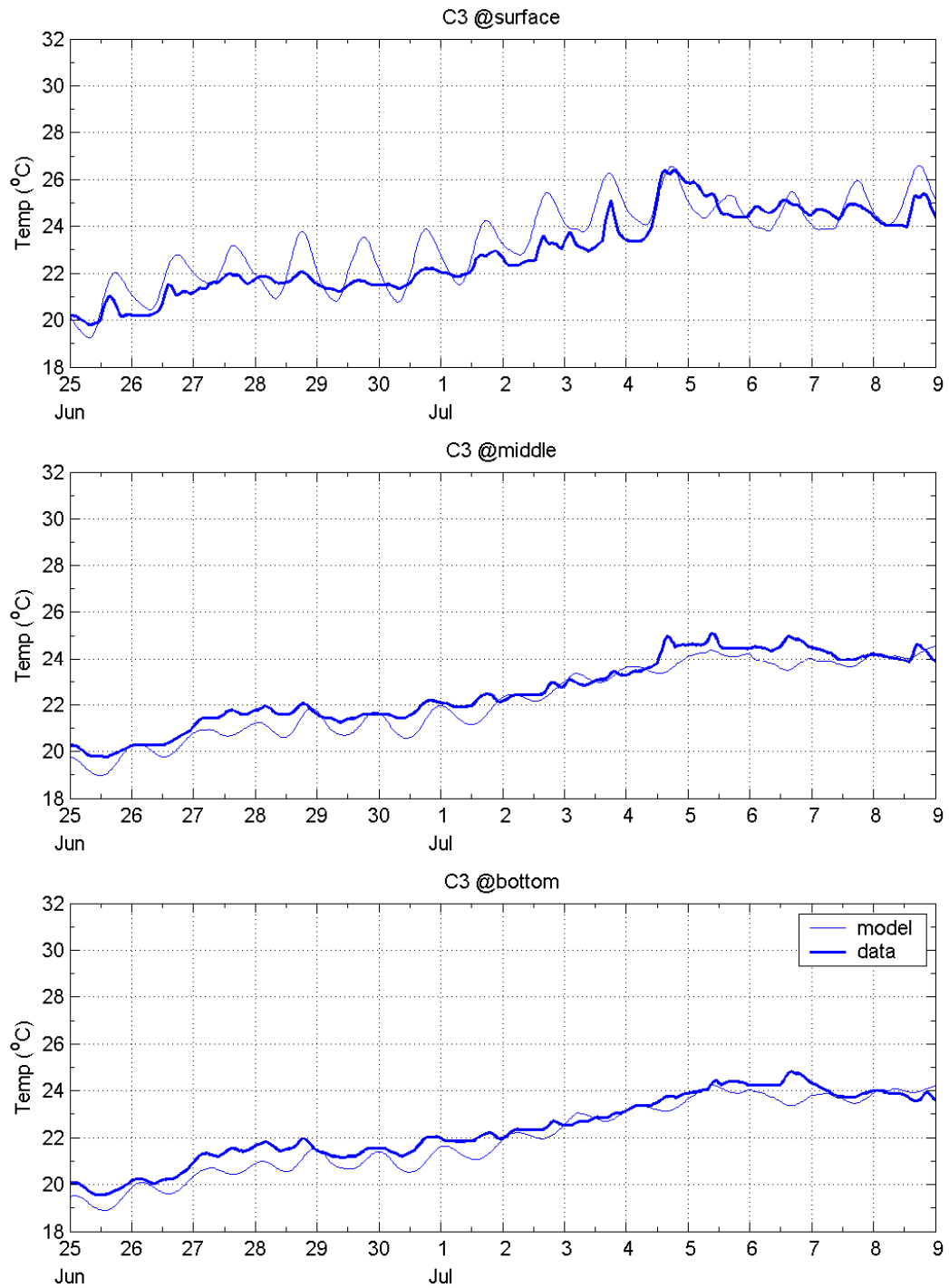


Figure 4.12 Comparison of the observed (thick line) and predicted (thin-dashed) temperatures at the surface, mid and bottom layers at station C3.

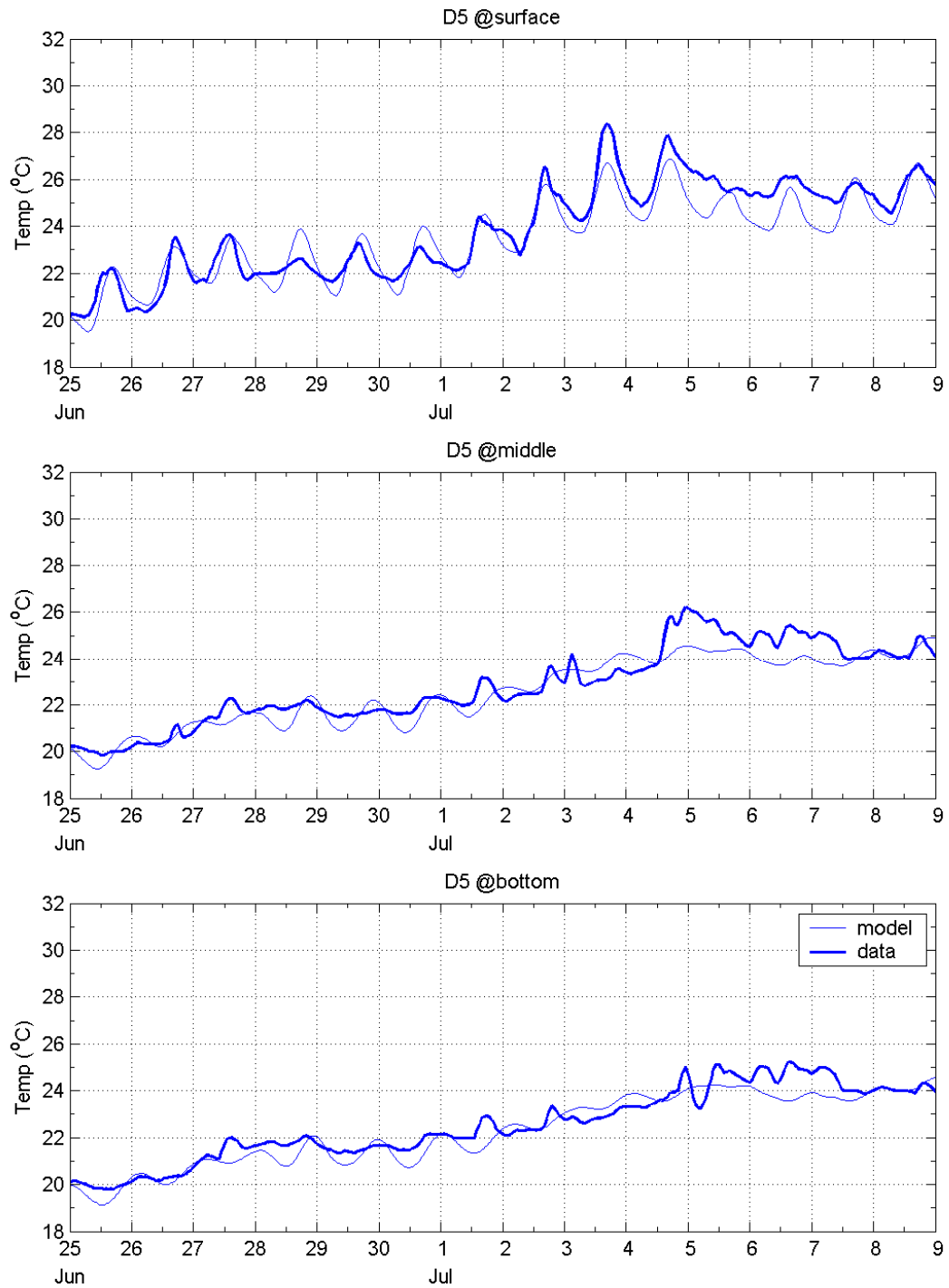


Figure 4.13 Comparison of the observed (thick line) and predicted (thin-dashed) temperatures at the surface, mid and bottom layers at station D5.

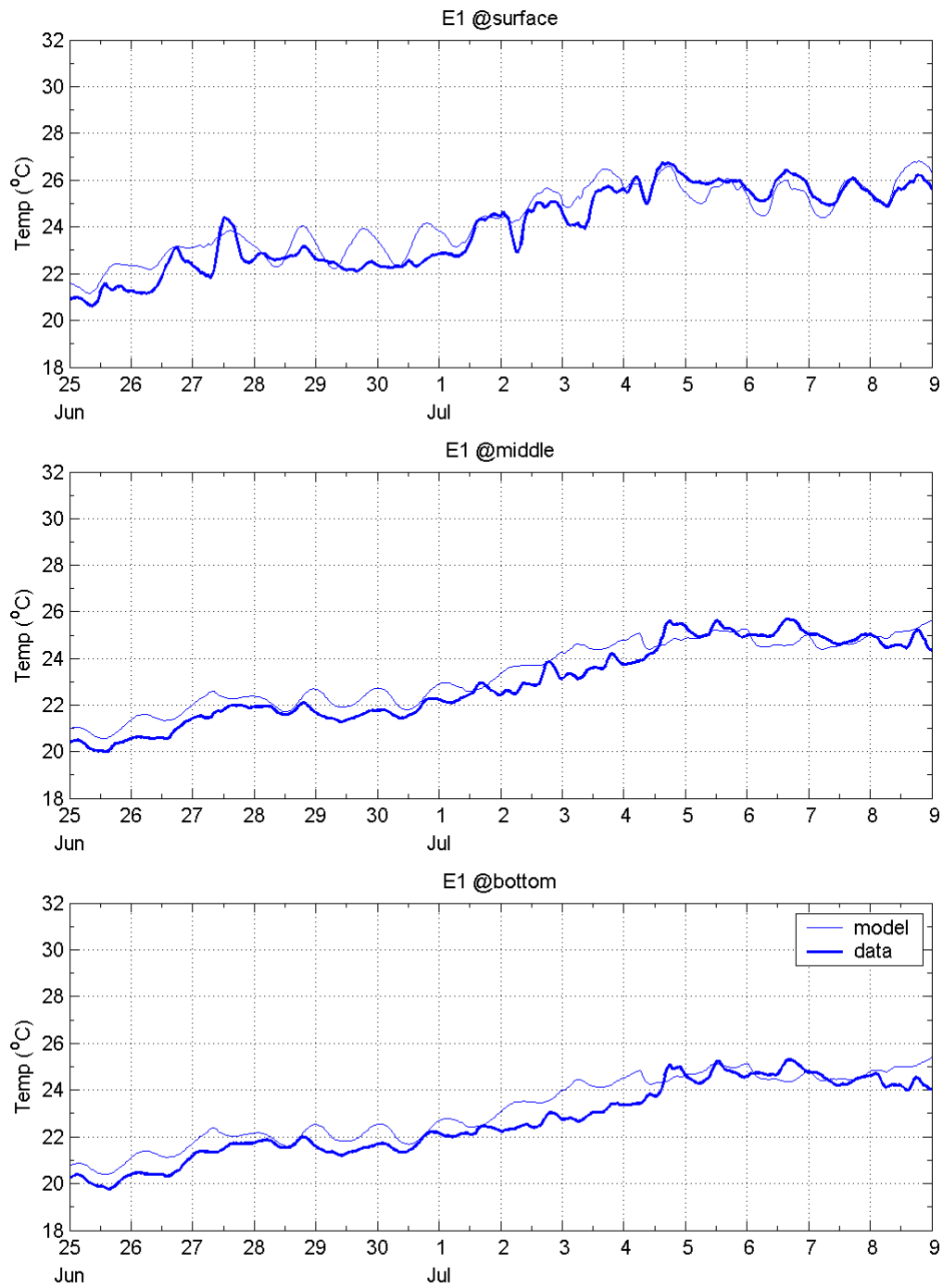


Figure 4.14 Comparison of the observed (thick line) and predicted (thin-dashed) temperatures at the surface, mid and bottom layers at station E1.

Table 4-8. Quantitative comparisons of the predicted and observed temperatures at the surface layer for the confirmation period from 25 June to 9 July 2002.

Thermistor	Model – Mean (°C)	Data - Mean (°C)	RME (%)	ECV (%)	r ²
C1	24.1	23.9	1.0	3.6	0.89
C2	24.1	23.8	1.1	3.4	0.89
C3	23.4	22.9	2.2	4.1	0.80
C4	23.4	23.0	1.7	3.7	0.81
C5	23.4	22.9	2.3	4.3	0.77
C6	23.4	22.8	2.8	4.6	0.77
D1	24.3	24.3	0.3	2.6	0.77
D2	24.3	24.0	1.6	3.1	0.78
D3	23.1	23.7	2.4	4.3	0.89
D4	23.1	23.6	2.4	4.1	0.90
D5	23.5	23.8	1.4	3.2	0.89
D6	23.5	23.4	0.6	3.3	0.85
E1	24.3	23.9	1.5	2.9	0.89
E2	24.3	23.2	4.5	5.9	0.81
E3	23.6	24.3	3.0	3.9	0.87
E4	23.6	24.3	2.9	4.0	0.86
E5	23.7	24.1	1.6	4.1	0.81
E6	23.7	23.9	0.8	4.0	0.81
F1	23.1	23.7	0.5	8.1	0.80
F2	23.1	22.6	2.3	4.6	0.71
F3	23.1	22.7	1.8	4.3	0.73
F4	23.1	22.4	2.9	5.2	0.66
Average			1.9	4.2	0.82
Guidance			25	45	0.71

Table 4-9. Quantitative comparisons of the predicted and observed temperatures at the middle depth for the confirmation period from 25 June to 9 July 2002. N/A stands for no data available.

Thermistor	Model – Mean (°C)	Data - Mean (°C)	RME (%)	ECV (%)	r ²
C1	23.6	23.3	1.0	3.1	0.90
C2	23.6	23.4	0.7	2.9	0.91
C3	22.2	22.6	1.7	2.4	0.94
C4	22.2	22.5	1.2	2.2	0.94
C5	23.1	22.6	2.1	3.9	0.80
C6	23.1	22.7	1.8	3.7	0.80
D1	24.0	23.1	3.9	4.8	0.83
D2	24.0	23.0	4.2	5.0	0.83
D3	22.8	N/A	N/A	N/A	N/A
D4	22.8	23.3	2.3	3.8	0.90
D5	22.6	22.8	1.2	2.9	0.87
D6	22.6	22.8	1.0	2.8	0.87
E1	23.3	23.0	1.7	2.8	0.92
E2	23.3	22.9	1.9	3.3	0.90
E3	22.7	N/A	N/A	N/A	N/A
E4	22.7	N/A	N/A	N/A	N/A
E5	23.7	24.0	1.1	4.0	0.82
E6	23.7	23.9	0.5	4.0	0.81
F1	22.8	22.6	0.9	3.5	0.77
F2	22.3	22.5	1.0	2.5	0.88
F3	22.2	22.3	1.9	2.6	0.94
F4	22.2	22.4	1.0	2.4	0.94
Average			1.6	3.3	0.87
Guidance			25	45	0.71

Table 4-10 Quantitative comparisons of the predicted and observed temperatures at the bottom layer for the confirmation period from 25 June to 9 July 2002.

Thermistor	Model – Mean (°C)	Data - Mean (°C)	RME (%)	ECV (%)	r ²
C1	22.5	22.4	0.6	2.4	0.92
C2	22.5	22.4	0.6	2.4	0.92
C3	22.0	22.4	1.7	2.4	0.95
C4	22.0	22.3	1.7	2.3	0.95
C5	22.2	22.5	1.3	2.2	0.93
C6	22.2	22.4	0.8	2.0	0.93
D1	23.3	22.5	3.2	3.8	0.91
D2	23.3	22.5	3.3	3.9	0.91
D3	22.3	22.7	1.9	2.9	0.91
D4	22.3	22.7	1.7	2.8	0.91
D5	22.3	22.6	1.1	2.5	0.89
D6	22.3	22.3	0.0	2.4	0.88
E1	23.2	22.6	2.3	3.1	0.91
E2	23.2	21.5	7.6	7.9	0.91
E3	22.3	23.4	4.6	5.4	0.84
E4	22.3	23.4	4.6	5.4	0.86
E5	22.7	23.9	5.3	6.6	0.86
E6	22.7	23.7	4.5	5.9	0.88
F1	21.9	22.5	2.8	3.2	0.94
F2	21.7	22.5	3.2	3.5	0.94
F3	21.6	22.4	3.4	3.8	0.94
F4	21.6	22.4	3.5	3.9	0.94
Average			2.7	3.7	0.91
Guidance			25	45	0.71

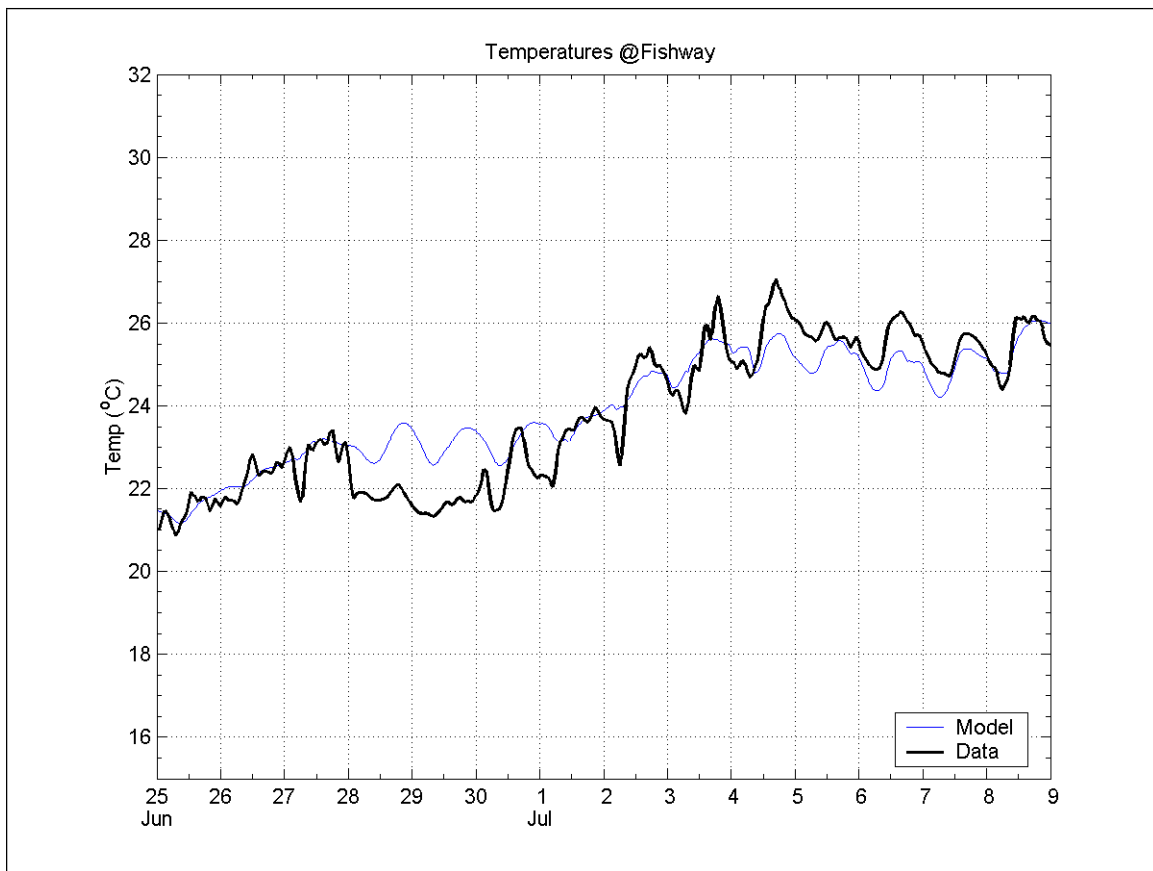


Figure 4-15. Comparison of predicted and observed temperatures at the fishway during the confirmation period.

4.4.3 Discussion

Model results were compared to water temperature and river flow data for two different periods to provide model calibration and confirmation. The August 2002 period served as the model calibration period and the June 2002 period served as the model confirmation period. Both calibration and confirmation of the model were successful, particularly when compared to target EPA guidance values for statistical measures as shown in Table 4-11.

Table 4-11. Vernon Pool hydrothermal model calibration and confirmation evaluation in comparison with EPA guidance (McCutcheon et al., 1990)

Error Measure	Property	Guidance Value	Calibration	Confirmation
Relative Mean Error, RME	Flow	30%	3.0	2.5
	Temperature (avg)	25%	1.1	1.9
Error Coefficient of Variation, ECV	Flow	10%	0	3.6
	Temperature (avg)	45%	2.2	4.2
Squared Correlation Coefficient, r^2	Flow	0.88	0.92	0.98
	Temperature (avg)	0.71	0.74	0.82

The calibration period was characterized by relatively low flow rates and high water temperatures. A number of model parameters, including bottom friction, horizontal and vertical dispersion, and atmospheric exchange rates, were adjusted to provide an optimal comparison to the observational data. Predicted flow rates for the calibration period compare very well to observational data. Predicted and observed flows are highly correlated, with statistical measures of correlation well within the target guidance levels provided by the U.S. EPA. Further, small differences between predicted and observed flows, where they occurred, can largely be attributed to two factors. First, there is a time lag of 1.5 hours between the predicted and observed flows, which is due to the travel time for water between the upstream and downstream boundaries. Second, there is an expected oscillation in the model predictions with a period of approximately 5 hours following large changes in flow amplitude, as a result of resonance at the natural frequency of the Vernon Pool. Neither of these differences effect overall calibration.

Predicted and observed temperatures also compare very well overall for the calibration period. The comparison is generally slightly better for the surface layers than for the bottom layers, where the model tends to attenuate higher frequency temperature variations (e.g., diel variations). One source of disagreement between predictions and observations may be the occasional underprediction of vertical stratification. In general, however, the temperatures throughout the study area compare very well with target guidance criteria as set forth by the U.S. EPA.

The June 2002 period, which featured high flows and low temperatures relative to the August calibration period, served as the model confirmation period. Model parameters were set at the values determined for the calibration period. Comparison of model predictions to observations for this period therefore provides an independent check on the validity of parameter values chosen for this system. Overall, predicted values of flow and temperature

compare very well with observations for the confirmation period. This may be due to the fact that the overall thermal pattern is more uniform during the June period, and flow rates are higher, with somewhat less abrupt variations, producing less overall variability in the system.

5. Thermal Plume Simulations

A total of ten scenarios were analyzed, four during the August warm river temperature, low flow period (Table 4-1) and six during the June-July fishway operation period (Table 4-2). Each simulation was run for seven days in order to bring the system to a quasi-steady state, which started on the third simulation day. Boundary forcings and environmental conditions used for the simulations were described in Section 4.3.3.2. This section presents results of the ten scenario simulations: four August scenarios (Table 4-1) and six June-July scenarios (Table 4-2).

Figures 5-1 to 5-3 show plan views of the predicted thermal fields at the surface, middle and bottom layers, respectively, in the lower Vernon Pool for one of the August scenarios, 50%-3°F rise (which had the highest thermal load) as an example of the three dimensional nature of the predicted thermal distribution. Temperature contours are color coded in 0.5 °C (0.9°F) increments as shown in the left portion of the figures. The contours show a maximum near the Vermont Yankee discharge with the plume of elevated temperatures attached to the western shore in all figures. The surface temperatures (Figure 5-1) are warmest, both in the plume and upstream of Vermont Yankee. The thermal plume is in a concentric elliptic shape, having larger extent downstream. The middle-layer temperatures (Figure 5-2) show a similar temperature at the center of plume as the surface layer, but the plume is smaller in size. The bottom temperatures (Figure 5-3) are coolest and show the smallest plume size.

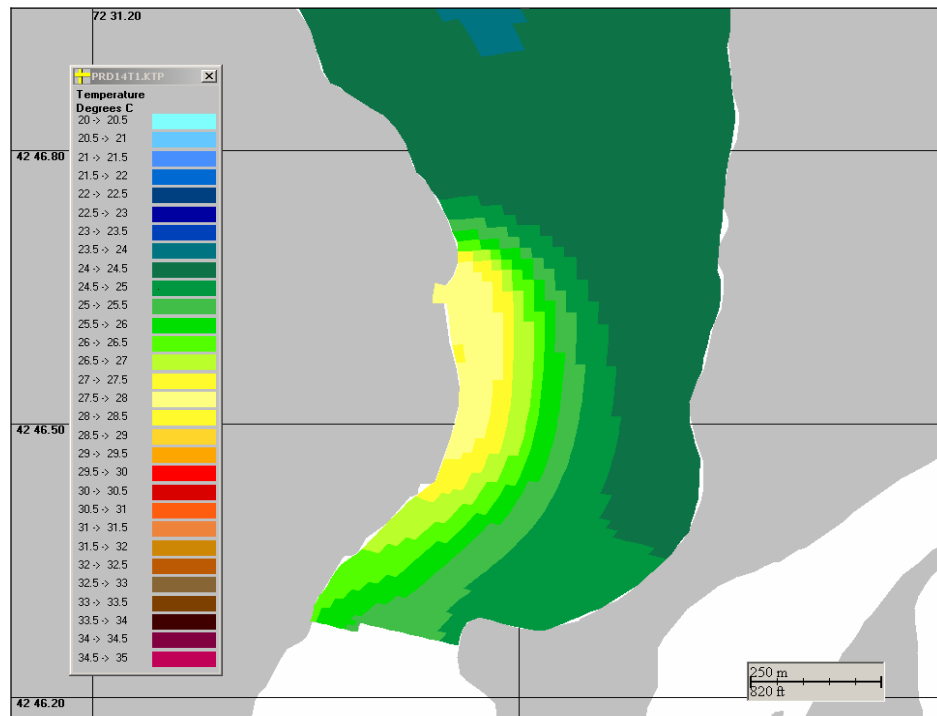


Figure 5-1. Predicted surface temperature distribution for August scenario 50%-3°F.

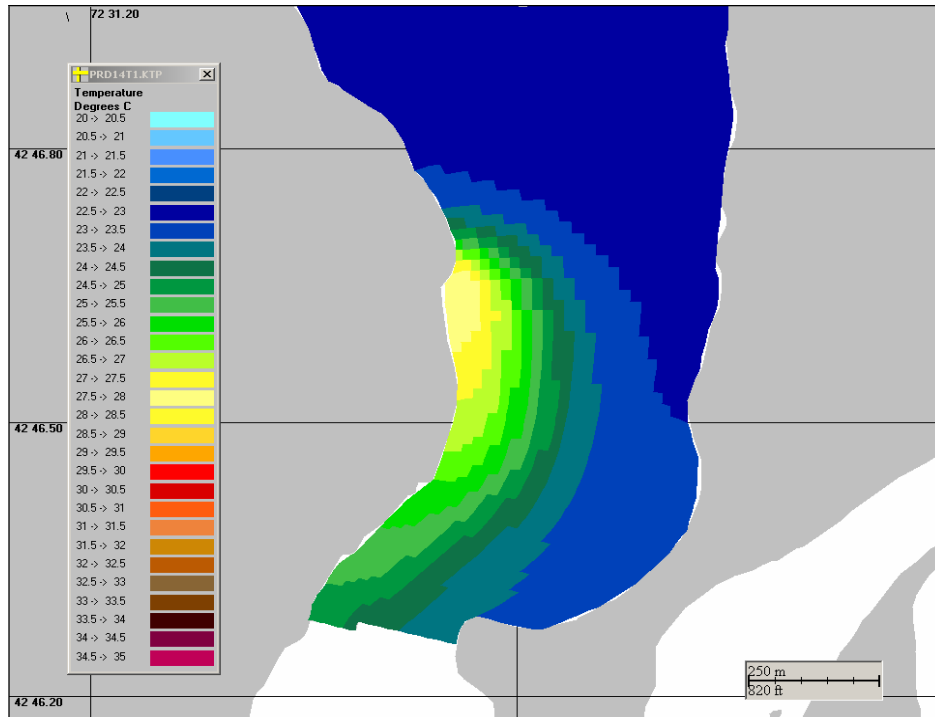


Figure 5-2. Predicted middle-layer temperature distribution for August scenario 50%-3°F.

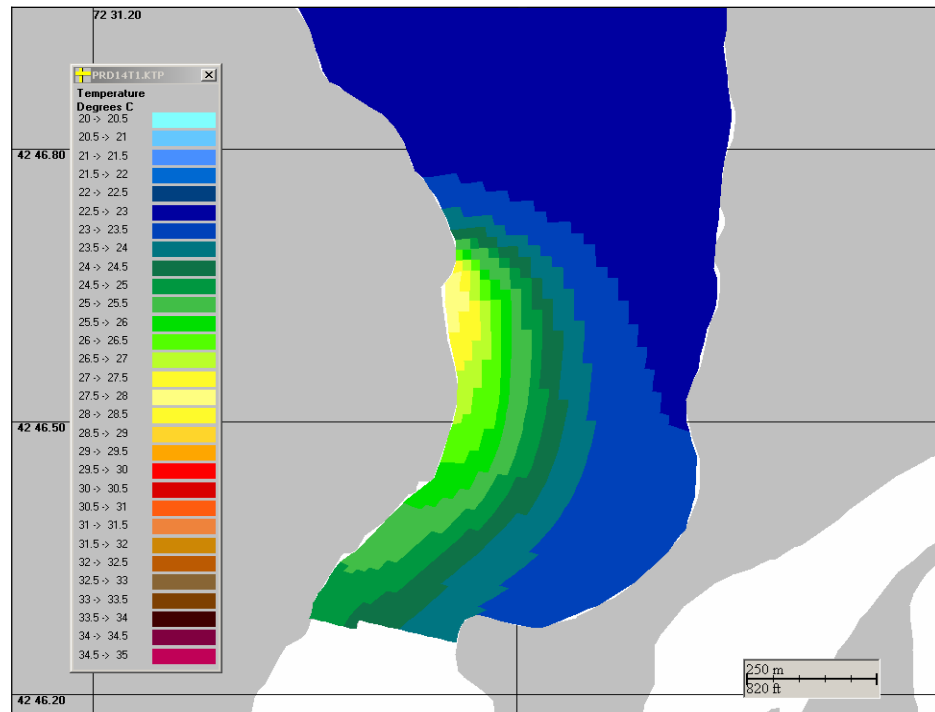


Figure 5-3. Predicted bottom-layer temperature distribution for August scenario 50%-3°F.

To compare the effects of the thermally impacted area for the different scenarios, the model output was post-processed to compute water volume and bottom area coverage for different temperatures. This analysis was performed for the lower Vernon Pool, since there was no

thermal impact north of the plant. Figure 5-4 shows the model grid cells used for the analysis. The total bottom area and water column volume based on these grid cells are $1.3 \times 10^6 \text{ m}^2$ ($14 \times 10^6 \text{ ft}^2$) and $5.5 \times 10^6 \text{ m}^3$ ($194 \times 10^6 \text{ ft}^3$), respectively.

Figure 5-5 shows the mean bottom area coverage as a function of temperature for all four August (low river flow and high river temperature) scenarios. The mean is calculated over a daily cycle. The figure shows total bottom area (y-axis) that equals or exceeds a given temperature (x-axis). Thus at low temperatures (e.g. 22°C) 100% of the bottom area exceeds this temperature. At high temperatures (e.g. 35°C) 0% of the bottom area exceeds this temperature. The results show that the mean bottom areas for scenarios 50%-2°F rise and 50%-3°F rise, with the highest river flow and lowest river temperature, begin to drop below 100% between 22 and 23°C , drop rapidly to 13 and 16 % of the bottom area exceeding 23.5°C for both the scenarios, and then gradually drop further to below 1% of the area above 27°C . The largest area and volume coverages occur for scenario 1%-3°F rise, although the rejected heat (253 MW) is about 40% smaller than scenario 50%-3°F rise (673 MW). Both scenario 1%-2°F rise and 1%-3°F rise have the same background conditions and same Vermont Yankee discharge temperature rise (3.9°C [11.7°F]), except the 1%-2°F rise scenario has a higher discharge volume ($5.2 \text{ m}^3/\text{s}$ [$182 \text{ ft}^3/\text{s}$] compared to $3.4 \text{ m}^3/\text{s}$ [$121 \text{ ft}^3/\text{s}$] for the 1%-3°F rise scenario). Similarly, the 50%-3°F rise scenario discharges more heated water volume by $4.6 \text{ m}^3/\text{s}$ ($162 \text{ ft}^3/\text{s}$) than 50%-2°F rise scenario. Figure 5-5 indicates that the higher discharge flow scenarios result in higher bottom area coverage.

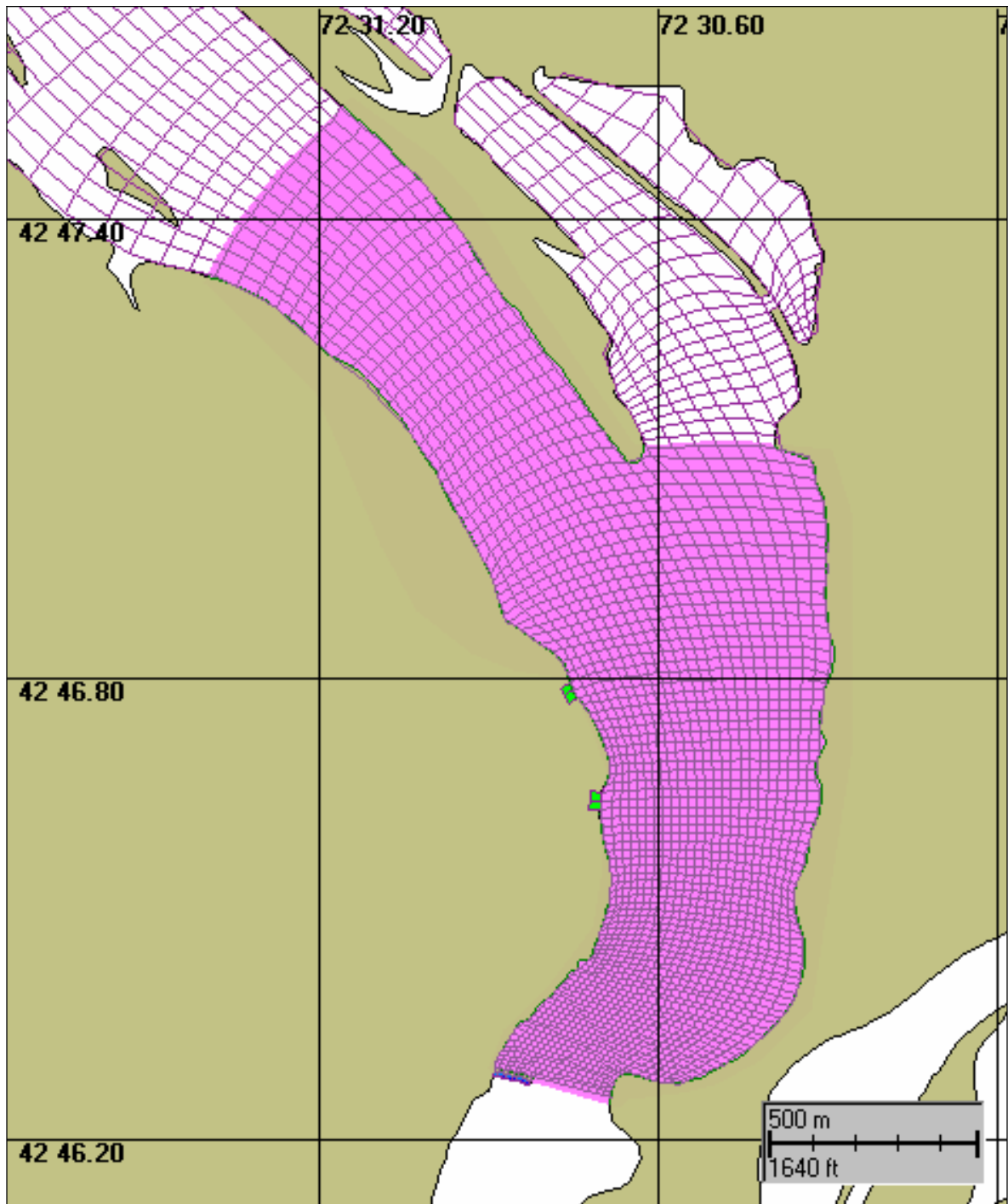


Figure 5-4. Model grid area (shaded in purple) used for the computation of the thermally effected area.

Figures 5-6 shows the mean water column volume coverage as a function of temperature for the four production August scenarios. The results are similar to those for bottom area with the relative position of each scenario in the figure the same.

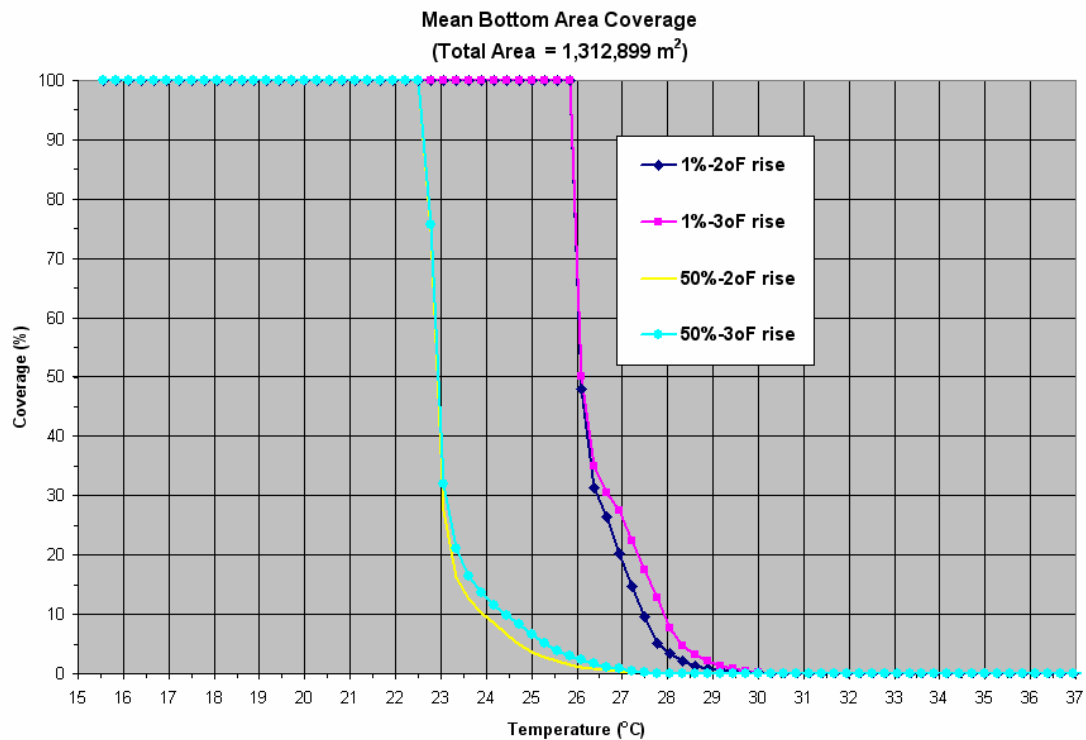


Figure 5-5. Mean percent bottom area coverages versus temperature for the four August scenarios.

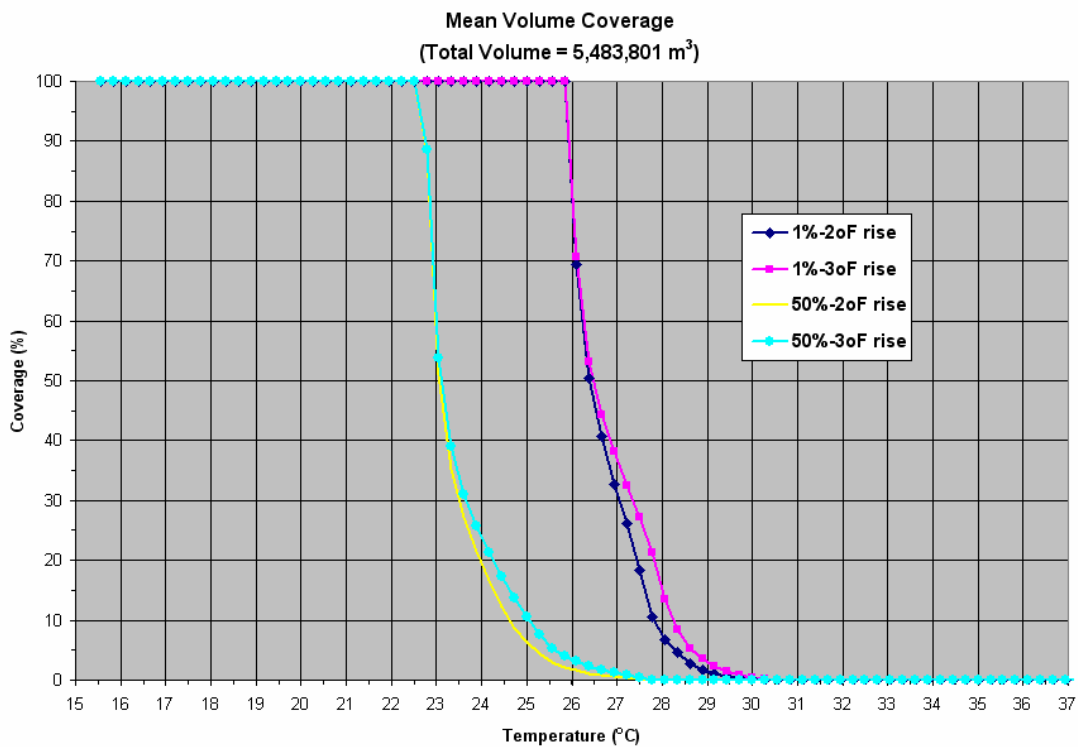


Figure 5-6. Mean percent water column volume coverages versus temperature for the four August scenarios.

Figures 5-1 through 5-3 show the model-predicted plume at different layers taken at 11:30 AM to illustrate the horizontal and vertical distribution of temperature. The data presented in Figures 5-5 and 5-6 represent averages computed over a 24-hr period. The peak temperature values in each layer occur at different times during the day, with deeper layers in the water column lagging behind the surface layers by several hours. Figures 5-7 and 5-8 show the peak bottom area coverage and peak volume coverage, respectively, as functions of temperature for all four August (low river flow and high river temperature) scenarios. It is seen that there are only minor differences compared to the mean coverages presented in Figures 5-5 and 5-6.

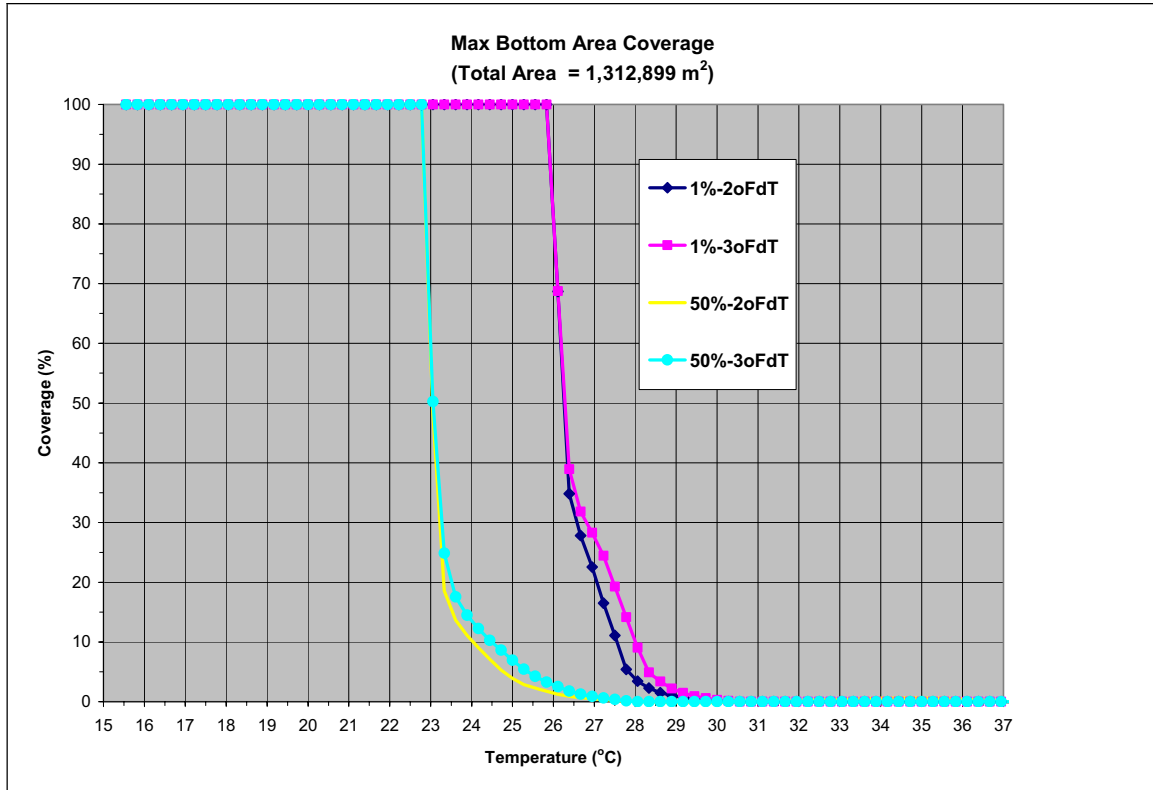


Figure 5-7 Maximum percent bottom area coverages versus temperature for the four August scenarios.

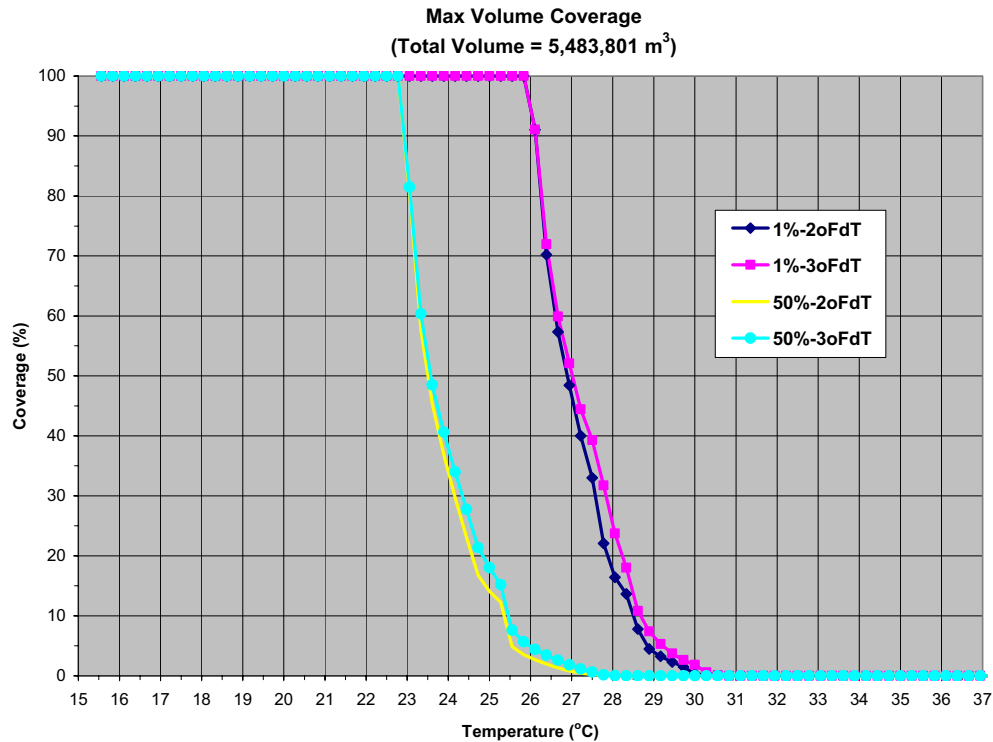


Figure 5.8 Maximum percent volume coverages versus temperature for the four August scenarios.

Another comparative measure of the scenarios is the amount of time that the mean fishway temperature at the Vernon Dam exceeds a specified temperature. Figure 5-9 shows percent time coverages of the mean surface-layer temperature at the fishway for the six June-July scenarios (Table 4-2). The temperatures were calculated as the mean value of the predictions for the top three layers (layers 11 to 9) of the western-most model cell located at the fishway.

Because of its high ambient water temperature (23.9°C [75.1°F]), the scenario 1% -3°F rise shows the largest impact on the fishway temperature, exhibiting 100% at 23°C (73.4°F) and 0% at 24.8°C (76.6°F), and scenario 10% -3°F rise shows the least effect, dropping from 100% at 20.8°C (69.4°F) to 0% at 22.2°C (72.0°F). A 1°F increase in temperature rise results in the same time coverages but at 0.4°C (0.7°F) higher temperatures. The scenario 1%-2°F rise showed 100% time coverage for temperatures less than 22.6°C (72.7°F), 50% coverage at 23.3°C (73.9°F), and 0% coverage for temperatures greater than 24.4°C (75.9°F), whereas the scenario 1%-3°F rise exhibited 100% coverage for temperatures less than 23°C (73.4°F), 50% coverage at 23.6°C (74.5°F), and 0% coverage for temperatures greater than 24.8°C (76.6°F). A similar variation in coverage was observed for the 10% occurrence set and the 50% occurrence set.

The temperature increase due to a 1°F rise in the permit limit was constant at 0.4°C (0.7°F) for the 1% and 10% scenarios. However, for the 50% scenario the temperature increase was generally somewhat larger, ranging between 0.43°C (0.77°F) and 0.55°C (1°F).

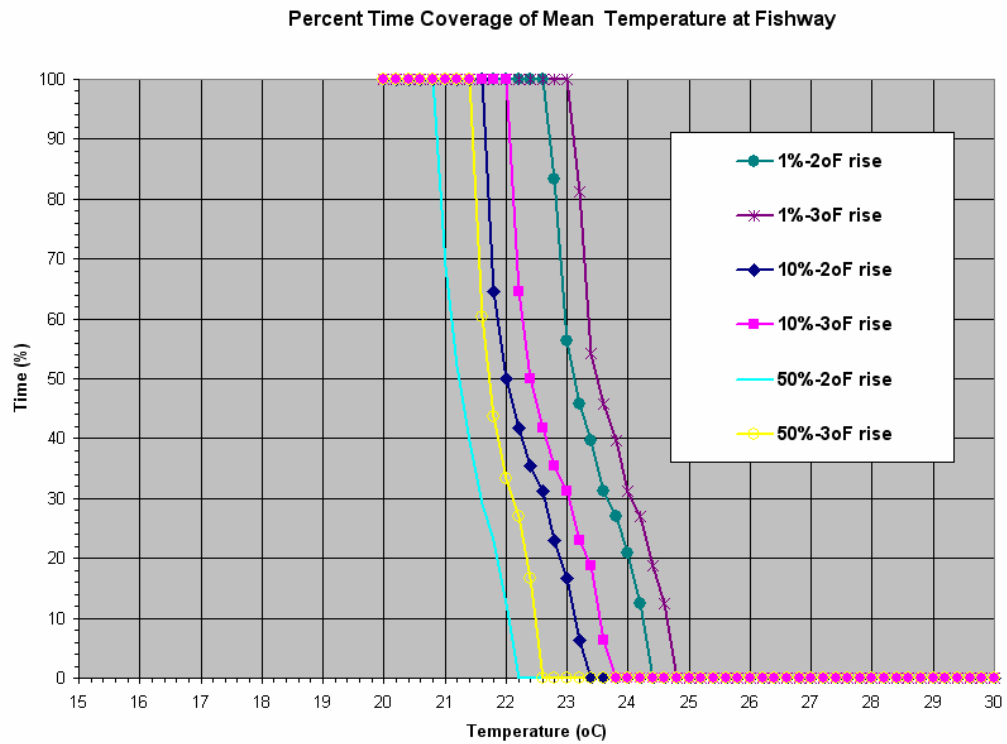


Figure 5-9. Percent time coverages of mean surface-layer temperature at the fishway.

6. Conclusions

A state-of-the-art, boundary-fitted, three-dimensional hydrothermal model was applied to the Vernon Pool on the Connecticut River to investigate the effects of the discharge from Vermont Yankee on the temperature distribution in the lower portion of the Pool. The model was calibrated and confirmed to data collected from a set of continuous monitoring thermistors as part of a field program from May through October 2002. The data also included river flows and water temperatures obtained from permanently deployed instruments used in Vermont Yankee operations. The model calibration and confirmation exercises used data sets acquired in August and June – July 2002, respectively. The August calibration period was chosen to be representative of warm river temperatures and low river flows. The June – July confirmation period was chosen to include warm river temperatures occurring during fishway operations.

Results of the calibration and confirmation indicated that the model predicted both flows and temperatures well. The flow predictions for the calibration and confirmation periods were very successful, exhibiting RME and ECV values less than 3% and 4%, respectively, which were smaller (better) than U. S. EPA guidance levels (30% and 10%, respectively). Correlations between the prediction and observations were excellent, with r^2 values of 0.92 and 0.98 for the calibration and confirmation periods, respectively, which were larger (better) than the guidance level of 0.88.

The calibration results indicated that temperature predictions were also good. Best results were obtained at the upper layer, but they became somewhat reduced with depth. Squared correlation coefficients at the surface were usually larger (better) than the U. S. EPA guidance level of 0.71, and the correlations became smaller with depth. However, RME and ECV for all three layers ranged between 0 and 5.6%, showing that they were smaller (better) than the EPA guidance levels (25% and 45%, respectively) and suggesting that the predictions throughout the water column were acceptable.

The confirmation results indicated that the model performed excellently in simulating the thermal conditions of June – July 2002. The surface temperature predictions showed RME values ranging between 0.6% to 3.0% compared to the guidance level of 25%, ECV values between 2.6% and 8.1% compared to the guidance level of 45%, and r^2 greater than 0.66 compared to the guidance level of 0.71. Similar variations in model error statistics were found at the middle and bottom layers. Based on the successful calibration and confirmation, the model could then be used for predictions under selected plant and river conditions.

Two sets of scenario simulations were performed for the August and June – July periods separately, to investigate the effect of proposed new temperature limits within the portion of the lower Vernon Pool affected by the Vermont Yankee discharge during the summer permit compliance period and during the period of fishway operation, respectively. For the August period, a 1°F (0.6°C) increase from 2°F (1.1°C) to 3°F (1.7°C) resulted in a marginal increase in the temperature of the water column or on the bottom. For worst conditions occurring only 1% of the time, 30% of the bottom area increased by at least 0.3°C (0.5°F) and 20%

increased by a maximum of 0.4°C (0.7°F). For typical conditions occurring 50% of the time, 30% of the bottom area increased by at least 0.1°C (0.2°F), 20% increased by at least 0.2°C (0.4°F) and 10% increased by a maximum of 0.6°C (1.1°F). Similar results were obtained for changes in water column volume.

Temperature predictions during June and July when the fishway was operating with warmest river temperatures indicated that a 1°F increase in temperature rise generally resulted in similar increases (0.4°C) [0.7°F] in water temperature regardless of whether conditions were worst (1% of the time), infrequent (10% of the time) or typical (50% of the time). There was a slight increase in effects under typical conditions of higher river flow and therefore higher plant flow. Results also indicated that the ambient water temperature primarily influenced the temperature in the fishway rather than Vermont Yankee's rejected heat.

Based on the hydrothermal modeling results, a 1°F (0.6°C) increase in the permit limit from 2°F (1.1°C) to 3°F (1.7°C) resulted in *de minimus* changes in the thermal structure of the Vernon Pool.

7. References

- Ambrose, R.B, T.A. Wool, J.P. Connolly, and R.W. Schanz, 1988. WASP4, a hydrodynamic and water quality model – model theory, user’s manual, and programmer’s guide. EPA 600/3-87/039, Environmental Research Laboratory, Office of Research and Development, U.S. Environmental Protection Agency, Athens, GA, January 1988.
- Applied Science Associates, Inc., 1996. WQMAP User’s Manual.
- Binkerd, R.C., W. D. Countryman, R. M. McNeer and D. J. Marx, 1978. 316 Demonstration, Vermont Yankee Nuclear Power Station, Connecticut River, Vernon, Vermont, Engineering, hydrological & biological information and environmental impact assessment, submitted to Vermont Yankee Nuclear Power Corporation. Aquatec, Incorporated.
- Bowie, G.L., W.B. Mills, D.B. Porcella, C.L. Campbell, J.R. Pagenkopf, G.L. Rupp, K.M. Johnson, P.W.H. Chen, S.A. Gherini, and C.E. Chamberlain, 1985. Rates, constants, and kinetics formulations in surface water quality modeling. EPA 600/3-85/040, Environmental Research Laboratory, Office of Research and Development, U.S. Environmental Protection Agency, Athens, GA, June 1985.
- Cole, T.M. and S.A. Wells, undated. CE-QUAL-W2: a two-dimensional laterally averaged, hydrodynamic and water quality model, version 3.1, user manual. Instruction Report EL-03-1, U.S. Army Corps of Engineers, Washington, DC.
- Hess, K. and K. Bosley, 1992. Methodology for validation of a Tampa Bay circulation model. 2nd ASCE Coastal and Estuarine Conference, Tampa, Florida, 1992.
- Huang, W. and M.L. Spaulding, 1995. A three dimensional numerical model of estuarine circulation and water quality induced by surface discharges. ASCE Journal of Hydraulic Engineering, 121:(4) April 1995, p. 300-311.
- Lynch, D. R., and A. M. Davies, 1995. Quantitative skill assessment for coastal ocean models. Coastal and Estuarine Studies No. 47. American Geophysical Union, Washington, DC.
- McCutcheon, S. C., Z. Dongwei, and S. Bird, 1990. Model calibration, validation, and use, Chapter 5 in Technical Guidance Manual for Performing Waste Load allocations. In: Book III: Estuaries, Part 2: application of estuarine waste load allocation models, J.J., Martin, R.B. Ambrose, and S. C. McCutcheon (eds.), US Environmental Protection agency, Office of Water, March 1990.

- Mendelsohn, D., et al, 1995. WQMAP in a Windows environment, published in proceedings of: 4th International Conference on Estuarine and Coastal Modeling, ASCE, San Diego, October 26-28, 1995.
- Muin, M. and M.L. Spaulding, 1997. A 3-D boundary-fitted circulation model. *Journal of Hydraulic Engineering*, Vol. 123, No. 1.
- Muin, M., 1993. A three-dimensional boundary-fitted circulation model in spherical coordinates, Ph.D. dissertation, Univ. of Rhode Island, Narragansett Bay Campus, Narragansett, RI.
- Spaulding, M. L., W. Huang, and D. Mendelsohn, 1989. Application of a boundary fitted coordinate hydrodynamic model. *Estuarine and coastal modeling: Proceedings of a conference*, Sponsored by the Waterways, Port, Coastal and Ocean Division of the American Society of Civil Engineers (ASCE), Newport, Rhode Island, November 15-17, 1989, p. 27-39.
- Spaulding, M.L., 1984. A vertically averaged circulation model using boundary fitted coordinates. *Journal of Physical Oceanography*, May, pp. 973-982.
- Swanson, J.C., D. Mendelsohn, 1993. Application of WQMAP to upper Narragansett Bay, Rhode Island. *Estuarine and Coastal Modeling III. Proceedings of the 3rd International Conference*, sponsored by the Waterway, Port, Coastal and Ocean Division of the ASCE, Oak Brook, IL, September 8-10, 1993.
- Swanson, J.C., M. Spaulding, J-P. Mathisen and O. O. Jenssen, 1989. A three dimensional boundary fitted coordinate hydrodynamic model, Part I: development and testing. *Dt. hydrog, Z.42*, 1989, p. 169-186.
- Swanson, J.C., 1986. A three-dimensional numerical model system of coastal circulation and water quality, Ph.D. Dissertation, Univ. of Rhode Island, Kingston, R.I.
- Thomann, R. V., and J. A. Mueller, 1987. *Principles of Surface Water Quality Modeling and Control*. Harper Collins, 644pp.
- Wallace, J.M, and P. V. Hobbs, 1977. *Atmospheric Science: An Introductory Survey*. Academic Press, 467 pp.

Appendix A: August 2002 Data

List of Figures

Figure A1. Temperature time series data for stations C1 and C2 from 8/01/02 to 8/07/02.	1
Figure A2. Temperature time series data for stations C1 and C2 from 8/08/02 to 8/16/02.	1
Figure A3. Temperature time series data for stations C1 and C2 from 8/17/02 to 8/23/02.	2
Figure A4. Temperature time series data for stations C3 and C4 from 8/01/02 to 8/07/02.	2
Figure A5. Temperature time series data for stations C3 and C4 from 8/08/02 to 8/16/02.	3
Figure A6. Temperature time series data for station C3 and C4 from 8/17/02 to 8/23/02.	3
Figure A7. Temperature time series data for stations C5 and C6 from 8/01/02 to 8/07/02.	4
Figure A8. Temperature time series data for stations C5 and C6 from 8/08/02 to 8/16/02.	4
Figure A9. Temperature time series data for stations C5 and C6 from 8/17/02 to 8/23/02.	5
Figure A10. Temperature time series data for stations D1 and D2 from 8/01/02 to 8/07/02.	5
Figure A11. Temperature time series data for stations D1 and D2 from 8/08/02 to 8/16/02.	6
Figure A12. Temperature time series data for stations D1 and D2 from 8/17/02 to 8/23/02.	6
Figure A13. Temperature time series data for stations D3 and D4 from 8/01/02 to 8/07/02.	7
Figure A14. Temperature time series data for stations D3 and D4 from 8/08/02 to 8/16/02.	7
Figure A15. Temperature time series data for stations D3 and D4 from 8/17/02 to 8/23/02.	8
Figure A16. Temperature time series data for stations D5 and D6 from 8/01/02 to 8/07/02.	8
Figure A17. Temperature time series data for stations D5 and D6 from 8/08/02 to 8/16/02.	9
Figure A18. Temperature time series data for stations D5 and D6 from 8/17/02 to 8/23/02.	9
Figure A19. Temperature time series data for stations E1 and E2 from 8/01/02 to 8/07/02.	10
Figure A20. Temperature time series data for stations E1 and E2 from 8/08/02 to 8/16/02.	10
Figure A21. Temperature time series data for stations E1 and E2 from 8/17/02 to 8/23/02.	11
Figure A22. Temperature time series data for stations E3 and E4 from 8/01/02 to 8/07/02.	11

Figure A23. Temperature time series data for stations E3 and E4 from 8/08/02 to 8/16/02.	12
Figure A24. Temperature time series data for stations E3 and E4 from 8/17/02 to 8/23/02.	12
Figure A25. Temperature time series data for stations E5 and E6 from 8/01/02 to 8/07/02.	13
Figure A26. Temperature time series data for stations E5 and E6 from 8/08/02 to 8/16/02.	13
Figure A27. Temperature time series data for stations E5 and E6 from 8/17/02 to 8/23/02.	14
Figure A28. Temperature time series data for stations F1 and F2 from 8/01/02 to 8/07/02.	14
Figure A29. Temperature time series data for stations F1 and F2 from 8/08/02 to 8/16/02.	15
Figure A30. Temperature time series data for stations F1 and F2 from 8/17/02 to 8/23/02.	15
Figure A31. Temperature time series data for stations F3 and F4 from 8/01/02 to 8/07/02.	16
Figure A32. Temperature time series data for stations F3 and F4 from 8/08/02 to 8/16/02.	16
Figure A33. Temperature time series data for stations F3 and F4 from 8/17/02 to 8/23/02.	17
Figure A34. Upstream and downstream temperature and river flow measured at Vernon Dam.	18
Figure A35. Upstream and downstream temperature and river flow measured at Vernon Dam.	19
Figure A36. Upstream and downstream temperature and river flow measured at Vernon Dam.	20
Figure A37. Water temperature and flow at the VYNPS discharge.	21
Figure A38. Water temperature and flow at the VYNPS discharge.	22
Figure A39. Water temperature and flow at the VYNPS discharge.	23
Figure A40. Wind stick plot and wind speed and direction as observed at the VYNPS. In the top figure, each stick points in the direction the wind is blowing to and stick length is proportional to wind speed. The bottom figure shows the direction the wind is blowing from relative to true north.	24
Figure A41. Wind stick plot and wind speed and direction as observed at the VYNPS. In the top figure, each stick points in the direction the wind is blowing to and stick length is proportional to wind speed. The bottom figure shows the direction the wind is blowing from relative to true north.	25
Figure A42. Wind stick plot and wind speed and direction as observed at the VYNPS. In the top figure, each stick points in the direction the wind is blowing to and stick length is proportional to wind speed. The bottom figure shows the direction the wind is blowing from relative to true north.	26
Figure A43. Air and dew point temperatures, relative humidity and atmospheric pressure as observed at Orange, MA.	27

Figure A44. Air and dew point temperatures, relative humidity and atmospheric pressure as observed at Orange, MA.....	28
Figure A45. Air and dew point temperatures, relative humidity and atmospheric pressure as observed at Orange, MA.....	29
Figure A46. Solar radiation at Orange, MA.....	30
Figure A47. Solar radiation at Orange, MA.....	30
Figure A48. Solar radiation at Orange, MA.....	30

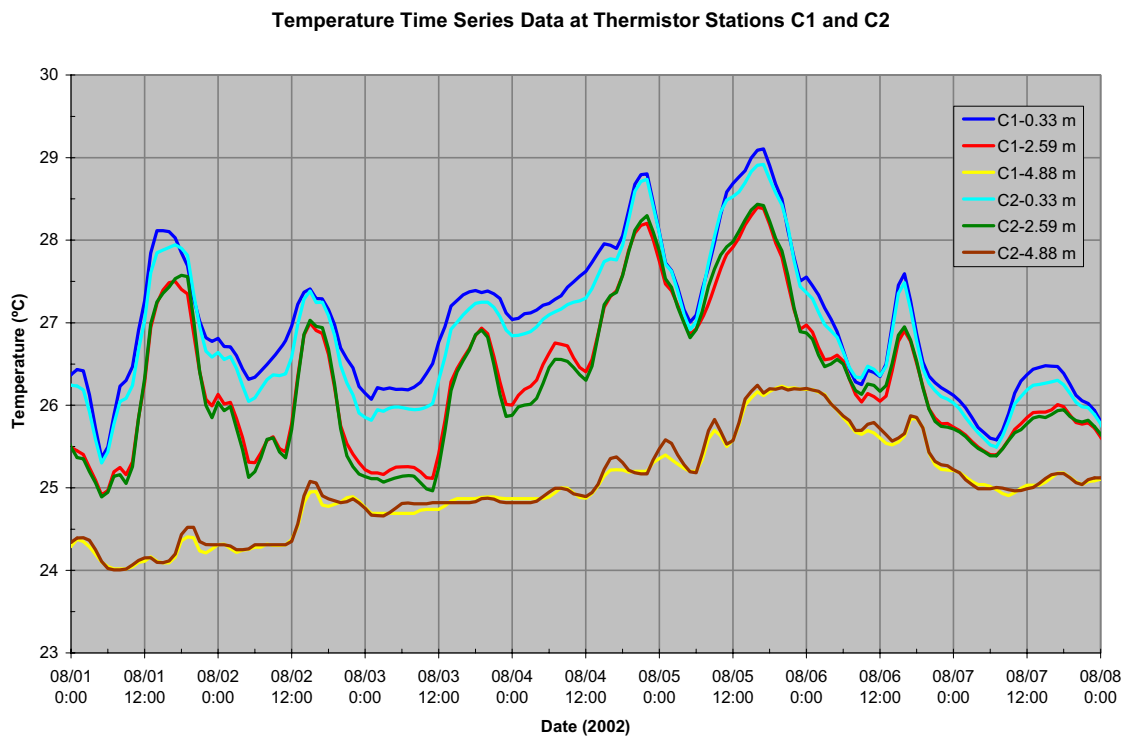


Figure A1. Temperature time series data for stations C1 and C2 from 8/01/02 to 8/07/02.

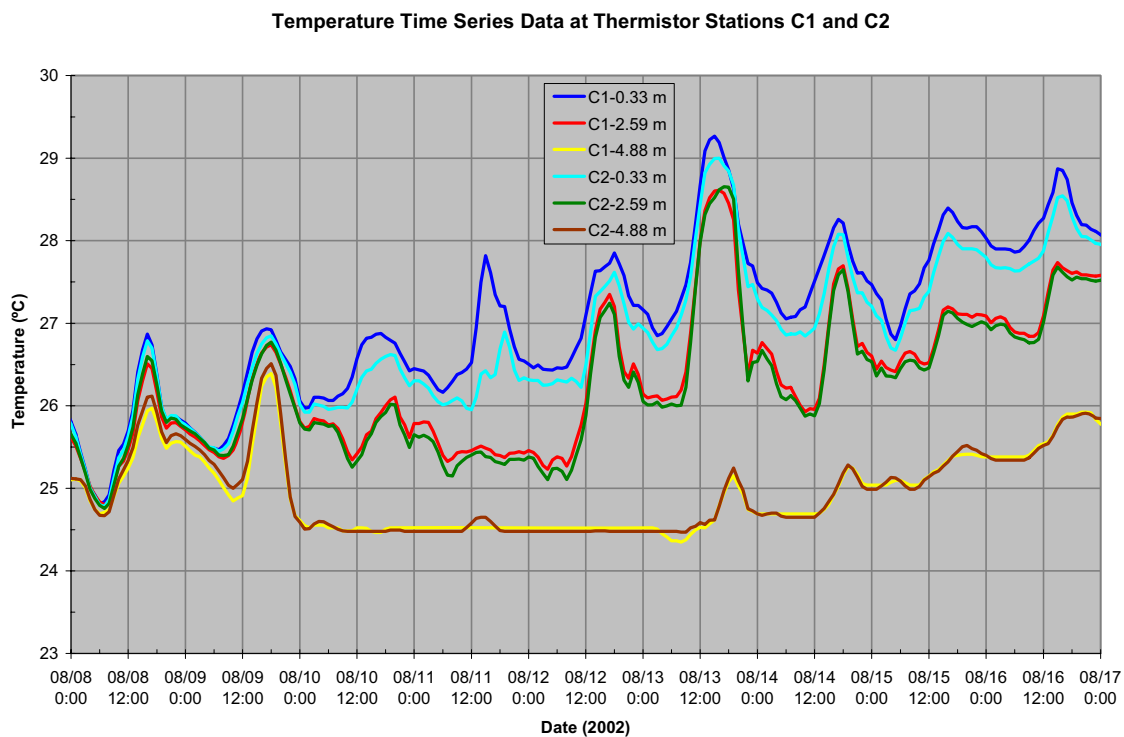


Figure A2. Temperature time series data for stations C1 and C2 from 8/08/02 to 8/16/02.

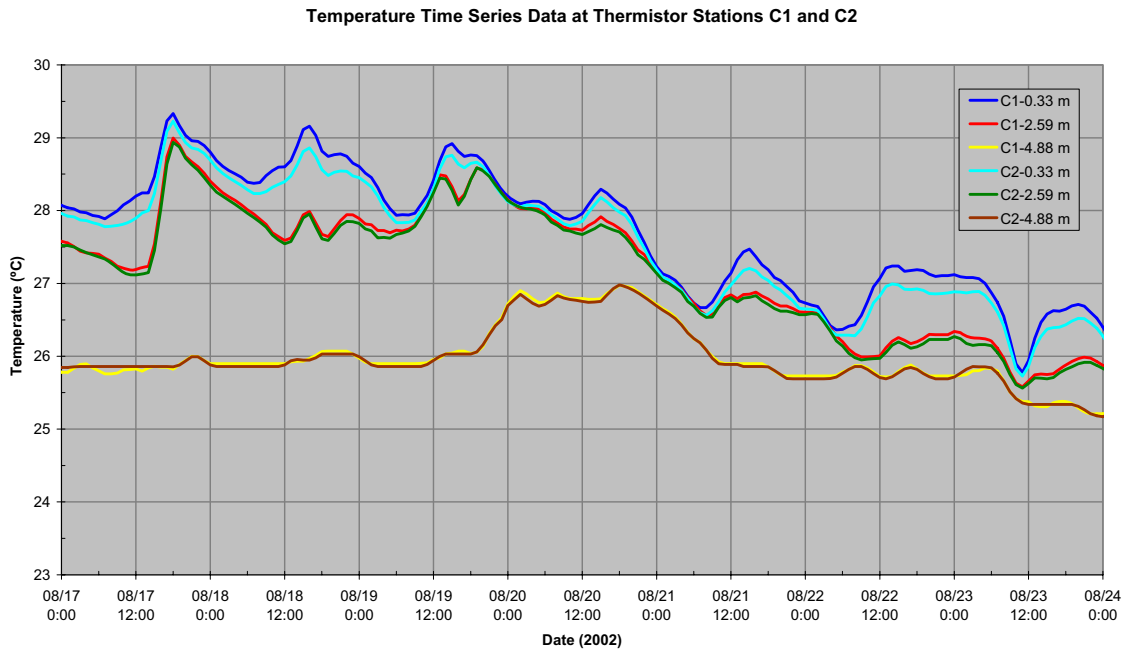


Figure A3. Temperature time series data for stations C1 and C2 from 8/17/02 to 8/23/02.

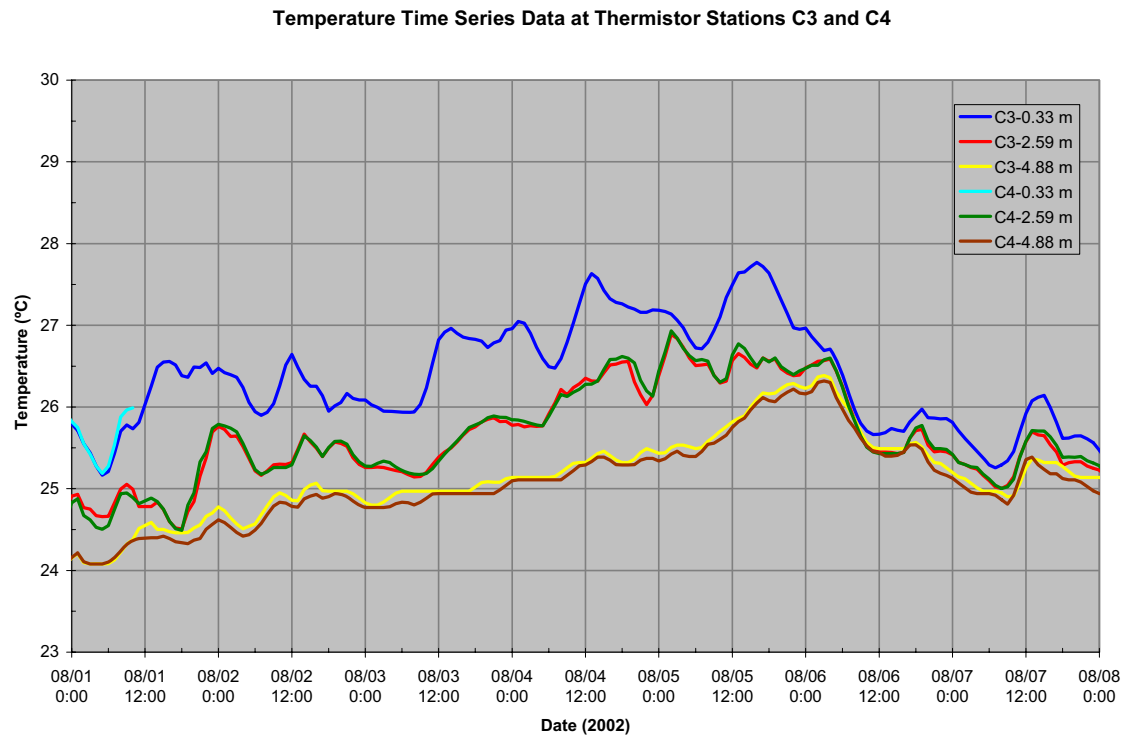


Figure A4. Temperature time series data for stations C3 and C4 from 8/01/02 to 8/07/02.

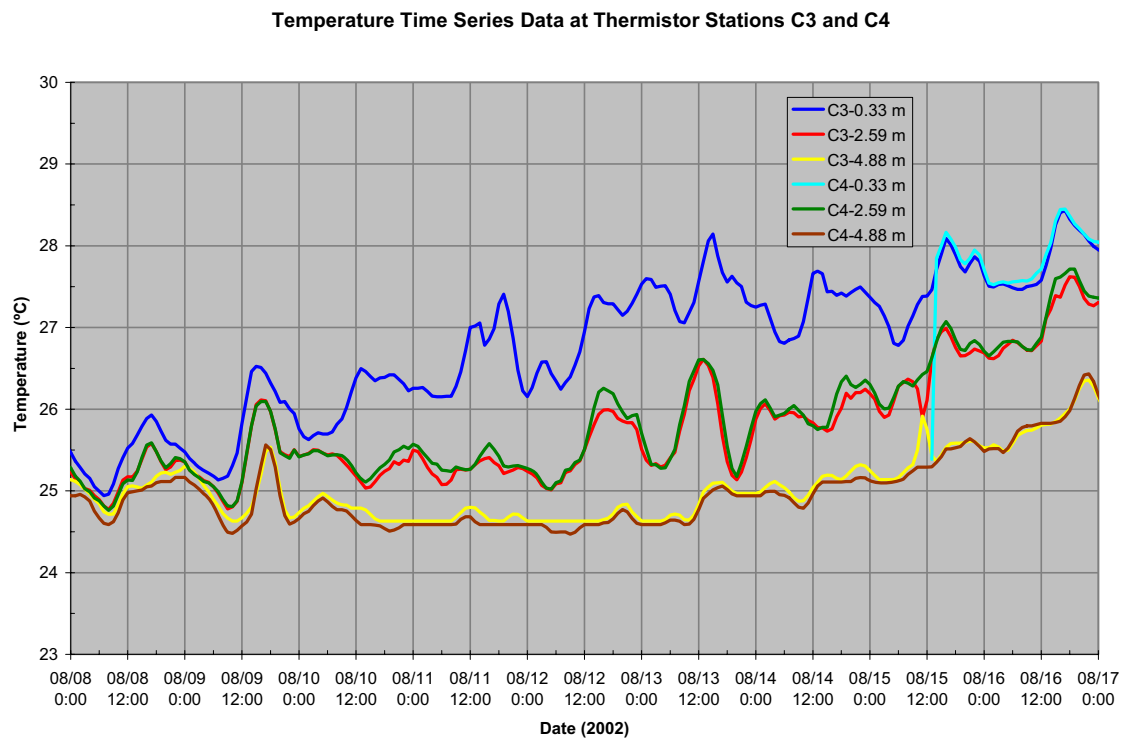


Figure A5. Temperature time series data for stations C3 and C4 from 8/08/02 to 8/16/02.

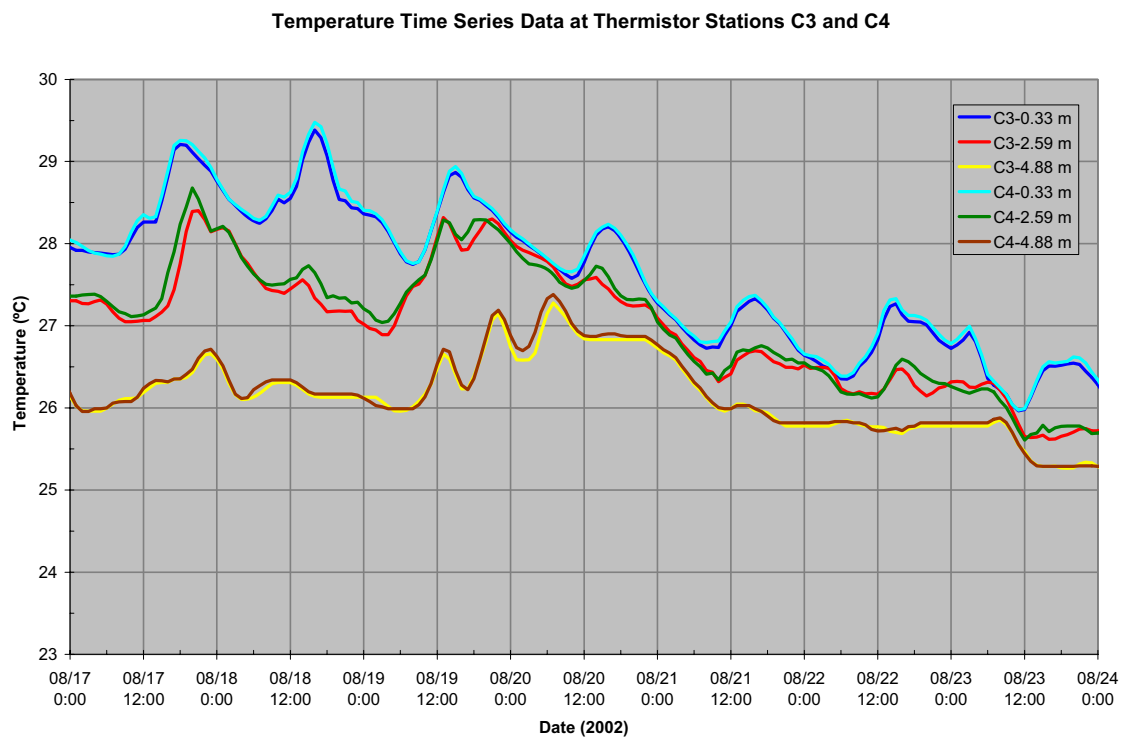


Figure A6. Temperature time series data for station C3 and C4 from 8/17/02 to 8/23/02.

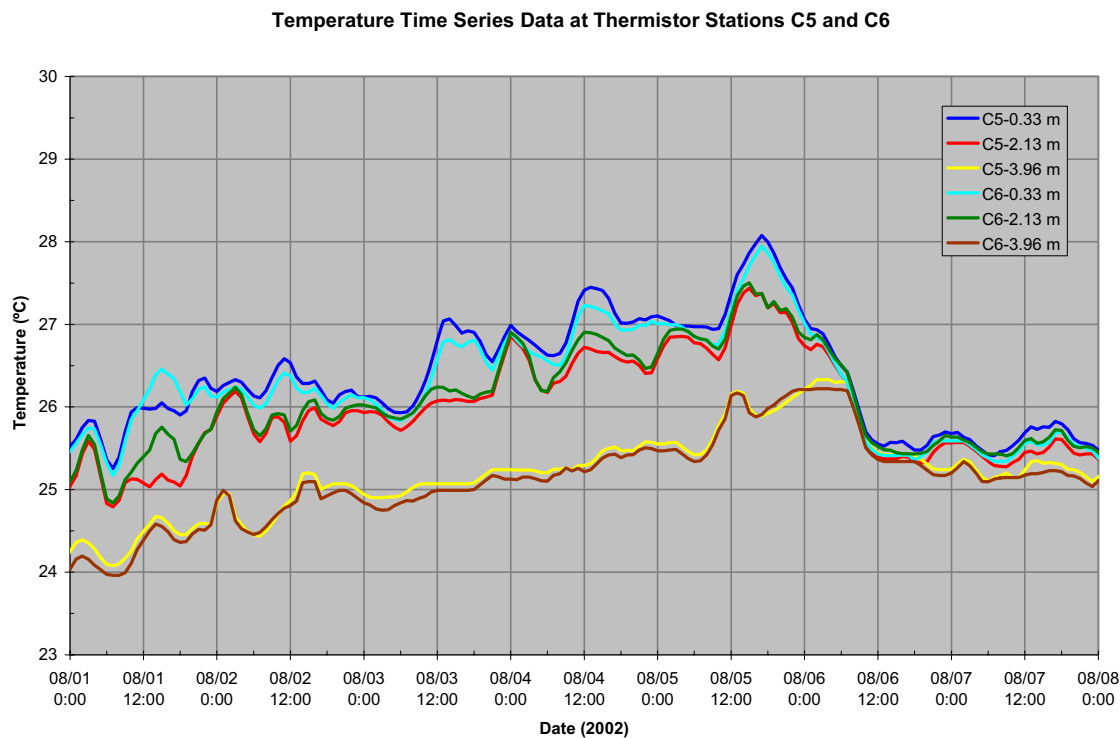


Figure A7. Temperature time series data for stations C5 and C6 from 8/01/02 to 8/07/02.

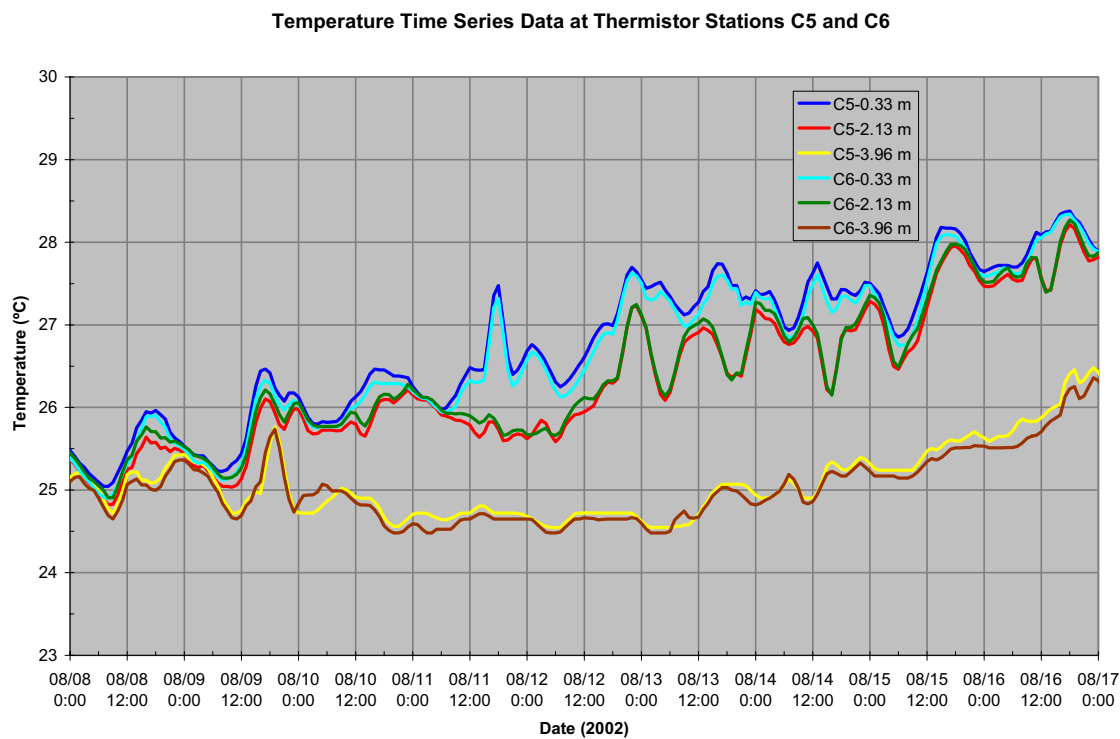


Figure A8. Temperature time series data for stations C5 and C6 from 8/08/02 to 8/16/02.

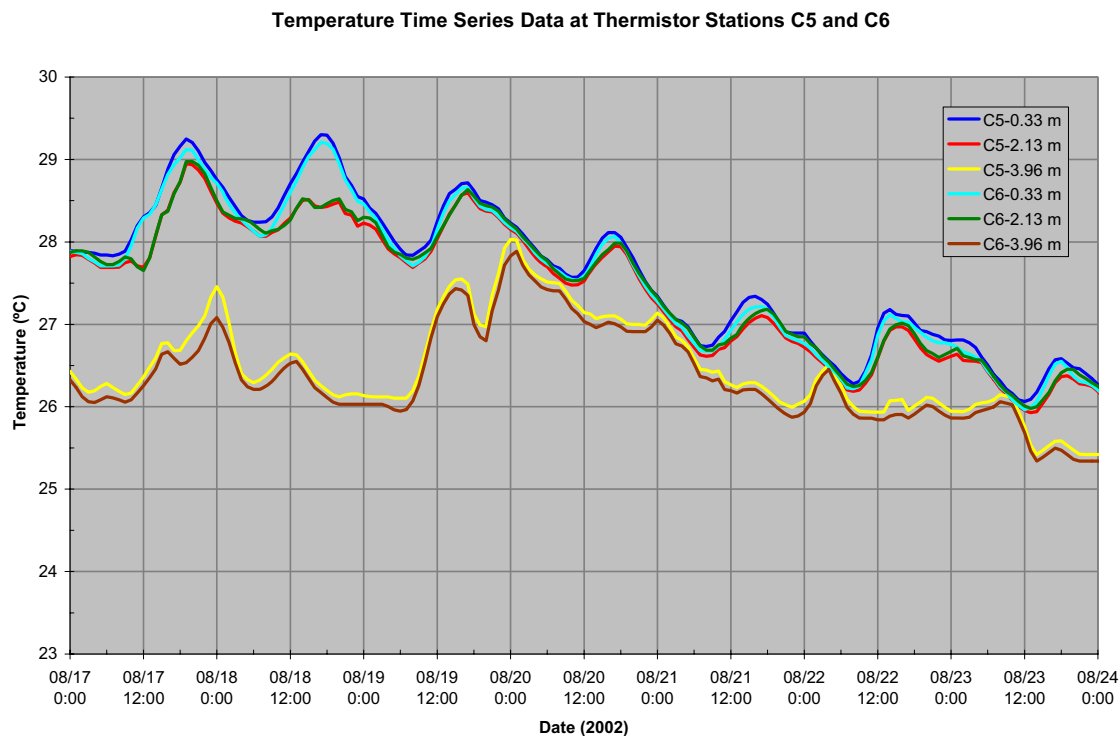


Figure A9. Temperature time series data for stations C5 and C6 from 8/17/02 to 8/23/02.

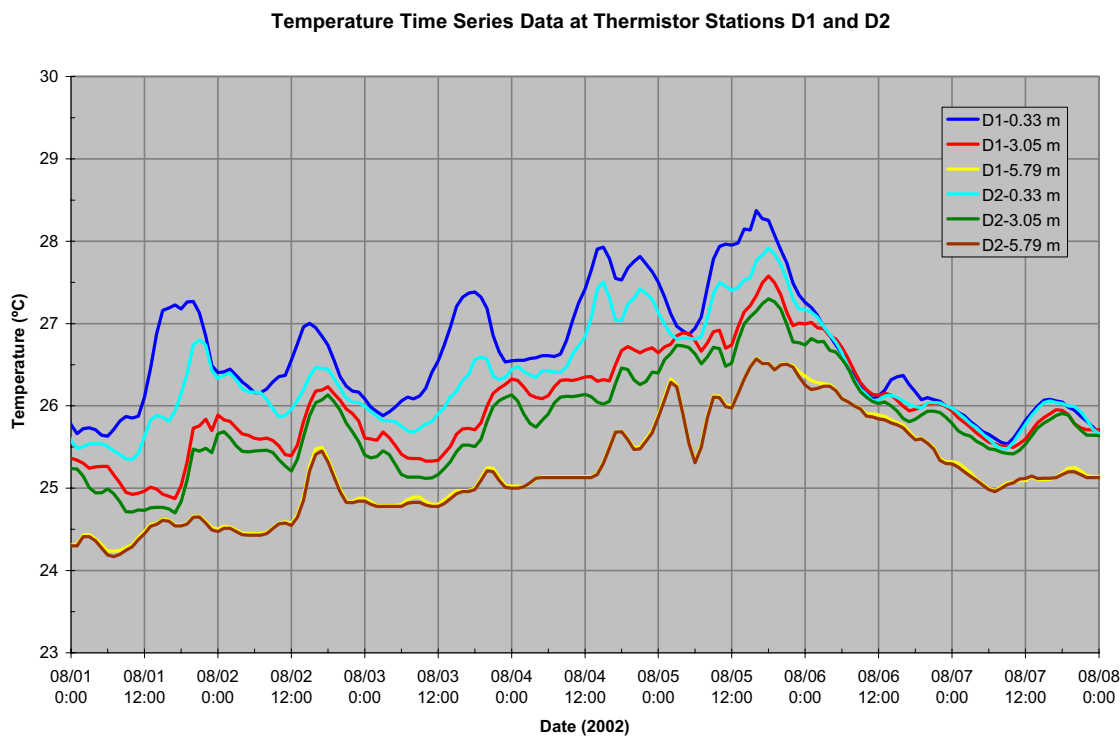


Figure A10. Temperature time series data for stations D1 and D2 from 8/01/02 to 8/07/02.

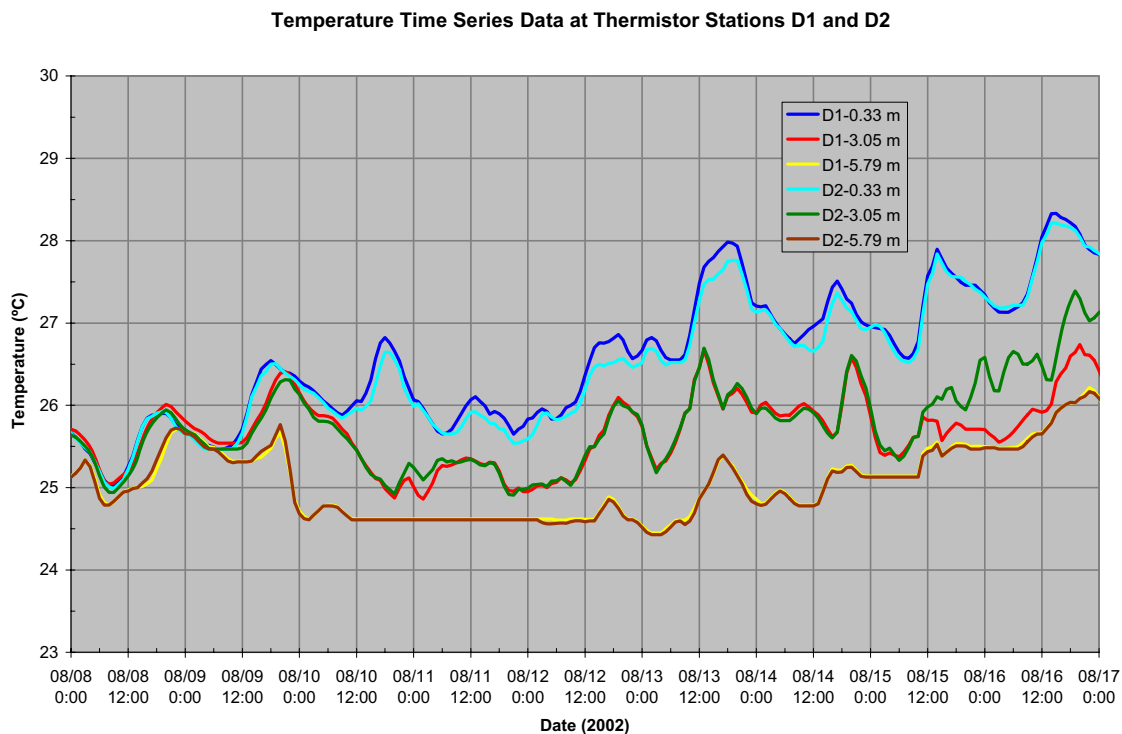


Figure A11. Temperature time series data for stations D1 and D2 from 8/8/02 to 8/16/02.

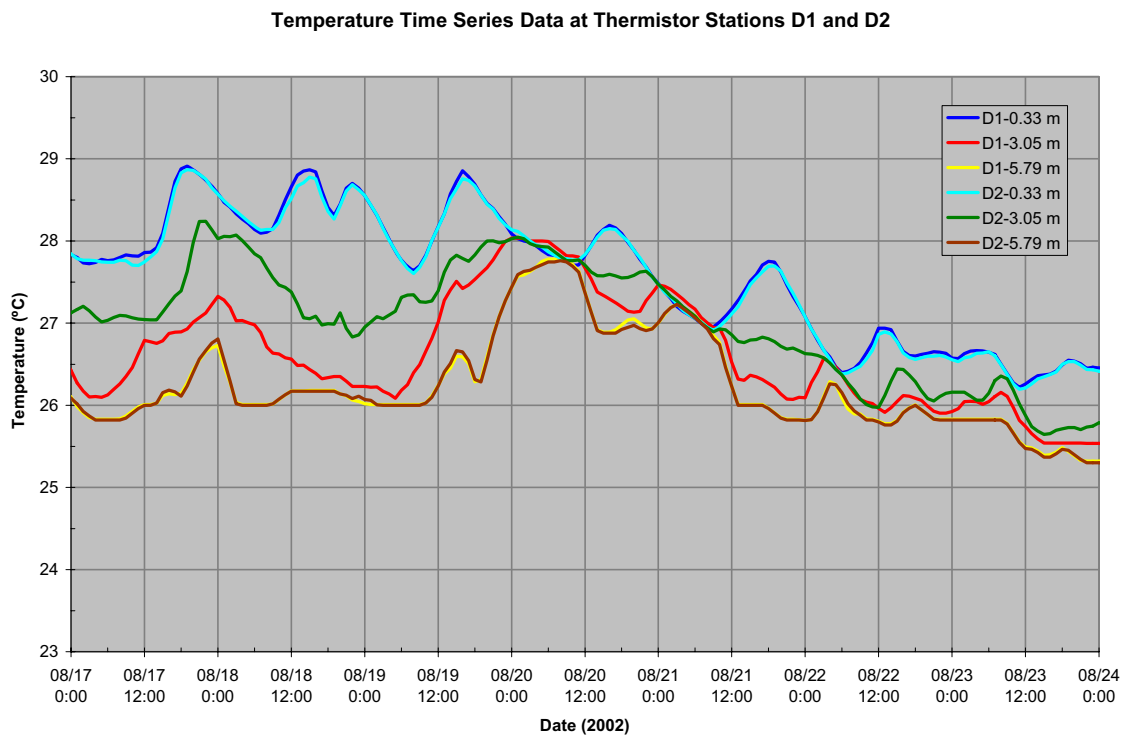


Figure A12. Temperature time series data for stations D1 and D2 from 8/17/02 to 8/23/02.

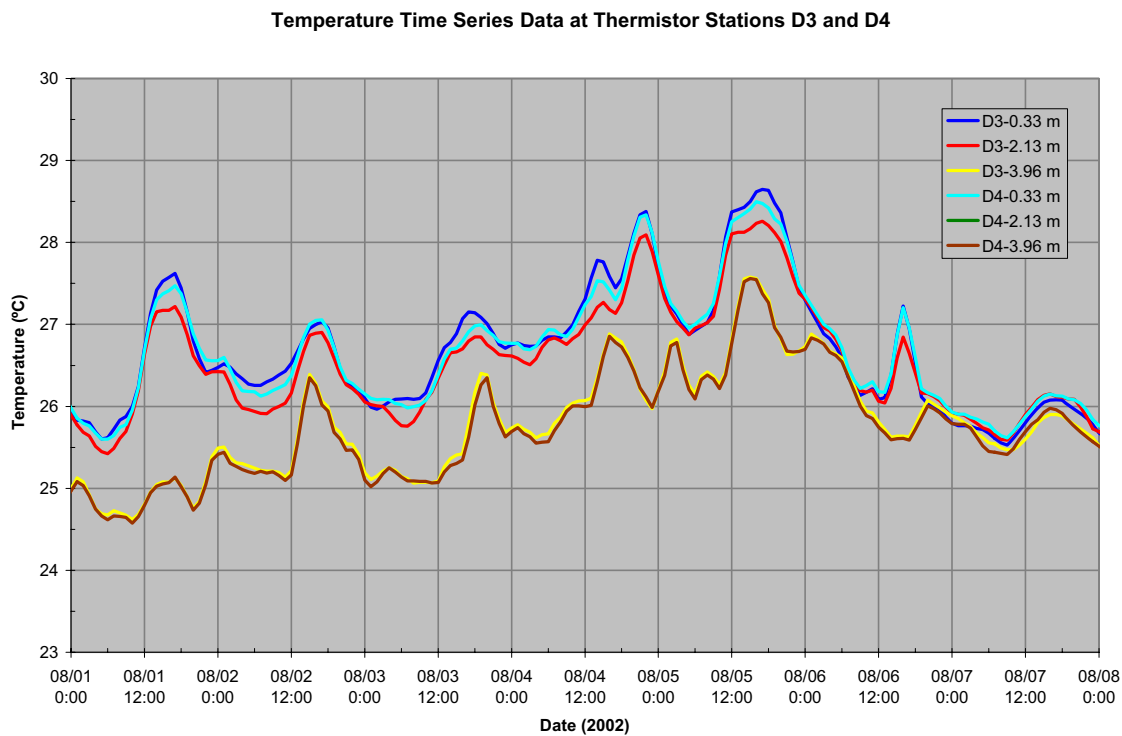


Figure A13. Temperature time series data for stations D3 and D4 from 8/01/02 to 8/07/02.

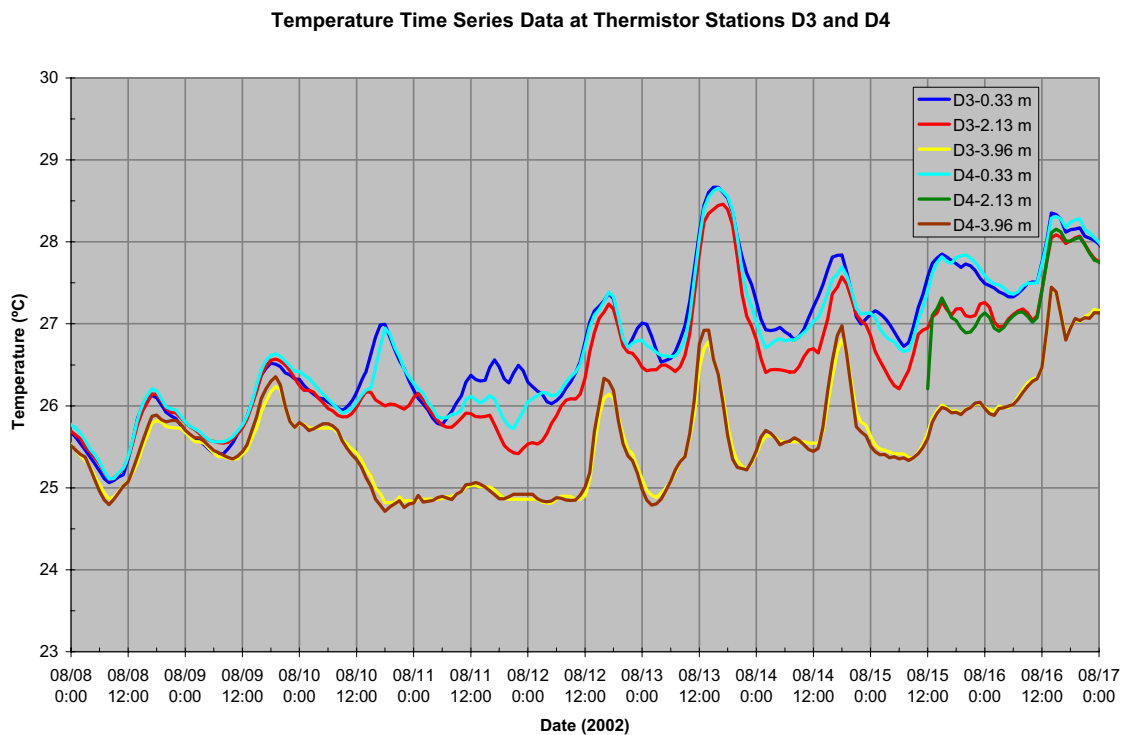


Figure A14. Temperature time series data for stations D3 and D4 from 8/08/02 to 8/16/02.

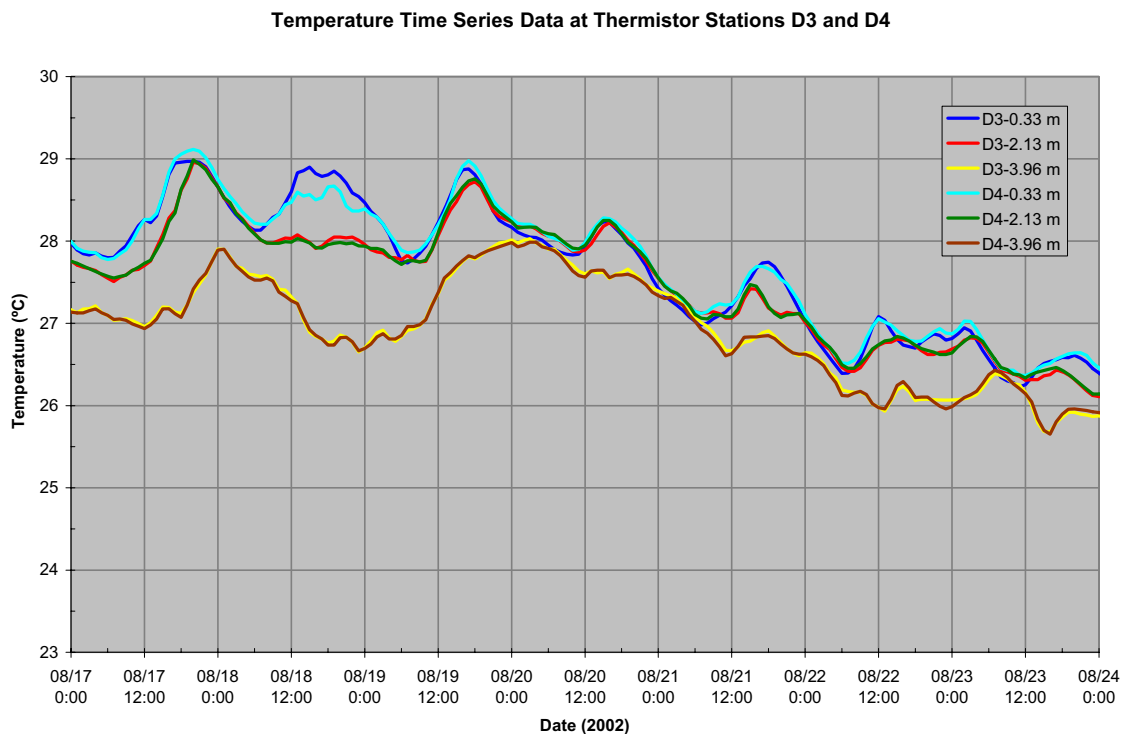


Figure A15. Temperature time series data for stations D3 and D4 from 8/17/02 to 8/23/02.

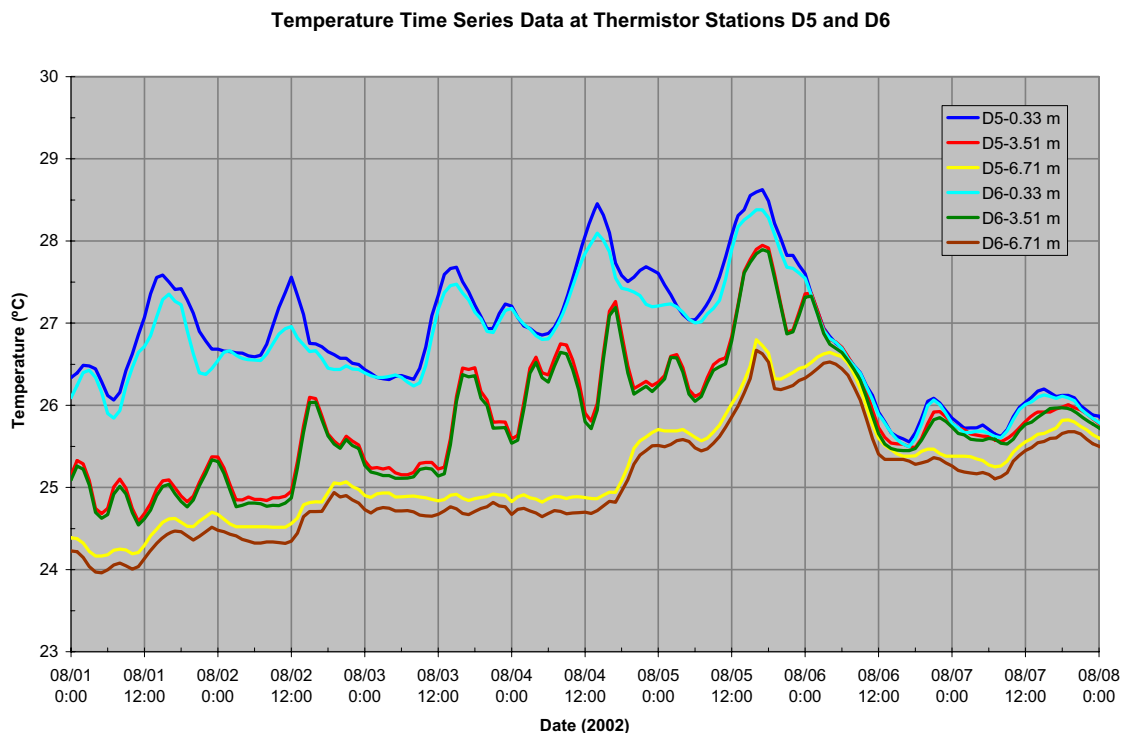


Figure A16. Temperature time series data for stations D5 and D6 from 8/01/02 to 8/07/02.

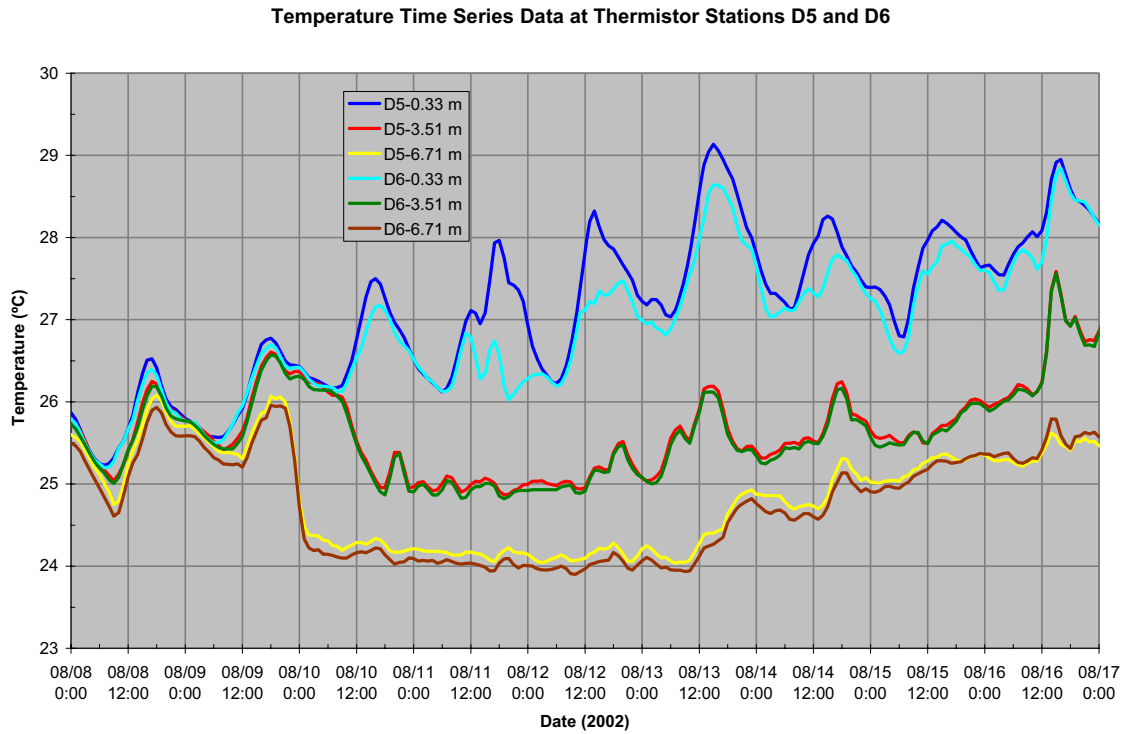


Figure A17. Temperature time series data for stations D5 and D6 from 8/08/02 to 8/16/02.

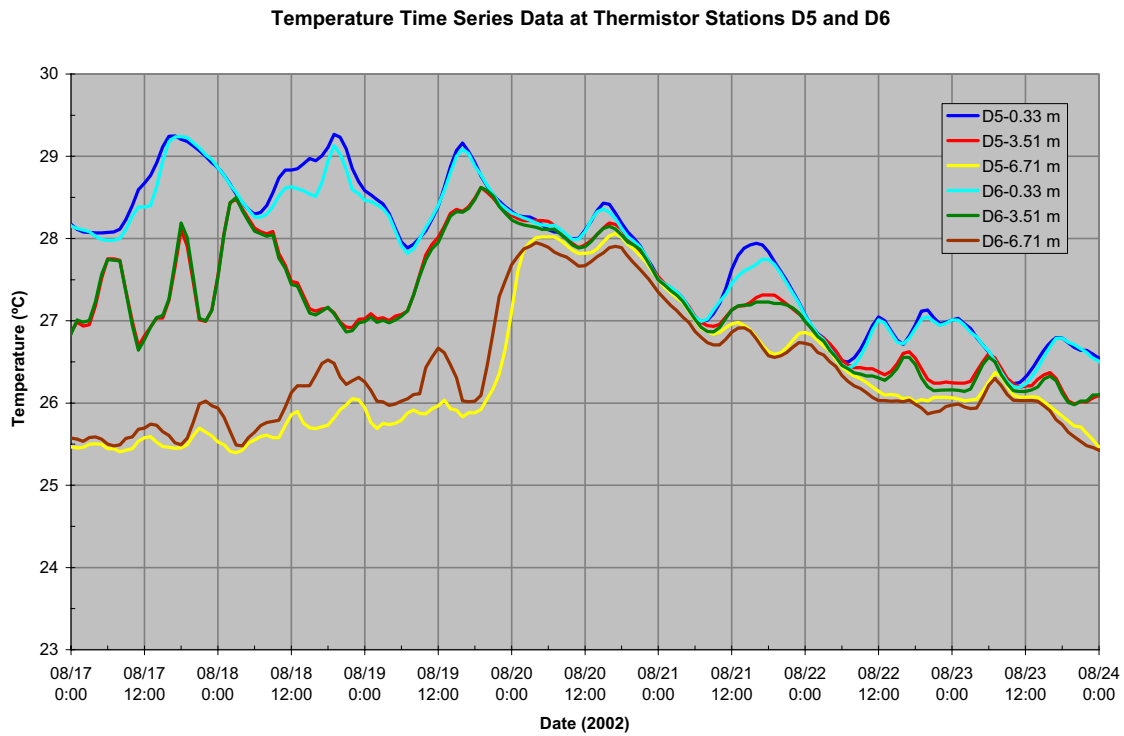


Figure A18. Temperature time series data for stations D5 and D6 from 8/17/02 to 8/23/02.

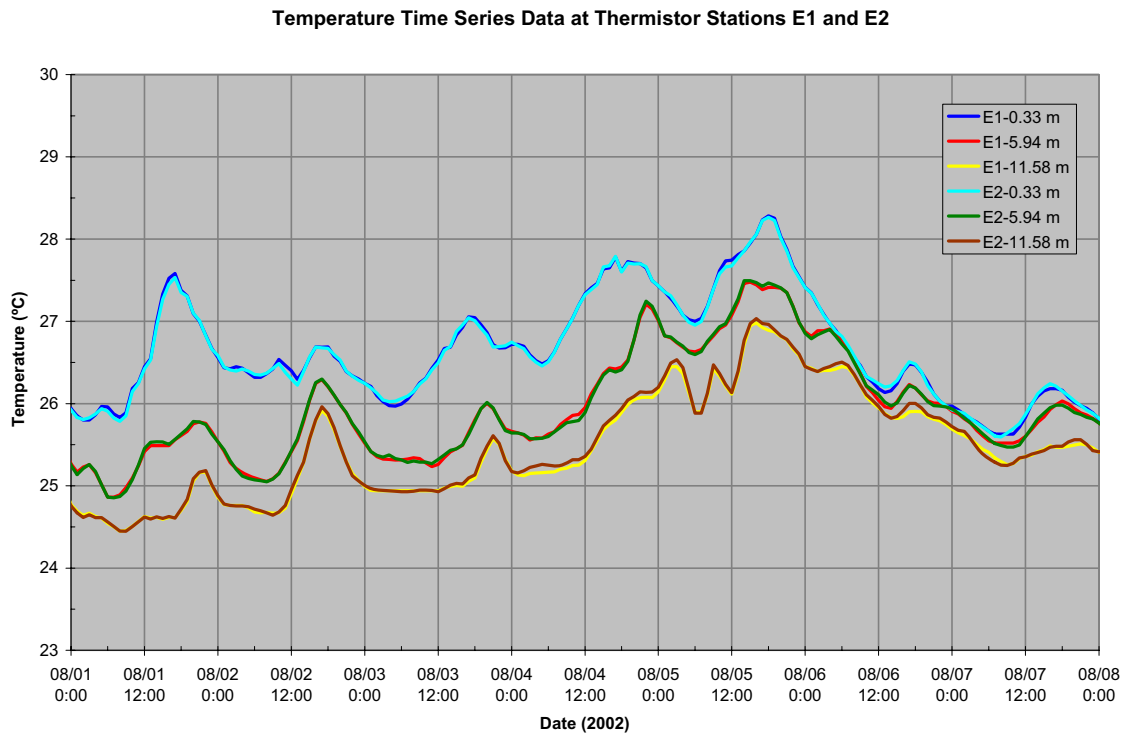


Figure A19. Temperature time series data for stations E1 and E2 from 8/01/02 to 8/07/02.

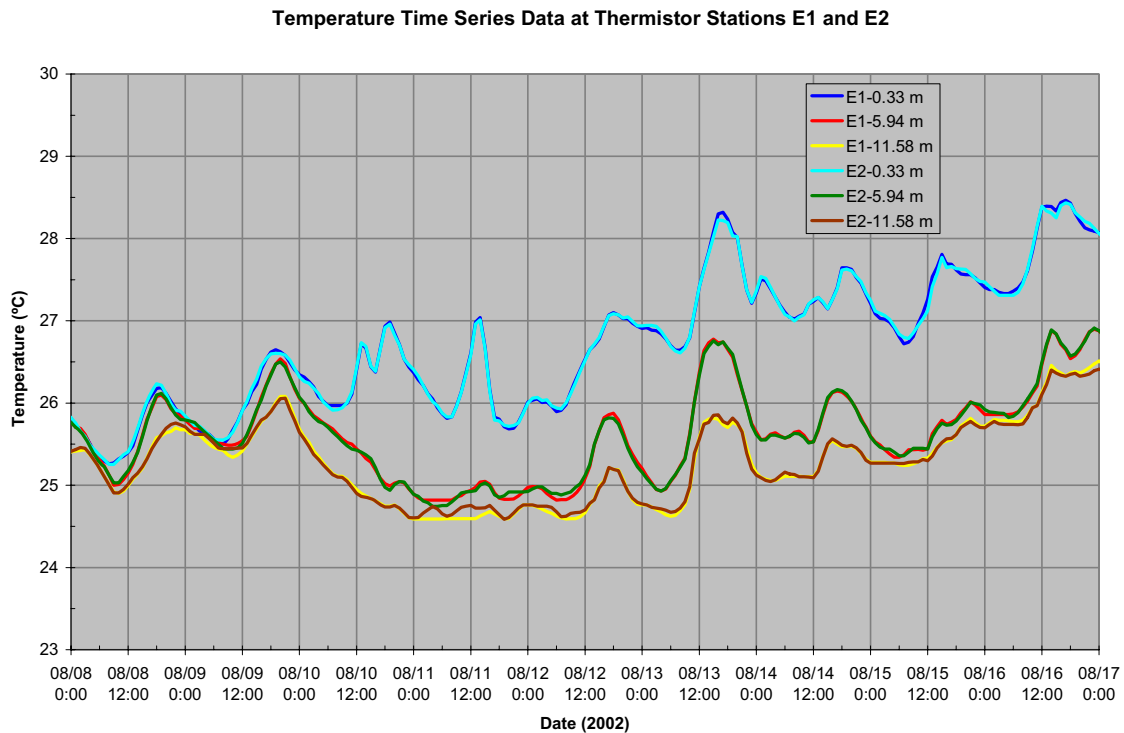


Figure A20. Temperature time series data for stations E1 and E2 from 8/08/02 to 8/16/02.

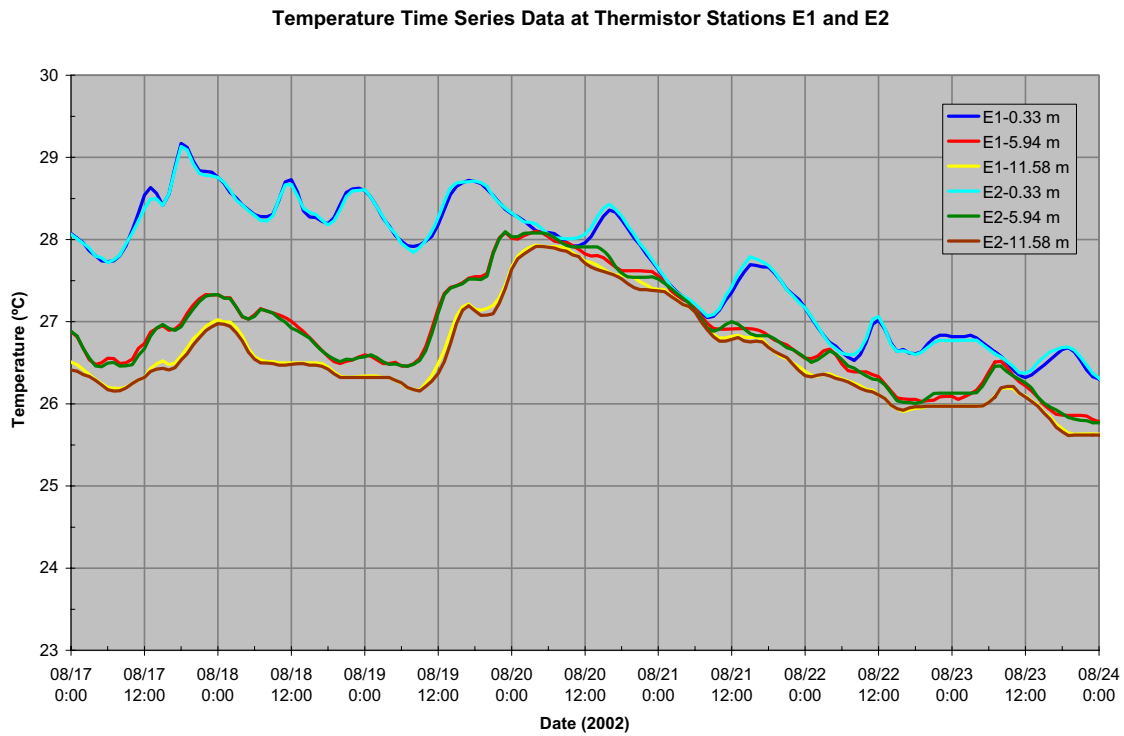


Figure A21. Temperature time series data for stations E1 and E2 from 8/17/02 to 8/23/02.

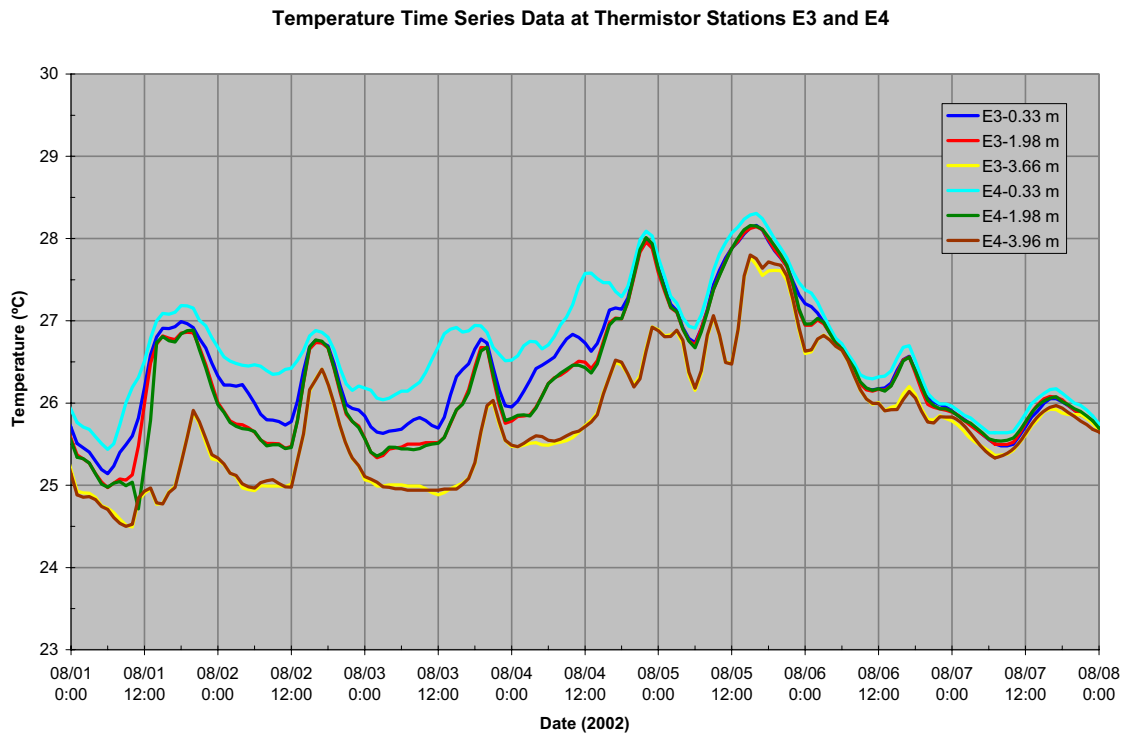


Figure A22. Temperature time series data for stations E3 and E4 from 8/01/02 to 8/07/02.

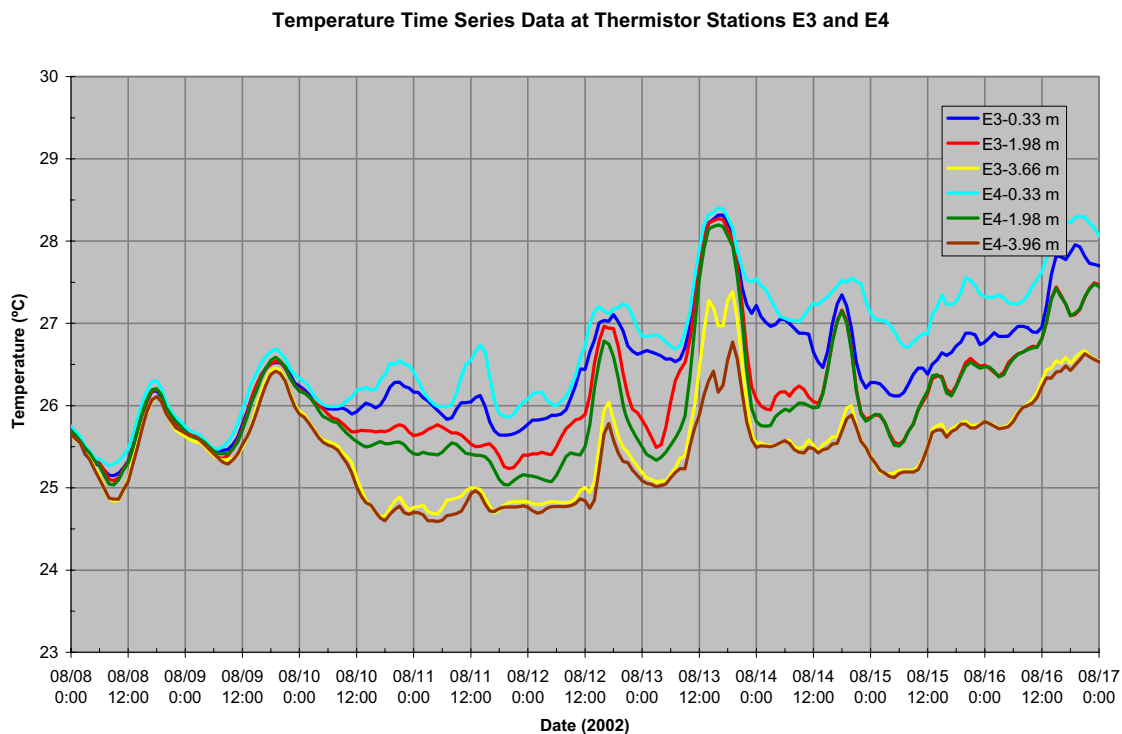


Figure A23. Temperature time series data for stations E3 and E4 from 8/08/02 to 8/16/02.

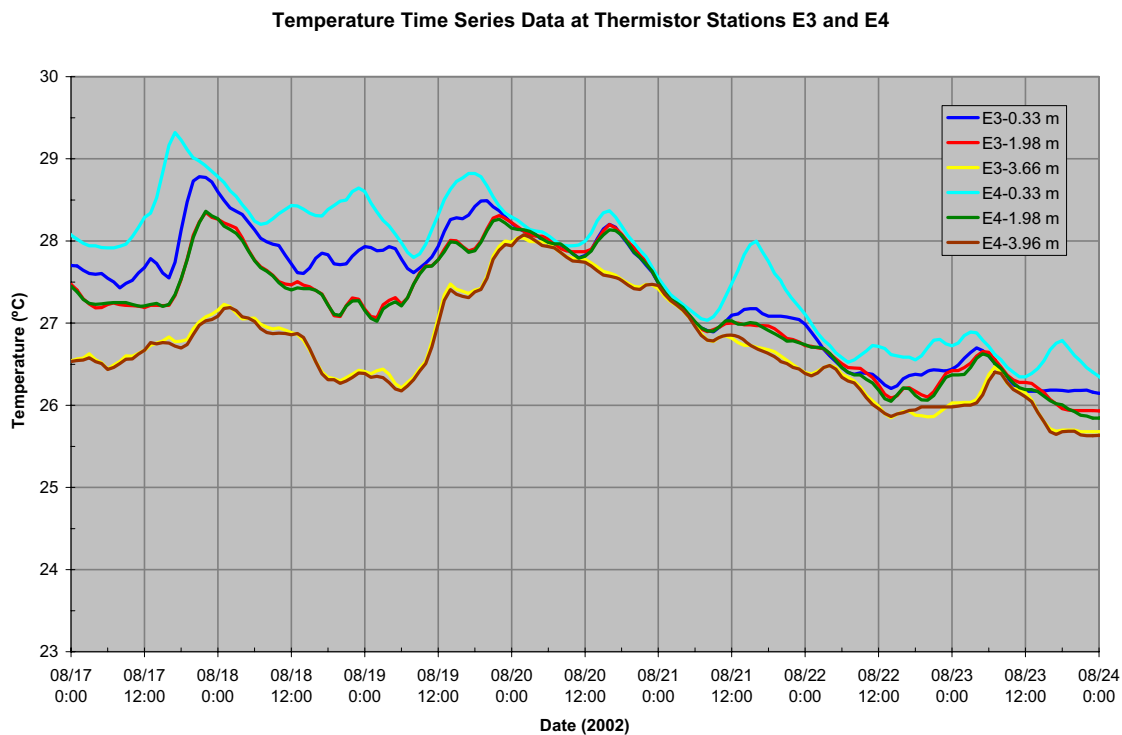


Figure A24. Temperature time series data for stations E3 and E4 from 8/17/02 to 8/23/02.

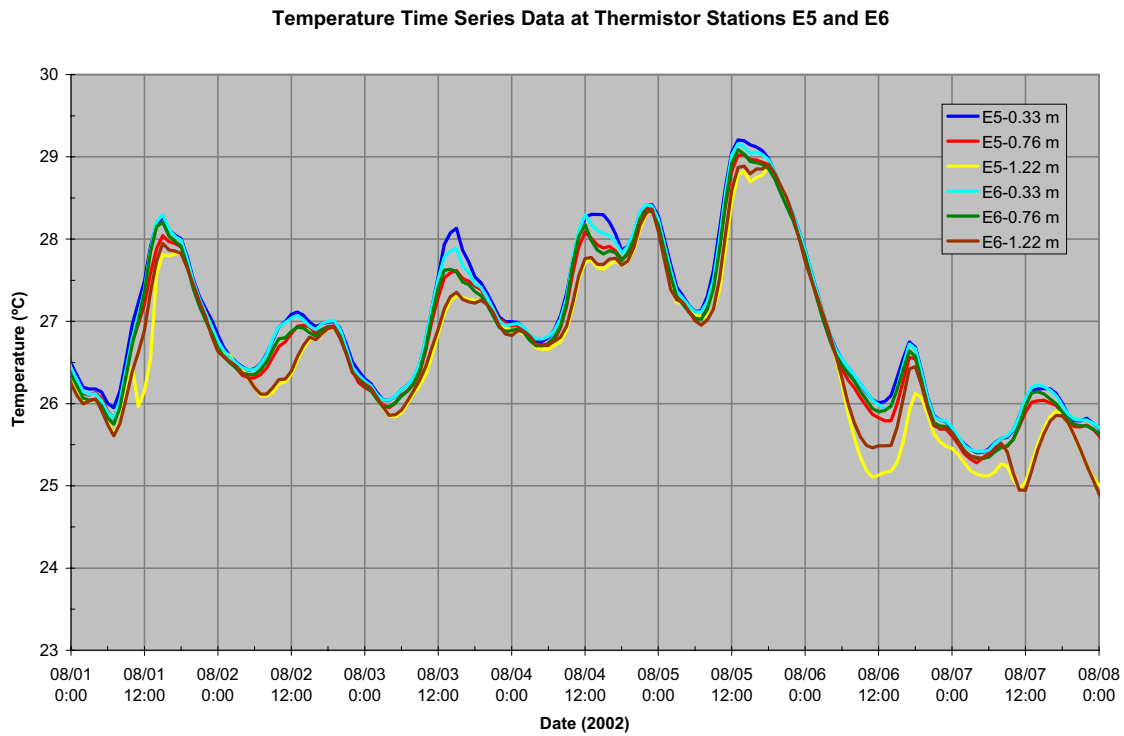


Figure A25. Temperature time series data for stations E5 and E6 from 8/01/02 to 8/07/02.

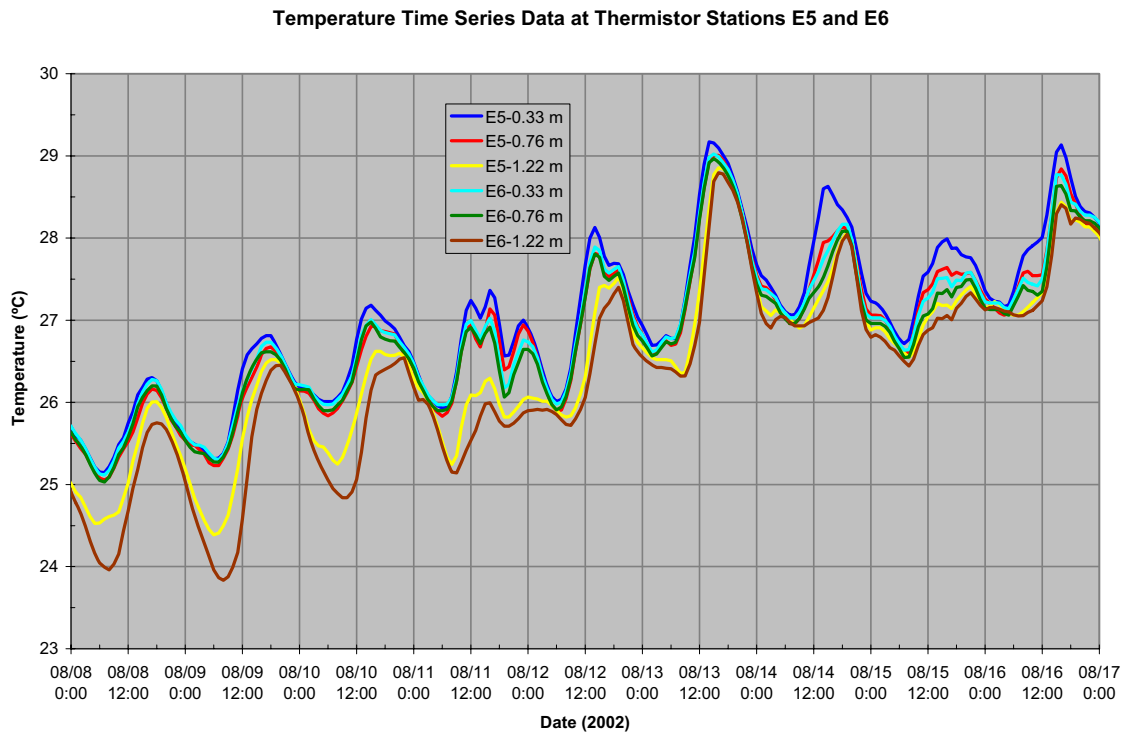


Figure A26. Temperature time series data for stations E5 and E6 from 8/08/02 to 8/16/02.

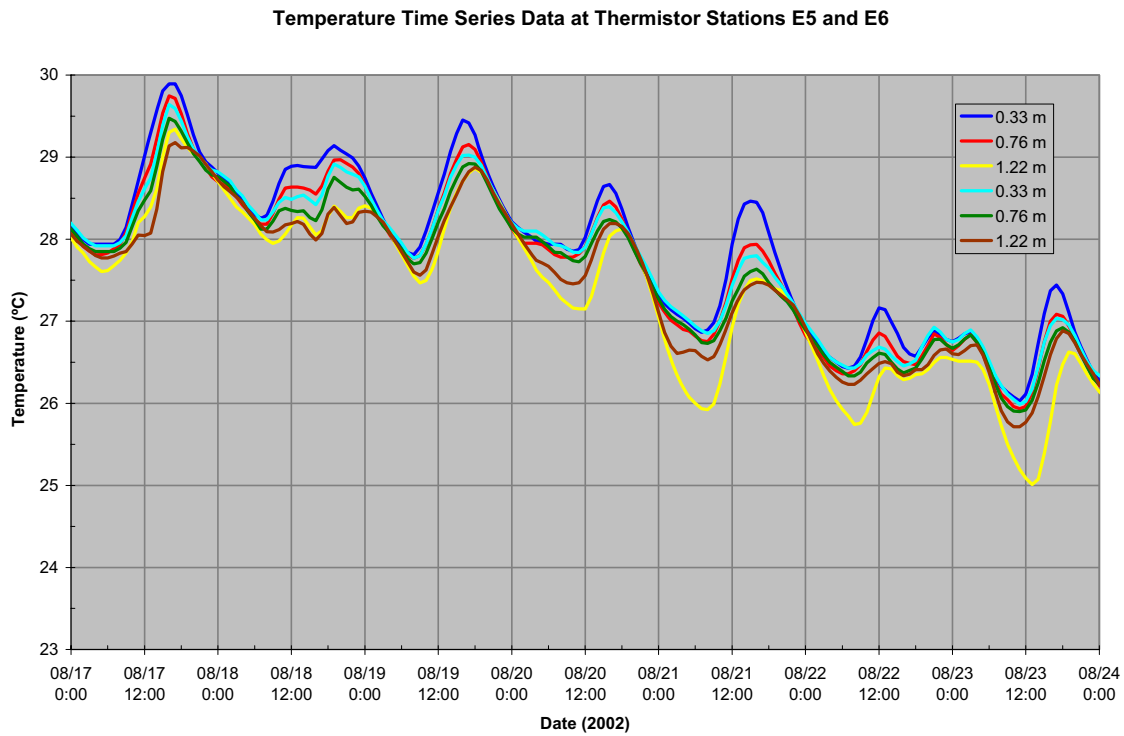


Figure A27. Temperature time series data for stations E5 and E6 from 8/17/02 to 8/23/02.

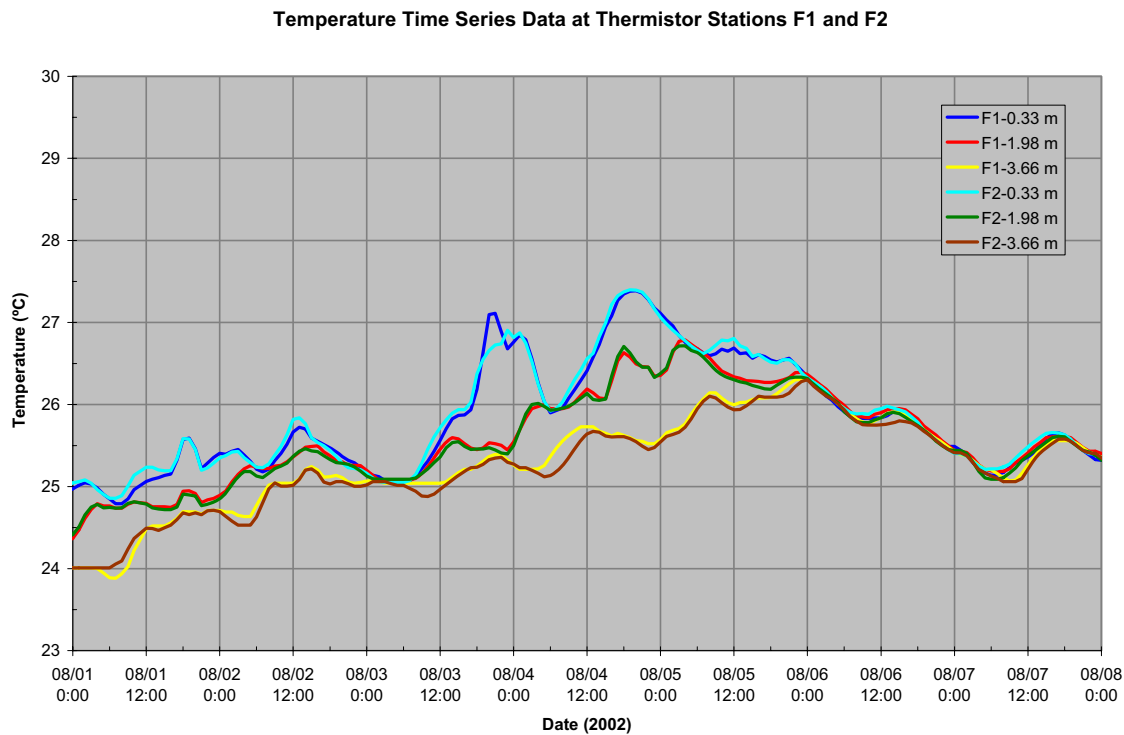


Figure A28. Temperature time series data for stations F1 and F2 from 8/01/02 to 8/07/02.

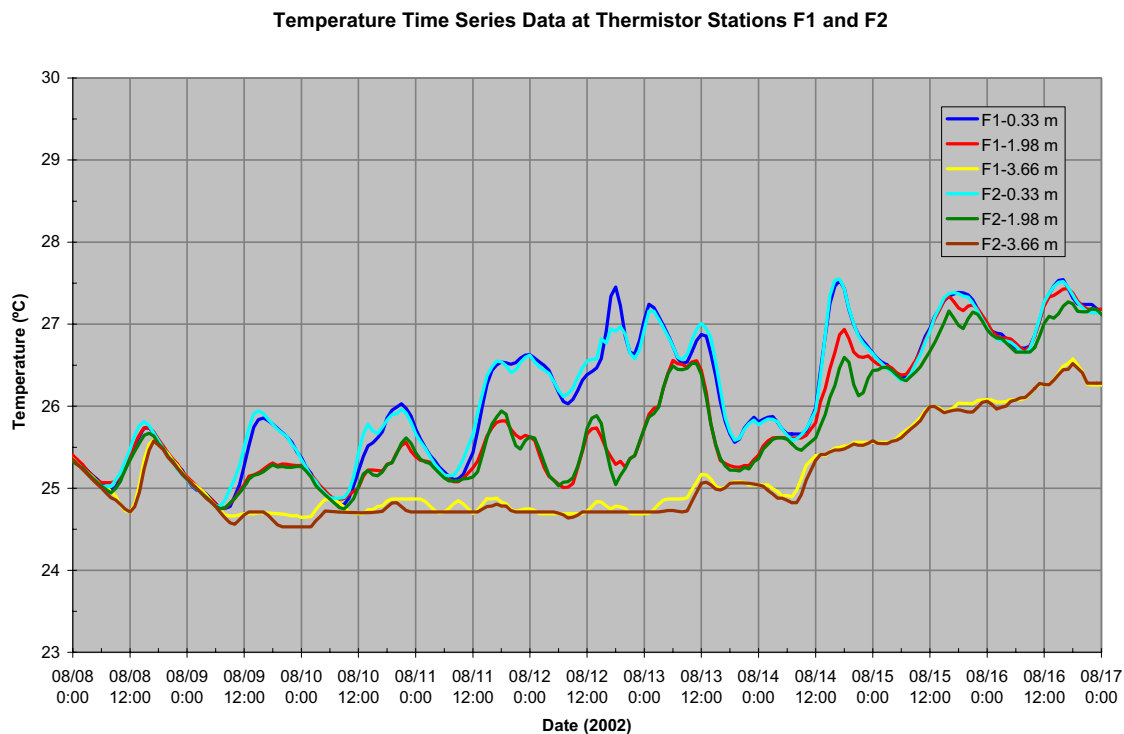


Figure A29. Temperature time series data for stations F1 and F2 from 8/08/02 to 8/16/02.

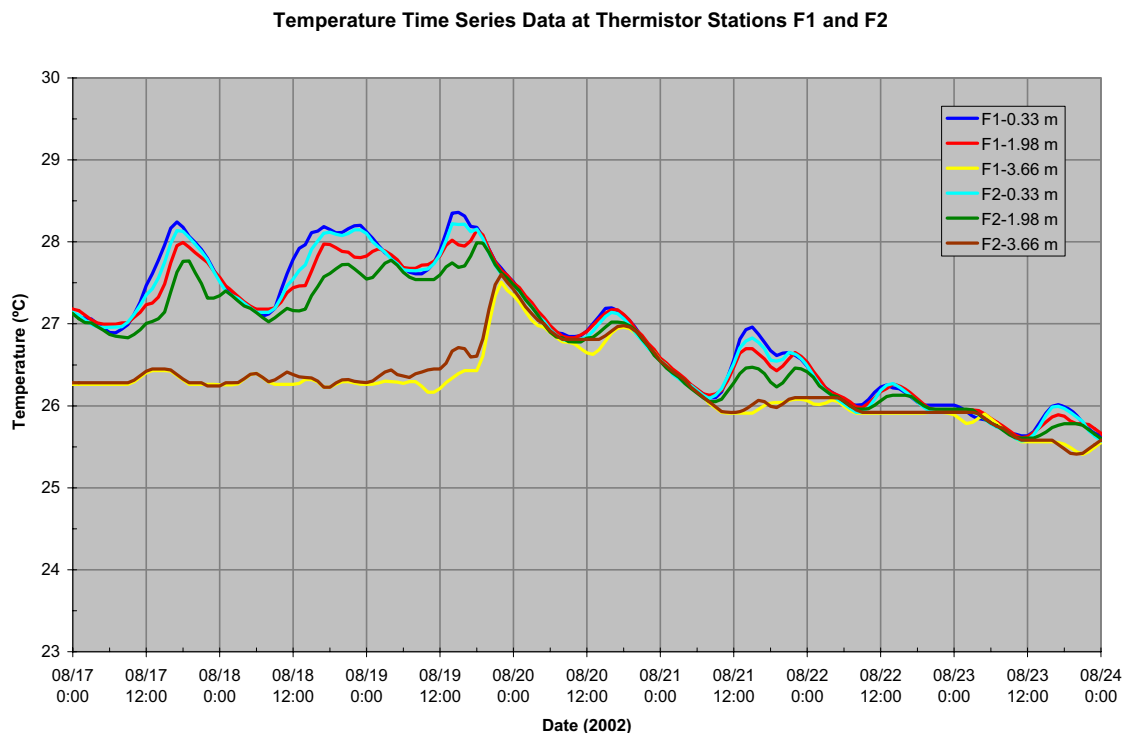


Figure A30. Temperature time series data for stations F1 and F2 from 8/17/02 to 8/23/02.

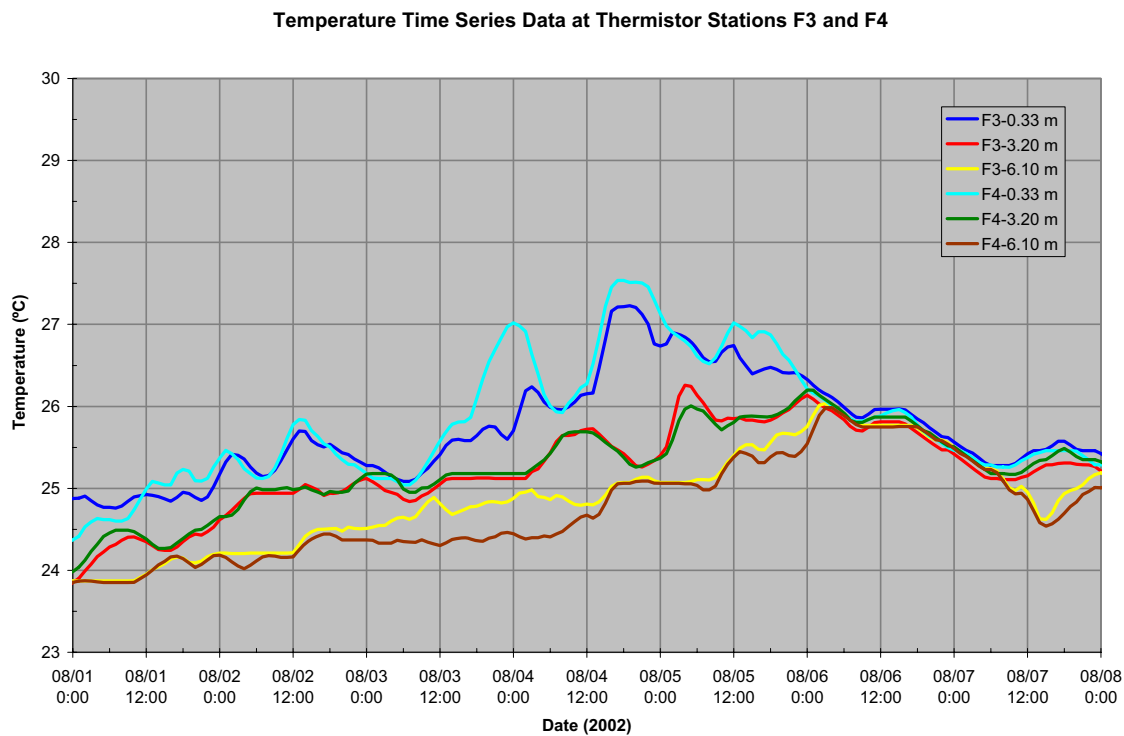


Figure A31. Temperature time series data for stations F3 and F4 from 8/01/02 to 8/07/02.

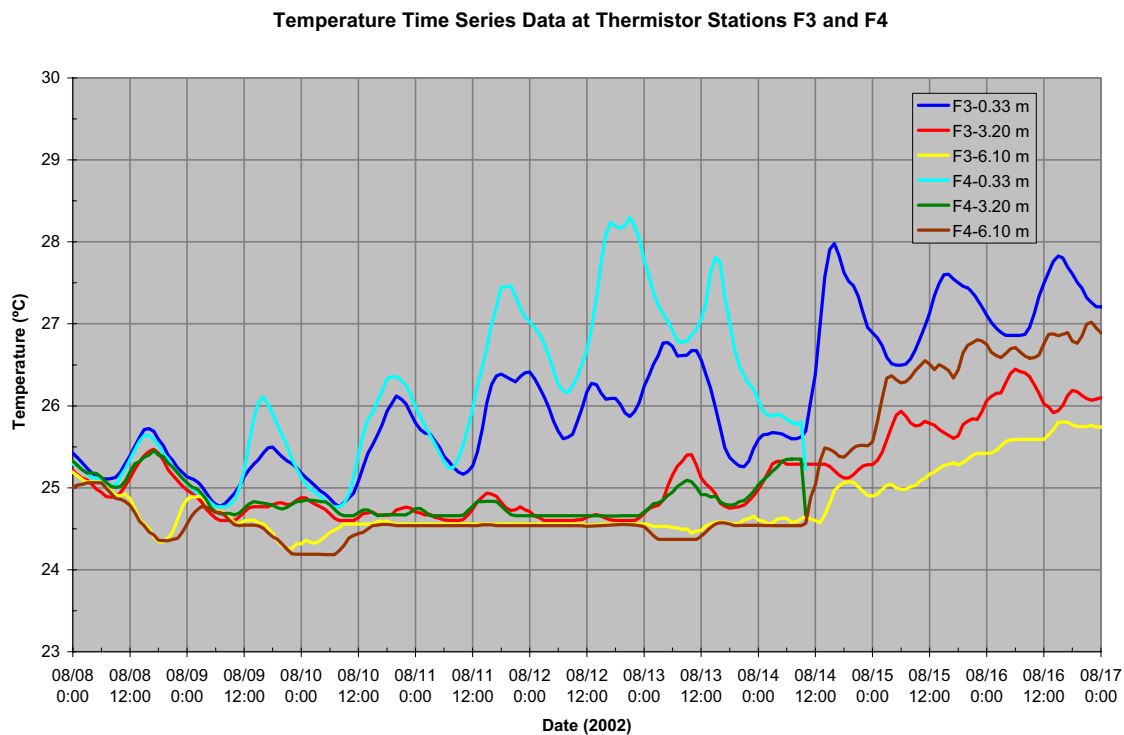


Figure A32. Temperature time series data for stations F3 and F4 from 8/08/02 to 8/16/02.

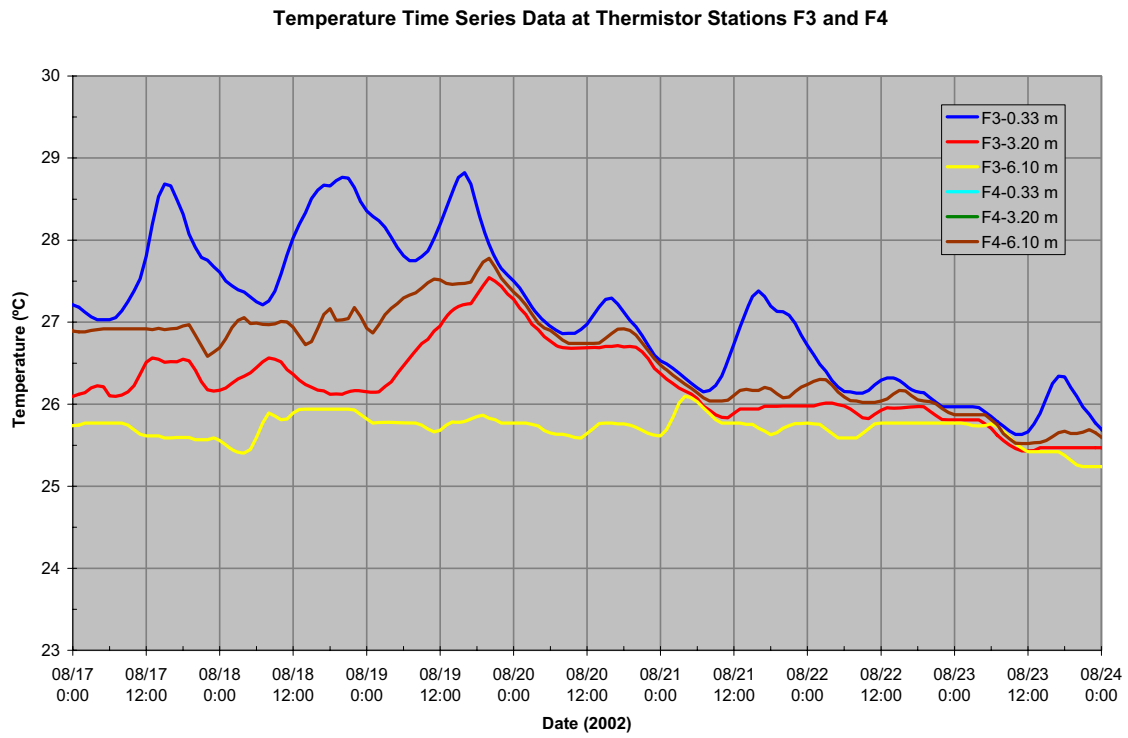


Figure A33. Temperature time series data for stations F3 and F4 from 8/17/02 to 8/23/02.

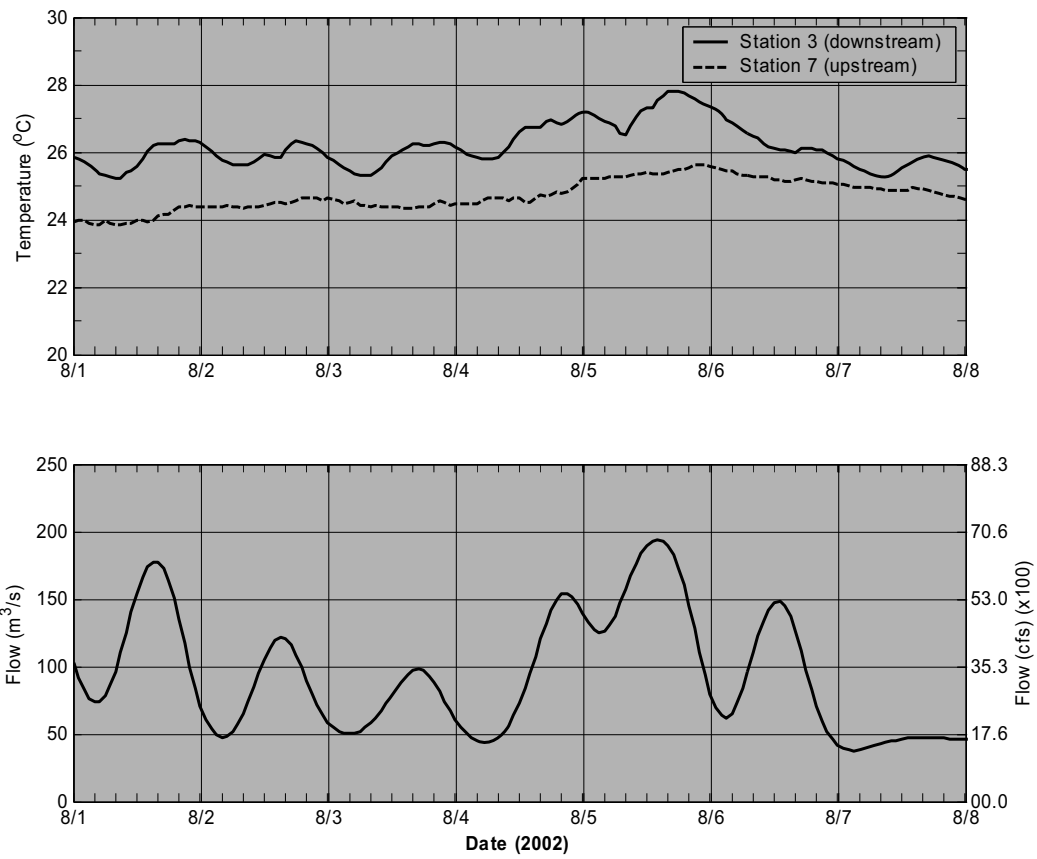


Figure A34. Upstream and downstream temperature and river flow measured at Vernon Dam.

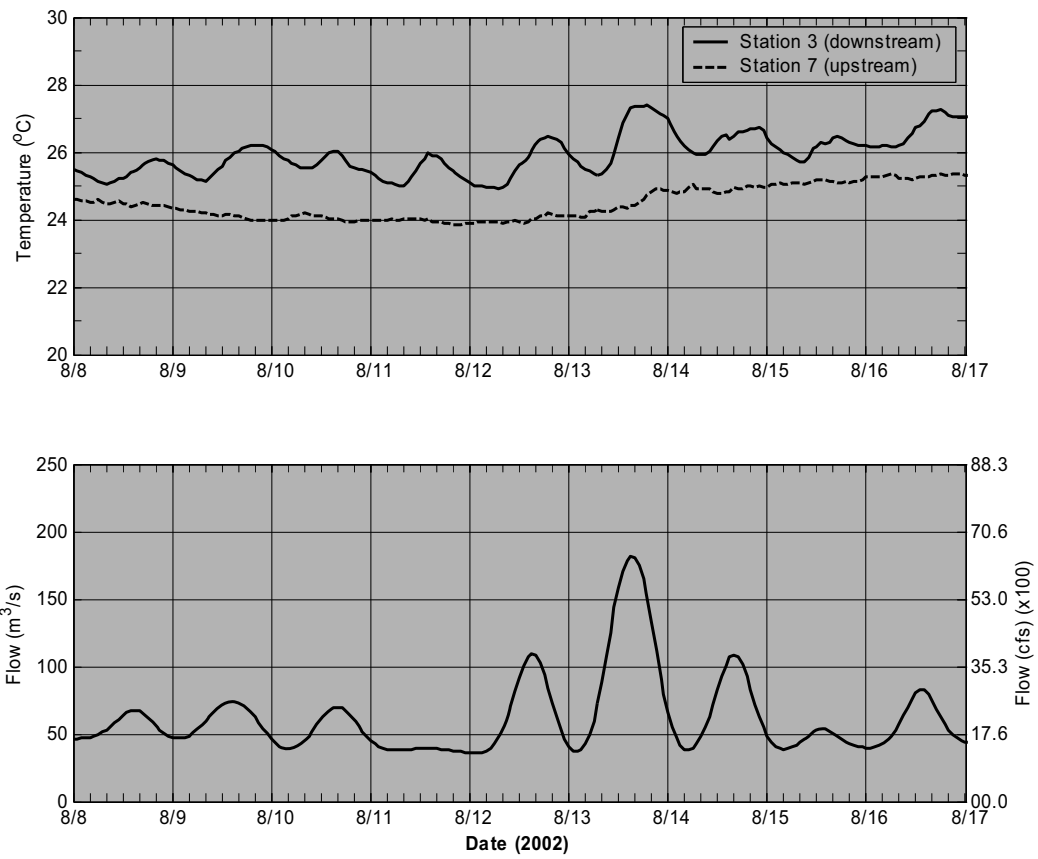


Figure A35. Upstream and downstream temperature and river flow measured at Vernon Dam.

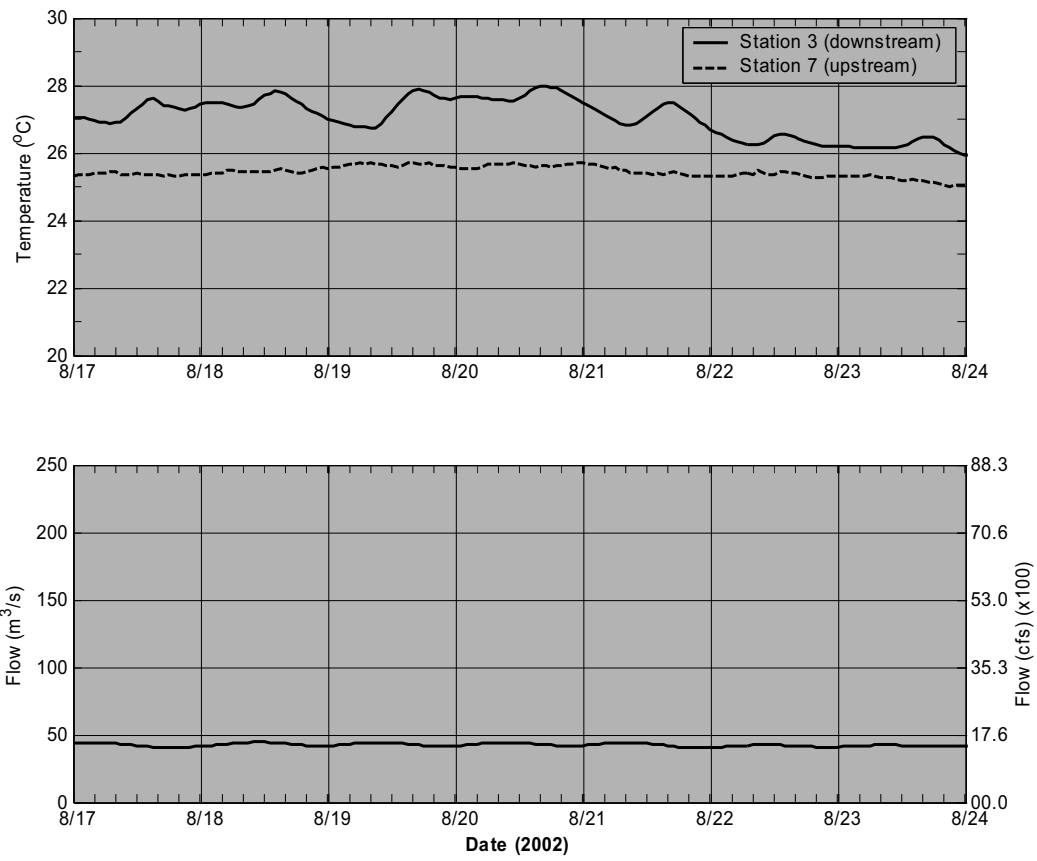


Figure A36. Upstream and downstream temperature and river flow measured at Vernon Dam.

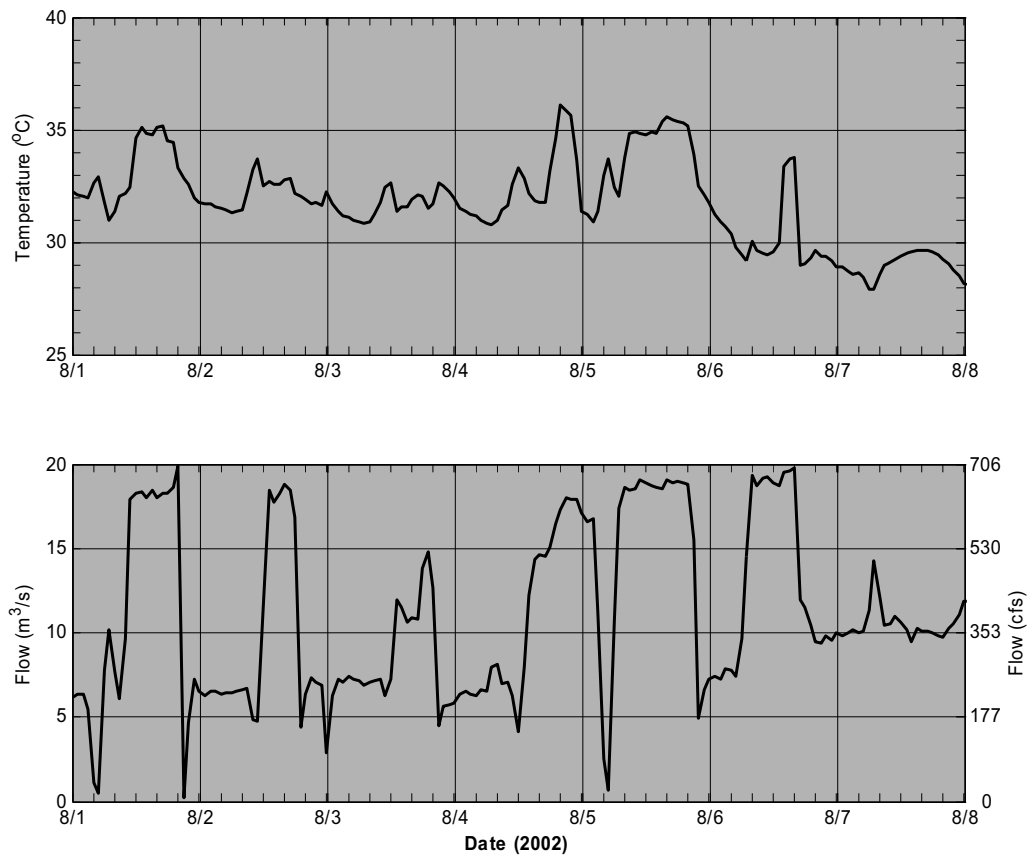


Figure A37. Water temperature and flow at the VYNPS discharge.

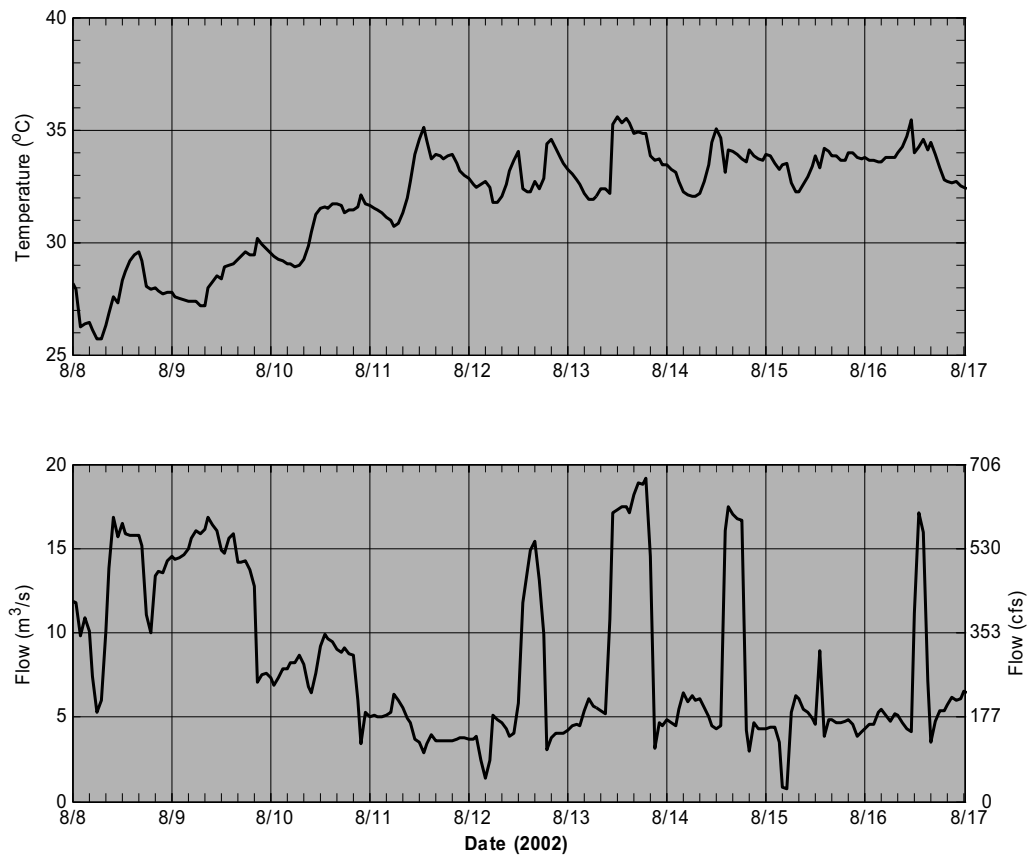


Figure A38. Water temperature and flow at the VYNPS discharge.

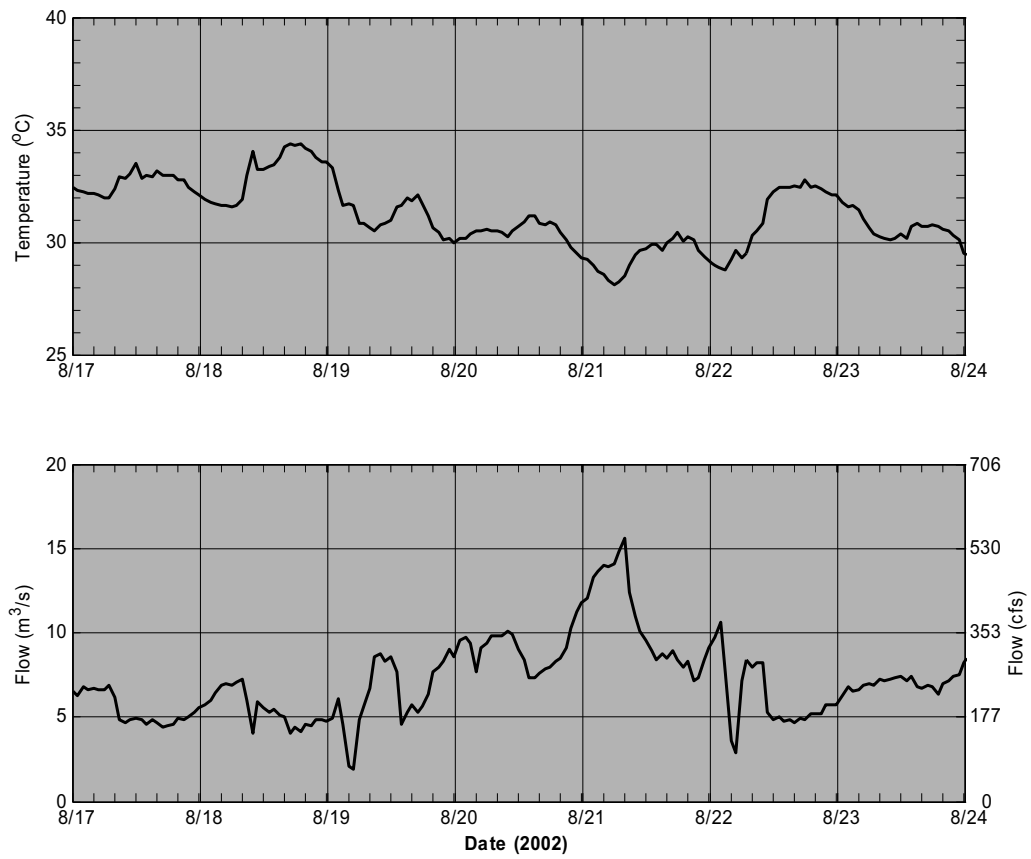


Figure A39. Water temperature and flow at the VYNPS discharge.

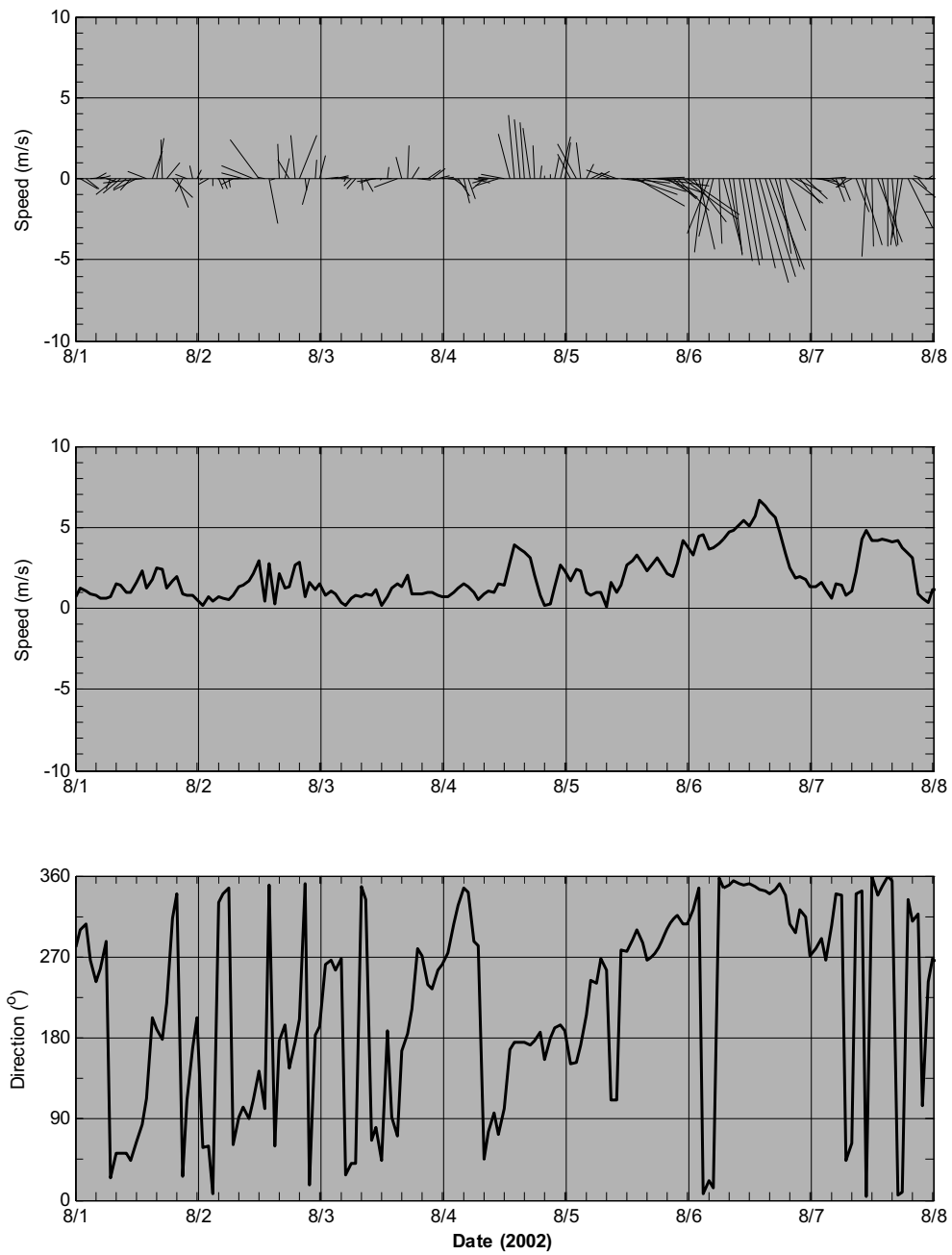


Figure A40. Wind stick plot and wind speed and direction as observed at the VYNPS. In the top figure, each stick points in the direction the wind is blowing to and stick length is proportional to wind speed. The bottom figure shows the direction the wind is blowing from relative to true north.

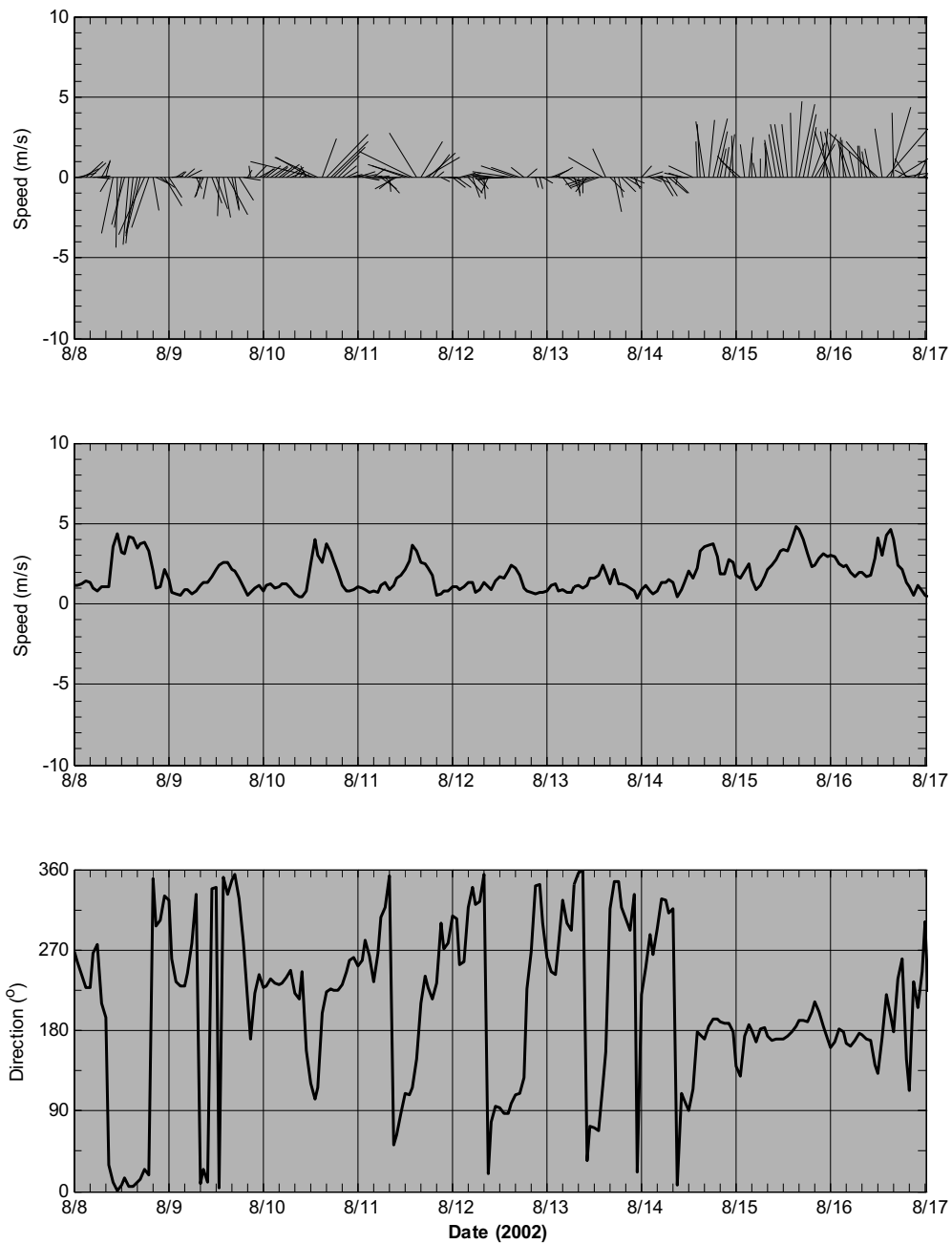


Figure A41. Wind stick plot and wind speed and direction as observed at the VYNPS. In the top figure, each stick points in the direction the wind is blowing to and stick length is proportional to wind speed. The bottom figure shows the direction the wind is blowing from relative to true north.

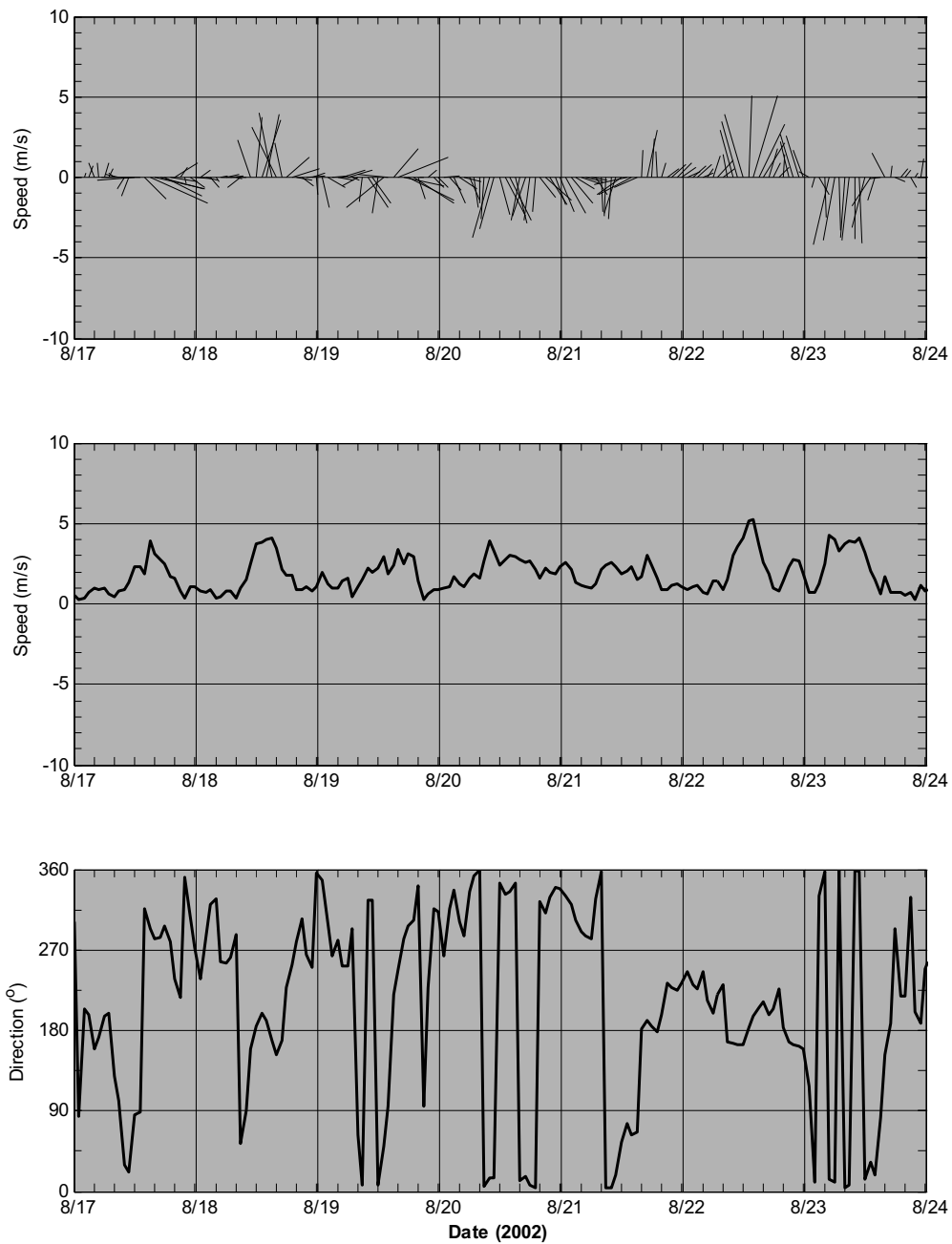


Figure A42. Wind stick plot and wind speed and direction as observed at the VYNPS. In the top figure, each stick points in the direction the wind is blowing to and stick length is proportional to wind speed. The bottom figure shows the direction the wind is blowing from relative to true north.

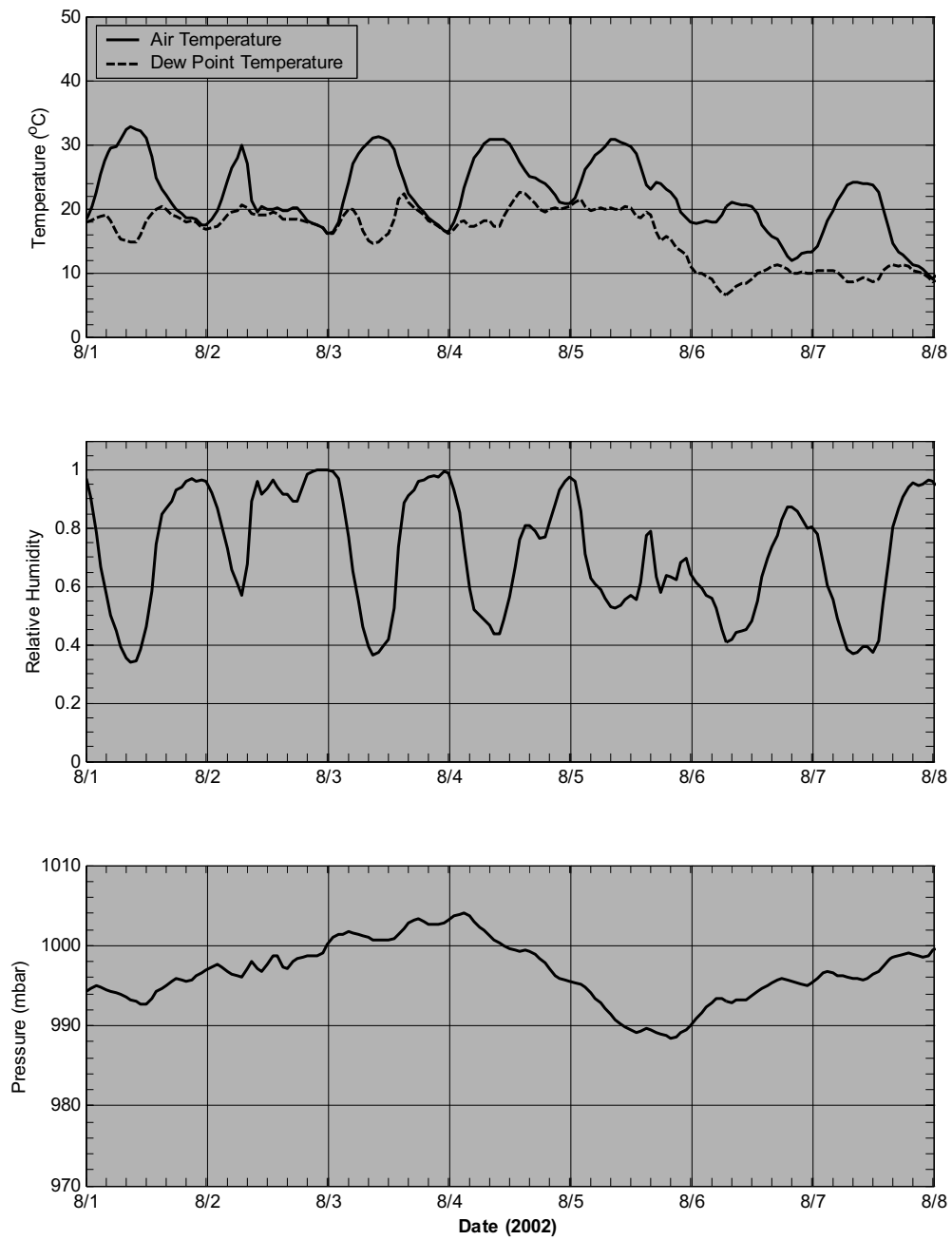


Figure A43. Air and dew point temperatures, relative humidity and atmospheric pressure as observed at Orange, MA.

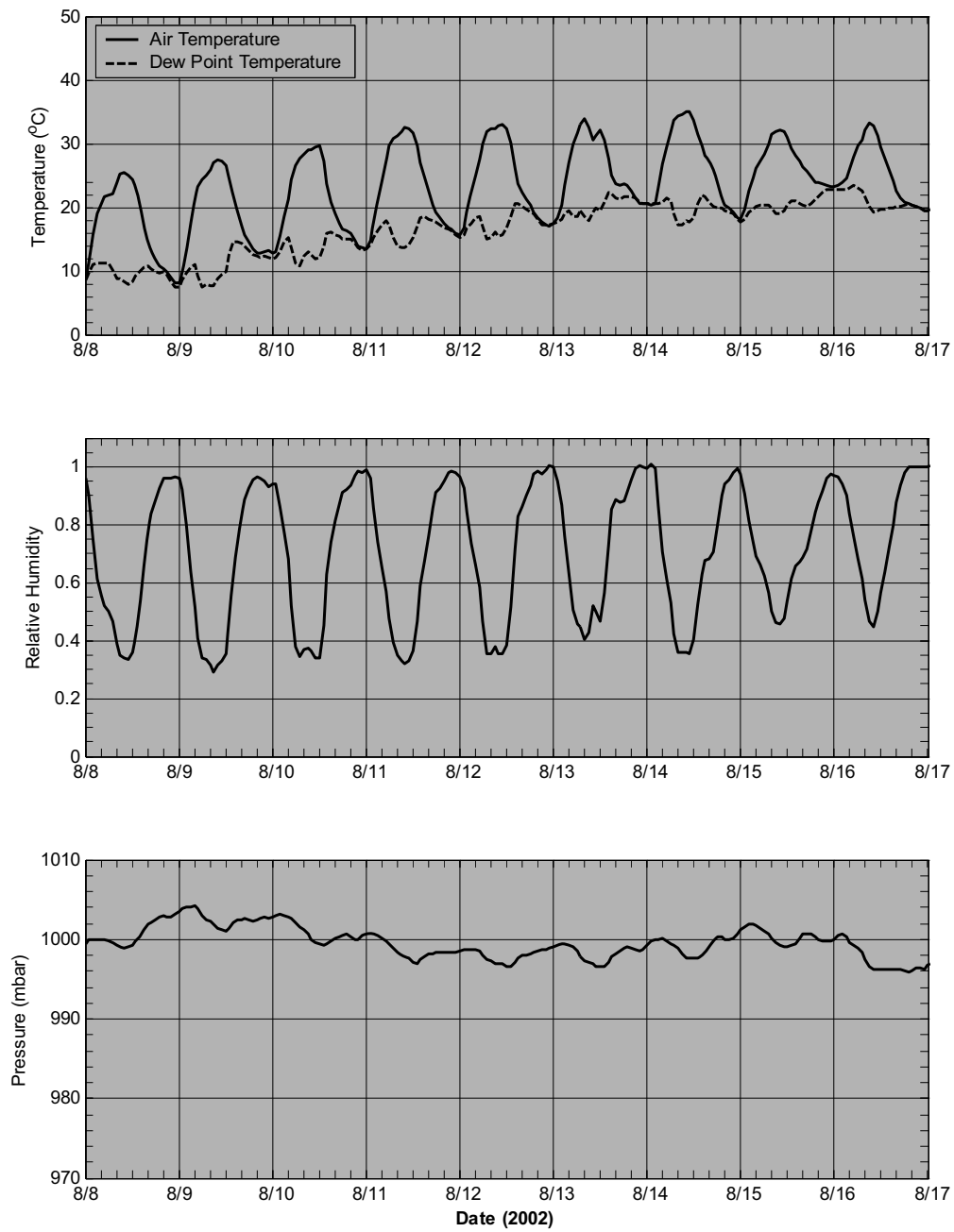


Figure A44. Air and dew point temperatures, relative humidity and atmospheric pressure as observed at Orange, MA.

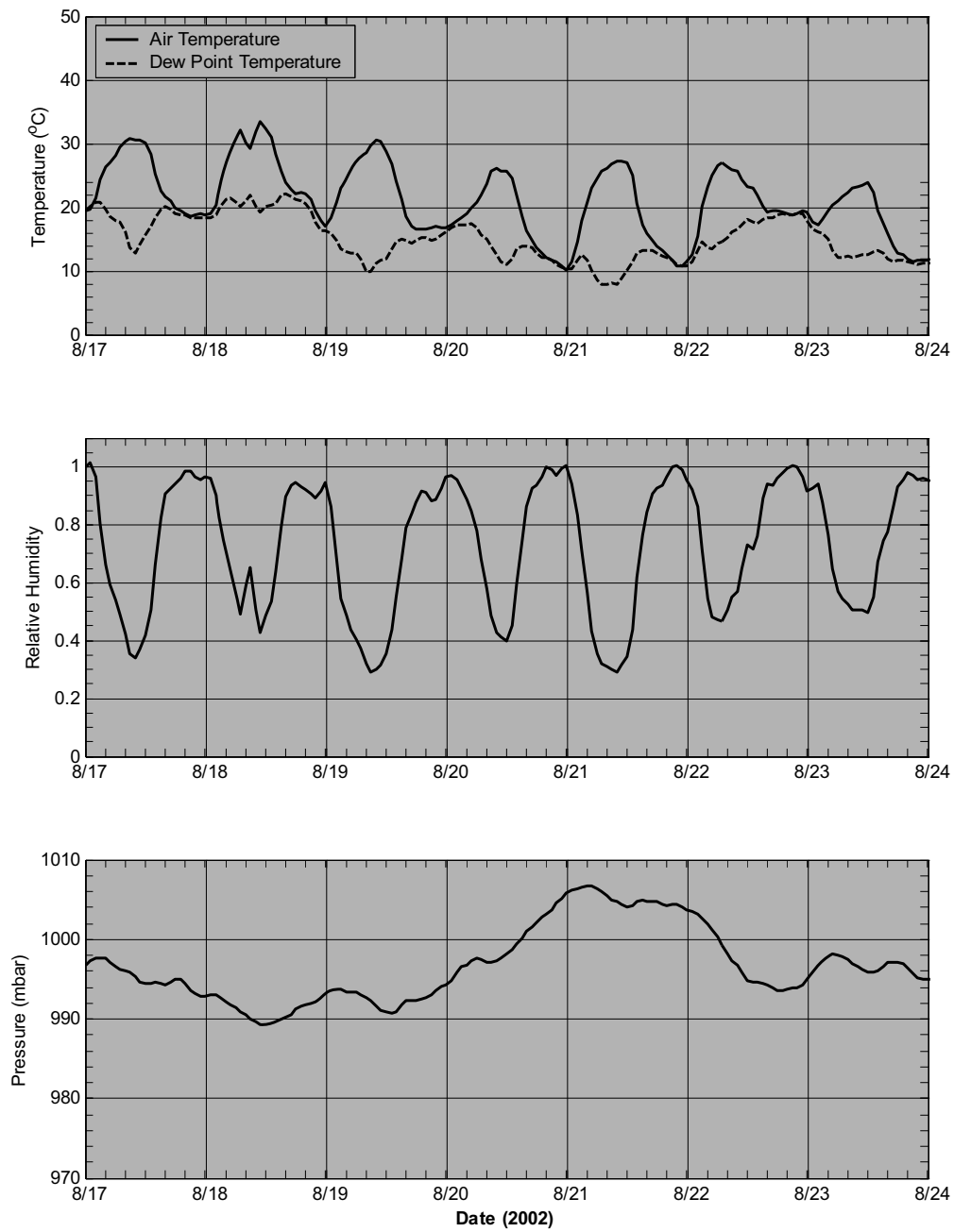


Figure A45. Air and dew point temperatures, relative humidity and atmospheric pressure as observed at Orange, MA.

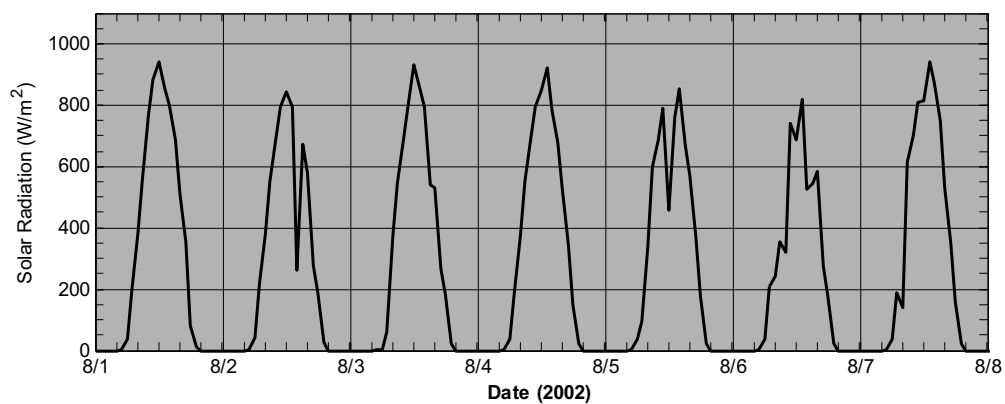


Figure A46. Solar radiation at Orange, MA.

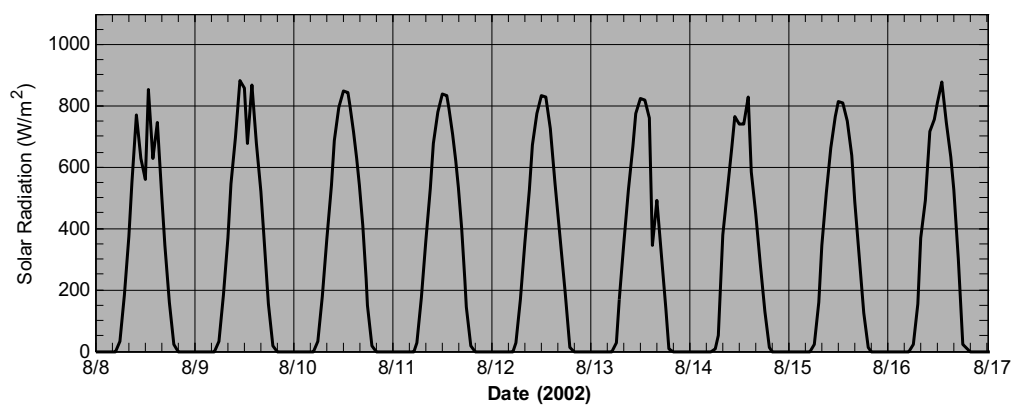


Figure A47. Solar radiation at Orange, MA.

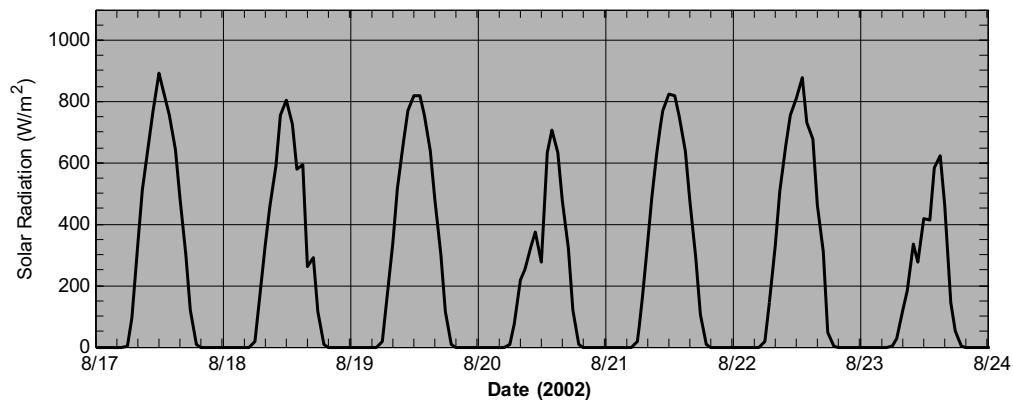


Figure A48. Solar radiation at Orange, MA.

Appendix B: June - July 2002 Data

List of Figures

Figure B1. Temperature time series data for stations C1 and C2 from 6/25/02 to 7/01/02.	1
Figure B2. Temperature time series data for stations C1 and C2 from 7/02/02 to 7/08/02.	1
Figure B3. Temperature time series data for stations C3 and C4 from 6/25/02 to 7/01/02.	2
Figure B4. Temperature time series data for stations C3 and C4 from 7/02/02 to 7/08/02.	2
Figure B5. Temperature time series data for stations C5 and C6 from 6/25/02 to 7/01/02	3
Figure B6. Temperature time series data for stations C5 and C6 from 7/02/02 to 7/08/02.	3
Figure B7. Temperature time series data for stations D1 and D2 from 6/25/02 to 7/01/02.	4
Figure B8. Temperature time series data for stations D1 and D2 from 7/02/02 to 7/08/02.	4
Figure B9. Temperature time series data for stations D3 and D4 from 6/25/02 to 7/01/02.	5
Figure B10. Temperature time series data for stations D3 and D4 from 7/02/02 to 7/08/02.	5
Figure B11. Temperature time series data for stations D5 and D6 from 6/25/02 to 7/01/02.	6
Figure B12. Temperature time series data for stations D5 and D6 from 7/02/02 to 7/08/02.	6
Figure B13. Temperature time series data for stations E1 and E2 from 6/25/02 to 7/01/02.	7
Figure B14. Temperature time series data for stations E1 and E2 from 7/02/02 to 7/08/02.	7
Figure B15. Temperature time series data for stations E3 and E4 from 6/25/02 to 7/01/02.	8
Figure B16. Temperature time series data for stations E3 and E4 from 7/02/02 to 7/08/02.	8
Figure B17. Temperature time series data for stations E5 and E6 from 6/25/02 to 7/01/02.	9
Figure B18. Temperature time series data for stations E5 and E6 from 7/02/02 to 7/08/02.	9
Figure B19. Temperature time series data for stations F1 and F2 from 6/25/02 to 7/01/02.	10
Figure B20. Temperature time series data for stations F1 and F2 from 7/02/02 to 7/08/02.	10
Figure B21. Temperature time series data for stations F3 and F4 from 6/25/02 to 7/01/02.	11
Figure B22. Temperature time series data for stations F3 and F4 from 7/02/02 to 7/08/02.	11

Figure B23. Upstream and downstream temperature and river flow measured at Vernon Dam.....	12
Figure B24. Upstream and downstream temperature and river flow measured at Vernon Dam.....	13
Figure B25. Water temperature and flow at the VYNPS discharge.	14
Figure B26. Water temperature and flow at the VYNPS discharge.	15
Figure B27. Water temperature recorded at the Fishway.	16
Figure B28. Water temperature recorded at the Fishway.	16
Figure B29. Wind stick plot and wind speed and direction as observed at the VYNPS. In the top figure, each stick points in the direction the wind is blowing to and stick length is proportional to wind speed. The bottom figure shows the direction the wind is blowing from relative to true north.	17
Figure B30. Wind stick plot and wind speed and direction as observed at the VYNPS. In the top figure, each stick points in the direction the wind is blowing to and stick length is proportional to wind speed. The bottom figure shows the direction the wind is blowing from relative to true north.	18
Figure B31. Air and dew point temperatures, relative humidity and atmospheric pressure as observed at Orange, MA.....	19
Figure B32. Air and dew point temperatures, relative humidity and atmospheric pressure as observed at Orange, MA.....	20
Figure B33. Solar radiation at Orange, MA.....	21
Figure B34. Solar radiation at Orange, MA.....	21

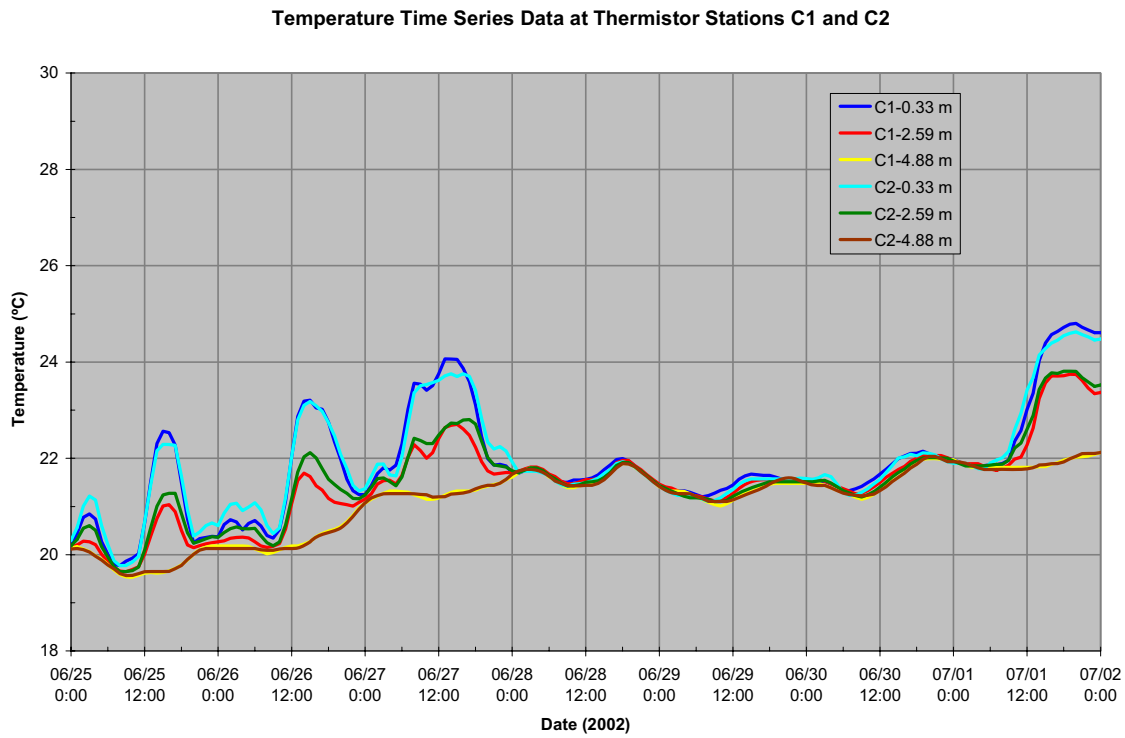


Figure B1. Temperature time series data for stations C1 and C2 from 6/25/02 to 7/01/02.

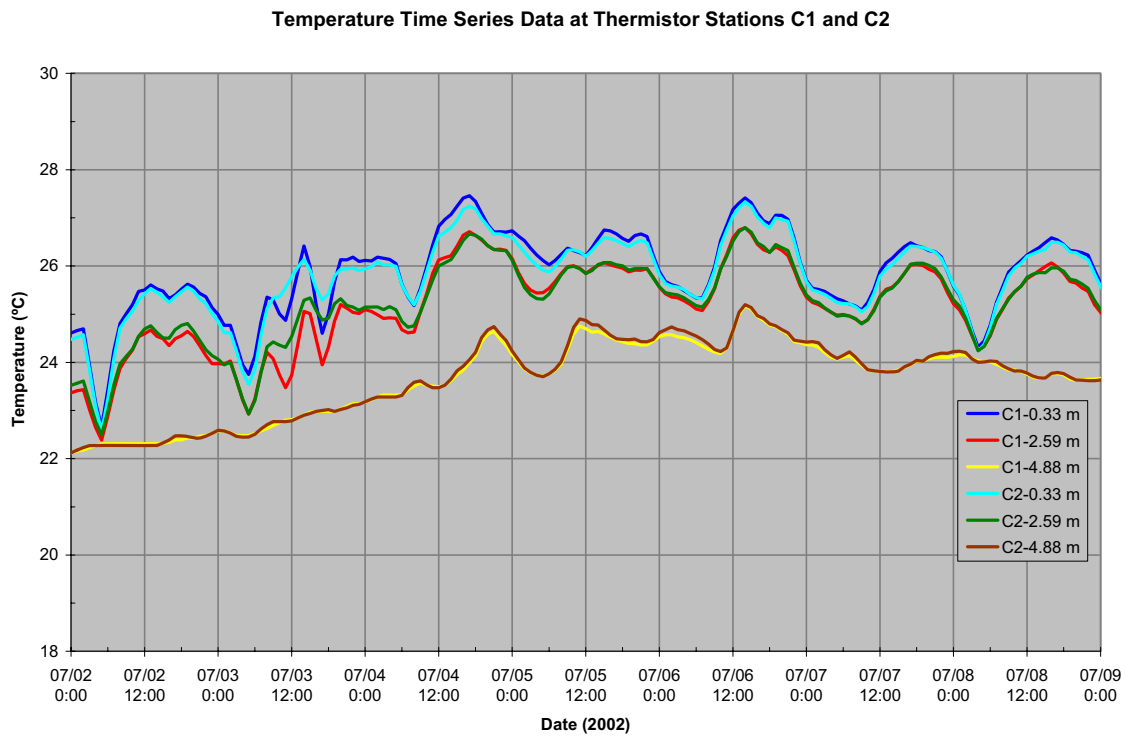


Figure B2. Temperature time series data for stations C1 and C2 from 7/02/02 to 7/08/02.

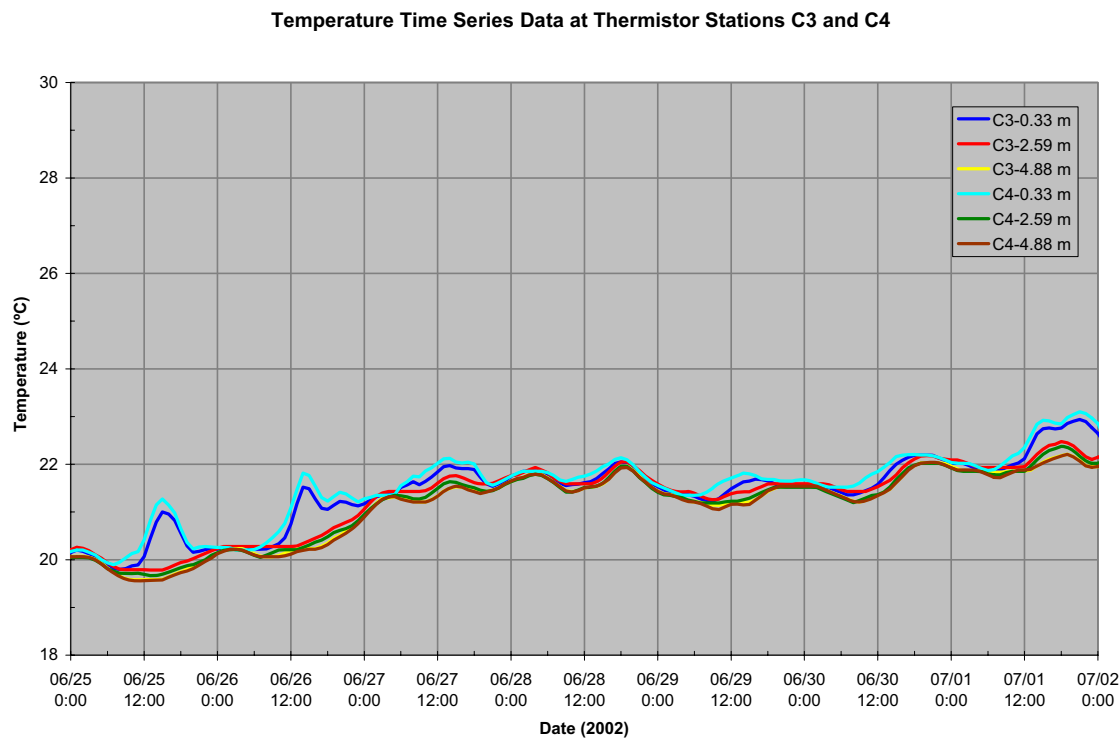


Figure B3. Temperature time series data for stations C3 and C4 from 6/25/02 to 7/01/02.

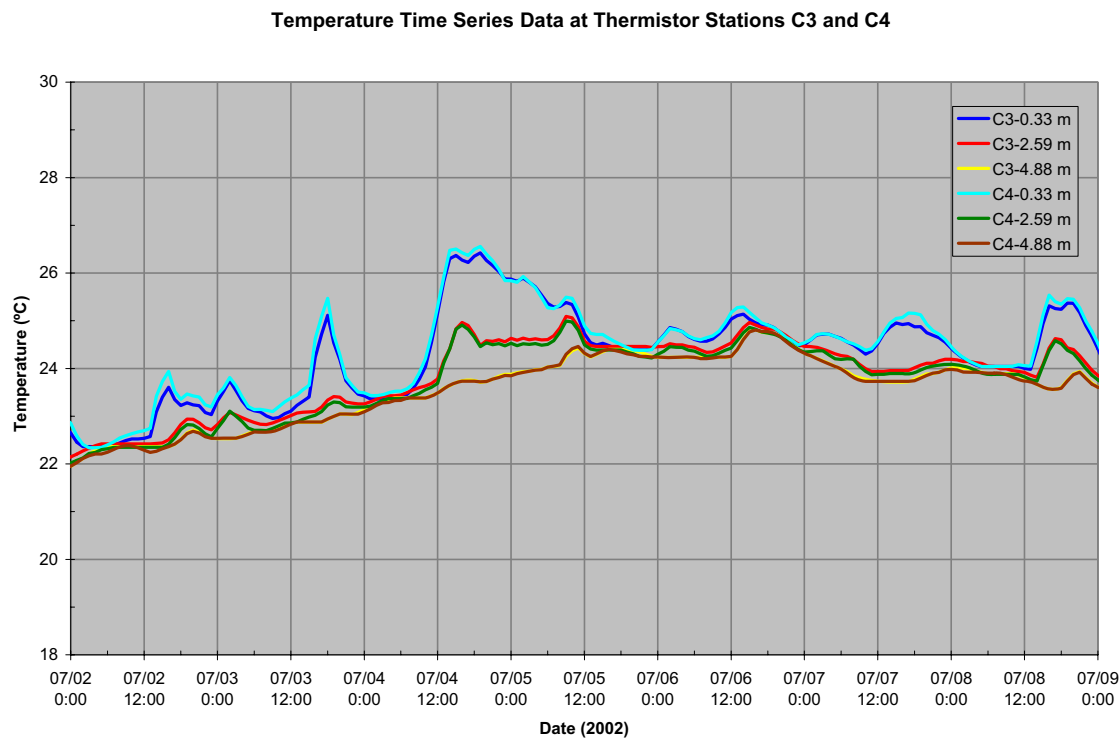


Figure B4. Temperature time series data for stations C3 and C4 from 7/02/02 to 7/08/02.

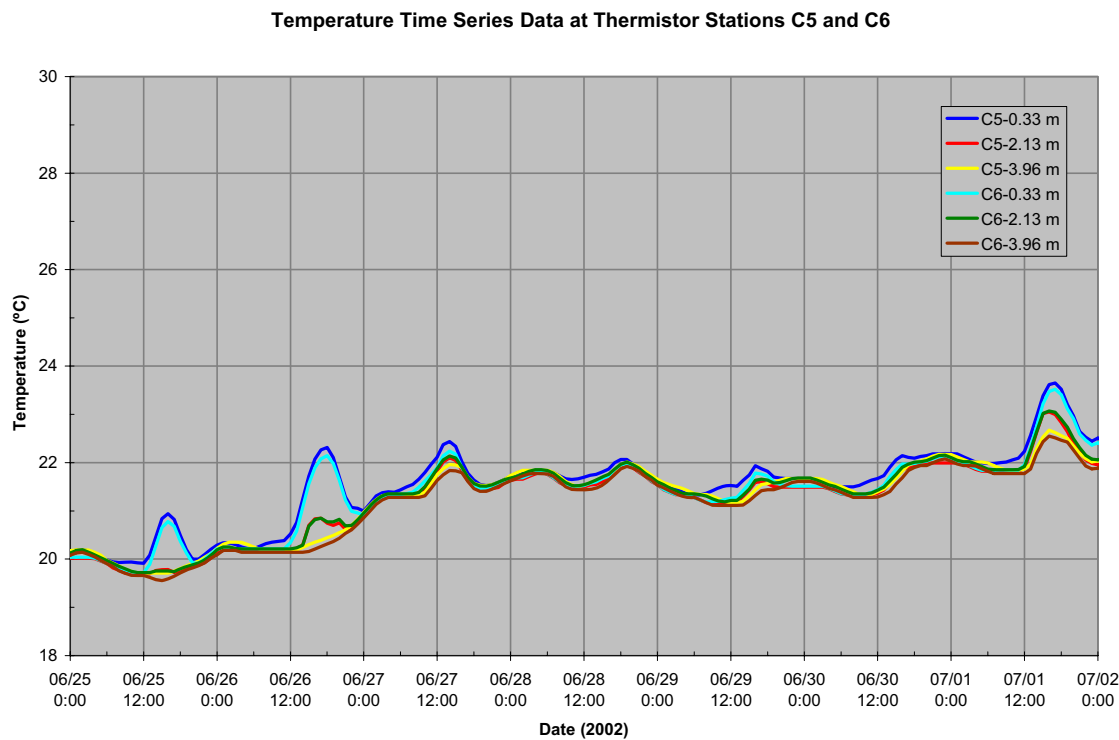


Figure B5. Temperature time series data for stations C5 and C6 from 6/25/02 to 7/01/02

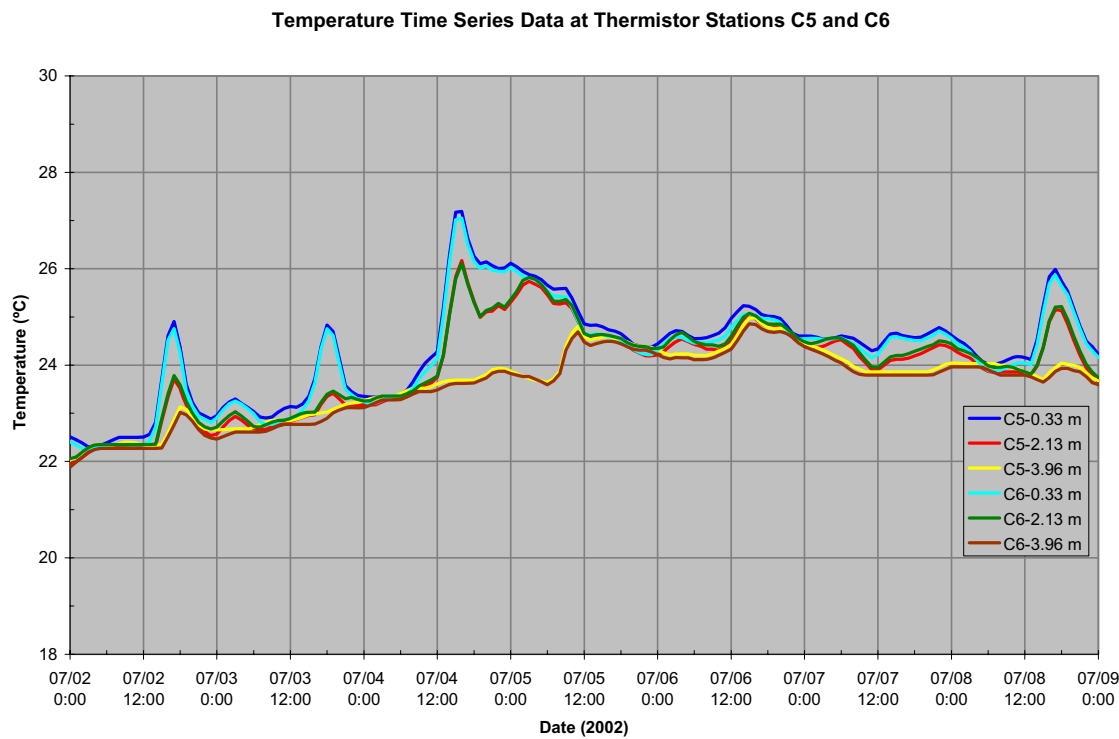


Figure B6. Temperature time series data for stations C5 and C6 from 7/02/02 to 7/08/02.

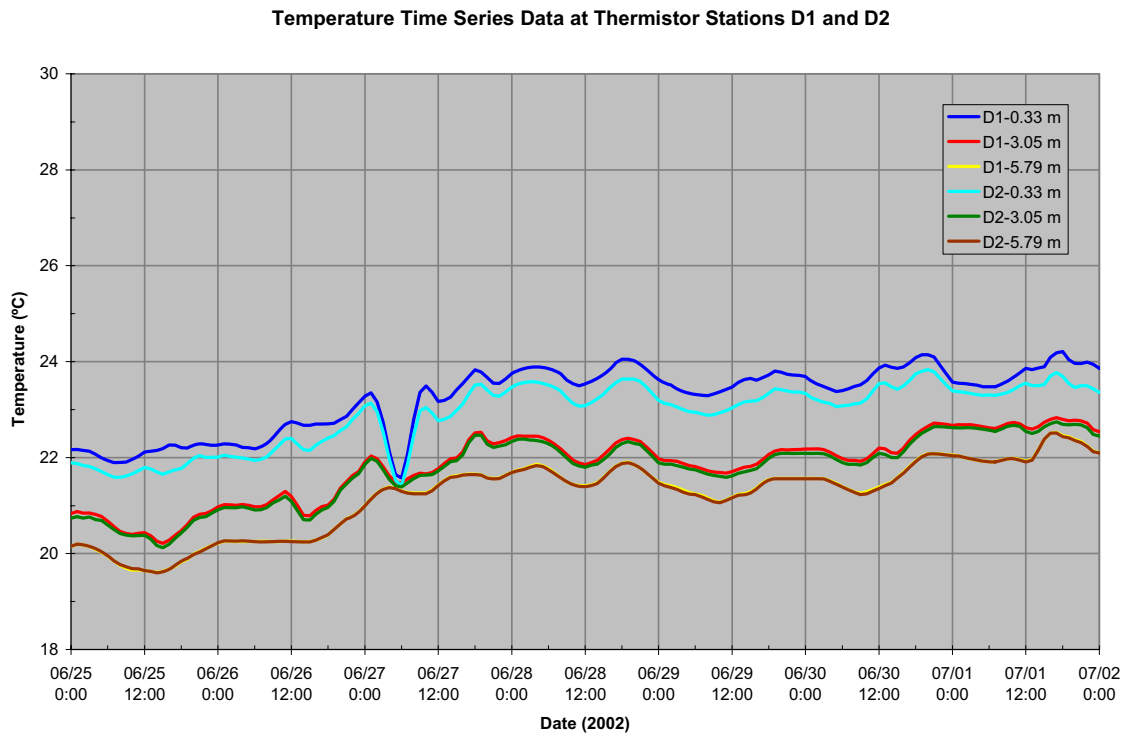


Figure B7. Temperature time series data for stations D1 and D2 from 6/25/02 to 7/01/02.

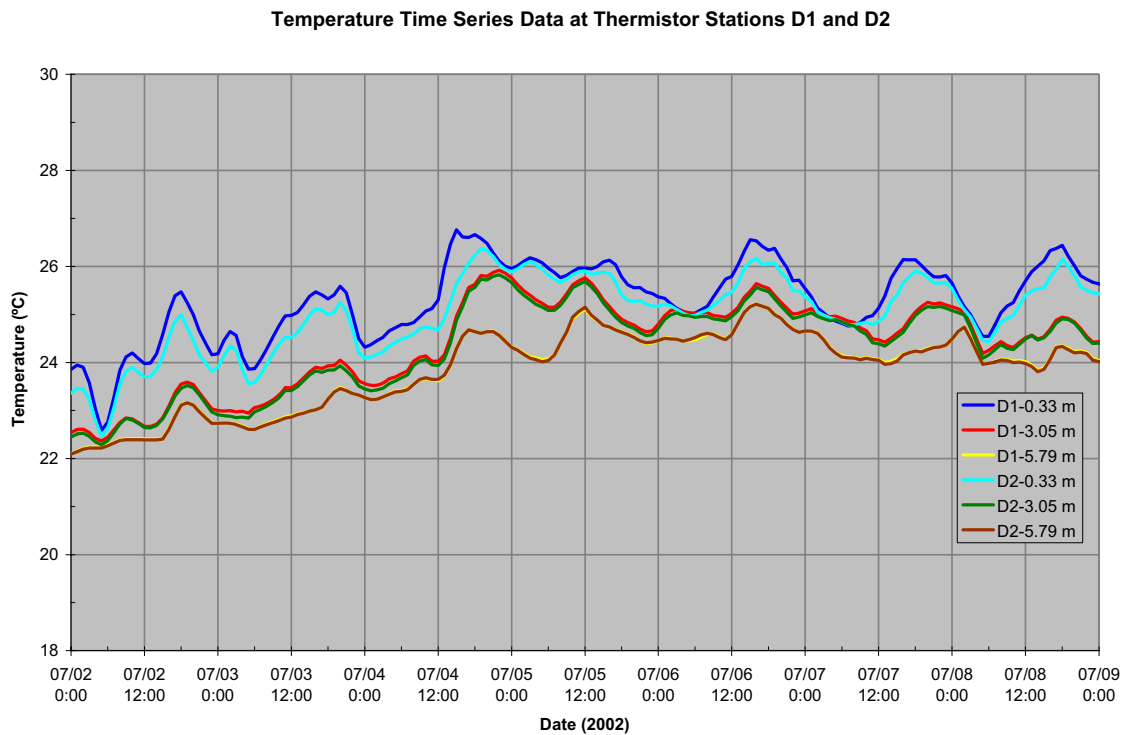


Figure B8. Temperature time series data for stations D1 and D2 from 7/02/02 to 7/08/02.

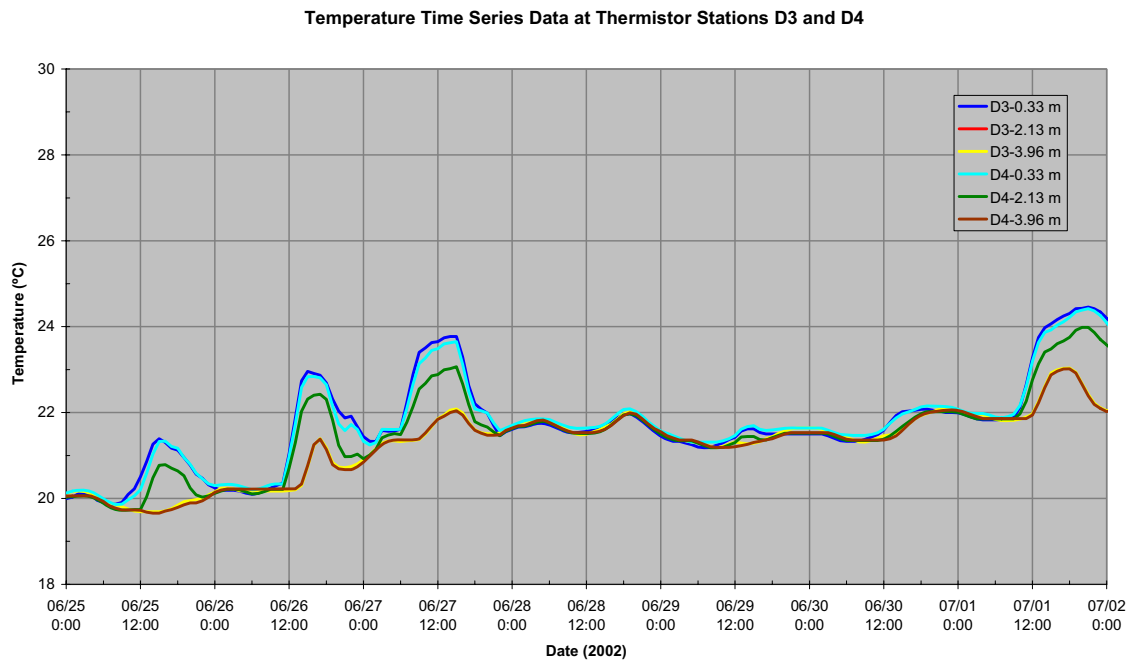


Figure B9. Temperature time series data for stations D3 and D4 from 6/25/02 to 7/01/02.

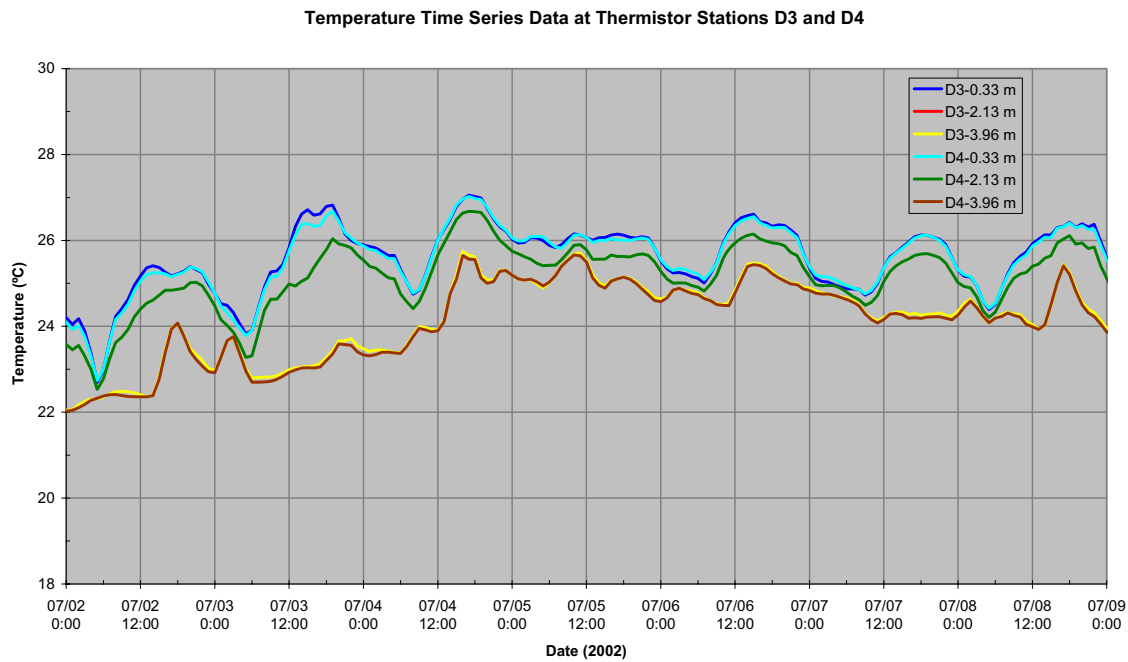


Figure B10. Temperature time series data for stations D3 and D4 from 7/02/02 to 7/08/02.

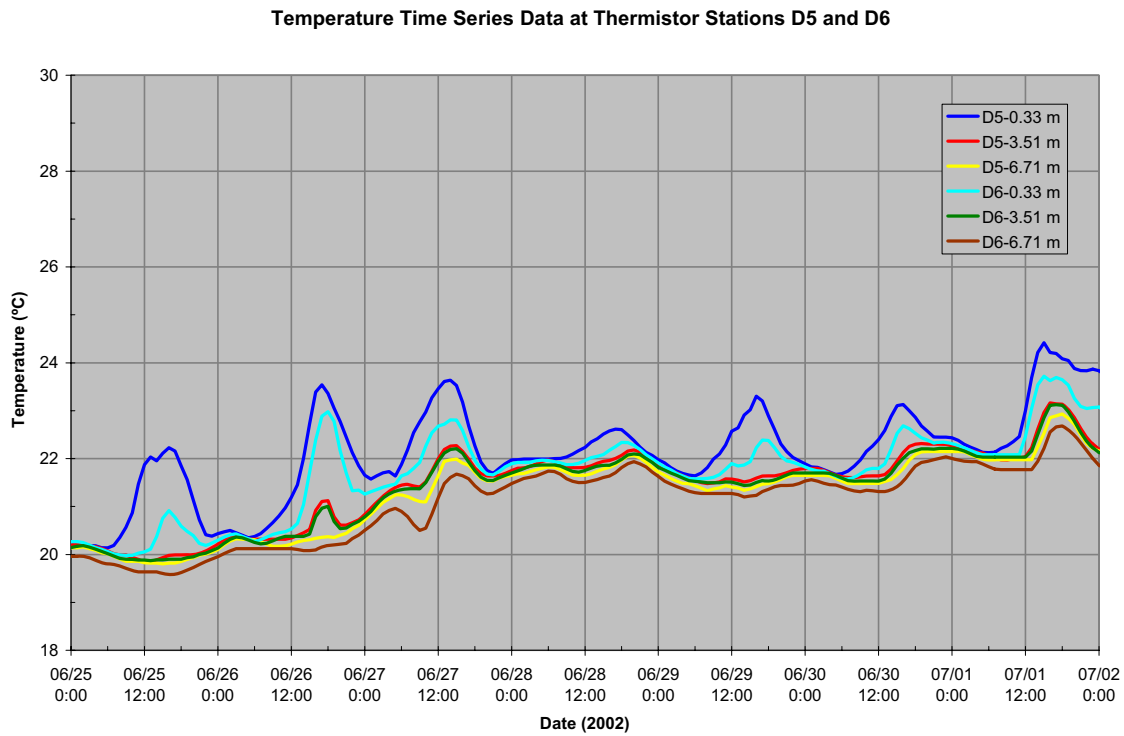


Figure B11. Temperature time series data for stations D5 and D6 from 6/25/02 to 7/01/02.

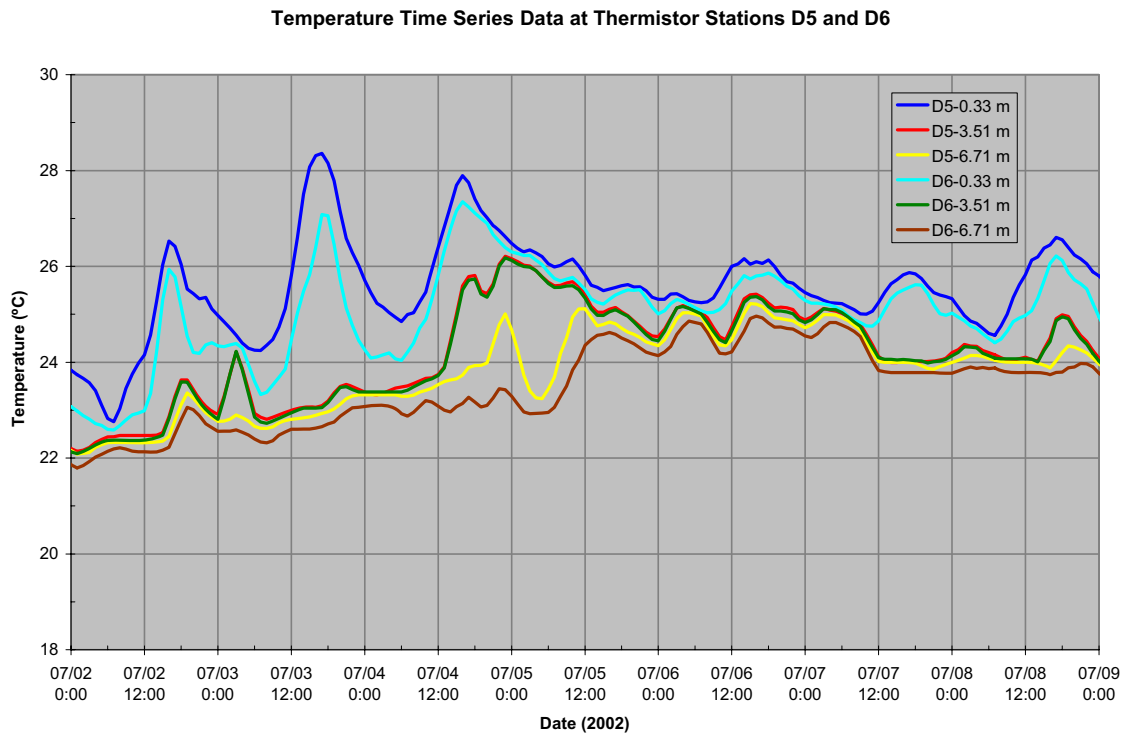


Figure B12. Temperature time series data for stations D5 and D6 from 7/02/02 to 7/08/02.

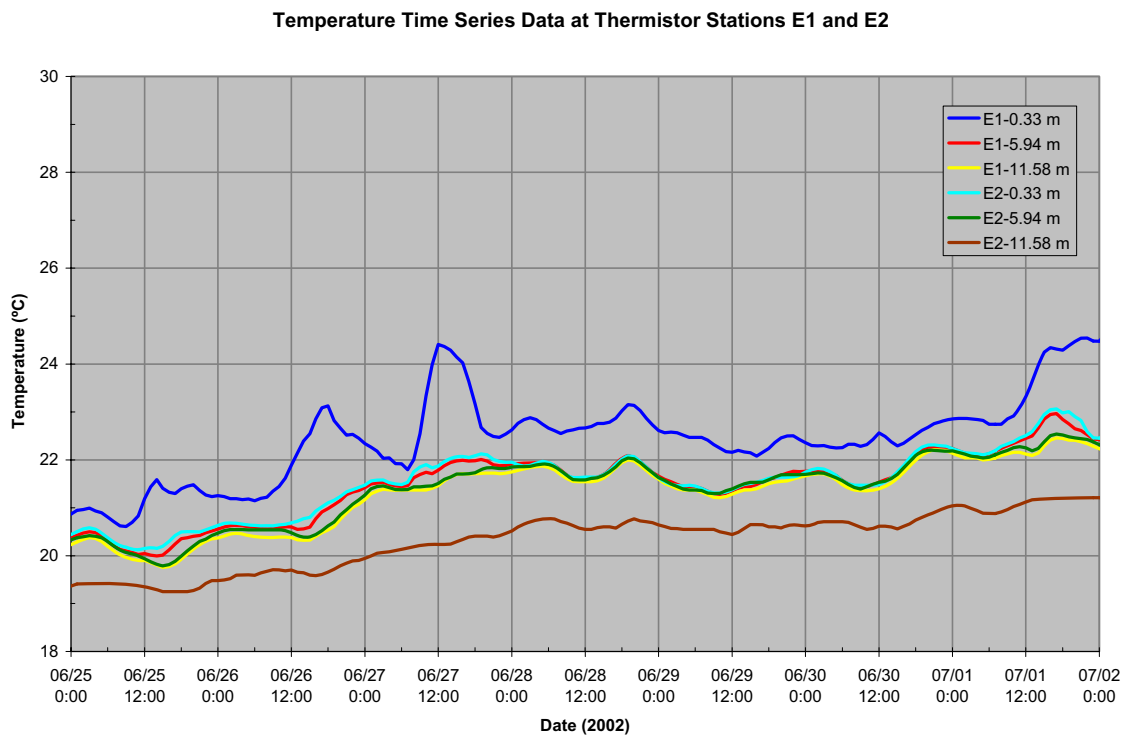


Figure B13. Temperature time series data for stations E1 and E2 from 6/25/02 to 7/01/02.

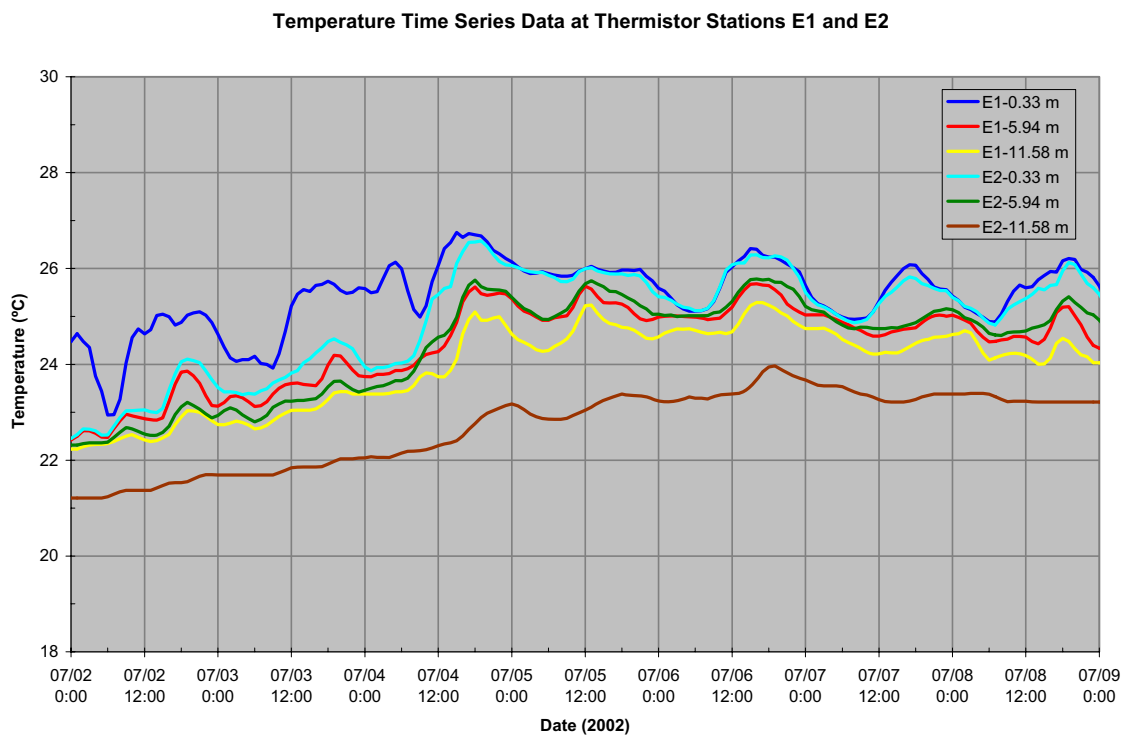


Figure B14. Temperature time series data for stations E1 and E2 from 7/02/02 to 7/08/02.

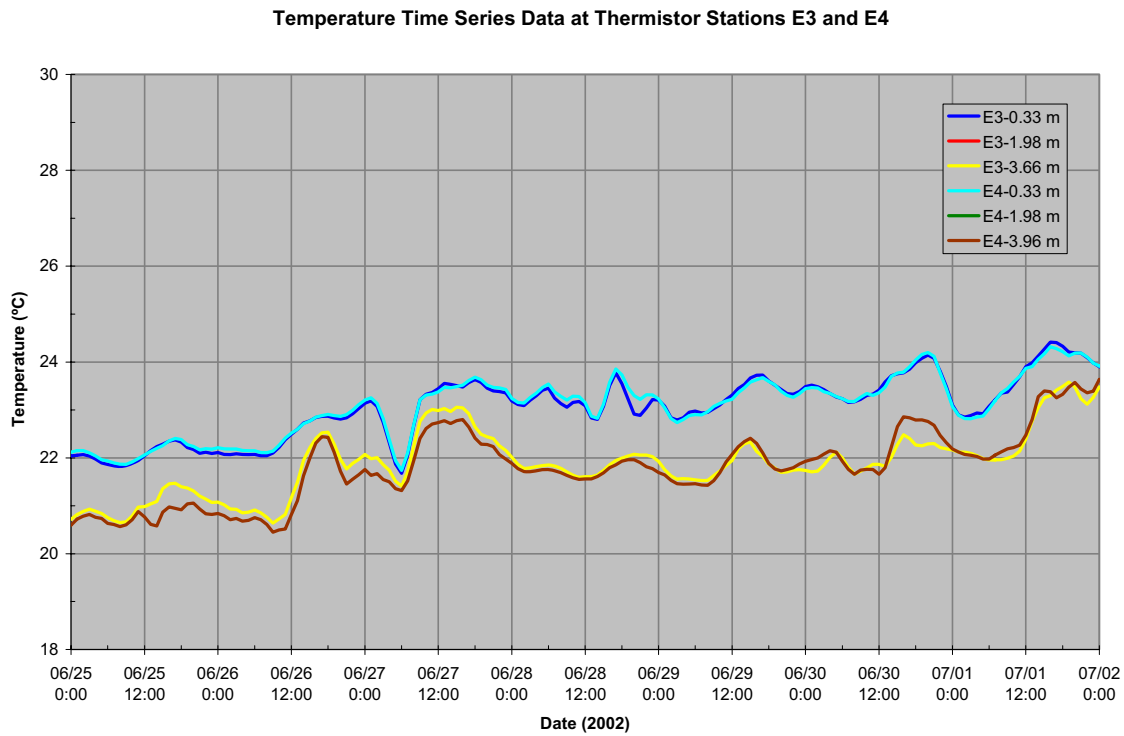


Figure B15. Temperature time series data for stations E3 and E4 from 6/25/02 to 7/01/02.

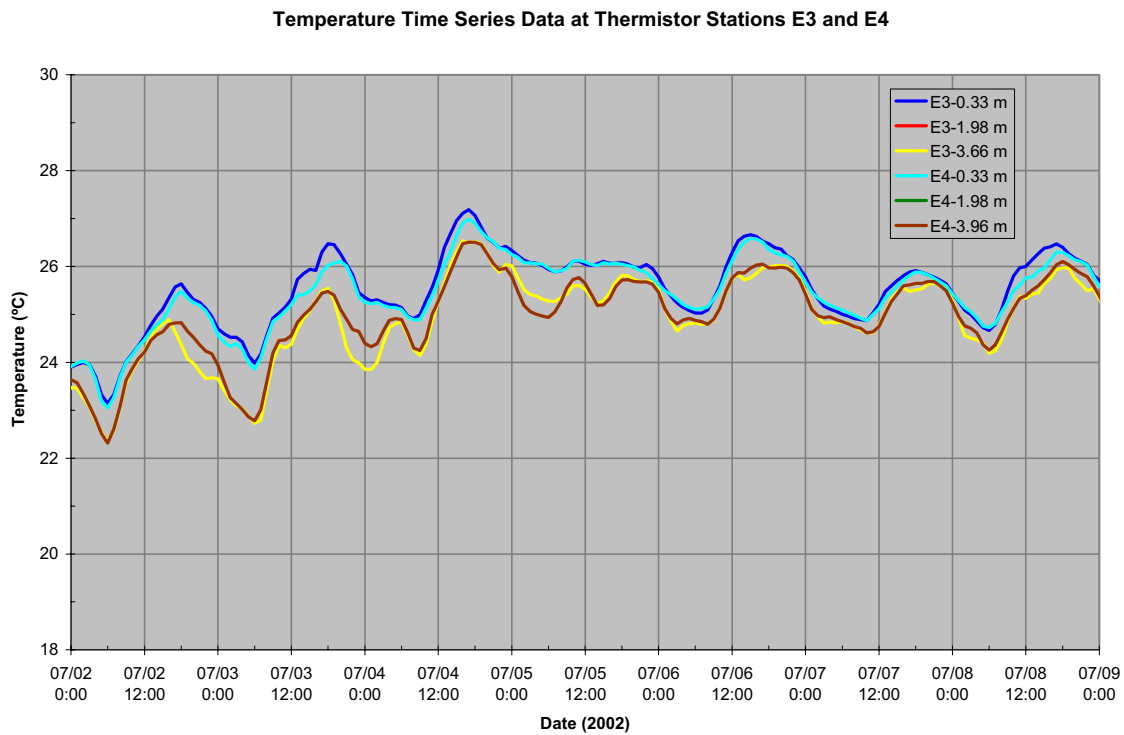


Figure B16. Temperature time series data for stations E3 and E4 from 7/02/02 to 7/08/02.

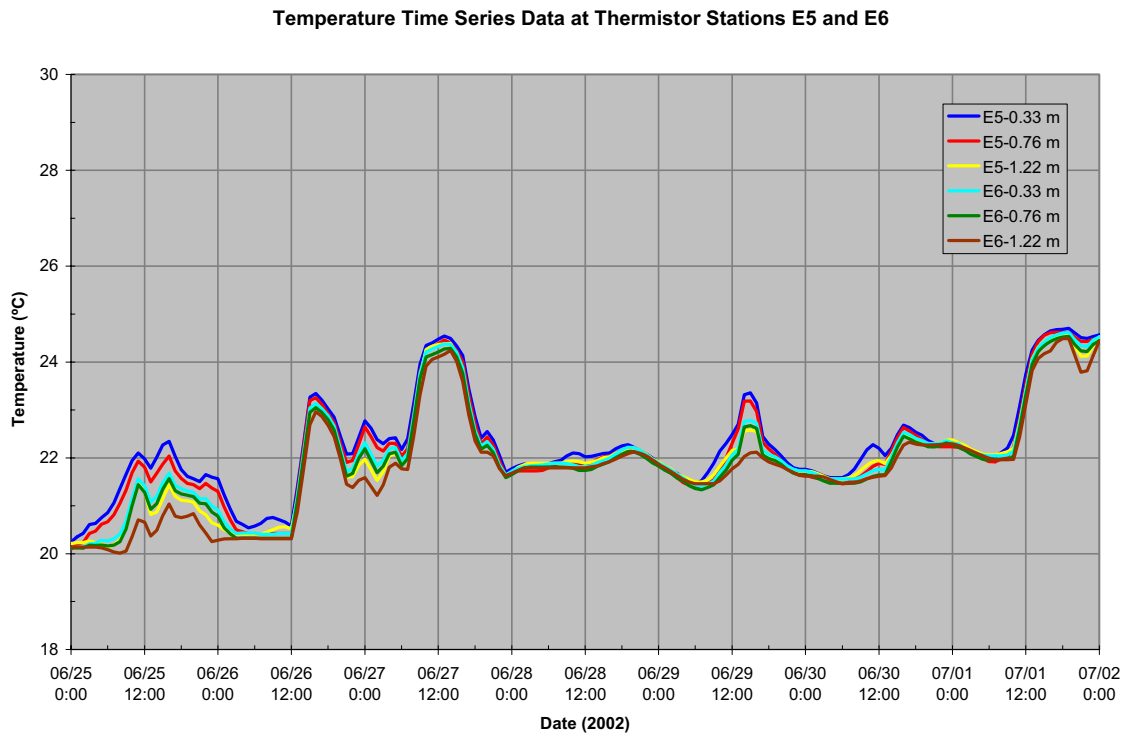


Figure B17. Temperature time series data for stations E5 and E6 from 6/25/02 to 7/01/02.

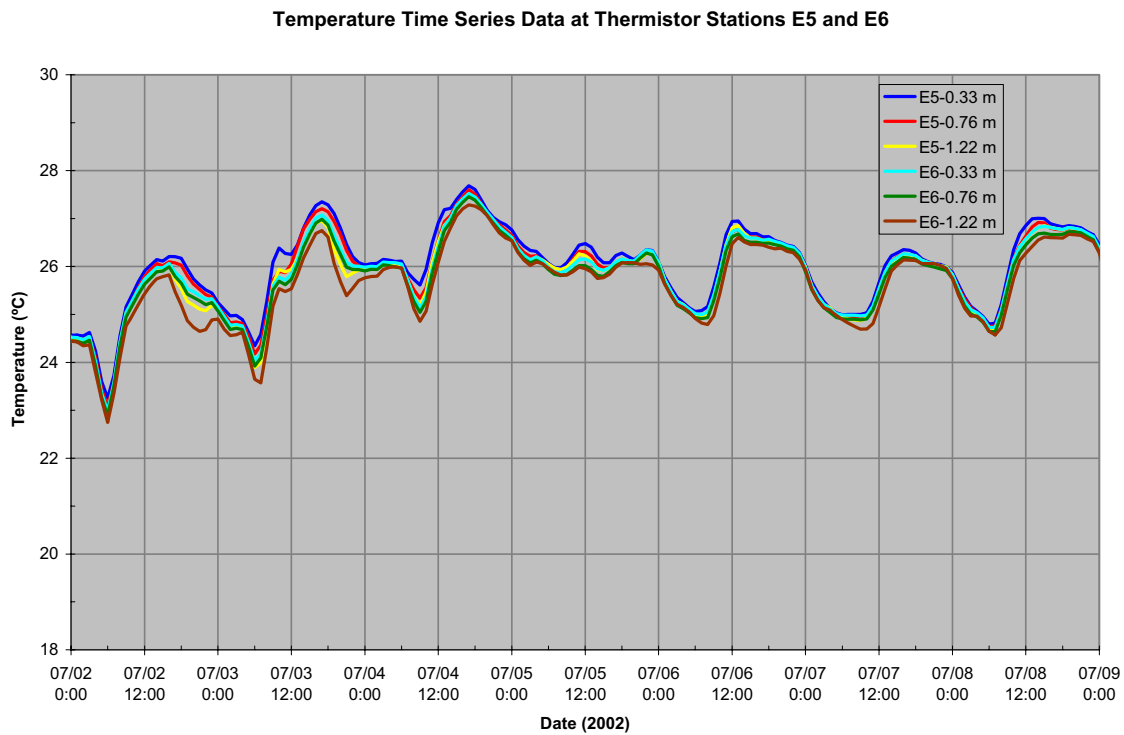


Figure B18. Temperature time series data for stations E5 and E6 from 7/02/02 to 7/08/02.

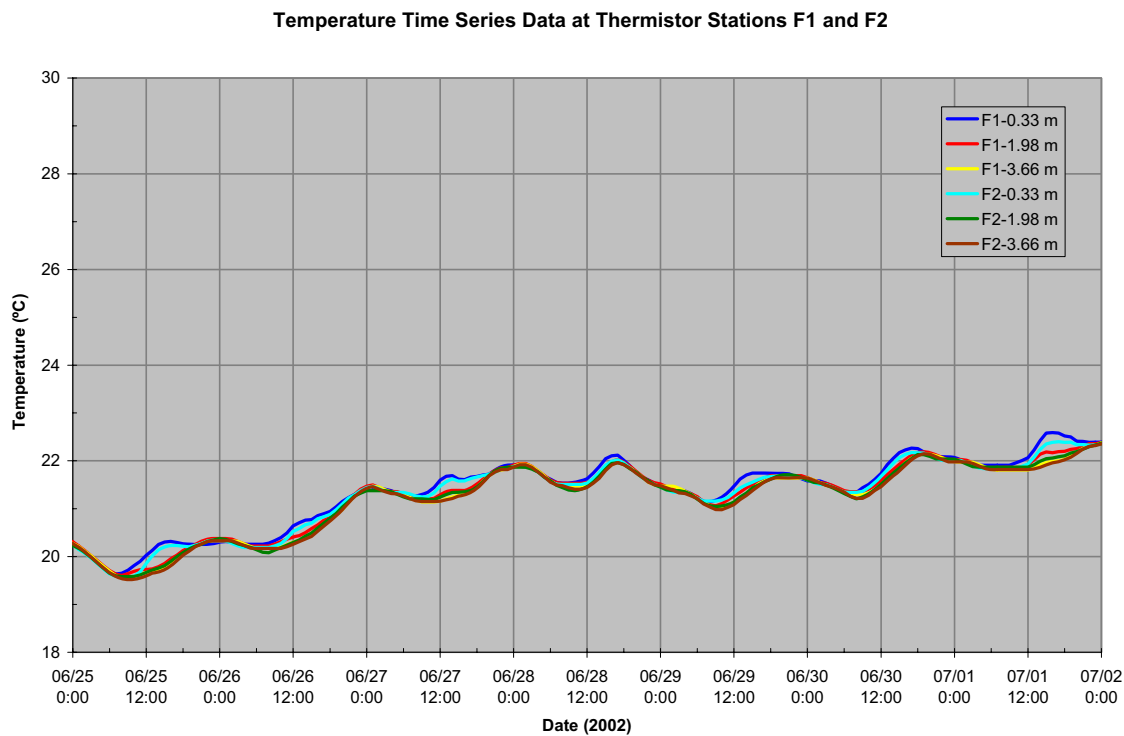


Figure B19. Temperature time series data for stations F1 and F2 from 6/25/02 to 7/01/02.

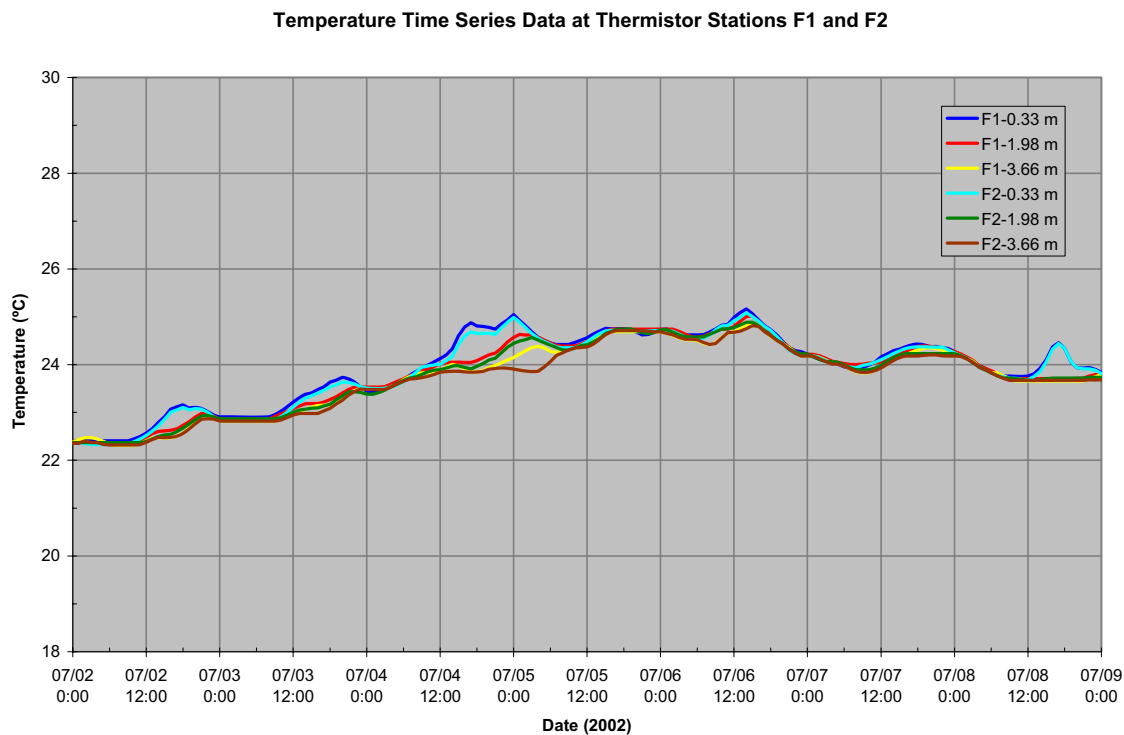


Figure B20. Temperature time series data for stations F1 and F2 from 7/02/02 to 7/08/02.

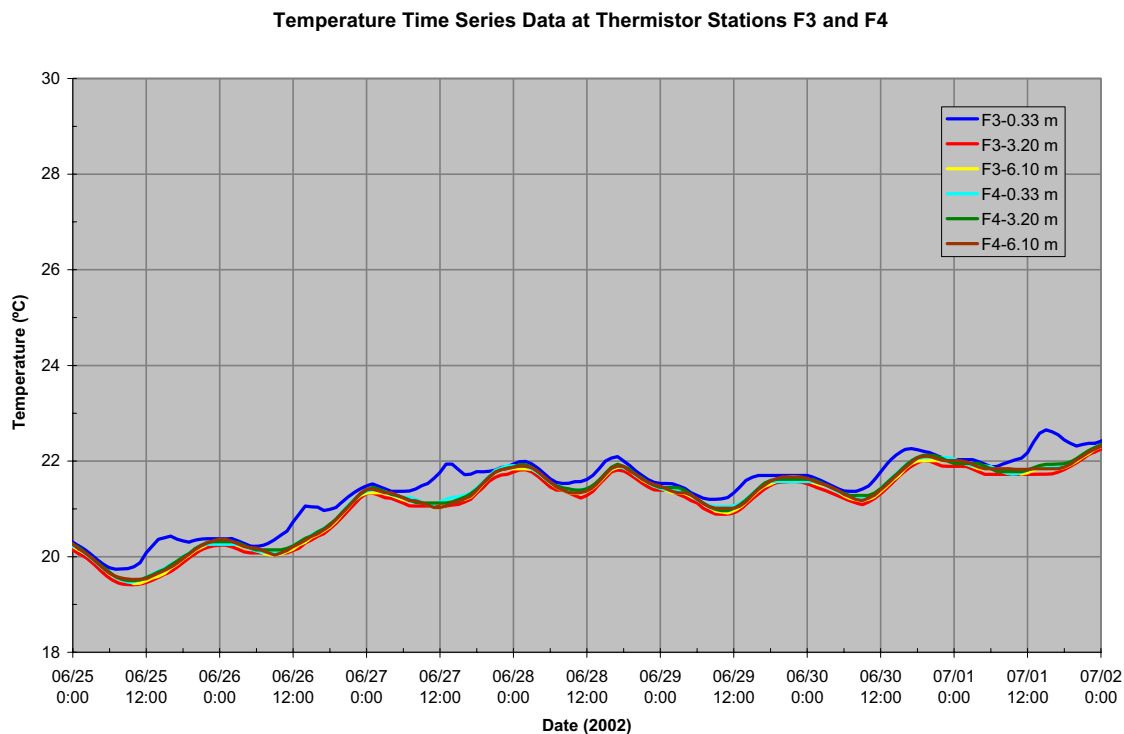


Figure B21. Temperature time series data for stations F3 and F4 from 6/25/02 to 7/01/02.

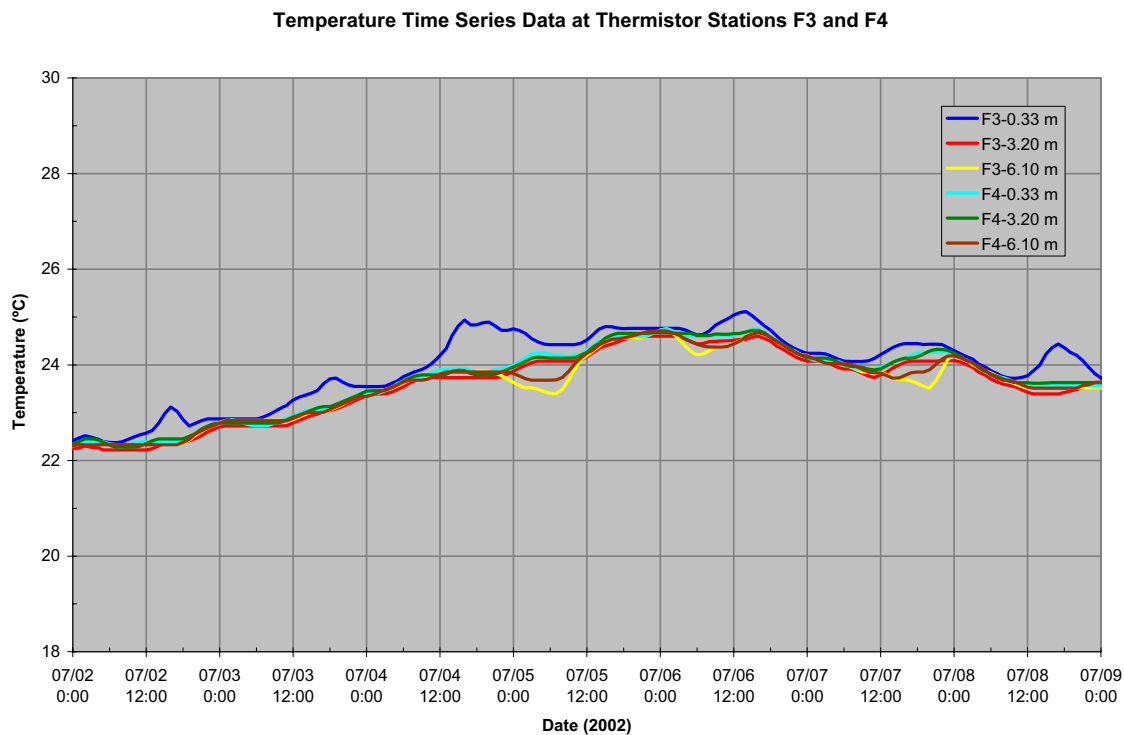


Figure B22. Temperature time series data for stations F3 and F4 from 7/02/02 to 7/08/02.

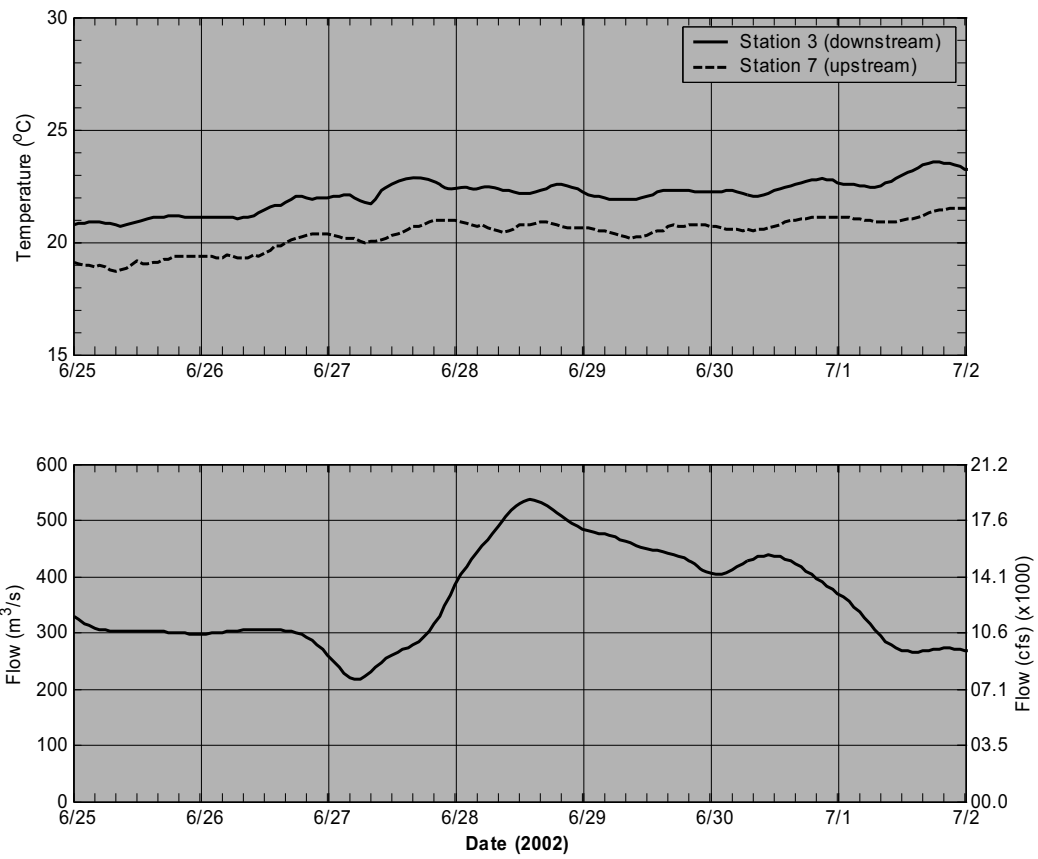


Figure B23. Upstream and downstream temperature and river flow measured at Vernon Dam.

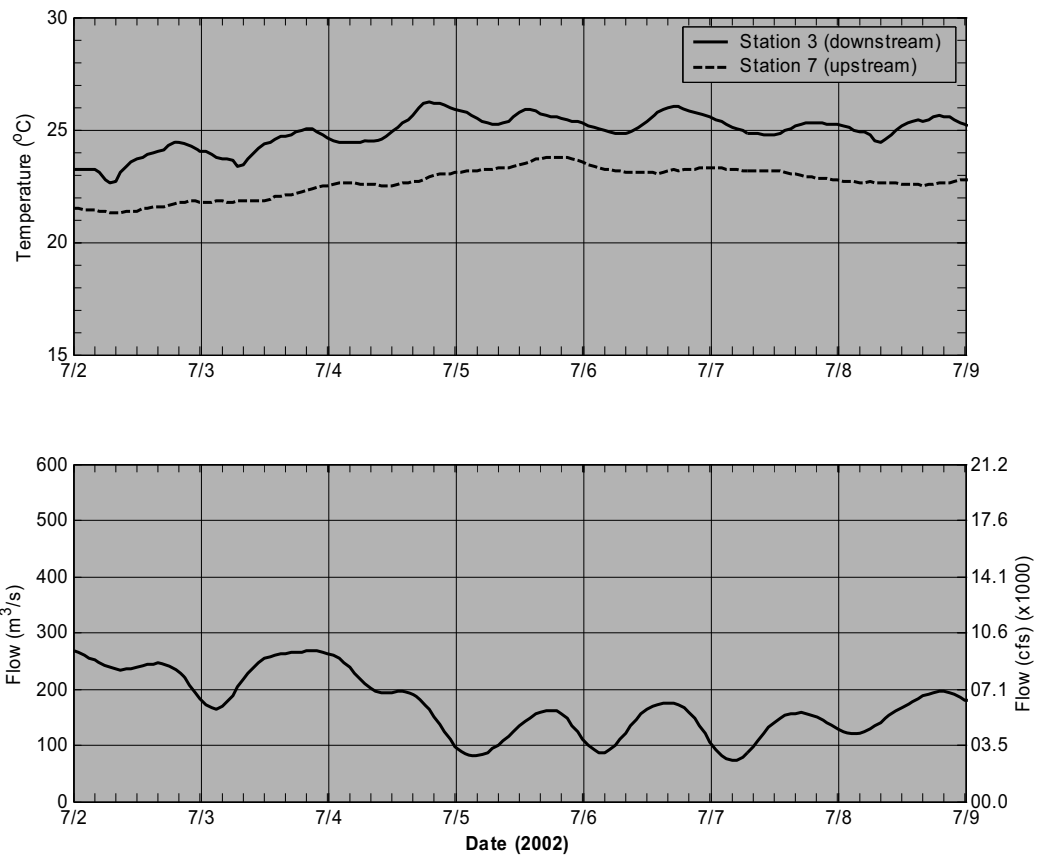


Figure B24. Upstream and downstream temperature and river flow measured at Vernon Dam.

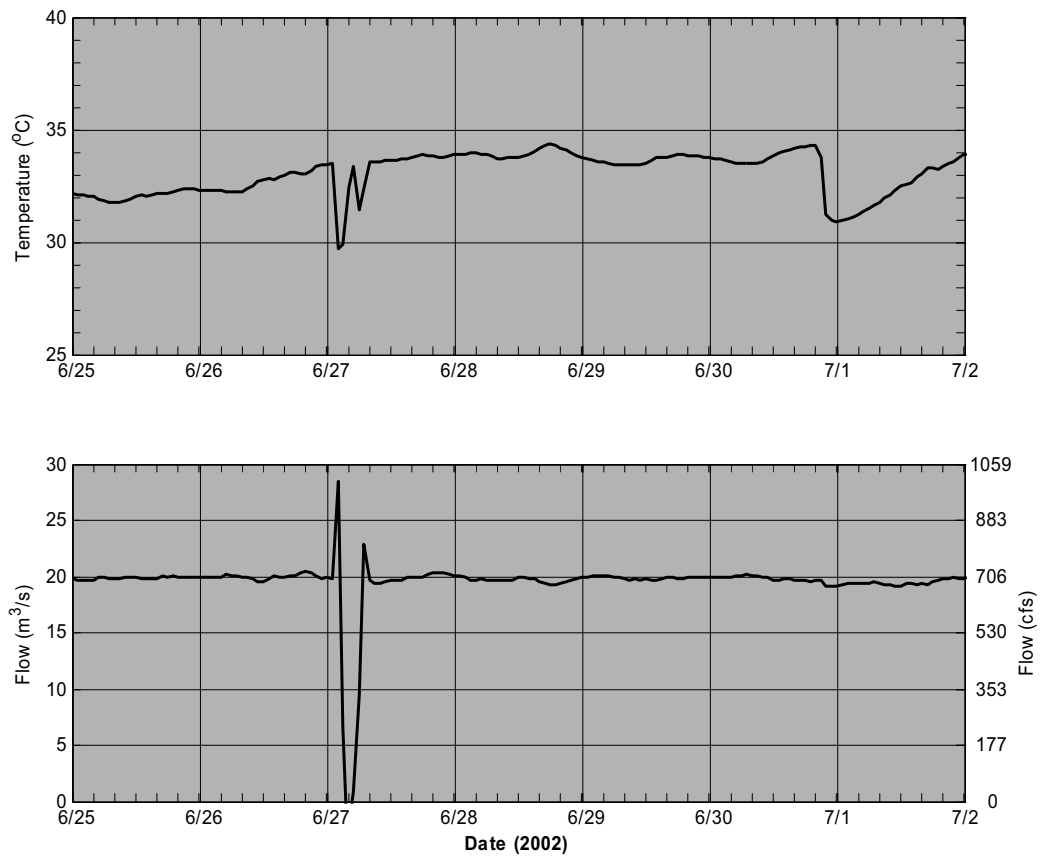


Figure B25. Water temperature and flow at the VYNPS discharge.

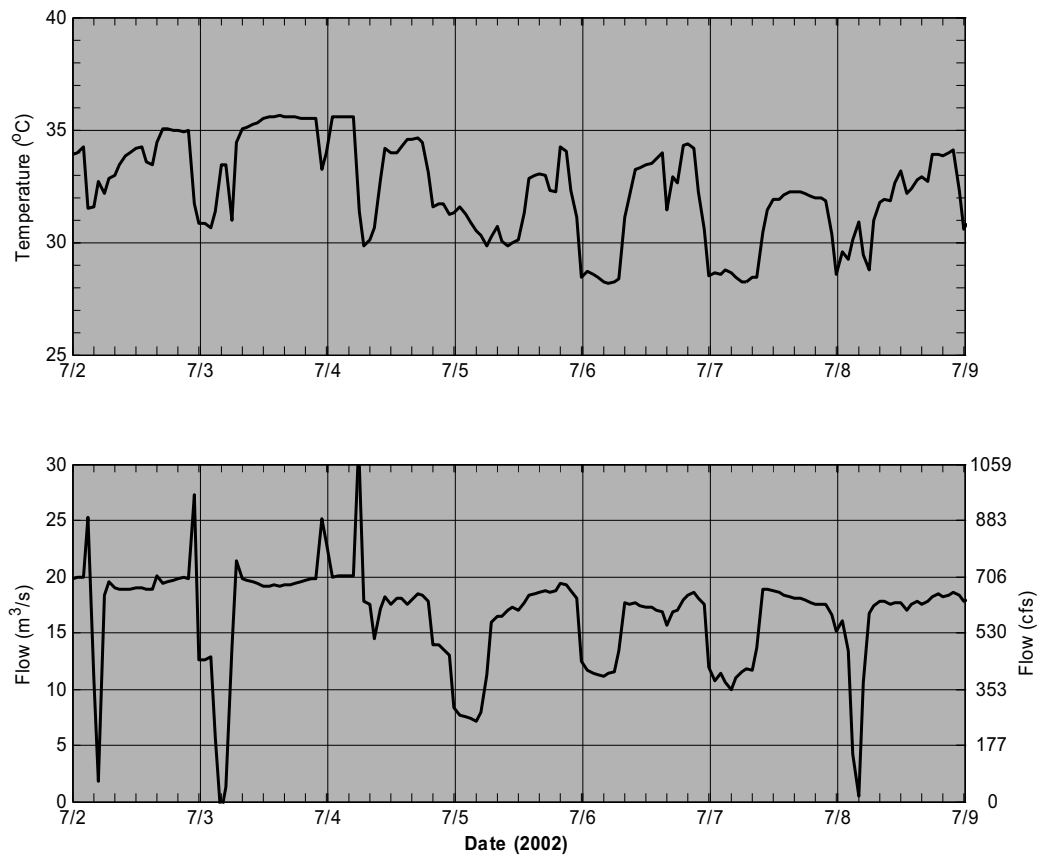


Figure B26. Water temperature and flow at the VYNPS discharge.

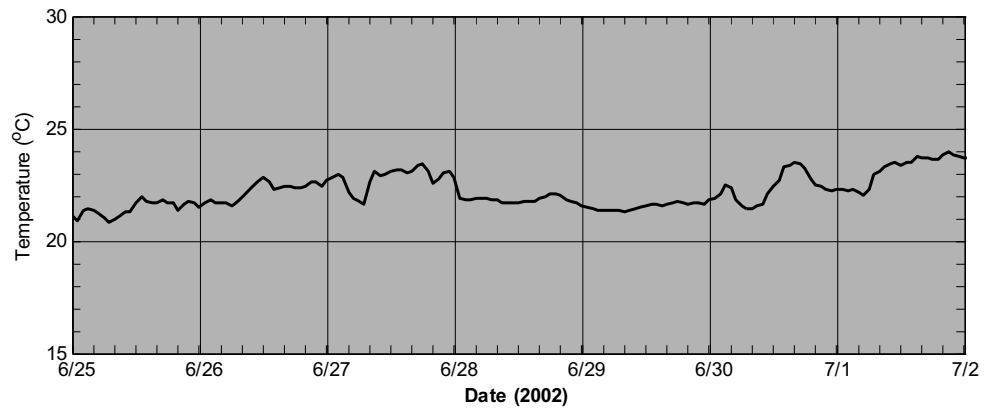


Figure B27. Water temperature recorded at the Fishway.

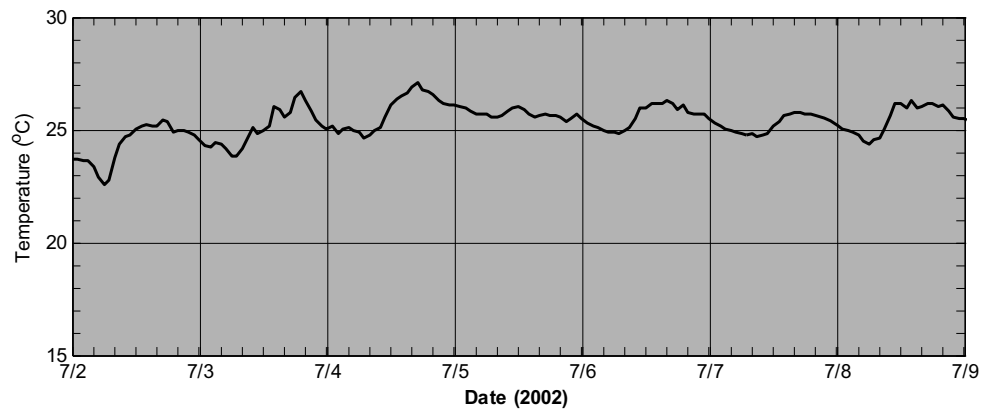


Figure B28. Water temperature recorded at the Fishway.

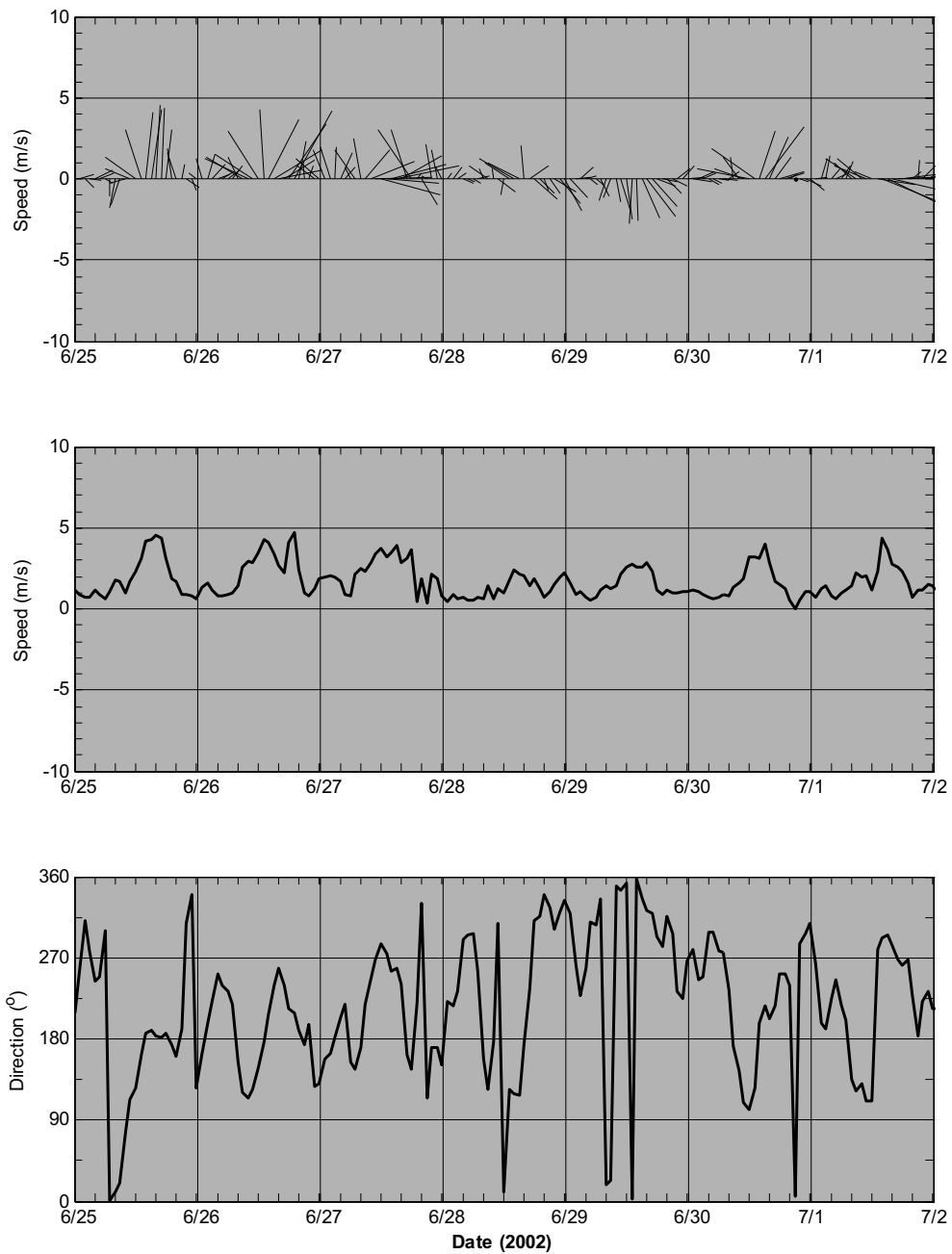


Figure B29. Wind stick plot and wind speed and direction as observed at the VYNPS. In the top figure, each stick points in the direction the wind is blowing to and stick length is proportional to wind speed. The bottom figure shows the direction the wind is blowing from relative to true north.

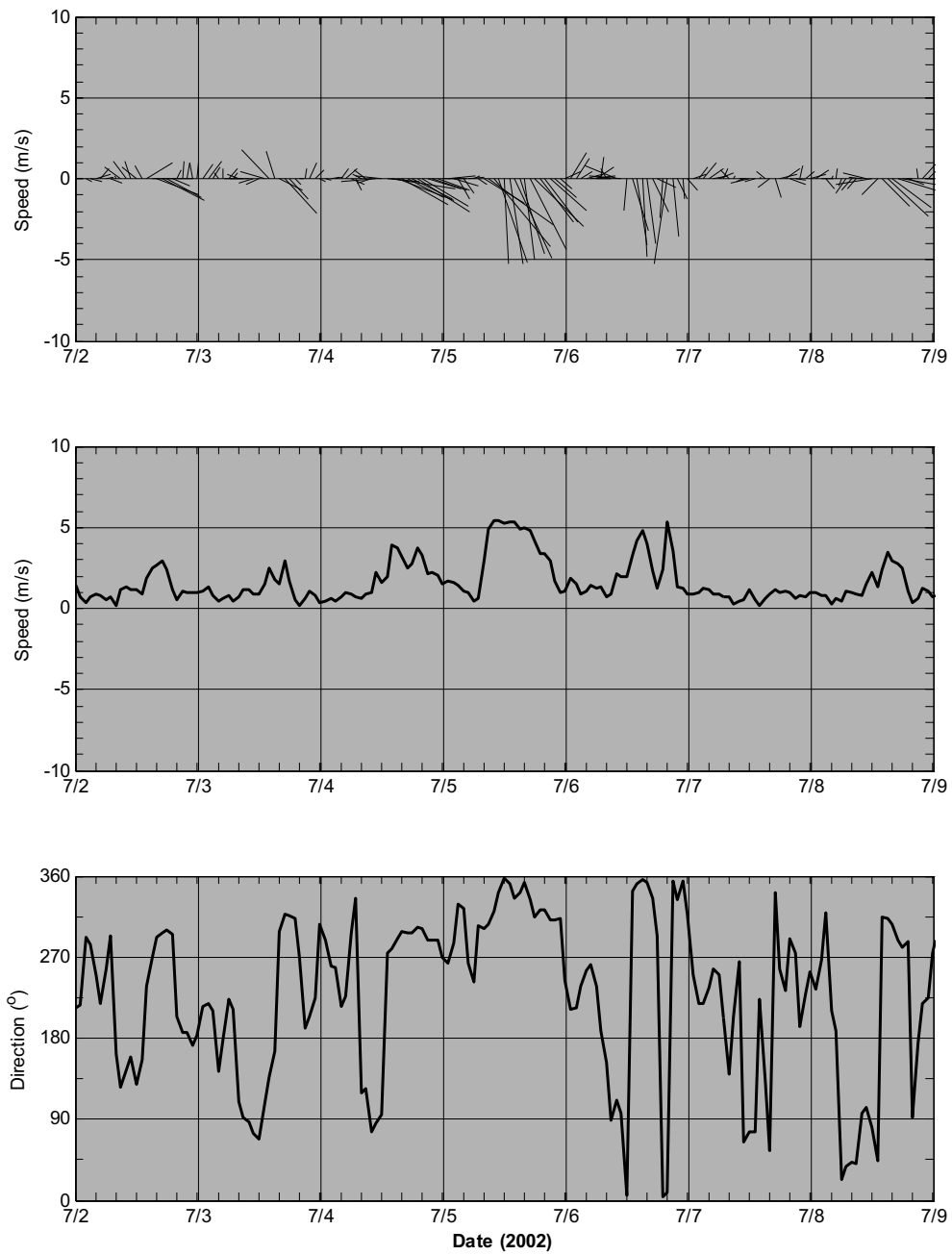


Figure B30. Wind stick plot and wind speed and direction as observed at the VYNPS. In the top figure, each stick points in the direction the wind is blowing to and stick length is proportional to wind speed. The bottom figure shows the direction the wind is blowing from relative to true north.

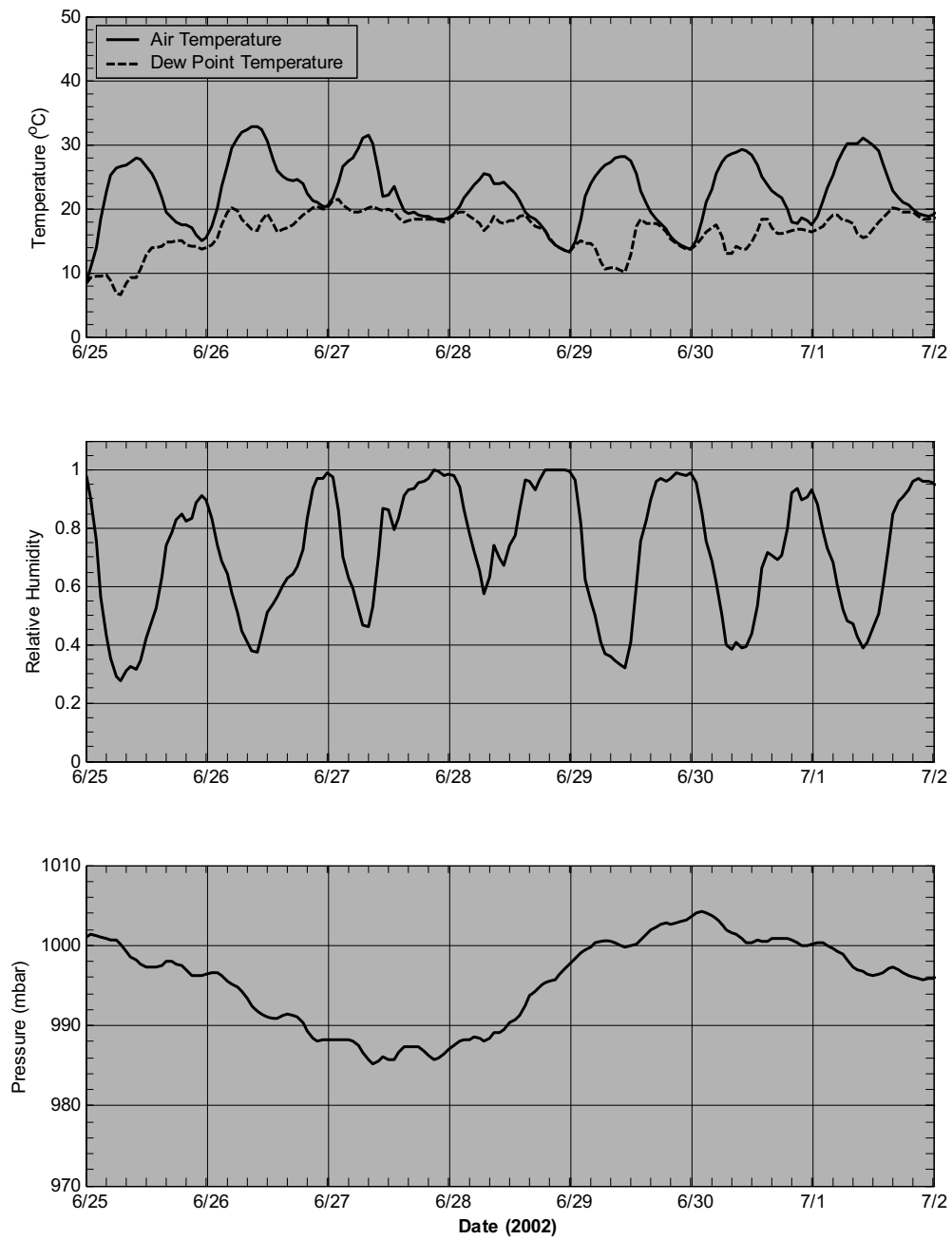


Figure B31. Air and dew point temperatures, relative humidity and atmospheric pressure as observed at Orange, MA.

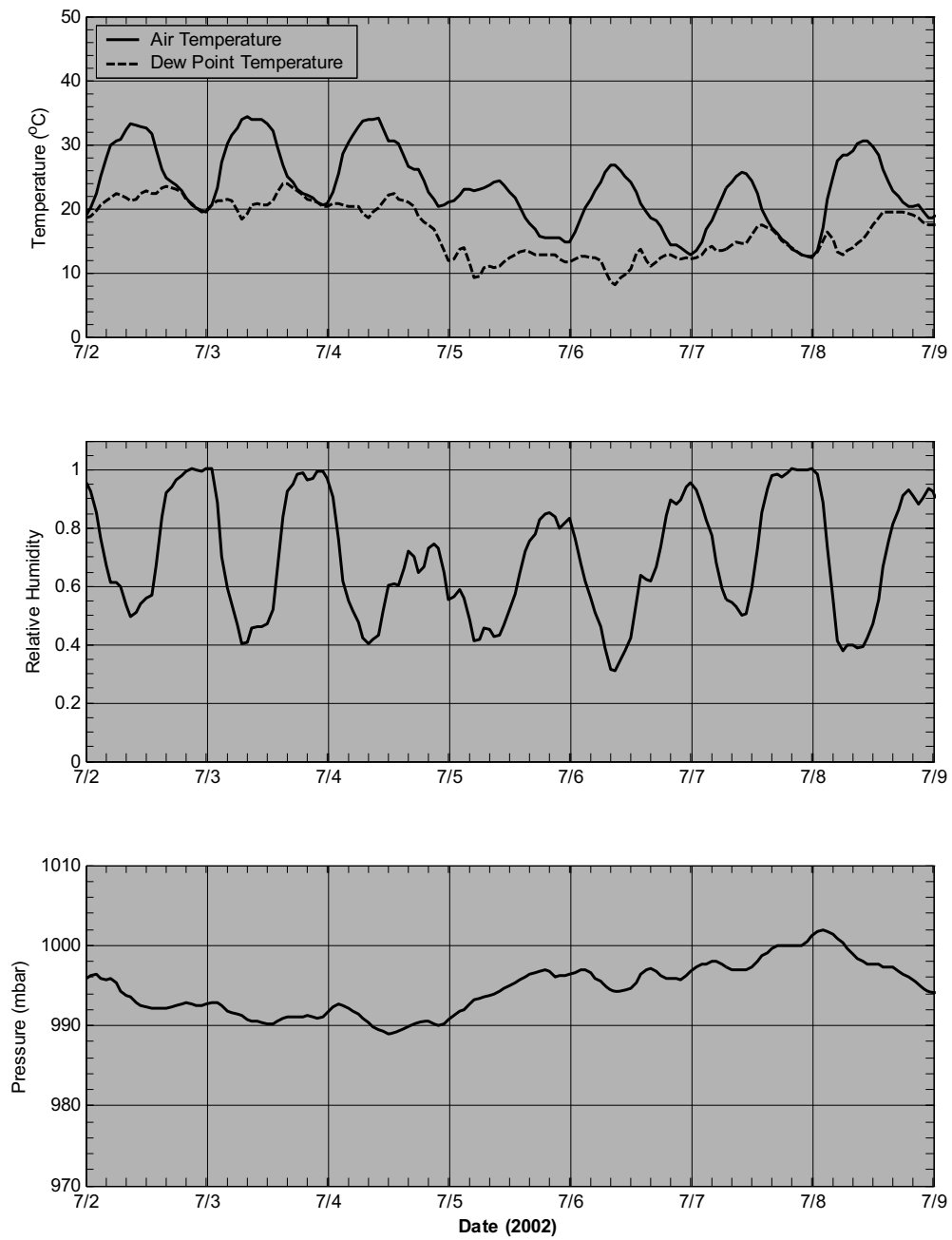


Figure B32. Air and dew point temperatures, relative humidity and atmospheric pressure as observed at Orange, MA.

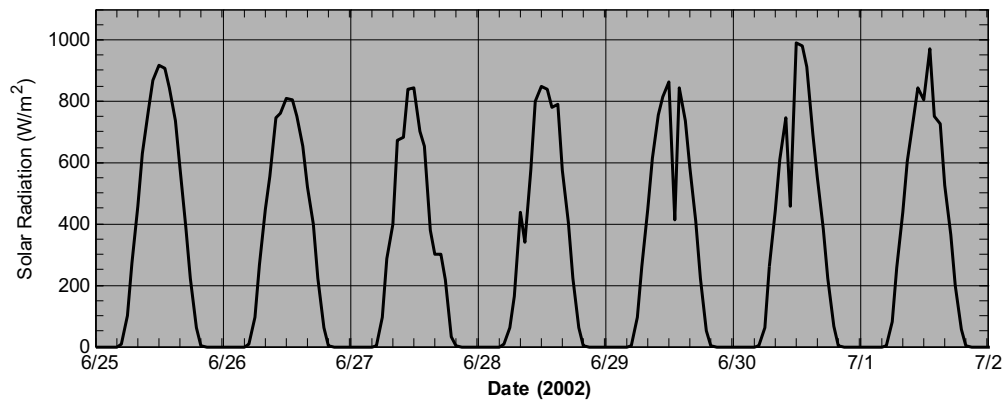


Figure B33. Solar radiation at Orange, MA.

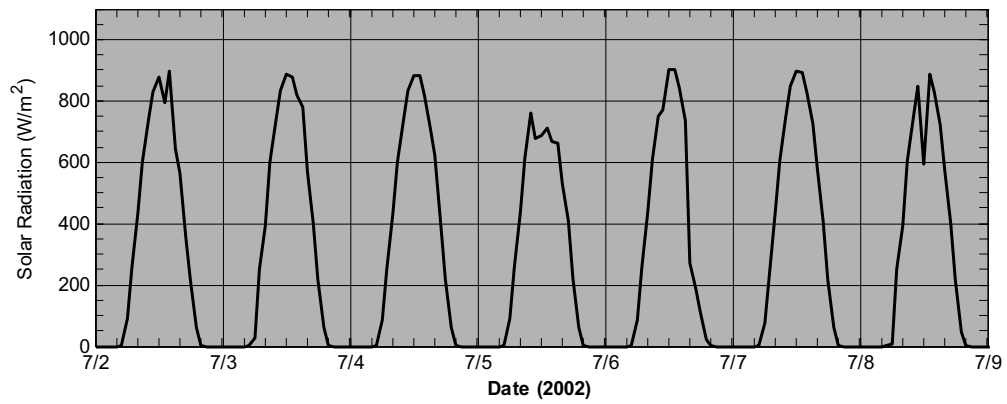


Figure B34. Solar radiation at Orange, MA.

Appendix C: Hydrodynamic Model Description (Muin and Spaulding, 1997)

THREE-DIMENSIONAL BOUNDARY-FITTED CIRCULATION MODEL

By Muslim Muin¹ and Malcolm Spaulding²

ABSTRACT: A spherical coordinate, three-dimensional, nonorthogonal, boundary-fitted circulation model (contravariant formulation) for application to estuarine, coastal sea, and continental shelf waters is presented. The model employs a split mode technique where the equations are decomposed into exterior and interior modes. The exterior mode (vertically averaged) described in an earlier paper (Muin and Spaulding 1996) is solved using a semiimplicit solution technique. The interior mode (vertical structure) is solved explicitly, except for the vertical diffusion terms that are solved implicitly. The temporally and spatially varying eddy viscosity and diffusivity are determined from a turbulent kinetic energy equation and an empirically specified length scale. A series of tests are presented to evaluate model performance where analytical solutions or other numerical solutions are available for comparison. The model's ability to predict the point vertical structure of tidal flow is tested against analytic solutions employing (1) constant viscosity; and (2) an eddy viscosity varying linearly with depth with a no-slip bottom boundary condition. The ability of the model to simulate three-dimensional tidal flow was tested against an exact solution for an annular section channel with quadratically varying bathymetry. The model was also tested against analytic solutions for steady residual flow generated by density gradient, wind, and river flow in a channel. The model predicted turbulent energy distributions generated from a bottom boundary were compared to those from a previous numerical study by Davies and Jones (1990). No-slip and bottom stress formulations at the sea bed, and their effect on the vertical structure of the flow are analyzed. The model was used to predict the salinity distribution in a simple rectangular channel identical to the Rotterdam Waterway. The computational method is very economical, stable, and accurate with the CFL stability condition up to 100.

INTRODUCTION

Numerical modeling techniques are routinely used to study circulation and pollutant transport in estuarine and coastal waters. The majority of models employ finite-difference techniques on square grid systems. While this has proven useful in various applications, it becomes expensive when the study region is geometrically and bathymetrically complex. Such difficulties motivate the use of alternative solution approaches that allow flexibility in the grid specification, for example finite elements (Lynch and Werner 1987) and boundary-fitted coordinates (Johnson 1980; Spaulding 1984; Sheng 1986; Swanson 1986; Muin and Spaulding 1996).

This paper presents the extension of a two-dimensional (2D) vertically averaged, boundary fitted, spherical coordinate circulation model developed by Muin and Spaulding (1996) to three dimensions. The paper first presents the governing equations in spherical coordinates with appropriate assumptions and boundary conditions. The equations are further transformed to a σ -coordinate. This is followed by presentations of the governing equations in a generalized curvilinear coordinate system, turbulence parameterization, the solution methodology, and model testing for which analytic (linear problems) solutions or other numerical solutions are readily available. Testing emphasizes calculations of the vertical structure of the flow. Testing of the 2D vertically averaged version of the model for a series of horizontal flow problems (see Lynch and Gray 1978) was presented in Muin and Spaulding (1996).

GOVERNING EQUATIONS

Using a spherical coordinate system, where ϕ = longitude positive east; θ = latitude positive north; and r = positive up,

¹Jurusan Teknik Sipil, Institut Teknologi Bandung, Bandung, Indonesia.

²Prof. and Chair, Dept. of Oc. Engrg., Univ. of Rhode Island, Narragansett Bay Campus, Narragansett, RI 02882.

Note. Discussion open until June 1, 1997. Separate discussions should be submitted for the individual papers in this symposium. To extend the closing date one month, a written request must be filed with the ASCE Manager of Journals. The manuscript for this paper was submitted for review and possible publication on January 10, 1994. This paper is part of the *Journal of Hydraulic Engineering*, Vol. 123, No. 1, January, 1997. ©ASCE, ISSN 0733-9429/97/0001-0002-0012/\$4.00 + \$.50 per page. Paper No. 7655.

the equations of continuity, momentum, and conservation of substance can be written as

Continuity

$$\frac{1}{r \cos \theta} \frac{\partial u}{\partial \phi} + \frac{1}{r} \frac{\partial v}{\partial \theta} - \frac{v}{r} \tan \theta + \frac{1}{r^2} \frac{\partial r^2 w}{\partial r} = 0 \quad (1)$$

Momentum

ϕ -direction

$$\begin{aligned} \frac{\partial u}{\partial t} + \frac{u}{r \cos \theta} \frac{\partial u}{\partial \phi} + \frac{v}{r} \frac{\partial u}{\partial \theta} - \frac{uv}{r} \tan \theta + w \frac{\partial u}{\partial r} + \frac{uw}{r} - fv \\ = -\frac{1}{\rho_e r \cos \theta} \frac{\partial p}{\partial \phi} + \frac{\partial}{\partial r} \left(A_v \frac{\partial u}{\partial r} \right) \end{aligned} \quad (2)$$

θ -direction

$$\begin{aligned} \frac{\partial v}{\partial t} + \frac{u}{r \cos \theta} \frac{\partial v}{\partial \phi} + \frac{v}{r} \frac{\partial v}{\partial \theta} + \frac{uv}{r} \tan \theta + w \frac{\partial v}{\partial r} + \frac{vw}{r} + fu \\ = -\frac{1}{\rho_e r \cos \theta} \frac{\partial p}{\partial \theta} + \frac{\partial}{\partial r} \left(A_v \frac{\partial v}{\partial r} \right) \end{aligned} \quad (3)$$

r -direction

$$\frac{\partial p}{\partial r} = -\rho g \quad (4)$$

Conservation of Substance

$$\begin{aligned} \frac{\partial q}{\partial t} + \frac{u}{r \cos \theta} \frac{\partial q}{\partial \phi} + \frac{v}{r} \frac{\partial q}{\partial \theta} + w \frac{\partial q}{\partial r} = \frac{\partial}{\partial r} \left[D_v \left(\frac{\partial q}{\partial r} \right) \right] \\ + \frac{D_h}{r^2} \left[\frac{\partial^2 q}{\cos^2 \theta \partial \phi^2} + \frac{\partial^2 q}{\partial \theta^2} \right] \end{aligned} \quad (5)$$

Equation of State of Sea Water

$$\rho = f(S, \theta) \quad (6)$$

where t = time; u , v and w = velocity components in ϕ , θ , and r directions, respectively; f = Coriolis parameter; p = pressure; g = gravity; ρ = water density; ρ_e = basin-averaged water density; A_v = vertical eddy viscosity; D_v = vertical eddy diffusivity.

ity; D_h = horizontal eddy diffusivity; Θ = temperature °C; S = salinity (ppt); and q = concentration of a conservative substance such as Θ or S .

The equations described previously assume the following: the flow is incompressible, density differences are neglected unless multiplied by gravity (Boussinesq approximation), the vertical acceleration is very small compared to gravity (hydrostatic assumption), and the horizontal stresses are neglected.

Boundary Conditions

The land boundaries are assumed impermeable where the normal component of velocity is set to zero

$$\vec{V} \cdot \vec{n} = 0 \quad (7)$$

On river boundaries, the velocities are specified and the pressure gradient is set to zero. At open boundaries the water elevation or vertically varying velocity as a function of time is known from field observations or otherwise specified.

At closed boundaries the transport of substance is zero. At an open boundary the concentration must be specified during inflow. On outflow the substance is advected out of the model domain according to

$$\frac{\partial q}{\partial t} + \frac{u}{r \cos \theta} \frac{\partial q}{\partial \phi} = 0 \quad (8a)$$

$$\frac{\partial q}{\partial t} + \frac{v}{r} \frac{\partial q}{\partial \theta} = 0 \quad (8b)$$

At the surface, the wind stress is specified as

$$\tau_{\phi} = \rho_a C_a W_{\phi} \sqrt{W_{\phi}^2 + W_{\theta}^2}, \quad \tau_{\theta} = \rho_a C_a W_{\theta} \sqrt{W_{\phi}^2 + W_{\theta}^2} \quad (9)$$

where W_{ϕ} and W_{θ} = wind speeds in the ϕ and θ directions, respectively; ρ_a = density of air; and C_a = drag coefficient at the surface.

The kinematic free surface boundary condition is given as

$$w = \frac{\partial \zeta}{\partial t} + \frac{u}{r \cos \theta} \frac{\partial \zeta}{\partial \phi} + \frac{v}{r} \frac{\partial \zeta}{\partial \theta} \quad (10)$$

Two options are available to specify the bottom boundary condition

1. Bottom stress condition

$$\tau_{b\phi} = \rho_b C_b u_b \sqrt{u_b^2 + v_b^2}, \quad \tau_{b\theta} = \rho_b C_b v_b \sqrt{u_b^2 + v_b^2} \quad (11)$$

where C_b = bottom drag coefficient; and u_b and v_b = velocity components at the bottom in the ϕ and θ directions, respectively.

2. No-slip condition

$$u_b = 0 \quad \text{and} \quad v_b = 0 \quad (12)$$

At the bottom boundary, no momentum flux is allowed and the kinematic condition is specified

$$w = -u_b \frac{1}{r \cos \theta} \frac{\partial h}{\partial \phi} - v_b \frac{1}{r} \frac{\partial h}{\partial \theta} \quad (13)$$

The governing equations are transformed to a σ -coordinate system to resolve bathymetric variations with a constant number of grids. The transformation is defined as

$$\phi = \phi', \quad \theta = \theta', \quad r = R + \zeta + (\sigma - 1)(\zeta + h)/2, \quad t = t' \quad (14)$$

The governing equations now become (dropping the primes for convenience)

Continuity

$$\frac{\partial \zeta}{\partial t} + \frac{1}{r \cos \theta} \frac{\partial u D}{\partial \phi} + \frac{1}{r} \frac{\partial v D}{\partial \theta} - \frac{v D}{r} \tan \theta + \frac{\partial \omega D}{\partial \sigma} = 0 \quad (15)$$

Momentum

ϕ -direction

$$\begin{aligned} \frac{\partial u D}{\partial t} + \frac{1}{r \cos \theta} \frac{\partial u u D}{\partial \phi} + \frac{1}{r} \frac{\partial u v D}{\partial \theta} - \frac{2 u v D}{r} \tan \theta + \frac{\partial u \omega D}{\partial \sigma} - f v D \\ = -\frac{g D}{2 \rho_s r \cos \theta} \left\{ [\lambda + (\rho_s - 2\rho)(1 - \sigma)] \frac{\partial D}{\partial \phi} \right. \\ \left. + (4\rho - 2\rho_s) \frac{\partial \zeta}{\partial \phi} + D \frac{\partial \lambda}{\partial \phi} \right\} + \frac{4}{D} \frac{\partial}{\partial \sigma} \left(A_v \frac{\partial u}{\partial \sigma} \right) \end{aligned} \quad (16)$$

θ -direction

$$\begin{aligned} \frac{\partial v D}{\partial t} + \frac{1}{r \cos \theta} \frac{\partial u v D}{\partial \phi} + \frac{1}{r} \frac{\partial v v D}{\partial \theta} - \frac{u u - v v}{r} D \tan \theta \\ + \frac{\partial v \omega D}{\partial \sigma} + f u D = -\frac{g D}{2 \rho_s r} \left\{ [\lambda + (\rho_s - 2\rho)(1 - \sigma)] \frac{\partial D}{\partial \theta} \right. \\ \left. + (4\rho - 2\rho_s) \frac{\partial \zeta}{\partial \theta} + D \frac{\partial \lambda}{\partial \theta} \right\} + \frac{4}{D} \frac{\partial}{\partial \sigma} \left(A_v \frac{\partial v}{\partial \sigma} \right) \end{aligned} \quad (17)$$

σ -direction

$$\frac{2}{D} \frac{\partial p}{\partial \sigma} = -\rho g \quad (18)$$

Conservation of Substance

$$\begin{aligned} \frac{\partial q}{\partial t} + \frac{u}{r \cos \theta} \frac{\partial q}{\partial \phi} + \frac{v}{r} \frac{\partial q}{\partial \theta} + \omega \frac{\partial q}{\partial \sigma} = \frac{4}{D^2} \frac{\partial}{\partial \sigma} \left[D_v \left(\frac{\partial q}{\partial \sigma} \right) \right] \\ + \frac{D_h}{r^2} \left(\frac{\partial^2 q}{\cos^2 \theta \partial \phi^2} + \frac{\partial^2 q}{\partial \theta^2} \right) \end{aligned} \quad (19)$$

where

$$\lambda = \int_{\sigma}^1 \rho \, d\sigma \quad (20a)$$

$$\omega = -\frac{1}{D} (1 + \sigma) \frac{\partial \zeta}{\partial t} + \gamma_{\phi} u + \gamma_{\theta} v + \frac{2}{D} w \quad (20b)$$

$$\gamma_{\phi} = \frac{1}{D} \left[\frac{1 - \sigma}{r \cos \theta} \frac{\partial h}{\partial \phi} - \frac{1 + \sigma}{r \cos \theta} \frac{\partial \zeta}{\partial \phi} \right] \quad (20c)$$

$$\gamma_{\theta} = \frac{1}{D} \left[\frac{1 - \sigma}{r \cos \theta} \frac{\partial h}{\partial \theta} - \frac{1 + \sigma}{r \cos \theta} \frac{\partial \zeta}{\partial \theta} \right] \quad (20d)$$

where $D = h + \zeta$ = total water depth.

The horizontal velocities and independent variables are next transformed to a curvilinear coordinate system. The equations of motion and continuity equation in a curvilinear coordinate system (ξ, η), in terms of the contravariant velocity components, are as follows:

Continuity

$$\begin{aligned} J r \cos \theta \frac{\partial \zeta}{\partial t} + \frac{\partial}{\partial \xi} (\cos \theta J u^c D) + \frac{\partial}{\partial \eta} (\cos \theta J v^c D) \\ + J r \cos \theta \frac{\partial (\omega D)}{\partial \sigma} = 0 \end{aligned} \quad (21)$$

Momentum Equation

ξ -direction

$$\begin{aligned} \frac{\partial u^e D}{\partial t} = & -\frac{\theta_\eta \theta_\xi + \cos^2 \theta \phi_\eta \phi_\xi}{J^2 \rho_e r \cos^2 \theta} \frac{Dg}{2} \left\{ [\lambda + (\rho_e - 2\rho)(1 - \sigma)] \frac{\partial D}{\partial \xi} \right. \\ & + (4\rho - 2\rho_e) \frac{\partial \zeta}{\partial \xi} + D \frac{\partial \lambda}{\partial \xi} \left. \right\} + \frac{\theta_\xi \theta_\eta + \cos^2 \theta \phi_\xi \phi_\eta}{J^2 \rho_e r \cos^2 \theta} \frac{Dg}{2} \\ & \cdot \left\{ [\lambda + (\rho_e - 2\rho)(1 - \sigma)] \frac{\partial D}{\partial \eta} + (4\rho - 2\rho_e) \frac{\partial \zeta}{\partial \eta} + D \frac{\partial \lambda}{\partial \eta} \right\} \\ & - \frac{\theta_\eta}{J^2 r \cos^2 \theta} \left[\frac{\partial}{\partial \xi} (\phi_\xi \cos^2 \theta J u^e u^e D + \phi_\eta \cos^2 \theta J u^e v^e D) \right. \\ & + \frac{\partial}{\partial \eta} (\phi_\xi \cos^2 \theta J u^e v^e D + \phi_\eta \cos^2 \theta J v^e v^e D) \left. \right] \\ & + \frac{\phi_\eta}{J^2 r \cos^2 \theta} \left[\frac{\partial}{\partial \xi} (\theta_\xi \cos^2 \theta J u^e u^e D + \theta_\eta \cos^2 \theta J u^e v^e D) \right. \\ & + \frac{\partial}{\partial \eta} (\theta_\xi \cos^2 \theta J u^e v^e D + \theta_\eta \cos^2 \theta J v^e v^e D) \left. \right] \\ & - \frac{\partial}{\partial \sigma} (\omega u^e D) + \frac{fD}{J \cos \theta} [(\theta_\xi \theta_\eta + \cos^2 \theta \phi_\xi \phi_\eta) u^e \\ & + (\theta_\xi \theta_\eta + \cos^2 \theta \phi_\xi \phi_\eta) v^e] + \frac{4}{D} \frac{\partial}{\partial \sigma} \left(A_v \frac{\partial u^e}{\partial \sigma} \right) \end{aligned} \quad (22)$$

η -direction

$$\begin{aligned} \frac{\partial v^e D}{\partial t} = & \frac{\theta_\eta \theta_\xi + \cos^2 \theta \phi_\eta \phi_\xi}{J^2 \rho_e r \cos^2 \theta} \frac{Dg}{2} \left\{ [\lambda + (\rho_e - 2\rho)(1 - \sigma)] \frac{\partial D}{\partial \xi} \right. \\ & + (4\rho - 2\rho_e) \frac{\partial \zeta}{\partial \xi} + D \frac{\partial \lambda}{\partial \xi} \left. \right\} - \frac{\theta_\xi \theta_\eta + \cos^2 \theta \phi_\xi \phi_\eta}{J^2 \rho_e r \cos^2 \theta} \frac{Dg}{2} \\ & \cdot \left\{ [\lambda + (\rho_e - 2\rho)(1 - \sigma)] \frac{\partial D}{\partial \eta} + (4\rho - 2\rho_e) \frac{\partial \zeta}{\partial \eta} + D \frac{\partial \lambda}{\partial \eta} \right\} \\ & + \frac{\theta_\xi}{J^2 r \cos^2 \theta} \left[\frac{\partial}{\partial \xi} (\phi_\xi \cos^2 \theta J u^e u^e D + \phi_\eta \cos^2 \theta J u^e v^e D) \right. \\ & + \frac{\partial}{\partial \eta} (\phi_\xi \cos^2 \theta J u^e v^e D + \phi_\eta \cos^2 \theta J v^e v^e D) \left. \right] \\ & - \frac{\phi_\xi}{J^2 r \cos^2 \theta} \left[\frac{\partial}{\partial \xi} (\theta_\xi \cos^2 \theta J u^e u^e D + \theta_\eta \cos^2 \theta J u^e v^e D) \right. \\ & + \frac{\partial}{\partial \eta} (\theta_\xi \cos^2 \theta J u^e v^e D + \theta_\eta \cos^2 \theta J v^e v^e D) \left. \right] \\ & - \frac{\partial}{\partial \sigma} (\omega v^e D) - \frac{fD}{J \cos \theta} [(\theta_\xi \theta_\eta + \cos^2 \theta \phi_\xi \phi_\eta) u^e \\ & + (\theta_\xi \theta_\eta + \cos^2 \theta \phi_\xi \phi_\eta) v^e] + \frac{4}{D} \frac{\partial}{\partial \sigma} \left(A_v \frac{\partial v^e}{\partial \sigma} \right) \end{aligned} \quad (23)$$

Conservation of Substance

$$\begin{aligned} \frac{\partial q}{\partial t} + \frac{u^e}{r} \frac{\partial q}{\partial \xi} + \frac{v^e}{r} \frac{\partial q}{\partial \eta} + \omega \frac{\partial q}{\partial \sigma} = & \frac{4}{D^2} \frac{\partial}{\partial \sigma} \left(D_v \frac{\partial q}{\partial \sigma} \right) + \frac{D_s}{r^2 J^2} \\ & \cdot \left[\left(\frac{\theta_\eta \theta_\xi}{\cos^2 \theta} + \phi_\eta \phi_\xi \right) \frac{\partial^2 q}{\partial \xi^2} - 2 \left(\frac{\theta_\xi \theta_\eta}{\cos^2 \theta} + \phi_\xi \phi_\eta \right) \frac{\partial^2 q}{\partial \xi \partial \eta} \right. \\ & + \left. \left(\frac{\theta_\xi \theta_\eta}{\cos^2 \theta} + \phi_\xi \phi_\eta \right) \frac{\partial^2 q}{\partial \eta^2} \right] \end{aligned} \quad (24)$$

where u^e and v^e = contravariant velocities in the (ξ, η) directions, respectively; ζ = water elevation; $D = \zeta + \text{depth}$; and

the Jacobian, $J = \phi_\xi \theta_\eta - \phi_\eta \theta_\xi$. The relationship between the contravariant velocities (u^e, v^e) and velocities in spherical coordinates (u, v) is given by

$$u = \cos \theta \phi_\xi u^e + \cos \theta \phi_\eta v^e \quad (25a)$$

$$v = \theta_\xi u^e + \theta_\eta v^e \quad (25b)$$

TURBULENCE PARAMETERIZATION

The turbulence parameterization is a key model component for predicting flow and mixing processes in stratified fluids. There is, however, no universally accepted procedure to represent turbulence (ASCE 1988; Cheng and Smith 1990). In this study, we employ a one equation turbulent kinetic energy model to calculate the vertical eddy viscosity and diffusivity. The length scale is specified using the approach suggested by Blackadar (1962) that has been successfully used in modeling turbulence for tidal problems (Davies and Jones 1990). The effect of stratification is accounted for by using an empirical relationship similar to the ones employed for the mixing length approach. This model accounts for the convection, diffusion, and time history of turbulent kinetic energy in unsteady flows.

Turbulent Energy

The turbulence kinetic energy equation in spherical and σ -coordinates is given as follows:

$$\begin{aligned} \frac{\partial b}{\partial t} + \frac{u}{r \cos \theta} \frac{\partial b}{\partial \phi} + \frac{v}{r} \frac{\partial b}{\partial \theta} + \omega \frac{\partial b}{\partial \sigma} = & \frac{4}{D^2} \frac{\partial}{\partial \sigma} \left(A_v \frac{\partial b}{\partial \sigma} \right) \\ & + A_v \left[\left(\frac{2}{D} \frac{\partial u}{\partial \sigma} \right)^2 + \left(\frac{2}{D} \frac{\partial v}{\partial \sigma} \right)^2 \right] + \beta g \frac{2A_v}{D\sigma} \frac{\partial \Phi}{\partial \sigma} - \epsilon \end{aligned} \quad (26)$$

where b = kinetic energy.

After transformation to curvilinear coordinates (ξ, η) , the preceding equation can be written as

$$\begin{aligned} \frac{\partial b}{\partial t} + \frac{u^e}{r} \frac{\partial b}{\partial \xi} + \frac{v^e}{r} \frac{\partial b}{\partial \eta} + \omega \frac{\partial b}{\partial \sigma} = & \frac{4}{D^2} \frac{\partial}{\partial \sigma} \left(A_v \frac{\partial b}{\partial \sigma} \right) \\ & + A_v \left[\left(\frac{2}{D} \frac{\partial u^e}{\partial \sigma} \right)^2 + \left(\frac{2}{D} \frac{\partial v^e}{\partial \sigma} \right)^2 \right] + \beta g \frac{2A_v}{D\sigma} \frac{\partial \Phi}{\partial \sigma} - \epsilon \end{aligned} \quad (27)$$

where β = volumetric expansion coefficient; σ_v = empirical diffusion constant; σ_s = Schmidt number; Φ = mean scalar quantity; and ϵ = dissipation. In this study the interchange between turbulent kinetic energy and potential energy or production/dissipation by buoyant forces is neglected. It is assumed that the turbulent kinetic energy is advected and diffused in a homogeneous fluid while the effect of stratification is accounted for by an empirical formula using a Richardson number (damping function). As argued by Abraham (1988), the reproduction of internal mixing at tidal slack is beyond the capability of present turbulence models and, hence, they should not be used where this aspect is important.

Eddy Viscosity and Diffusivity Relationships

Based on dimensional reasoning the eddy viscosity is related to the kinetic energy b and mixing length L_m by

$$A_v = C_\mu L_m \sqrt{b} \quad (28)$$

where C_μ = empirical constant.

In homogeneous water, the vertical eddy viscosity and diffusivity are considered to be equal, $A_v = D_v$. In the presence of a stable vertical density gradient, both A_v and D_v are lower than their homogeneous values. The magnitude of A_v is always greater than the corresponding value of D_v .

The general form for the eddy viscosity and diffusivity are given as

$$A_v = f(R_i) C_\mu L_m \sqrt{b} \quad (29a)$$

$$D_v = g(R_i) C_\mu L_m \sqrt{b} \quad (29b)$$

Several semiempirical relations for $f(R_i)$ and $g(R_i)$ have been proposed by Munk and Anderson (1948) and Officer (1976).

Munk and Anderson (1948)

$$f(R_i) = (1 + 10.0 R_i)^{-1/2} \quad (30a)$$

$$g(R_i) = (1 + 3.33 R_i)^{-3/2} \quad (30b)$$

Officer (1976)

$$f(R_i) = (1 + R_i)^{-1} \quad (31a)$$

$$g(R_i) = (1 + R_i)^{-2} \quad (31b)$$

where the Richardson number, R_i , is defined by

$$R_i = -\frac{2g}{\rho D} \frac{\frac{\partial \rho}{\partial \sigma}}{\left[\frac{\partial(u)}{\partial \sigma} \right]^2 + \left[\frac{\partial(v)}{\partial \sigma} \right]^2} \quad (32)$$

Dissipation

From dimensional analysis the expression for dissipation, in terms of the turbulent kinetic energy and mixing length, is given by

$$\epsilon = C_d (b^{3/2} / L_m) \quad (33)$$

where C_d = empirical constant.

Mixing Length

The mixing length formulation proposed by Blackadar (1962) is

$$L_m = \frac{KD[1 + (\sigma - 1)/2]}{1 + \frac{KD[1 + (\sigma - 1)/2]}{L_o}} \quad (34)$$

where K = Von Karman's constant; D = total water depth and in which the mixing length, L_m , increases from the sea bottom to the surface and the value of L_o is determined by the vertical distribution of the turbulent energy as follows:

$$L_o = \gamma D \frac{\int_{-1}^1 b^{1/2} [1 + (\sigma - 1)/2] d\sigma}{\int_{-1}^1 b^{1/2} d\sigma} \quad (35)$$

The constant γ determines the vertical extent of the boundary layer and vertical eddy viscosity, and is adjusted to match field observations. The viscosity increases rapidly with increasing γ in both amplitude and vertical extent (Moffeld and Lavelle 1983). The constant γ typically ranges from 0.05 to 0.3. The coefficients in (28), (34), and (35) have values $C_\mu = 0.463$; $C_d = 0.1$; $\sigma_b = 1.37$; and $K = 0.4$ (Davies and Jones 1990).

Boundary Conditions

The boundary condition at the surface is specified as

$$\frac{2\alpha_b A_v}{D} \frac{\partial b}{\partial \sigma} = \alpha_w U_*^3 \quad (36)$$

where U_* = friction velocity due to the wind stress and α_b , α_w are coefficients. A similar boundary condition is used by Davies and Jones (1988) in which $\alpha_b = 0.73$, and $\alpha_w = 2.6$. In the absence of wind forcing the flux of turbulence at the surface disappears.

For a no-slip bottom boundary condition, the turbulent kinetic energy flux into the sea bed is zero (Davies and Jones 1988) and, therefore

$$\frac{\partial b}{\partial \sigma} = 0 \quad (37)$$

For the bottom stress boundary condition, the bottom boundary layer is not resolved in detail. The turbulent kinetic energy, b , at the first grid point near the wall (where the turbulence is assumed in equilibrium and the velocity follows the log-law) is given as follows:

$$b = U_*^2 / \sqrt{C_\mu C_d} \quad (38)$$

where U_* = friction velocity associated with the bottom stress. While this boundary condition is not always rigorously satisfied under unsteady conditions (Celik and Rodi 1985), it is used as a first-order approximation.

SOLUTION TECHNIQUE

The basic approach is to transform the dependent, as well as independent, variables in spherical coordinates to a curvilinear coordinate system. The equation of motion is split into exterior and interior modes to increase the allowable time step and, hence, reduce the computational time.

The velocity is decomposed into

$$u^c = U^c + u^{c'} \quad (39a)$$

$$v^c = V^c + v^{c'} \quad (39b)$$

where (U^c, V^c) and $(u^{c'}, v^{c'})$ = vertically averaged velocities and deviation velocity (from the vertically averaged velocity) in (ξ, η) directions, respectively. Solution of the exterior mode using a semiimplicit (space staggered grid) solution, methodology, and presentations of the approach used to generate the boundary conforming grid are presented by Muin and Spaulding (1996). The focus here is on three-dimensional (3D) aspects, including the deviation velocity and the turbulence equation.

Subtracting the vertically averaged momentum equations from the 3D momentum equations gives the vertical deviation velocity equations of motion

$$\frac{\partial u^{c'} D}{\partial t} = \frac{4}{D} \frac{\partial}{\partial \sigma} \left(A_v \frac{\partial u^{c'}}{\partial \sigma} \right) + A \quad (40a)$$

$$\frac{\partial v^{c'} D}{\partial t} = \frac{4}{D} \frac{\partial}{\partial \sigma} \left(A_v \frac{\partial v^{c'}}{\partial \sigma} \right) + B \quad (40b)$$

where A and B = nonbarotropic terms in the equations of motion. These terms are solved explicitly. The diffusion term in (40) is solved implicitly using a three-level scheme to damp out spurious oscillations (Fletcher 1988). The algorithm is second-order accurate both in time and space. A tridiagonal set of equations in the unknown velocity deviation is solved using a Thomas algorithm. Both the exterior and interior modes are solved at the same time step.

The finite difference procedure used to solve the turbulent kinetic energy equations has been described by Davies and Jones (1990). In the present study, a three-level time discretization (Fletcher 1988) is used instead of the Crank-Nicholson method of Davies and Jones (1990). A nonstaggered grid is used in the vertical. The C form of Davies and Jones' (1990) numerical scheme is employed to calculate the dissipation term

in the energy equation to ease the time step restriction. No iteration or filtering is employed. The time step is restricted by the horizontal advection term. As will be shown in model testing, a CFL equal to 100 can be used to predict the vertical structure of tidally induced flows.

The transport model (24) is solved by a simple explicit technique, except for the vertical diffusion that is solved by an implicit scheme to ease the time step restriction due to the small vertical length scale. In the present model, two options are available to solve the advection term. The first option is a Lax-Wendroff scheme, which is consistent with a second-order truncation error (Fletcher 1988). The second option is an upwind-differencing scheme (first-order accurate) that introduces artificial diffusivity. The horizontal diffusion term is solved by a centered-in-space, explicit technique. The diffusive and advective stability criteria in these numerical techniques are $\Delta t < \Delta s^2/(2D_h)$, and $\Delta t < \Delta s/U_s$, where Δs and U_s = horizontal grid size and velocity, respectively. To avoid spatial oscillations, the Lax-Wendroff scheme requires $D_h > U_s \Delta s/2$. This gives approximately the same amount of artificial viscosity as inherent in the upwind scheme.

MODEL TESTING

Model formulation and implementation, in computer code, were compared to analytical solutions in which the nonlinear convective acceleration and Coriolis terms were removed and the governing equations solved on a spherical coordinate system, which because of the limited domain approximated a Cartesian grid. Additional test simulations were performed to confirm the operation of the turbulent closure equations to predict the vertical structure of tidal flow and compared to a previous numerical study by Davies and Jones (1990). The model was tested in an application to salinity intrusion in a simple rectangular channel representative of the Rotterdam Waterway.

Residual Flow

The ability of the model to predict residual flow was tested for a basin with vertically constant density and viscosity. The surface boundary was forced by a constant wind stress if wind forcing was used. The test was performed in a simple, rectangular, and constant depth channel open at one end (west). The model was run for two bottom boundary conditions: (1) no-slip condition; and (2) bottom stress condition.

Following Officer's (1976) approach and neglecting advection, the horizontal diffusion of momentum, and the cross channel terms (equations laterally averaged), the steady-state expression for the vertical velocity profiles with linearized bottom friction can be given as follows

$$u = -g\Lambda \left(\frac{z^3}{6\rho A_v} + \frac{h^2}{2\rho k} + \frac{h^3}{6\rho A_v} \right) - g\iota \left(\frac{h}{k} + \frac{h^2}{2A_v} - \frac{z^2}{2A_v} \right) + \frac{\tau_s}{\rho} \left(\frac{1}{k} + \frac{h}{A_v} + \frac{z}{A_v} \right) \quad (41)$$

where

$$g\iota = \frac{\left[-g\Lambda \left(\frac{h^3}{2\rho k} + \frac{h^4}{8\rho A_v} \right) + \frac{\tau_s}{\rho} \left(\frac{h}{k} + \frac{h^2}{2A_v} \right) - hu_o \right]}{\left(\frac{h^2}{k} + \frac{h^3}{3A_v} \right)} \quad (42)$$

where Λ = horizontal density gradient; g = gravity; ι = water elevation slope; τ_s = wind stress; u_o = river flow per width; and k = linearized bottom friction. A similar equation for a no-slip condition at the bottom is given on page 120 of Officer (1976).

Three separate simulations with different forcings were studied: (1) density gradient flow; (2) wind driven flow; and (3) density gradient, wind, and river-induced flow. In these simulations, the following conditions were assumed: the density increases linearly from the head (closed end) to the mouth (open end) $\Lambda = -0.00036 \text{ kg/m}^4$; wind stress $\tau_s = 0.01 \text{ N/m}^2$ (1 dyne/cm^2); river flow $u_o = -0.1 \text{ m/s}$; depth $h = 10 \text{ m}$; vertical viscosity $A_v = 10 \text{ cm}^2/\text{s}$; and linearized bottom friction $k = 0.05 \text{ cm/s}$. Depending on the case the appropriate forcing parameters were used. Testing was performed using five, 10, and 20 vertical levels. The model was started with zero velocities and elevation. The density gradient was applied gradually until a steady state was achieved.

Density Gradient Forcing

Fig. 1(a) shows a comparison of the model prediction to analytic solution for the bottom stress formulation under density gradient forcing. Model predictions approach the analytic solution as the grid resolution is increased. The model overpredicts the currents near the bottom and surface at low grid resolution. The maximum errors are about 7% for five levels, 2% for 10 levels, and less than 1% for 20 levels. The model was also run with a no-slip bottom boundary condition, as shown in Fig. 1(b). When the surface boundary condition was specified using a second-order accurate representation, the model never reached steady state even with 80 levels. This problem may be caused by an underestimate of the bottom friction, which is only first-order accurate. The model, however, reached steady state when the surface boundary was reduced to first order. For this approximation the model overpredicted the velocity near the surface by 20% [Fig. 1(b)] independent of the number of the vertical levels.

Wind Forcing

Comparison of model predictions with the analytic solution under constant wind forcing with a bottom stress condition is

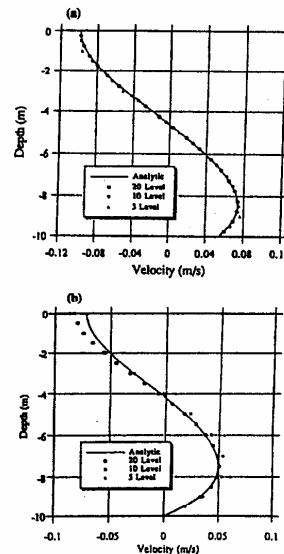


FIG. 1. Comparison of Model Predicted Vertical Structure of Velocity with Analytic Solution for Density-Induced Forcing ($A_v = 10 \text{ cm}^2/\text{s}$, $\Lambda = -0.00036 \text{ kg/m}^4$, $k = 0.05 \text{ cm/s}$) for: (a) Bottom Stress; and (b) No-Slip Bottom Boundary Condition (Model Results Are Presented for 5, 10, and 20 Vertical Levels)

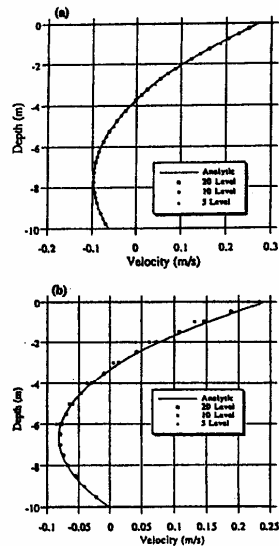


FIG. 2. Comparison of Model Predicted Vertical Structure of Velocity with Analytic Solution for Wind Driven Flow ($A_v = 10 \text{ cm}^2/\text{s}$, $\tau_b = 0.1 \text{ N/m}^2$ (1 dyne/cm²), $k = 0.05 \text{ cm/s}$) for: (a) Bottom Stress; and (b) No-Slip Bottom Boundary Condition (Model Results Are Presented for 5, 10, and 20 Vertical Levels)

shown in Fig. 2(a). It can be seen that as the resolution increases the model predictions approach the analytic solution, especially near the bottom. The model represents the vertical velocity structure more accurately than for the density induced flow problem. The maximum errors are about 2% for five levels, 0.6% for 10 levels, and 0.2% for 20 levels. A similar problem, as in the density-induced flow, was found for the no-slip condition at the bottom and the boundary condition at the surface was modified to first order. The results are shown in Fig. 2(b). Again model prediction for this case is more accurate than in the baroclinic forcing problem.

Density Gradient Wind and River Forcing

The last test case considered flow driven by a combination of density gradient, wind, and river flow. The model was run using 20 levels. The results, not shown here, were simulated for bottom stress and no-slip bottom specifications, respectively. The agreement is excellent (<0.5%) for the bottom stress bottom boundary condition. The model underpredicts the velocity by about 5% in the mid-depth region for the no-slip bottom boundary condition.

Tidal Driven Flow

Two tests were employed to check the model's ability to simulate the vertical structure of tidal flow. The first test case is a point model in which the bottom boundary is specified using a no-slip condition, and the water slope is assumed known. The model was tested against constant and linearly varying vertical eddy viscosities. In the second test a bottom stress condition was employed at the sea bed. The bottom friction was linearized and related to the vertically averaged velocity.

Point Model Test

Constant Viscosity

The analytic solution for this problem was given in article 347 in Lamb (1945). The following data are used in model

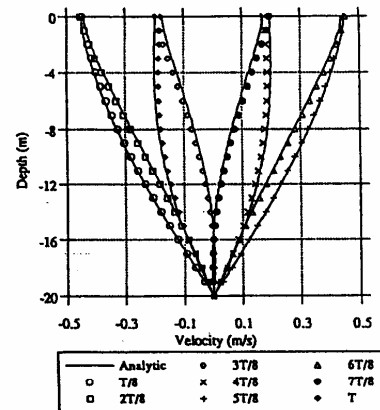


FIG. 3. Comparison of Model Predicted Velocity Structure with Analytic Solution for Tidally Driven Flow (Imposed Pressure Gradient of 0.058 N/m^2) with Constant Vertical Viscosity, $A_v = 0.011 \text{ m}^2/\text{s}$ at $1/8$ Time Intervals Through One Tidal Cycle (Time Step, $\Delta t = 279.45 \text{ s}$)

testing. The imposed pressure gradient was 0.058 N/m^2 ; period $T = 12.42 \text{ h}$; depth $h = 20 \text{ m}$; vertical viscosity $A_v = 0.011 \text{ m}^2/\text{s}$; and time step $\Delta t = 279.45 \text{ s}$ (160 steps per cycle). The test was performed using 20 levels. The model was started with zero velocities. The water slope was applied gradually (linear ramp over 4 cycles) until a steady state was achieved. Comparison between the analytic solution and the model prediction is shown in Fig. 3. The agreement is excellent throughout the water column.

Viscosity Varying Linearly with Height

Two simulations were studied with viscosity; one increasing and one decreasing linearly from the sea bed to the sea surface. The analytic solution is presented in Prandle (1982). Simulations were performed using the same depth, grid size, period, time step, sea surface slope, and initial condition as the constant viscosity test case.

In the case of viscosity increasing linearly from the bottom (sea surface), the viscosity at the sea bed (surface) is set at $A_v = 0.001 \text{ m}^2/\text{s}$; and the viscosity at the sea surface (bed) $A_v = 0.021 \text{ m}^2/\text{s}$. The results of these simulations are in excellent agreement with the analytic solutions. The boundary layer in the linearly increasing case is (referenced from the sea bed) thinner than the constant viscosity case due to the lower viscosity near the bottom. The boundary layer for the linearly decreasing case is thicker than for the constant viscosity case and occupies the whole water column due to the fact that the vertical viscosity at the bottom is higher than in the two previous cases.

3D Testing

Lynch and Officer (1985) derived an analytic solution for the 3D flow driven by periodic forcing, with linearized bottom stress (ku_b , kv_b) and linked to the vertically averaged solution for an annular channel. The solutions were assembled from one-dimensional (1D) vertical diffusion and 2D vertically averaged solutions of the governing equations.

Consider the quarter-circle geometry with quadratically varying bathymetry $h = h_0 r^2$. Note r refers to the radius of the annular channel. The sketch of geometry, bathymetry, and grid configuration are shown in Fig. 4. The viscosity is constant throughout the depth. The analytic solution, however, requires that $A_v/(\Omega h^2)$ and kh/A_v be constant, and hence A_v and k must

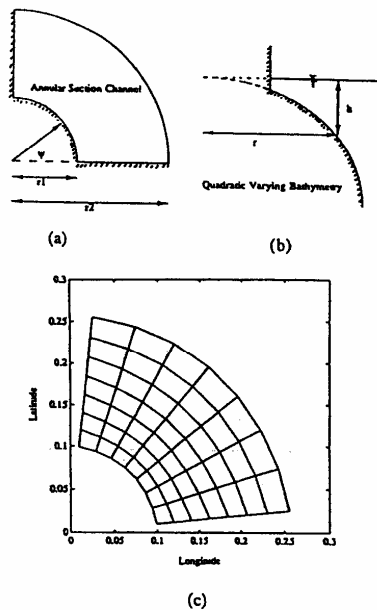


FIG. 4. Three-Dimensional Tidally Driven Model Test for: (a) Geometry; (b) Bathymetry; and (c) Grid Configuration [$r_1 = 9,950$ m; $r_2 = 31,250$ m; $h = 5 (r/r_1)^2$]

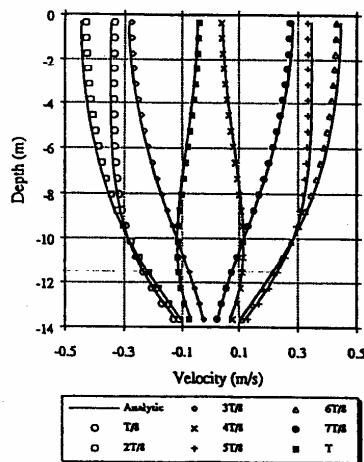


FIG. 5. Vertical Structure of Velocity at increments of $1/8$ of M_2 Tidal Period at $r = 16,660$ m and $\Psi = 39.4^\circ$ for Three-Dimensional Model Test in Annular Section Channel, $r_1 = 9,950$ m; $r_2 = 31,250$ m; $A_o/(\Omega h^2) = 0.1$; $kh/A_o = 10$; $\Delta t = 558.9$ s

vary horizontally. Model tests were performed using a coarse, slightly nonorthogonal 7×7 grid system. The following parameters were used: inner radius $r_1 = 9,950$ m; outer radius $r_2 = 31,250$ m; $\Omega = 1.4 \times 10^{-4} \text{ s}^{-1}$; $kh/A_o = 10$; $A_o/(\Omega h^2) = 0.1$; and $h_o = 5/r_1^2 \text{ m}^{-1}$. The open boundary was specified by varying the tidal amplitude $\zeta_o = 0.1 \cos(2\psi)$ m, where ψ = rotation angle. The model was run using eight and 20 levels in the vertical and time steps of 279.45, 558.9, and 1117.8 s.

Comparison of the model and analytical solution at point (5, 5) or at radius 16,660 m and $\psi = 39.375^\circ$ for 20 levels with a time step of 558.9 s at one-eighth period increment is

shown in Fig. 5. The agreement is very good. The largest errors ($<10\%$) are near the surface area.

Sensitivity of the model predicted near surface currents (at $T/8$, $T/4$, $3T/8$, $T/2$) to grid resolution and time step in the near surface region is shown in Table 1. The maximum errors occur at slack tide (at $T/2$). The model predicted errors decrease with decreasing time step. Model errors using eight vertical levels are approximately the same as those using 20 vertical levels.

A vector plot of the velocity field at the surface at $T/4$ (not presented) shows that the agreement between model predictions and analytic solution is excellent, even though the grid was relatively coarse and slightly nonorthogonal. The errors are less than 5%, except at the corner point of the inner radius $r = r_1$. Here they are about 10% due to the fact that the velocity is very small at this location. The errors become much smaller ($<0.6\%$) at the outer radius near the open boundary. Comparison of the model-predicted velocity time series at a radius of 16,660 m, $\psi = 39.375^\circ$, and for 0.35 m and 13.65 m below the sea surface with the analytic solution are shown in Fig. 6. The bottom velocity leads the surface velocity by 0.85 h. Predictions are again in excellent agreement with the analytic solution.

Turbulence Model Simulations

A simulation was performed in an open-closed, rectangular channel driven with tidal forcing, and a water depth of 10 m. The channel length is 51.34 km, and is represented by 20 horizontal grids. The tidal amplitude was 1.2 m, with a period of 12.42 h, $\gamma = 0.4$. A point 5.55 km from the open channel, where the pressure gradient has a magnitude that would give a current with amplitude 1.0 m/s in an inviscid calculation, was chosen to study the vertical structure of the velocity, eddy viscosity, and turbulent energy. The simulation assumed a ho-

TABLE 1. Model Prediction Errors (%) of Surface Velocity at $r = 16,660$ m and $\Psi = 39.4^\circ$ for Annular Section Channel with Quadratic Bathymetry Using 8 and 20 Vertical Levels with Time Steps of 279.45, 558.9, and 1117.8 s

t (1)	8 Level			20 Level		
	279.45 s (CFL = 0.5)	558.9 s (CFL = 1.0)	1117.8 s (CFL = 2.0)	279.45 s (CFL = 3.1)	558.9 s (CFL = 6.2)	1117.8 s (CFL = 12.4)
	(2)	(3)	(4)	(5)	(6)	(7)
$T/8$	4.1	4.2	4.8	3.9	4.0	4.6
$T/4$	3.7	3.7	4.0	3.5	3.5	3.9
$3T/8$	3.1	3.0	3.0	3.1	3.0	3.0
$T/2$	8.7	10.0	12.6	7.6	8.8	11.6

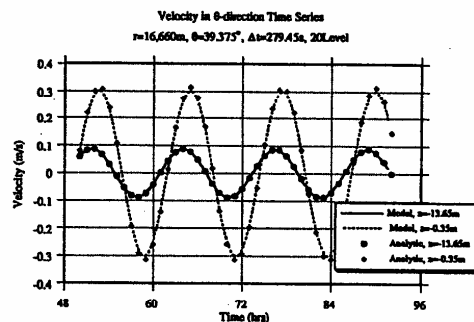


FIG. 6. Comparison of Model Predicted Velocity Time Series with Analytical Solution at $r = 16,660$ m and $\Psi = 39.4^\circ$ for Three-Dimensional Model Test in Annular Section Channel Driven by M_2 Tide at Open Boundary with Varying Amplitude of $\zeta_o = 0.1 \cos(2\psi)$ m; $r_1 = 9,950$ m; $r_2 = 31,250$ m; $A_o/(\Omega h^2) = 0.1$; $kh/A_o = 10$; $\Delta t = 279.45$ s; and 20 Vertical Levels

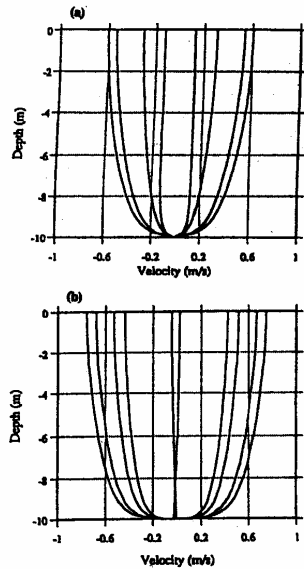


FIG. 7. Comparison of (a) Model Predicted Vertical Structure of Velocity with (b) Numerical Simulations of Davies and Jones (1990) for One-Dimensional Turbulence Model Test Driven by M_2 Tide with Imposed Pressure Gradient of 0.14 N/m^2 ; No-Slip Bottom Boundary Condition; $\gamma = 0.4$; $\Delta t = 558.9 \text{ s}$; and 40 Vertical Levels

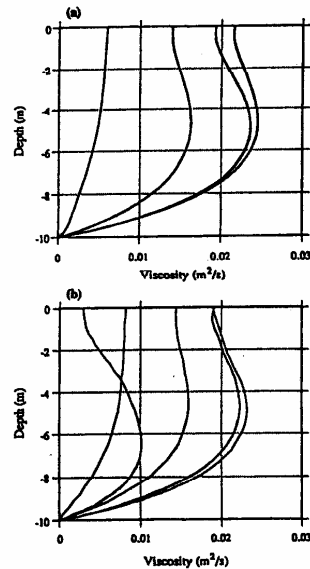


FIG. 8. Comparison of (a) Model Predicted Vertical Structure of Viscosity with (b) Numerical Simulations of Davies and Jones (1990) for One-Dimensional Turbulence Model Test Driven by M_2 Tide with Imposed Pressure Gradient of 0.14 N/m^2 ; No-Slip Bottom Boundary Condition; $\gamma = 0.4$; $\Delta t = 558.9 \text{ s}$; and 40 Vertical Levels

homogeneous fluid. The Coriolis, baroclinic, and advective terms were neglected to compare the present results with the circulation and turbulence model developed by Davies and Jones (1990).

For a no-slip condition at the bottom boundary, simulations

were conducted using 40 levels with a time step of 558.9 s . A comparison between the results of the present model (40 levels) and Davies and Jones' (1990) with 100 levels and a logarithmic transformation is shown in Figs. 7–10. Results are given at one-eighth intervals during the tidal cycle. The maximum surface velocity of the present model is about 20%

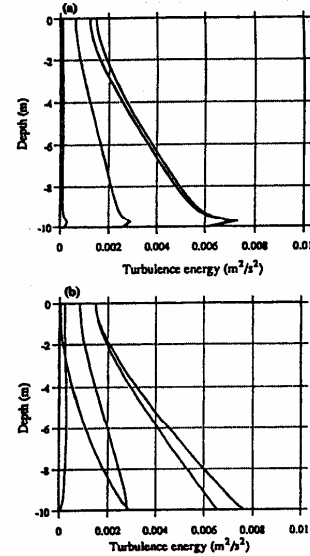


FIG. 9. Comparison of (a) Model Predicted Vertical Structure of Turbulence Energy with (b) Numerical Simulations of Davies and Jones (1990) for One-Dimensional Turbulence Model Test Driven by M_2 Tide with Imposed Pressure Gradient of 0.14 N/m^2 ; No-Slip Bottom Boundary Condition; $\gamma = 0.4$; $\Delta t = 558.9 \text{ s}$; and 40 Vertical Levels

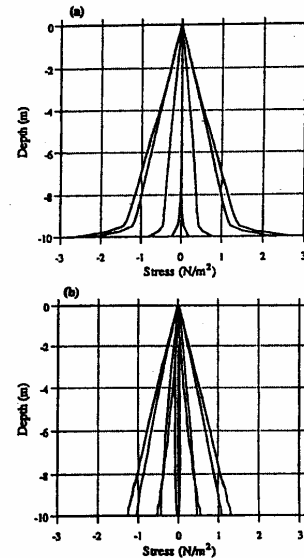


FIG. 10. Comparison of (a) Model Predicted Vertical Structure of Shear Stress with (b) Numerical Simulations of Davies and Jones (1990) for One-Dimensional Turbulence Model Test Driven by M_2 Tide with Imposed Pressure Gradient of 0.14 N/m^2 ; No-Slip Bottom Boundary Condition; $\gamma = 0.4$; $\Delta t = 558.9 \text{ s}$; and 40 Vertical Levels

lower than their results. The structure of the eddy viscosity, turbulent energy, and shear stress are similar. However, the bottom shear stresses are twice as high in Davies and Jones (1990) than in the present simulation because the present grid structure does not provide sufficient resolution in the near-bed region. This problem is more severe at low grid resolution.

For the bottom stress specification, simulations were performed using 10 and 40 levels with a time step of 279.45 s. In these simulations the bottom drag coefficient was set at 0.0025, and $\gamma = 0.4$. A comparison between simulations using high (40 levels) and low vertical resolution (10 level) is shown in Fig. 11 for the velocity profile. The maximum viscosity, shear stress, and energy (not shown) computed using the low resolution grid are approximately 25% higher than simulations using the high resolution grid. The velocity structure (Fig. 11), however, is not significantly affected. Further tests showed that a stable and accurate velocity prediction can be obtained using

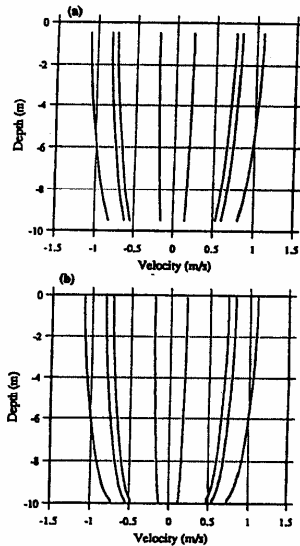


FIG. 11. Comparison of Model Predicted Vertical Structure of Velocity Using (a) 10 and (b) 40 Vertical Levels at Location 5.55 km from Open Boundary for Turbulence Model Test Driven by M_2 Tide; Bottom Stress Condition; $\gamma = 0.4$; $C_b = 0.0025$; $\Delta t = 558.9$ s

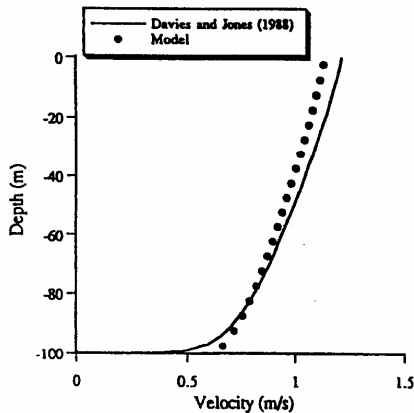


FIG. 12. Comparison of Model (Bottom Stress Condition) Predicted Vertical Structure of Velocity with Numerical Simulations of Davies and Jones (1988) Driven by Wind Stress; $\tau_a = 1.0 \text{ N/m}^2$; $C_b = 0.0025$; and $\gamma = 0.2$

a time step of 1117.8 s (550 CFL, based on the diffusive time scale for 40 levels).

The model was also tested against steady wind-induced flow with a depth of 100 m, a wind stress of 1 N/m^2 , a bottom stress specification; 20 levels, with a friction coefficient of, $C_b = 0.0025$, and $\gamma = 0.2$. A comparison of the velocity computed using the present model and similar results by Davies and Jones (1988) with 100 levels and a logarithmic transformation is presented in Fig. 12. The agreement is very good. A maximum difference of 5% is predicted near the surface and the sea bed. The model-predicted vertical structure of viscosity gives excellent agreement at middepth and near the surface, but slightly overpredicts at the bottom. The turbulent energy simulated by the present model is higher than Davies and Jones' (1988) model both at the surface and bottom. Differences that occur near the bottom are due to differences in the bottom boundary condition specification. The present simulations employ a bottom stress condition where the turbulent energy at the sea bed is specified while Davies and Jones (1988) use a no-slip bottom condition and specify no energy flux at the sea bed. In general the agreement is excellent although the present work uses relatively low grid resolution compared to Davies and Jones (1988).

Salinity Intrusion Simulations

Ippen and Harleman (1961) derived an analytical solution for salinity intrusion under the assumption that the salinity distribution can be represented by the equilibrium of the 1D convective-diffusion processes where the time and cross-sectionally averaged fresh water (seaward) flux of salt is balanced by the horizontal diffusive flux of salt (landward). The effect of gravitational convection by density differences (density included) is neglected. Consider a rectangular channel with a length of 105.5 km, a river flow velocity of 0.000714 m/s , and horizontal diffusion coefficients of 4, 6, 8, and $10 \text{ m}^2/\text{s}$. The advective term in the salt transport equation is solved by the Lax-Wendroff method. The open boundary is specified by a constant salinity of 30 ppt. Comparison between model predictions and the analytic solution for various values of the horizontal diffusion coefficient D_h is shown in Fig. 13. The agreement between the model and analytical solution is excellent.

Finally the model was used to predict the salinity intrusion in Rotterdam Waterway using identical conditions to those employed by Smith and Takhar (1981). The simulation was intended to evaluate the ability of the model to predict salinity intrusion. The waterway was represented by a rectangular channel with a length of 99 km. The width and depth were

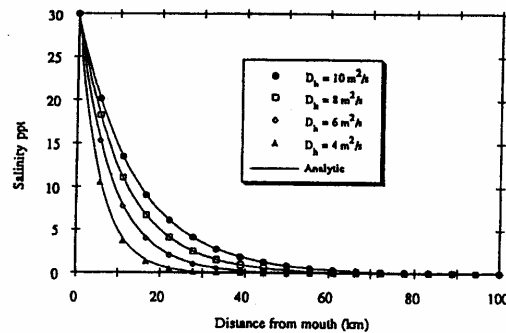


FIG. 13. Comparison of Model Predicted Salinity Distribution with Analytic Solution for One-Dimensional Salinity Intrusion Test (Transport Equation is Solved by Lax-Wendroff Method; River Flow Velocity is 0.000714 m/s ; and Horizontal Diffusion Coefficients of 4, 6, 8, and $10 \text{ m}^2/\text{s}$ Are Used)

kept constant with values of 400 and 13 m, respectively. The river inflow was 1,000 m³/s. The model was run using 40 grids along the channel and 20 levels in the vertical. The initial conditions for velocity, elevation, and salinity were set to zero. Along the open boundary (mouth) the salinity distribution is assumed to vary from 30 ppt at the bottom to 20 ppt at the surface on inflow. The model was run with an M_2 tide. The time step was 558.9 s with a tidal amplitude at the open boundary of 0.9 m. The advective term in the salt transport equation was solved using the upwind method. The Lax-Wendroff method was not used because it required a large horizontal diffusivity (~ 5000 m²/s) to maintain stability. The model was run for 66 d to achieve steady state.

A simulation was performed in which the vertical viscosity and diffusivity were calculated by the turbulence model. The bottom friction, C_b , was 0.0010. It was found that the model was very sensitive to the value of γ in the mixing length specification. Since the turbulent energy source is from the bottom boundary, the bottom drag coefficient, C_b , is also important in determining the vertical velocity structure. Fig. 14 shows the salinity distribution along the channel for $C_b = 0.0005$ and $\gamma = 0.03$ with the empirical formulation of (30), which was taken from Officer (1976), implemented to represent stratification effects. Smith and Takhar's (1981) model predictions and field observations are also shown [Fig. 14(a)]. The results show that the model-predicted high tide salinity distribution is in reasonable agreement with and an improvement over Smith and Tak-

har's results. Both the present and Smith and Takhar (1981) models do not accurately predict the low tide salinity distribution. As analyzed by Smith and Takhar (1981), the poor model performance for the low water salinity distribution is caused by the dock system in the waterway acting as a source and sink of salt on the ebb and flood tide, respectively.

CONCLUSION

A detailed description of the 3D boundary-fitted circulation model in spherical coordinates for coastal waters is presented. Both the dependent and independent horizontal variables are transformed to a boundary-fitted coordinate system. The equations are also transformed to σ -coordinates to resolve the variation in bathymetry. Both the exterior and interior mode are solved using the same time step. The numerical scheme is second order in time and space. The time step is not restricted by the shallow water gravity wave and vertical diffusion CFL criteria. The eddy viscosity/diffusivity can be specified or obtained from a one equation turbulence energy model.

A series of model tests to linear problems shows that the present model is fully capable of predicting the vertical structure of the flow in response to tidal, wind, river, and density forcing. The 3D model test in an annular section channel with quadratic bathymetry under tidal forcing has shown the model's ability to resolve a more complicated geometry and bathymetry.

The model, with a bottom stress condition, gives good predictions of the vertical structure of the velocity, shear stress, turbulence energy, and eddy viscosity even at modest vertical grid resolutions. No iteration or filtering is employed. The no-slip bottom boundary condition version of the present model fails to accurately predict the shear stress and energy distributions at the sea bed for 40 vertical levels because of the lack of vertical resolution near the sea bed.

Agreement between the model and analytic solution is excellent for the 1D salinity intrusion problem where the density gradient induced flow is neglected. The model accurately predicted the salinity distribution at high tide in the Rotterdam Waterway where the viscosity/diffusivity were obtained from a turbulence model. The poor results at low tide were probably caused by the lack of consideration of the effect of the dock system on the salinity field (Smith and Takhar 1981).

The CPU time of the internal mode with turbulence model for each water cell per computational step is 3.1×10^{-6} min on a 486/50 MHz personal computer system using a Lahey F7732 Version 5.1 Fortran compiler. The CPU time of the external mode is 2.9×10^{-6} min using the same machine and compiler.

APPENDIX I. REFERENCES

- Abraham, G. (1988). "Turbulence and mixing in stratified tidal flows." *Physical processes in estuaries*, P. Dronkers and R. Leussen, eds., Springer-Verlag KG, Berlin, Germany.
- ASCE Task Committee on Turbulence Models in Hydraulic Computations. (1988). "Turbulence modeling of surface water flow and transport: Part I." *J. Hydr. Engrg.*, ASCE, 114(9), 970-991.
- Blackadar, A. K. (1962). "The vertical distribution of wind and turbulent exchange in a neutral atmosphere." *J. Geophys. Res.*, 67, 3095-3120.
- Celik, I., and Rodi, W. (1985). "Calculation of wave-induced turbulent flows in estuaries." *Oc. Engrg.*, 12(6), 531-542.
- Cheng, R. T., and Smith, P. E. (1990). "A survey of three-dimensional numerical estuarine models." *Estuarine and coastal modeling*, M. L. Spaulding, ed., ASCE, New York, N.Y., 1-15.
- Davies, A. M., and Jones, J. E. (1988). "Modelling turbulence in shallow sea regions." *Small-scale turbulence and mixing in the ocean, Proc., 19 Liege Colloquium on Oc. Hydrodyn.*, J. C. Nihoul and B. M. Jamart, eds., Univ. of Liege, Liege, Belgium.
- Davies, A. M., and Jones, J. E. (1990). "On the numerical solution of the turbulence energy equations for wave and tidal flows." *Int. J. for Numer. Meth. in Fluids*, 11, 1-25.

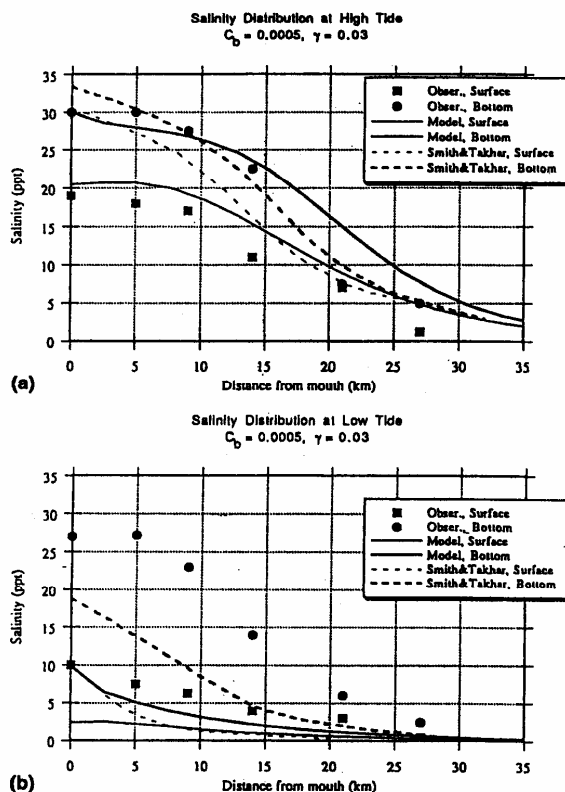


FIG. 14. Comparison of Model Predicted Salinity Distribution along Channel with Observations and Numerical Simulation of Smith and Takhar (1981) for Rotterdam Waterway at: (a) High Tide; and (b) Low Tide (Vertical Viscosity and Diffusivity Are Obtained from Turbulence Model Using Bottom Friction; $C_b = 0.0005$; and $\gamma = 0.3$)

- Fletcher, C. A. J. (1988). *Computational techniques for fluid dynamics, volume I, fundamental and general techniques*. Springer-Verlag New York, Inc., New York, N.Y.
- Ippen, A. T., and Harleman, D. R. F. (1961). "One-dimensional analysis of salinity intrusion in estuaries." *Tech. Bull. No. 5*, Com. on Tidal Hydr., U.S. Army Corps of Engrs., Fort Belvoir, Va.
- Johnson, B. H. (1980). "VAHM-A vertically averaged hydrodynamic model using boundary-fitted coordinates." *MP HL-80-3*, U.S. Army Corps of Engrs. Wtrwy. Experiment Station, Vicksburg, Miss.
- Lamb, H. (1945). *Hydrodynamics*. Dover Publications, Inc., New York, N.Y.
- Lynch, D. R., and Gray, W. G. (1978). "Analytic solutions for computer flow model testing." *J. Hydr. Div.*, ASCE, 104(00), 1409-1428.
- Lynch, D. R., and Officer, C. B. (1985). "Analytic solutions for three-dimensional hydrodynamic model testing." *Int. J. for Numer. Meth. in Fluids*, 5, 529-543.
- Lynch, D. R., and Werner, F. E. (1987). "Three-dimensional hydrodynamics on finite-element. Part I: Linearized harmonic model." *Int. J. for Numer. Meth. in Fluids*, 7, 871-909.
- Moffeld, H. O., and Lavelle, J. W. (1984). "Setting the length scale in a second-order closure model of the unstratified bottom boundary layer." *J. Phys. Oceanography*, 14, 833-839.
- Muin, M. (1993). "A three-dimensional boundary-fitted circulation model in spherical coordinates." PhD dissertation, Univ. of Rhode Island, Narragansett Bay Campus, Narragansett, R.I.
- Muin, M., and Spaulding, M. L. (1996). "Two-dimensional boundary-fitted circulation model in spherical coordinates." *J. Hydr. Engrg.*, ASCE, 122(9), 512-521.
- Munk, W. H., and Anderson, E. R. (1948). "Notes on theory of thermocline." *J. Marine Res.*, 7, 276.
- Officer, C. B. (1976). *Physical oceanography of estuaries*. John Wiley & Sons, Inc., New York, N.Y., 120.
- Prandt, D. (1982). "The vertical structure of tidal currents." *Geophys. Astrophys. Fluid Dyn.*, 22, 29-49.
- Sheng, Y. P. (1986). "A three-dimensional mathematical model of coastal, estuarine and lake currents using boundary-fitted grid." *Tech. Rep. No. 585*, Aeronautical Research Associates of Princeton, Princeton, N.J.
- Smith, T. J., and Takhar, H. S. (1981). "A mathematical model for partially mixed estuaries using the turbulence energy equation." *Estuarine, Coast., and Shelf Sci.*, 13, 27-45.
- Spaulding, M. L. (1984). "A vertically averaged circulation model using boundary-fitted coordinates." *J. Phys. Oceanography*, 14, 973-982.
- Swanson, J. C. (1986). "A three-dimensional numerical model system of coastal circulation and water quality." PhD dissertation, Univ. of Rhode Island, Kingston, R.I.

APPENDIX II. NOTATION

The following symbols are used in this paper:

- A_v = vertical eddy viscosity;
 a = tidal wave amplitude;
 b = turbulence kinetic energy;
 C_μ = empirical constant in eddy viscosity relationship;
 C_s = drag coefficient at surface;
 C_b = drag coefficient at bottom;
 C_d = empirical constant in energy dissipation relationship;
 D = elevation + water depth;

- D_h = horizontal eddy diffusivity;
 D_v = vertical eddy diffusivity;
 g = gravitation;
 h = water depth;
 J = Jacobian of curvilinear coordinate;
 K = Von Karman constant;
 k = linearized bottom friction;
 L = wave length;
 L_m = mixing length;
 l = length of channel;
 n = node number;
 p = pressure;
 q = concentration of substance;
 R = radius of earth;
 R_i = Richardson number;
 S = salinity;
 T = wave period;
 t = time;
 u_o = river flow;
 U_{*s} = friction velocity due to wind stress;
 U_{*b} = friction velocity due to bottom stress;
 U, V = vertically averaged velocity in ϕ and θ direction;
 U^*, V^* = vertically averaged velocity in curvilinear coordinate;
 u, v, w = water velocity in ϕ, θ, r direction;
 u^*, v^* = water velocity in curvilinear coordinate;
 u_b = bottom velocity in ϕ direction;
 v_b = bottom velocity in θ direction;
 W_ϕ = wind speed in ϕ direction;
 W_θ = wind speed in θ direction;
 β = volumetric expansion coefficient;
 γ = constant parameter in mixing length formulation;
 ϵ = dissipation rate of energy;
 ζ = water elevation;
 ζ_o = water elevation amplitude at open boundary;
 Θ = temperature °C;
 ι = water surface slope;
 κ = wave number;
 Λ = horizontal density gradient;
 ξ, η = generalized curvilinear coordinate system;
 ρ = water density;
 ρ_a = air density;
 ρ_o = water density average;
 $\bar{\rho}$ = vertically averaged of water density;
 ρ' = vertically density difference;
 σ = vertical coordinate transformation;
 σ_s = empirical diffusion constant;
 σ_r = Schmidt number;
 τ_b = bottom shear stress;
 τ_s = wind shear stress;
 Φ = mean scalar quantity;
 ϕ, θ, r = spherical coordinate system;
 Ω = wave frequency; and
 ω = vertical velocity in σ transform coordinate.

**Appendix D: Development of an Estuarine Thermal Environmental Model in a Boundary
Fitted, Curvilinear Coordinate System (Mendelsohn, 1998)**

Development of an Estuarine Thermal Environmental Model in a Boundary-Fitted, Curvilinear Coordinate System

**Daniel L. Mendelsohn
Applied Science Associates, Inc.
Narragansett, Rhode Island 02882**

INTRODUCTION

With the deregulation of the power industries in the United States there has been a rekindled interest in the development of new power generation station and the re-permitting of existing older or dormant stations. In the last two decades however increased public awareness of the possible adverse environmental effects of using ‘once through cooling’ in natural water bodies has lead to substantial pressure on regulators as well as the utilities to study, understand and mitigate against potential degradation. Once through cooling involves the intake of water from a natural water body, (e.g. river, lake, estuary), the use of that water to cool process water, (e.g. to condense steam) and the subsequent expulsion of the now warmer water back into the environment. The incentives for this form of cooling are both efficiency and economics.

The two most prevalent and more important concerns associated with once through cooling are: 1) the potential an unacceptable increase in temperatures in the power station effluent receiving waters; 2) the possibility that increased surface water temperatures will enhance thermal stratification of the water column resulting in a reduction of hypolimnetic reaeration. Increased temperature and reduced oxygen are both considered degradation of habitat and can cause avoidance and increased mortality to indigenous marine floral and faunal populations. For the case of an existing facility, when measurements of temperature and dissolved oxygen are made in the environment, the question is, to what extent are those measurements influenced by the thermal effluent? These are difficult concerns to address in both the scientific and the regulatory realms. Increasingly, parties involved in the decision making process have come to rely on computer modeling to address the physical, chemical and, occasionally, biological aspects of a problem, allowing regulatory and engineering decisions to be made on a solid scientific basis.

Recent improvements in computing power and observational data retrieval, storage and dissemination have made possible the development and application of a new generation of hydro-thermal models capable of addressing the concerns listed above.

THERMAL MODEL DEVELOPMENT

The development of the temperature model follows the formulation of the coupled, three-dimensional, boundary-fitted, general curvilinear coordinate, hydrodynamic and salinity transport model system for which it is to become a component. For a detailed description of the hydrodynamic model system development and testing the interested reader is referred to Muin and Spaulding, 1997 a; Mendelsohn et al. 1995 and Muin, 1993. Additional model applications can be found in Muin and Spaulding, 1997 b; Huang and Spaulding, 1995a,b; Swanson and Mendelsohn, 1996, 1993; Peene et.al. 1998.

The temperature model is designed to be integrated into and coupled with the hydrodynamic model system and use the transformed currents directly. The temperature equation must therefore be transformed as well.

Conservation of Temperature

Starting with the differential form of the conservation of energy equation, the three-dimensional conservation of temperature equation in spherical polar coordinates can be written as follows:

$$\frac{\partial T}{\partial t} + \frac{u}{r \cos \theta} \frac{\partial T}{\partial \phi} + v \over r \frac{\partial T}{\partial \theta} + w \frac{\partial T}{\partial r} = \frac{Q_s}{\rho C_p V} + \frac{q_{env}}{\rho C_p \delta r} + \frac{\partial}{\partial r} (A_v) + \frac{A_h}{r^2} \left[\frac{\partial^2 T}{\cos^2 \theta \partial \phi^2} + \frac{\partial^2 T}{\partial \theta^2} \right] \quad (1)$$

where,

- T = temperature, (°C)
- t = time, (s)
- u = east, ϕ , velocity vector component, (m/s)
- v = north, θ , velocity vector component, (m/s)
- w = vertical, r, velocity vector component, (m/s)
- A_v = vertical eddy diffusivity, (m²/s)
- A_h = horizontal eddy diffusivity, (m²/s)

Q_s	= system heat sources and sinks, (W)
q_{env}	= net surface heat exchange with the environment, (W/m ²)
ρ	= water density, (kg/m ³)
C_p	= specific heat of water, (J/kg °C)
V	= volume, (m ³)

The horizontal velocities and independent variables are next transformed to a general curvilinear coordinate system in the horizontal and at the same time the well known sigma transform, (Phillips, 1956) is applied in the vertical. The equations for the conservation of substance in a curvilinear coordinate system (ξ, η) in terms of the contravariant velocity components are as follows:

$$\frac{\partial T}{\partial t} + \frac{u^c}{r \cos \theta} \frac{\partial T}{\partial \xi} + \frac{v^c}{r} \frac{\partial T}{\partial \eta} = \frac{Q_s}{\rho C_{sub} V} + \frac{2q_{env}}{\rho C_p D \delta \sigma} + \frac{4}{D^2} \frac{\partial}{\partial \sigma} \left(A_v \frac{\partial T}{\partial \sigma} \right) + \frac{A_h}{r^2 J^2} \left[\left(\frac{\theta_\eta \theta_\eta}{\cos^2 \theta} + \phi_\eta \phi_\eta \right) \frac{\partial^2 T}{\partial \xi^2} - 2 \left(\frac{\theta_\xi \theta_\eta}{\cos^2 \theta} + \phi_\xi \phi_\xi \right) \frac{\partial^2 T}{\partial \xi \partial \eta} + \left(\frac{\theta_\xi \theta_\xi}{\cos^2 \theta} + \phi_\xi \phi_\xi \right) \frac{\partial^2 T}{\partial \eta^2} \right] \quad (2)$$

where,

u^c	= contravariant velocity component in the ξ direction
v^c	= contravariant velocity component in the η direction
σ	= transformed vertical coordinate
ζ	= water surface elevation, (m)
D	= total depth = ζ + local depth, (m)
J	= the Jacobian = $\phi_\xi \phi_\eta - \phi_\eta \theta_\xi$

The relationship between the contravariant transformed velocities (u^c, v^c) and physical velocities in spherical coordinates (u, v) is given by

$$\begin{aligned} u &= \cos \theta \phi_\xi u^c + \cos \theta \phi_\eta v^c \\ v &= \theta_\xi u^c + \theta_\eta v^c \end{aligned} \quad (3)$$

The temperature transport model (Eq. 2) is solved by a simple explicit technique except for the vertical diffusion term which is solved by a three time level, implicit scheme to ease the time step restriction due to the small vertical length scale. The advection terms are solved using either an upwind-differencing scheme which introduces minor numerical (artificial) diffusivities and is first order accurate or the second order accurate QUICKEST formulation.

Experimentation found that although the QUICKEST scheme was for the most part more conservative it was also less stable, requiring a smaller time step and consequently longer run-times than when using the 1st order upwind scheme. Horizontal gradients in temperature, (as well as in salinity, density and pressure) are evaluated along lines of constant depth to reduce the artificial numerical dispersion in the vertical associated with the sigma transform system.

The horizontal diffusion terms are solved by a centered-in-space, explicit technique. The diffusive and advective stability criteria for the numerical techniques are, $\Delta t < \Delta s^2 / (2D_h)$, and $\Delta t < \Delta s / U_s$, where Δs and U_s are horizontal grid size and velocity, respectively.

Bottom Boundary Condition

The water bottom boundary condition is specified to assume that the water and bottom material are in thermal equilibrium, therefore there is no heat transfer between the water in the bottom layer and the bottom boundary. This may be written as:

$$\frac{\partial T_b}{\partial \sigma} = 0 \quad (4)$$

Surface Boundary Condition

At the water surface the temperature is influenced by a number of factors in the environment above. The most important terms in the heat transfer with the environmental can be summarized as follows:

- shortwave solar radiation
- longwave atmospheric radiation
- longwave radiation emitted from the water surface
- convection, (sensible) heat transfer between water and air
- evaporation, (latent) heat transfer between water and air

The net rate of heat transfer with the environment, q_{env} in Eq(2), including the primary forcing factors listed above can be written as:

$$q_{env} = q_{sw} - q_{swr} + q_{lw} - q_{lwr} - q_{lwb} + q_c + q_e \quad (5)$$

where,

- q_{sw} = solar short wave radiation, (W/m²)
- q_{swr} = reflected solar short wave radiation, (W/m²)
- q_{lw} = atmospheric long wave radiation, (W/m²)

$$\begin{aligned}
q_{lwr} &= \text{reflected atmospheric long wave radiation, (W/m}^2\text{)} \\
q_{lw\ b} &= \text{long wave, (back) radiation, emitted by the water surface, (W/m}^2\text{)} \\
q_c &= \text{convection, (sensible) heat transfer, (W/m}^2\text{)} \\
q_e &= \text{evaporation, (latent) heat transfer, (W/m}^2\text{)}
\end{aligned}$$

Each of the terms in the surface heat balance is described below.

Solar shortwave radiation

The solar short wave radiation is often an available, measured quantity, in which case it can be entered directly into the model as data. It can often be obtained from local airport records or from radiation model analyses for example, (DeGaetano et. al., 1993). Local measured radiation data is valued in that it contains information on both the solar radiation and the cloud cover and its influence, and is the actual radiation hitting the water surface at that date and time.

In the absence of data, solar radiation can be predicted following the method as presented by Duffie and Beckman, (1980). Starting with the clear sky radiation, G_{ctot} :

$$G_{ctot} = G_{cb} + G_{cd} \quad (6)$$

where

$$G_{cb} = G_{on} \tau_b \cos \theta_z = \text{clear sky beam radiation} \quad (7)$$

$$G_{cd} = G_{on} \tau_d \cos \theta_z = \text{clear sky diffuse radiation} \quad (8)$$

and the extraterrestrial, normal radiation, G_{on} is defined as

$$G_{on} = G_{sc} [1 + 0.33 \cos (360n / 365)] \quad (9)$$

where

$$G_{sc} = 1353 \text{ (W/m}^2\text{)} = \text{solar constant}$$

The beam and diffuse atmospheric transmittance coefficients, τ_b and τ_d , respectively, can be defined as:

$$\tau_b = a_0 + a_1 e^{-k / \cos \theta_z} \quad (10)$$

where

$$\begin{aligned}
a_0 &= r_0 a_0^* & , a_0^* &= 0.4237 - 0.00821 (6 - A)^2 \\
a_1 &= r_1 a_1^* & , a_1^* &= 0.5055 - 0.00595 (6.5 - A)^2 \\
k &= r_k k^* & , k^* &= 0.2711 - 0.01858 (2.5 - A)^2
\end{aligned}$$

and

$$r_0 = 0.97$$

$$\begin{aligned}
r_l &= 0.99 \\
r_k &= 1.02 \\
A &= \text{altitude, (km)}
\end{aligned}$$

and the diffuse transmittance is,

$$\tau_d = 0.2710 - 0.2939 \tau_b \quad (11)$$

The zenith angle, $\cos \theta_z$ is defined as:

$$\cos \theta_z = \cos \delta \cos \varphi \cos \omega + \sin \delta \sin \varphi \quad (12)$$

where,

$$\begin{aligned}
\varphi &= \text{lattitude, (deg)} \\
\delta &= \text{declination of the sun, (deg)} = 23.45 \sin [360 (284 + n) / 365] \\
n &= \text{day of the year} \\
\omega &= \text{hour angle, (deg)}
\end{aligned}$$

Finally, the hour angle, ω is calculated from the local longitude and solar time as:

$$\omega = (t_s - 12) 15^\circ/\text{hr}$$

where,

$$\begin{aligned}
t_s &= \text{solar time} = \text{standard time} + 4 (L_{st} - L_{loc}) + E \\
L_{st} &= \text{standard meridian, (deg)} \text{ (e.g. } 75^\circ \text{ W for Rhode Island)} \\
L_{loc} &= \text{local longitude, (deg)}
\end{aligned}$$

and E is the equation of time defined by:

$$E = 9.87 \sin 2B - 7.53 \cos B - 1.5 B$$

where,

$$B = [360 (n - 81) / 364]$$

The total clear sky radiation, G_{ctot} can then be corrected for cloud cover effects with the use of a clearness index, K_T . This value can be defined on an monthly, daily or hourly basis dependent on available data and use and is often available with meteorological data when measured radiation data is not. The clearness index is the ratio of the average radiation on an horizontal surface to the average extraterrestrial radiation at the same latitude and longitude;

$$K_t = \frac{\overline{G}}{G_{on}} \quad (13)$$

The value \overline{G} would then be used in place of G_{on} in equations (7) and (8) to create G_{tot} .

Finally, the net solar shortwave radiation, q_{net} , absorbed through the water surface, can be calculated as;

$$q_{net} = q_{sw} - q_{swr} = \alpha_w (1 - \text{albedo}_w) G_{tot} \quad (14)$$

where,

$$\begin{aligned} \alpha_w &= \text{water absorptivity, } (-) \cong 0.97 \\ \text{albedo}_w &= \text{albedo of the water surface } (-), \text{ (see below)} \end{aligned}$$

Reflected solar short wave radiation

The reflected solar short wave radiation, as included in Equation (14), and can defined as;

$$q_{swr} = \text{albedo}_w G_{tot} \quad (15)$$

where the albedo is a measure of the reflective property of the material surface, (water in this case) and can be defined as:

$$\text{albedo}_w = \text{reflected energy} / \text{incident energy}$$

Values for the albedo for water are both a function of wave state and strongly of solar altitude, Stull, (1988). They can range from 0.03 when the sun is overhead to near 1.0 at low elevation angles. Stull, (1988) gives an equation for calculating the albedo for varying solar altitudes, (azimuth angle):

$$\text{albedo}_w = -0.0139 + 0.0467 \tan \theta_z \quad (16)$$

Atmospheric long wave radiation

In addition to the short wave radiation, the atmosphere and the water surface are also exchanging long wave radiation. The atmospheric long wave radiation is a function of the air temperature and water vapor content and may be calculated from an effective sky temperature, (Duffie & Bechman, 1980). From the Stephan-Bolzmann law long wave radiation to the water surface is then:

$$q_{lw} = \sigma_{sb} T_{sky}^4 \quad (17)$$

where,

$$\begin{aligned}\sigma_{sb} &= \text{Stephan-Boltzmann constant, } (5.669 \times 10^{-8} \text{ W / m}^2 \text{ K}^4) \\ T_{sky} &= \text{effective sky temperature, (K)}\end{aligned}$$

Duffie and Beckman suggest that the sky temperature be calculated from an empirical relationship, (Bliss, 1961) as:

$$T_{sky} = \left[0.8 + \frac{(T_{dp} - 273)}{250} \right]^{\frac{1}{4}} \quad (18)$$

where

$$T_{dp} = \text{dew point temperature, (C).}$$

Thomann and Mueller suggest an alternate formulation:

$$q_{lw} = \sigma_{sb} T_{ak}^4 (A + 0.031 \sqrt{e_a}) \quad (19)$$

where

$$\begin{aligned}T_{ak} &= \text{air temperature, (K)} \\ e_a &= \text{vapor pressure at air temperature, } T_a \text{ (mm Hg)} \\ &= (\text{relative humidity fraction}) \times (e_{sat} @ T_a) \\ e_{sat} &= \text{saturation vapor pressure (mm Hg)} \\ T_a &= \text{air temperature, (C)} \\ A &= \text{coefficient to account for air temperature and clearness index, with a} \\ &\quad \text{range of 0.5 - 0.7.}\end{aligned}$$

The saturation vapor pressure can be calculated from the air temperature (T_a) using the following equation, (List, 1951):

$$e_{sat} = 4.58123 \times 10^{[7.5 T_a / T_{ak}]} \quad (20)$$

Results for the two long wave radiation formulations only vary slightly for a given set of conditions with Equation (19) consistently giving a larger value, by approximately 3%, than (17). No independent confirmation for either formulation has been given to date.

Reflected atmospheric long wave radiation

The reflected long wave radiation over a water body is generally small, about 3% of the incoming long wave, (Thomann & Mueller, 1987) and can be calculated as:

$$q_{lwr} = (1 - \epsilon_w) q_{lw} \quad (21)$$

where

$$\epsilon_w = \text{emissivity of water} \cong 0.97$$

Long wave radiation, emitted by the water surface

The water surface also emits long wave radiation at a rate proportional to the surface temperature in Kelvins:

$$q_{lw} = \varepsilon_w \sigma_{sb} T_{wk}^4 \quad (22)$$

where

$$T_{wk} = \text{water surface temperature, (K)}$$

Convection heat transfer

The rate of convective heat transfer between the water surface and the air depends on the temperature difference between the two and is suggested to be proportional to the square of the wind speed, (Thomann and Mueller, 1987; Edinger et. al. 1974). This can be written as,

$$q_c = c_1 (19.0 + 0.95 U_w^2) (T_a - T_w) \quad (23)$$

where

$$T_w = \text{water surface temperature, (C)}$$

$$c_1 = \text{Bowen's coefficient} = 0.47 \text{ mm Hg} / ^\circ\text{C}$$

Evaporation heat transfer

Similar to the rate of convective heat transfer the evaporative heat transfer between the water and the air can be thought of as depending on the difference between the vapor pressures of the two and is also suggested to be proportional to the square of the wind speed, (Thomann and Mueller, 1987; Edinger et. al. 1974). This can be written as,

$$q_c = (19.0 + 0.95 U_w^2) (e_a - e_w) \quad (24)$$

where

$$e_w = \text{vapor pressure at water surface temperature, } T_w \text{ (mm Hg)}$$

REFERENCES

- DeGaetano, Arthur T., Keith L. Eggleston and Warren W. Knapp, 1993. Daily Solar Radiation Estimates for the Northeast United States. Northeast Regional Climate Center Research Series, Publication No. RR93-4, May 1993.
- Duffie, John A. and William Beckam, 1980. Solar Engineering of Thermal Processes. John Wiley and Sons, New York.
- Edinger, J.E., D.K.Brady and J.C. Geyer, 1974. Heat Exchange and Transport in the Environment. Report No. 14, Electric Power Res. Inst. Pub. No. EA-74-049-00-3, Palo Alto, Ca, Nov. 1974, 125pp.
- Huang, W. and M.L. Spaulding, 1995a. Modeling of CSO-induced pollutant transport in Mt. Hope Bay. ASCE J. of Environmental Engineering, Vol. 121, No. 7, July, 1995, 492-498.
- Huang, W. and M.L. Spaulding, 1995b. A three dimensional numerical model of estuarine circulation and water quality induced by surface discharges. ASCE Journal of Hydraulic Engineering, 121:(4) April 1995, p. 300-311.
- List, R.J. 1951/1984. Smithsonian Meteorological Tables. Smithsonian Institution Press, Washington DC.
- Mendelsohn, D.L., E. Howlett and J.C. Swanson, 1995. WQMAP in a Windows Environment. published in proceedings of: 4th International Conference on Estuarine and Coastal Modeling, ASCE, San Diego, October 26-28, 1995.
- Muin, M. and M.L. Spaulding, 1997a. A 3-D boundary-fitted circulation model. Journal of Hydraulic Engineering, Vol. 123, No. 1.
- Muin, M., M.L. Spaulding, 1997b. Application of Three-Dimensional Boundary-Fitted Circulation Model To Providence River, published in: Journal of Hydraulic Engineering, Vol. 123, No. 1.
- Muin, M., 1993. A Three-Dimensional Boundary-Fitted Circulation Model in Spherical Coordinates, Ph.D. Dissertation, Univ. of Rhode Island, Narragansett Bay Campus, Narragansett, RI.
- Peene, S., E. Yassuda and D. Mendelsohn, 1998. Development of a Waste Load Allocation Model within Charleston Harbor Estuary. Phase I: Barotropic Circulation. published in proceedings of: 5th International Conference on Estuarine and Coastal Modeling. Ed Malcolm L. Spaulding and Alan F. Blumberg. ASCE, Alexandria, Virginia, October 22-24, 1997.

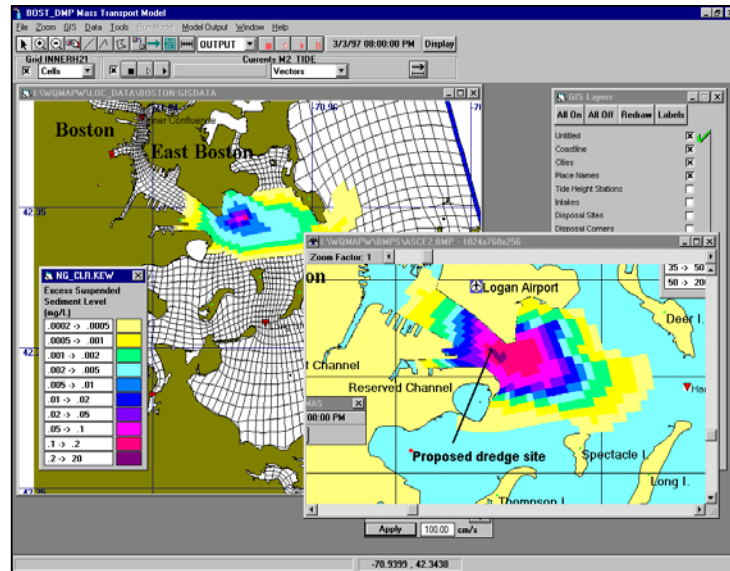
- Phillips, Norman, 1956. Monthly Weather Review, AGU.
- Stull, Roland B., 1988. An Introduction to Boundary Layer Meteorology. Kluwer Academic Publishers, P.O. Box 17, 3300 AA Dordrecht, The Netherlands.
- Swanson, J. C. and D. Mendelsohn, 1996. Water Quality Impacts of Dredging and Disposal Operations in Boston Harbor. presented at: ASCE North American Water and Environmental Congress '96 (NAWEC '96), Anaheim, CA, 22-28 June 1996.
- Swanson, J.C., D. Mendelsohn, 1993. Application of WQMAP to upper Narragansett Bay, Rhode Island. Estuarine and Coastal Modeling III. Proceedings of the 3rd International Conference, sponsored by the Waterway, Port, Coastal and Ocean Division of the ASCE, Oak Brook, IL, September 8-10, 1993.
- Thomann and Mueller, 1987. Principles of Surface Water Quality Modeling and Control. Harper and Row, Publishers Inc., New York, N.Y.

Appendix E: WQMAP Description



Applied Science Associates, Inc.
 70 Dean Knauss Drive
 Narragansett, RI 02882-1143
 U.S.A.
 Tel: 401-789-6224
 Fax: 401-789-1932
 Email: asa@appsci.com
<http://www.appsci.com>

Applied Science Associates, Ltd.
 54 South Street
 St. Andrews, KY16 9JT
 Scotland
 Tel: 01334 478 354
 Fax: 01334 472 893
 Email: asa@sol.co.uk
<http://www.appsci.com>



WWQMAP Product Description

The ASA Water Quality Mapping and Analysis Package (WQMAP) is a set of hydrodynamic and water quality models integrated with a geographical information and environmental data system through an intuitive graphical user interface that runs under Microsoft Windows™. WQMAP is designed with modular elements. A customized suite of hydrodynamic and water quality models is incorporated into WQMAP, reflecting the needs of each user's application.

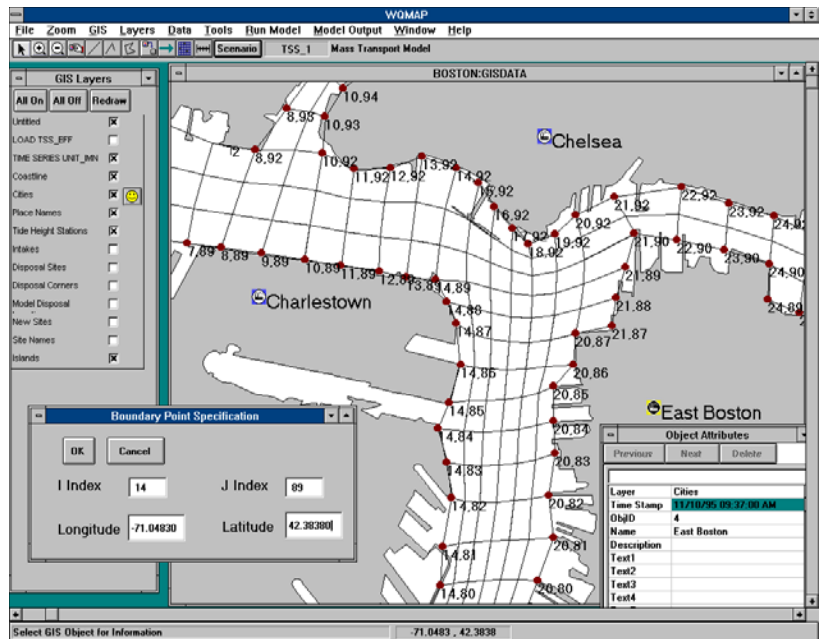
The WQMAP system is based on a state-of-the-art boundary-fitted coordinate modeling technique. Model types include two and three dimensional, time dependent numerical solutions to the basic conservation equations for water mass, momentum, constituent mass, energy, salt, sediment, and other conservative and non-conservative constituents. These models simulate a wide range of physical, chemical, and biological processes in various types of water bodies. They can help analyze system dynamics and predict the impacts of actual events or possible design or management alternatives. The models can be used to estimate currents and water surface elevations, assess water quality and eutrophication, identify pollutant sources, and perform environmental impact assessments.

The basic WQMAP model structure consists of four components:

- **BFGRID: Boundary Fitted Coordinate Grid Generation**
- **BFHYDRO: Boundary Fitted Hydrodynamic Model**
- **BFMASS: Boundary Fitted Pollutant Transport Model**
- **BFWASP: Boundary Fitted Eutrophication Model**

WQMAP COMPONENTS

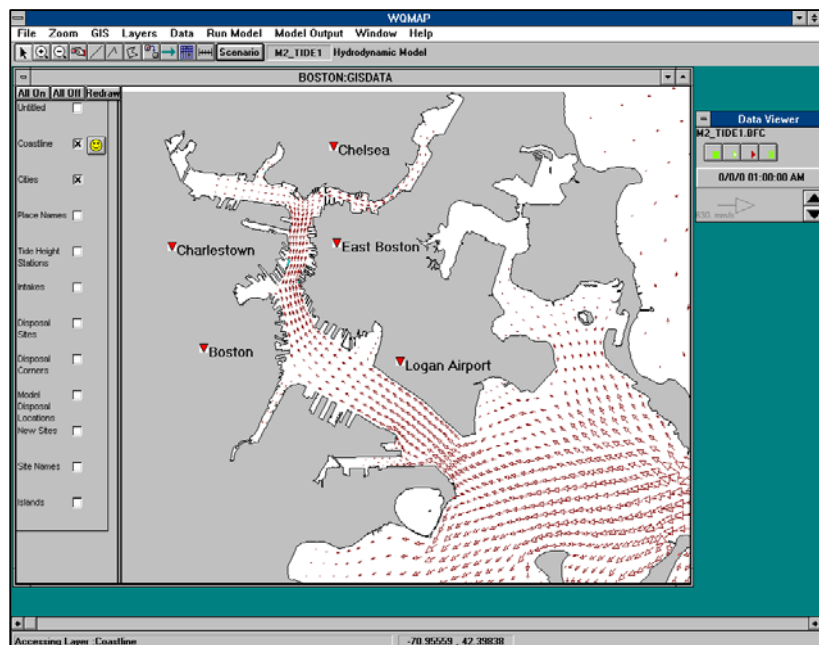
BFGRID: Boundary Fitted Coordinate Grid Generation



The grid generation software is a tool to build a grid, which segments the water body of interest. After the user specifies key grid nodes (grid corners) along the domain boundary, the model interpolates the remaining boundary node locations and then solves a Poisson equation to locate the interior nodes. Editing tools are included to add, delete, and move nodes. The resulting non-orthogonal grid contains quadrilateral areas of various sizes and orientation to resolve fine detail where needed, to cover large areas at coarse resolution where detail is not needed and to map the grid boundaries to the geographical features of the water body being studied. The hydrodynamic and water quality models use this grid to numerically solve the appropriate conservation equations.

BFHYDRO: Boundary Fitted Hydrodynamic Model

The hydrodynamic model solves the water mass and momentum equations on the boundary fitted grid to predict a time varying field of surface elevations and velocity vectors. Boundary forcing includes tides, winds, and river flows and density distributions. The standard model is configured to run in a vertically averaged mode, but can optionally run in a three dimensional mode with prognostic calculation of

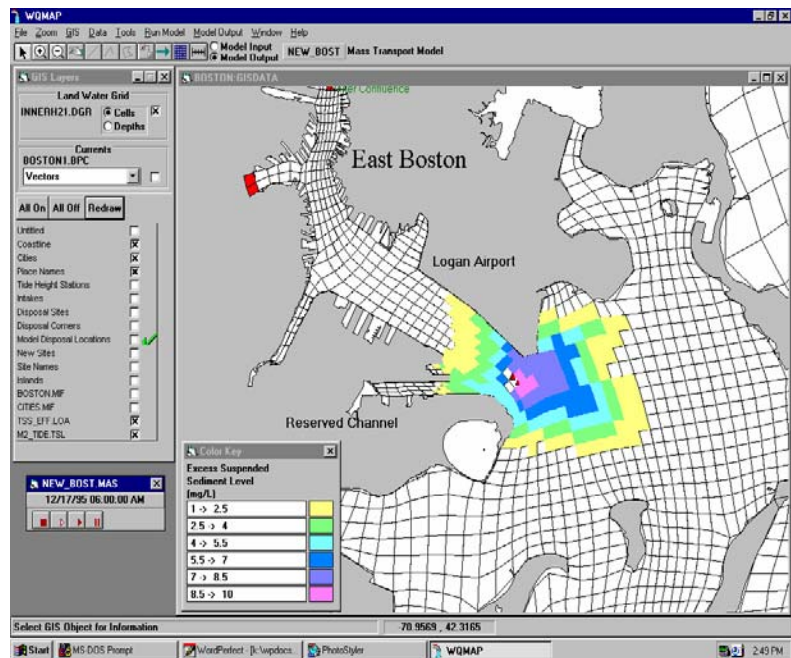


density induced flow, which also predicts a time varying field of salinity and temperature.

BFMASS: Boundary Fitted Pollutant Transport Model System

The pollutant transport model system solves the conservation of mass equation on the boundary fitted grid to predict time varying fields of constituent concentration. Single and multiple, constant and time varying loads can be applied.

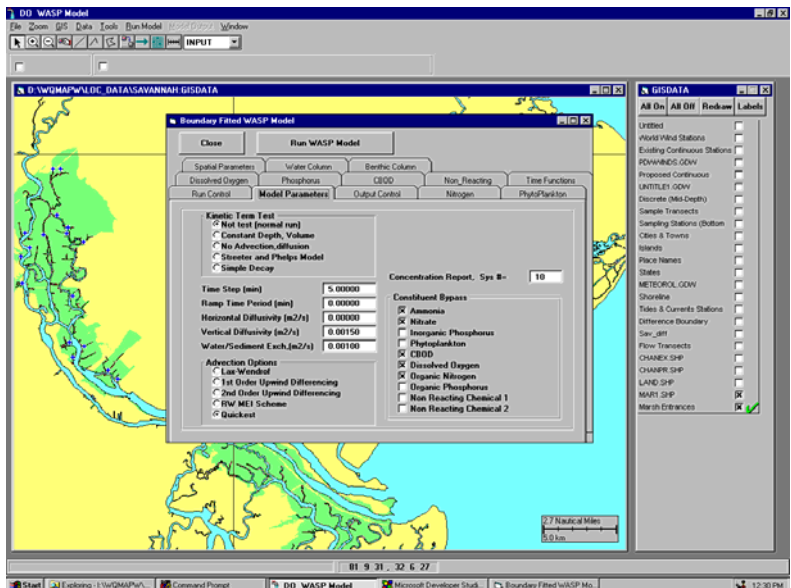
Constituents can include pathogens, excess temperature, metals, suspended sediment, nutrients, organics and conservative tracers. The standard model is configured to run in a vertically averaged mode but can optionally run in three dimensions. The constituent fates model consists of two possible configurations for single independent and multiple, linked or independent constituents incorporating increasingly complex reaction kinetics:



- Single constituent model including first order loss rate terms
- Multiple constituent model linked by a user defined reaction matrix

BFWASP: Boundary Fitted Eutrophication Model System

BFWASP is a multiple constituent eutrophication model incorporating the full EPA WASP EUTRO model kinetic rate equations into the transport model system. The model solves the conservation of mass equations on the boundary fitted grid and the kinetic rate equations to predict the transport and transformation of up to eight state variables. The state variables are components of four basic interacting systems simulating the phosphorus cycle, the nitrogen cycle, phytoplankton kinetics and the dissolved oxygen balance. The model is configured to run in three dimensions with sediment compartments. The formulation includes benthic interactions.



Data Management

For most models, input data describing the study area (land-water grid, bathymetry, and topography), boundary conditions, discharge description, model parameters and output display parameters are required. In general, spatial information input to the model is handled through the gridding module or the WQMAP Geographical Information System, (GIS), time series data through the environmental data management tools and output display through a set of menu options or icon interrogation. Model parameters/options are managed through input forms or optionally through ASCII files.

While output varies with the model or problem of interest, the system supports plan and transect views of scalar and vector quantities. Typical displays include gridded bathymetry, concentration levels, and velocity vectors and particle distributions. In addition, models allow visualization of global mass or term balances of the constituent of concern. For predictions that are time dependent (e.g. velocity vectors, surface elevations, particle trajectories, constituent concentrations) the user interface allows single frame or animated views. In animations the user can use pause, stop, forward/reverse (fast/slow) and single step to assist in viewing the predictions.

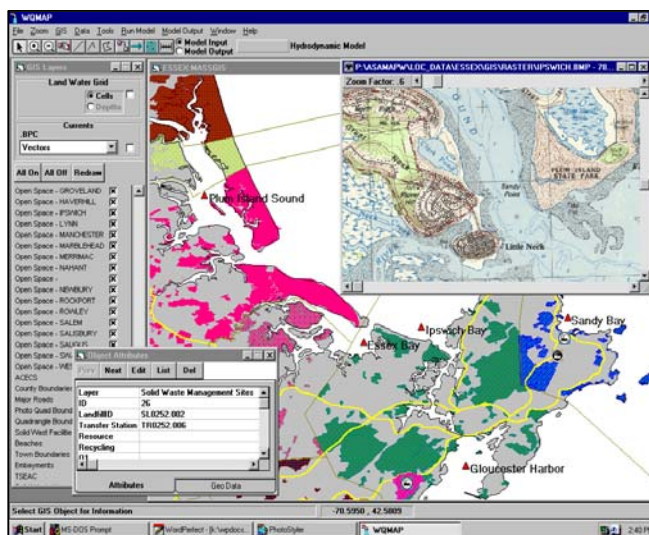
Geographic Location

WQMAP is supplied with one base map, or location. Additional areas may be added as enhancements to the basic system. This base map serves as the largest domain over which the model will be employed. Application locations range from small rivers, lakes and estuarine systems with scales of kilometers to bays, seas and continental shelves, with scales of tens to hundreds of kilometers. For each location a geo-referenced shoreline and bathymetry is created from either charts or electronic data.

The user can have as many locations in the system as computer storage allows. Locations may be geographically distinct or may be embedded within an existing location at a higher resolution. The user can rapidly change from one location to another by simply pointing to the appropriate data set.

Geographic Information System (GIS)

The embedded GIS allows the user to input, store, manipulate and display geographically referenced information. The simplified GIS has been designed to be user friendly, interactive, and fast. GIS data is often helpful in analyzing and interpreting model predictions. The GIS allows an unlimited number of geographic databases to be created each with multiple layers of data. Typical uses of the GIS include storing location names, natural resources (bird colonies, shellfishing areas, beaches, marshes, vegetation), pollutant sources, geographical reference points such as buoys and channels, and environmental data (bathymetry, sediment type, rivers and flow data etc.). Through the use of linking procedures, additional information about geographically referenced data can be accessed. These link files include charts, graphics, tables, tutorials, bibliographies, text, scanned charts, photographs, or animations. Examples of data which might be stored in the



GIS for a typical sewage outfall siting problem include: contaminant source strengths versus time for the discharge, details and photographs of outfall locations and configurations, water column and sediment quality information, distribution and abundance of biota including shellfish, fish, birds, and marine mammals.

Sample Applications

The following are some examples of various configurations of WQMAP that have been assembled to respond to our client's needs:

Dredging Impacts

A two-dimensional time dependent hydrodynamic and pollutant transport model application to predict the distribution of suspended sediments and pollutants as a result of dredging and disposal operations. Required inputs are tidal constituents at the open boundary and river flows for the hydrodynamic model. Inputs for the pollutant transport model are time varying loads simulating material release from dredging operations. Output includes contours of pollutant levels over time and maximum impacts.

Two Layer Channel Flow

A three-dimensional time-dependent hydrodynamic model application to predict the occurrence of two layer flow in a channel connecting water bodies of different densities. Required inputs are system geometry and basin densities and elevations. Output is a time varying velocity structure through the channel.

Thermal Impacts

A three-dimensional time dependent hydrodynamic model application to predict the extent of thermal plume from an electrical generating facility using once through cooling. Required inputs are open boundary tide height, temperature and salinity; river flow and temperature; and solar and atmospheric radiation. Outputs include the contours of temperature and temperature rise due to the plant over time.

Fecal Coliform Exceedance

A three-dimensional hydrodynamic and pollutant transport model application to predict the distribution of fecal coliforms (FC). Required inputs are freshwater flows and tidal elevations for the hydrodynamic model and FC loads and decay rate for the pollutant transport model. Output is a time varying set of FC concentrations and area-time exceedances of water quality standards.

Causeway Removal Impacts

A three-dimensional time-dependent hydrodynamic and pollutant transport model application to predict the changes in circulation and water quality from the removal of a highway causeway. Required inputs are system geometry, altered system geometry, river flow and load inputs. Outputs are, time varying velocity, numerical flushing estimates, sedimentation rates and phosphorus concentrations.